



UNIVERSITY OF
KWAZULU-NATAL

INYUVESI
YAKWAZULU-NATAL

CARBON DIOXIDE ENCAPSULATION IN METHANE HYDRATES

Ndlovu Phakamile

B. Eng. (Chemical Engineering), NUST - Bulawayo, Zim

MSc. Eng. (Chemical Engineering), UKZN - Durban, South Africa

Submitted in fulfillment of the Academic Requirements for the Awards of the Doctor of
Philosophy in Engineering at the School of Chemical Engineering,
University of KwaZulu-Natal.

December 2022

Supervisors: Prof Paramespri Naidoo, Dr. Saeideh Babaee, Dr. Kuveneshan Moodley

DECLARATION 1 - Plagiarism

I, **Ndlovu Phakamile**, declare that

1. The research reported in this thesis, except where otherwise indicated, is my original research.
2. This thesis has not been submitted for any degree or examination at any other university.
3. This thesis does not contain other persons' data, pictures, graphs, or other information unless expressly acknowledged as being sourced from others.
4. This thesis does not contain other persons' writing unless expressly acknowledged as being sourced from other researchers. Where other written sources have been quoted, then:
 - a. Their words have been re-written, but the general information attributed to them has been referenced
 - b. Where their exact words have been used, their writing has been placed in italics, inside quotation marks, and referenced.
5. This thesis does not contain text, graphics, or tables copied and pasted from the Internet unless expressly acknowledged. The source is detailed in the thesis and the References sections.

Signed

12/12/2022

Date

As the candidate's supervisor, I agree to the submission of this thesis:

Supervisor

Date

DECLARATION 2 - Publications

DETAILS OF CONTRIBUTION TO PUBLICATIONS that form part and include research presented in this thesis (include publications in preparation, submitted, *in the press* and published and give details of the contributions of each author to the experimental work and writing of each publication)

Publication 1: Fuel Journal 320, (2022) 123795.

Title: Review on CH₄-CO₂ replacement for CO₂ sequestration and CH₄/CO₂ hydrate formation in porous media.

Authors: Ndlovu, P., Babae, S., Naidoo, P.,

Publication 2: Journal of Molecular Liquids 371 (2023) 121109.

Title: Experimental Study of CH₄-CO₂ Replacement in Gas Hydrates in the Presence of Nitrogen and Graphene Nanoplatelets

Authors: Ndlovu, P., Babae, S., Naidoo, P.,

Publication 3: Journal of Greenhouse Gas (Manuscript ready for submission)

Title: Kinetics of CO₂ Hydrate in the Presence of Nanoparticles: Application of Gas Hydrate in CO₂ Capture.

Author: Ndlovu, P., Babae S., Naidoo, P., Moodley K.,

Publication 4: Energy & Fuels (Manuscript ready for submission)

Title: The use of Nanoparticles to Improve the Kinetics of CH₄ Gas Hydrates in Gas Storage applications

Author: Ndlovu, P., Babae S., Naidoo, P., Moodley K.,

Publication 5: Chemical Engineering Journal (Manuscript in preparation)

Title: Bubbling of CO₂ Gas for Storage in CH₄-Silica Gas Hydrates through Thermal Stimulation and addition of a Secondary gas in the presence of Graphene nanoplatelets.

Author: Ndlovu, P., Babae S., Naidoo, P., Moodley K.,

Acknowledgments

- I acknowledge my supervisors, Prof Paramespri Naidoo, Dr. Saeideh Babae, and Prof. Kuveneshan Moodley, for their guidance, assistance, and patience in this study.
- My colleagues from the University of KwaZulu-Natal for their friendship, advice, and support, as well as the support staff in the department in this study.
- The financial support of the Department of Science and Technology and the National Research Foundation, Grant UID 16808, and the Thermodynamics Research Unit (TRU) is acknowledged.
- My parents, Parton and Zondi Ndlovu, the family uGwalisa omkhulu, my brothers, sisters, and friends, thank you for the support and encouragement throughout this journey. My niece Onesisa and my nephew Phokuhle I love you.
- Above all to God, the omniscient one “In whom we live and move and have our being”

*“Go into the world and do well. But more importantly, go into the world and do good”. -
Minor Myers*

Abstract

Coal mining and petroleum refining processes face extreme pressure under climate change and global warming threats. Hence alternative sustainable and renewable energy sources must be made available for the rising energy demands. Natural gas found in permafrost and seabed areas in the form of gas hydrates possess vast amounts of low-carbon methane gas, which can replace fossil-based energy sources. The capture and storage of carbon dioxide gas in natural gas hydrate beds with the release of methane gas is a sustainable route under intense research.

This study investigates the methane-carbon dioxide ($\text{CH}_4\text{-CO}_2$) replacement reaction mechanisms and the improvement of the process using different techniques, namely, additives, secondary gas, and thermal stimulation. Firstly, the gas hydrate dissociation measurements for the former gases utilized in the study were performed. This was followed by kinetic measurements with nanoparticles (aluminum oxide, copper oxide, and graphene nanoplatelets) and chemical additives (zinc oxide powder, graphite powder, and magnesium nitrate hexahydrate crystals) in the presence of sodium dodecyl sulfate (SDS) to affect kinetic or thermodynamic improvement in hydrate formation. The kinetic parameters investigated were induction time, hydrate storage capacity, water consumed in hydrate formation, fugacity of the gaseous phase, and the ratio of gas consumed to moles of water. Graphene nanoplatelets were selected for replacement reaction based on promising results obtained from the kinetic studies. The $\text{CH}_4\text{-CO}_2$ replacement process was performed in a 52 cm^3 equilibrium cell using deionized water and nanoparticles. Also, a new experimental setup with a 300 cm^3 reaction vessel was designed and assembled for $\text{CH}_4\text{-CO}_2$ replacement in the presence of synthetic silica sand.

The results from kinetic studies showed an improvement in the hydrate formation kinetics due to the presence of nanoparticles. The CO_2 hydrate formation kinetics obtained a maximum storage capacity of 51 (v/v), with 1.2 wt.% graphene nanoplatelets which also produced a maximum water conversion of 25%. When nanoparticles were added, the induction time for CO_2 hydrate in deionized water was reduced from 9 minutes to less than one minute. Graphite powder with a concentration of 1.2 wt.% had the highest rate of gas uptake of 0.0024 (mol of gas/ mol of water. min). In CH_4 kinetics, the induction time was reduced from 18 minutes with deionized water to less than one minute due to addition of nanoparticles. A maximum storage capacity of 28.5 (v/v), water-to-hydrate conversion of 13.09%, rate of gas uptake of 0.0089 (mol of gas/ mol of water. min), and gas consumption of 0.0238 moles were obtained with 0.1 wt.% CuO + 0.05 wt.% SDS. Also, $\text{CH}_4\text{-CO}_2$ replacement measurements showed that an 80 mol% N_2 /20 mol% CO_2 gas mixture yielded a CH_4 replacement efficiency of 17.04% at a

temperature of 274.77 K and pressure of 5.34 MPa. The highest amount of CO₂ sequestered was 57.03%, and 28.77% was the highest CH₄ replacement efficiency. These results were obtained using pressurized CO₂ with application of thermal stimulation at a temperature of 275.90 K and pressure of 5.66 MPa. In the replacement reaction with silica sand, the maximum amount of CH₄ replaced was 37.49% with the pressurized CO₂ at a pressure of 7.01 MPa and temperature of 276.43 K. Applying thermal stimulation and adding secondary gas (N₂) improved CO₂ sequestration from 51.73% to 76.63%. These outcomes are vital in applying hydrates in gas storage and CO₂ sequestration.

Table of Contents

DECLARATION 1 - Plagiarism	i
DECLARATION 2 - Publications	ii
Acknowledgments	iii
Abstract	iv
List of Figures	x
List of Tables	xiii
Nomenclature	xiv
List of Symbols	xvi
Greek Alphabet	xvii
Chapter 1	1
1 Introduction.....	1
1.1 Aim and Objectives.....	6
1.2 Thesis Overview	7
Chapter 2: Literature Review	9
2 Introduction.....	9
2.1 Hydrates Structure	9
2.1.1 Gas Hydrates Formation Kinetics	10
2.1.2 Thermodynamics.....	12
2.2 Hydrate promoters and inhibitors	12
2.3 Hydrate formation in porous media	14
2.4 Hydrate formation with nanoparticles.....	17
2.5 The effect of porous media on CH ₄ and CH ₄ /CO ₂ hydrate formation	19
2.6 The effects of additives utilized with adsorbents in CH ₄ and CO ₂ hydrate formation.....	22
2.7 Replacement of CH ₄ with CO ₂ from its Hydrate.....	25
2.7.1 Factors affecting replacement reaction	25
2.7.2 Limitations in the replacement process.....	26
2.8 Hydrates as a Carbon capture and storage (CCS) technology	27
2.8.1 Commercial CO ₂ Capture Technologies	27
2.8.2 Hydrates in CO ₂ capture.....	28
2.9 Hydrates as an Energy Resource.....	31
2.10 Gas storage in solid systems	33
2.10.1 Various Gas Storage Technologies	34
2.10.2 Current trends in South African Energy Sector	36
Chapter 3: Review of equipment and experimental techniques for CH₄-CO₂ replacement	37
3. Introduction.....	37
3.1 Principles of equilibrium apparatus and technique development.....	37

3.1.2	Classification of techniques and equipment.....	38
3.2	Techniques for determination of dissociation point measurement	38
3.3	Apparatuses utilized in hydrate phase equilibrium measurements	40
3.3.1	Summary of equipment utilized in hydrate phase equilibrium	41
3.3.2	Equipment for investigating the hydrate structure	42
3.4	Equipment used for CH ₄ -CO ₂ replacement reactions without porous media	43
3.5	Equipment Designs for CH ₄ -CO ₂ dioxide replacement with porous media	46
Chapter 4: Kinetics Studies, Measurements, Modeling and Results.....		49
4	Introduction.....	49
4.1	Apparatus	49
4.2	Materials	50
4.3	Experimental method	51
4.3.1	Calibration of Sensors	51
4.3.3	Uncertainty in measured variables	53
4.4	Experimental Measurements.....	54
4.4.1	Leak Testing.....	54
4.4.2	Preparation of the equilibrium cell.....	54
4.4.3	Sample preparation	55
4.4.4	Hydrate formation measurements	55
4.4.5	Shutdown procedure	56
4.5	Kinetic Model	56
4.6	Results and Discussions	57
4.6.1	Test systems	57
4.7	Carbon Dioxide Kinetics Results.....	58
4.7.1	Kinetics of Hydrate Formation	58
4.7.2	Induction time	59
4.7.3	Temperature Variations.....	62
4.7.4	Pressure Variation	63
4.7.5	Storage Capacity	65
4.7.7	Rate of gas uptake	68
4.7.8	Water to hydrate conversion percentage	70
4.8	Methane Gas Kinetics	71
4.8.1	Induction Time.....	72
4.8.2	Effects of temperature variation on kinetic parameter	73
4.8.3	Effects of pressure variations on kinetic parameter	74
4.8.4	Kinetic Parameter with Additives	74
4.9	Summary	78

Chapter 5: CH₄ replacement with CO₂ in CH₄ hydrates.....	80
5 Introduction.....	80
5.1 Apparatus.....	80
5.2 Materials.....	81
5.3 Experimental methods.....	81
5.3.2 Gas Chromatography detector calibration.....	82
5.3.3 Uncertainty in measurements.....	87
5.4 Experimental Section.....	88
5.4.1 Sample preparation.....	88
5.4.2 Methane hydrate formation.....	88
5.4.3 Purging of CH ₄ in the gas phase.....	89
5.4.4 Preparation of Gas Mixtures.....	89
5.4.5 Replacement reaction procedure.....	89
5.4.6 Shutdown procedure.....	90
5.5 Calculation of CH ₄ and CO ₂ in the replacement.....	90
5.6 Results and Discussion.....	92
5.6.1 Test systems - hydrate dissociation data.....	92
5.6.2 Replacement using pressurized CO ₂	93
5.6.3 Addition of a secondary gas in the replacement process.....	97
5.6.4 Addition of Nanoplatelets.....	99
5.6.5 Thermal stimulation.....	109
5.7 Summary.....	110
Chapter 6: CH₄- replacement with CO₂ in CH₄-silica sand hydrates.....	111
6 Introduction.....	111
6.1 Equipment description.....	111
6.1.1 Equilibrium cell.....	113
6.1.2 Sparger design.....	114
6.1.3 Sampling points.....	115
6.1.4 Gas vessels.....	115
6.1.5 Keysight DAQ970A data logging system.....	115
6.1.6 Edwards Vacuum pump.....	116
6.1.7 Pressure regulator.....	116
6.1.8 Gas flowmeter.....	116
6.1.9 Temperature sensors.....	116
6.1.10 Pressure transducer.....	117
6.1.11 Temperature Controller.....	117
6.1.12 Water bath.....	117

6.1.13 ISCO Syringe pump	117
6.2 Materials	118
6.3 Experimental methods	118
6.3.1 Calibrations of sensors	118
6.3.2 Uncertainty in measured variables	119
6.4 Experimental Procedure	120
6.4.1 Leak testing	120
6.4.2 Preparation of the equilibrium cell.....	120
6.4.3 Sample preparation	120
6.4.4 Methane hydrate formation in porous media	121
6.4.5 CH ₄ -CO ₂ hydrate replacement	121
6.4.6 Preparation of gas mixtures.....	122
6.5 Calculations of CH ₄ and CO ₂ in the Replacement Process	122
6.6 Results and Discussions	124
6.6.1 Test Systems- silica hydrate dissociation data	124
6.6.2 Methane-silica hydrate formation	125
6.6.3 Analysis of silica-CH ₄ hydrate	127
6.6.4 Addition of carbon dioxide	129
6.6.5 Analysis of CH ₄ -CO ₂ replacement reactions	133
6.7 Summary	137
Chapter 7: Conclusions	138
7.1 Implications.....	139
Chapter 8: Recommendations	140
References	141
Appendices	168
Appendix A	168
Appendix B	186
Appendix C	193
Appendix D	198
Appendix E	204
Appendix F.....	219
Appendix G.....	229

List of Figures

Figure 1.1: Natural occurring methane gas in natural gas hydrates in various areas underground (Machens 2006).	4
Figure 2.1: The three hydrate unit crystals and their cavity arrangements (Koh et al., 2011).	9
Figure 2.2: Mechanism of formation of gas hydrates formation from the labile theory (Extracted from Sloan and Koh, 2008).	11
Figure 2.3: Pictorial view of three steps of CH ₄ hydrate formation at the CH ₄ -H ₂ O interface (Koga et al., 2010).	11
Figure 2.4: Phase diagram for CH ₄ , CO ₂ , N ₂ flue gas (85.4%N ₂ and 14.6% CO ₂) and mixtures of flue gas with CH ₄ (broken line) with respect to temperature (Hassanpouryouzbznd et al., 2019).	12
Figure 2.5: Schematic view of structures of SDS micelles and M-micelles promoting hydrate formation (He et al., 2019).	14
Figure 2.6: Schematic illustration of the four types of gas hydrate growth habits in porous media (Priegnitz, 2015).	15
Figure 2.7: Hydrate formation in porous media with different particle sizes (Bhattacharjee et al., 2015).	16
Figure 2.8: Methane hydrate formation on graphite in the presence of SDS (Deng et al., 2021).	22
Figure 2.9: Overview of Carbon capture Technologies (Adu et al. 2019).	27
Figure 2.10: Pictorial representation of terrestrial and marine occurrences of hydrates (Hassanpouryouzbznd et al., 2020).	31
Figure 3.1: Pressure-Temperature plot utilizing the isochoric method for methane hydrate (figure produced in this work).	40
Figure 4.1: A schematic of the experimental setup:	50
Figure 4.2: Temperature calibration chart for and uncertainty scatter for the temperature probe for the kinetics cell.	52
Figure 4.3: Pressure calibration chart and uncertainty scatter for the pressure probe of the equilibrium cell utilised in kinetic measurements.	53
Figure 4.4: Hydrate dissociation points for the CO ₂ and water system:(♦) Kinetics cell (*) Deaton and Frost (1946); (Δ) Englezos and Hall (1994); (○) Mohammadi et al. (2005).	58
Figure 4.5: Hydrate dissociation points for the CH ₄ and water system:(●) Kinetics cell (◇) Deaton and Frost (1946); (*) Roberts (1940); (Δ) Gallowing et al. (1970).	58
Figure 4.6: The driving force between the initial kinetic experimental conditions and CO ₂ hydrate equilibrium line (○) initial pressure, (●) dissociation points for CO ₂	59
Figure 4.7: Illustration of determination of induction time from a temperature - pressure vs. time plot.	60
Figure 4.8: Effects of temperature variation on a) storage capacity, b) gas consumption, c) mol of gas consumed to mole of water, d) water consumed in CO ₂ hydrate formation at a pressure 4.07 MPa. Uncertainty U(T) = ±0.1 K, U(P) = 0.01 MPa Uconcentration (wt%)=0.06% U(t)=0.01s.	62
Figure 4.9: Effects of pressure variation on a) storage capacity, b) gas consumption, c) mol of gas consumed to mole of water, d) water consumed in CO ₂ hydrate formation at a temperature 275.8K. Uncertainty U(T) = ±0.1 K, U(P) = 0.01 MPa Uconcentration (wt%)=0.06% U(t)=0.01s.	64
Figure 4.10: Storage capacity of CO ₂ hydrate formation for a) aluminum oxide (Al ₂ O ₃) nanoparticles, b) copper oxide (CuO) nanoparticles, c) graphene (GPN) nanoplatelets, d) graphite (C-C) powder, e) zinc Oxide (ZnO) powder, f) magnesium nitrate hexahydrate (H ₁₂ MgN ₂ O ₁₂) crystals at 275.8 K and	

3.41 MPa in concentrations specified. Uncertainty $U(T) = \pm 0.1$ K, $U(P) = 0.01$ MPa $U_{concentration}$ (wt%)=0.06% $U(t)=0.01$ s.....	66
Figure 4.11: Carbon dioxide consumed in hydrate formation for a) aluminium oxide (Al_2O_3) nanoparticles, b) copper oxide (CuO) nanoparticles, c) graphene (GPN) nanoplatelets, d) graphite (C-C) powder, e) zinc Oxide (ZnO) powder, f) magnesium nitrate hexahydrate ($H_{12}MgN_2O_{12}$) crystals at 275.8 K and 3.41 MPa in concentrations specified. Uncertainty $U(T) = \pm 0.1$ K, $U(P) = 0.01$ MPa $U_{concentration}$ (wt%)=0.06% $U(t)=0.01$ s.....	67
Figure 4.12: Rate of CO_2 consumption during hydrate formation for a) aluminum oxide (Al_2O_3) nanoparticles, b) copper oxide (CuO) nanoparticles, c) graphene (GPN) nanoplatelets, d) graphite (C-C) powder, e) zinc Oxide (ZnO) powder, f) magnesium nitrate hexahydrate ($H_{12}MgN_2O_{12}$) crystals at 275.8 K and 3.41 MPa in concentrations specified. Uncertainty $U(T) = \pm 0.1$ K, $U(P) = 0.01$ MPa $U_{concentration}$ (wt%)=0.06% $U(t)=0.01$ s.....	69
Figure 4.13: Percentage of water conversion in CO_2 hydrate formation for a) aluminium oxide (Al_2O_3) nanoparticles, b) copper oxide (CuO) nanoparticles, c) graphene (GPN) nanoplatelets, d) graphite (C-C) powder, e) zinc Oxide (ZnO) powder, f) magnesium nitrate hexahydrate ($H_{12}MgN_2O_{12}$) crystals at 275.8 K and 3.41 MPa in concentrations specified. Uncertainty $U(T) = \pm 0.1$ K, $U(P) = 0.01$ MPa $U_{additive}$ (wt%)=0.06% $U(t)=0.01$ s.....	71
Figure 5.1: Schematic diagram of the experimental setup utilized in CH_4 - CO_2 replacement without porous media.....	81
Figure 5.2: Calibration of the temperature probe (LHS) and plot of the temperature deviation (RHS) used for the temperature probe utilized in the equilibrium cell.	82
Figure 5.3: Calibration plot of the WIKA pressure transducer (LHS) and pressure deviation (RHS) used in a reactor vessel.	82
Figure 5.4: GC detector calibration curve for pure CO_2 (LHS) and deviations in measurements in the calibration (RHS).	85
Figure 5.5: GC detector calibration curve for pure CH_4 (LHS) and deviations in measurements in the calibration (RHS).	85
Figure 5.6: GC detector calibration of methane (2)/carbon dioxide (1) binary mixture (LHS) and methane (2)/carbon dioxide (1) binary mixture. (RHS).	86
Figure 5.7: Comparison of GC detector response calibration curves for pure gases and binary mixture (*..... Pure gases, ● - - - - Gas mixture).	86
Figure 5.8: GC detector calibration for methane-carbon dioxide (LHS) and nitrogen-carbon dioxide (RHS) calibration curve for nitrogen-methane-carbon dioxide system.	87
Figure 5.9: Hydrate dissociation points (LHS) and L.N. P vs $1/T$ correlation (RHS) for the CO_2 and water system: (◆) Exp, This work, (◐) Deaton and Frost (1946); (△) Englezos and Hall (1994); (●) Mohammadi et al. (2005).	93
Figure 5.10: Hydrate dissociation points (LHS) and L.N. P vs $1/T$ (RHS) for the CH_4 and water system:(●) Exp, this work, (◆) Deaton and Frost (1946); (×) Roberts (1940); (△) Gallowing et al. (1970).	93
Figure 5.11: Picture of the cell showing CH_4 hydrate after formation without replacement reaction.	96
Figure 5.12: CH_4 - CO_2 Replacement reaction profile for experimental run 2 (◆ CO_2 , ○ CH_4) $U(ni) = 0.005$	97
Figure 5.13: Photograph of the cell content showing the hydrate at the end of CH_4 - CO_2 replacement reaction.....	98
Figure 5.14: $CH_4 + 80$ mol% $N_2/20$ mol% CO_2 gas mixture + H_2O replacement reaction profile for experimental run 4 (◆ CO_2 , ○ N_2 , ●. CH_4) ($U(ni) = 0.03$).....	99
Figure 5.15: Picture of the cell contents showing the methane hydrate - 0.0.5wt.% SDS + 0.5wt.% graphene nanoplatelets solution hydrate.	103

Figure 5.16: Pictures of different views of the hydrate formed with 0.05 wt.% SDS + 0.5wt.% graphene nanoplatelets over 12 minutes time period in an open environment. **Error! Bookmark not defined.**

Figure 5.17: CH₄ + 80mol% N₂/20mol% CO₂ + 0.05wt.% SDS+0.5wt.% graphene nanoplatelets replacement reaction profile for experimental run 7 (♦ CH₄, ●CO₂, □N₂) (U (ni) = 0.03). 106

Figure 5.18: CH₄ + 90mol% CO₂/10mol% N₂ + 0.05wt.%SDS + 0.05wt.% graphene nanoplatelets replacement reaction profile for experimental run 8 (♦ CO₂, ●CH₄, ○N₂). (U (ni) = 0.03)..... 107

Figure 5.19: Temperature-pressure against time for run 5, carried out at 7.6 MPa and 275 K (-) pressure, (-) temperature. 108

Figure 5.20: Temperature-Pressure against time for experimental run 9, 0.05 wt.% SDS + 0.5wt.% graphene at 7.5MPa and 275 K (-) pressure, (-) temperature..... 108

Figure 5.21: Comparison of the percentages of CO₂ sequestrated and CH₄ replaced in all the runs carried out in the study..... 109

Figure 6.1: Equipment setup designed for use in this study for the CH₄ replacement CO₂ in the CH₄-silica hydrate. 112

Figure 6.2: Pictorial view of the replacement cell with some of its auxiliary components. 113

Figure 6.3: Pictorial view of a) sparger, b) bottom flange with the sparger c) testing of sparger in a beaker. 114

Figure 6.4: Calibration of the temperature probe 101 (LHS) and plot of the temperature deviation (RHS) used for the temperature probe utilized in the reactor vessel. 118

Figure 6.5: Calibration plot of the WIKA pressure transducer (LHS) and pressure deviation (RHS) used in a reactor vessel. 119

Figure 6.6: Hydrate dissociation points (LHS) and ln P vs 1/T (RHS) CH₄ -water system with different additives(*) CH₄ -water system in 52 ml cell, (o) 75-90 μm silica – CH₄-H₂O in 52 ml cell, (●) 280 μm silica -CH₄-H₂O in a 300 ml cell (utilized in this study), (□) 280 μm silica – CH₄-H₂O in 52 ml cell, (×) 100 nm porous glass (Uchida et al., 2002), (◇) 50nm porous glass (Uchida et al., 2002). 124

Figure 6.7: Photograph of silica sand in the cell a) before hydrate formation b) - c) after hydrate formation d) 0.5 wt.% graphene-silica sand-methane hydrate. 127

Figure 6.8: Photographs of hydrates formed with silica sand-methane gas-water examined from the surface to the core. 128

Figure 6.9: Photographs of hydrates formed with 0.5 wt.% graphene-silica sand-methane gas-water examined from the surface to the centre. 129

Figure 6.10: Replacement profile for an experimental run one between CH₄-silica-H₂O and CO₂... 131

Figure 6.11: Replacement profile for experimental run 4 between CH₄-silica-H₂O and CO₂. 131

Figure 6.12: Replacement profile for experimental run 6 between CH₄-silica-H₂O and CO₂ (-) Pressure, (-) Temperature..... 132

Figure 6.13: Photograph obtained from CH₄-CO₂ replacement reaction in the presence of 0.5 wt.% graphene nanoplatelets a) bottom view b) top view c) & d) side view of the hydrate, e) length of the gas hydrate, f) side view of the hydrate with the top layer scraped off g) side view of the gas hydrate after 5 minutes of cell opening h) side view after 10 minutes of cell opening. 135

Figure 6.14: Percentages of CO₂ sequestrated and CH₄ replacement efficiency..... 136

List of Tables

Table 2.1: Studies on effects of nanoparticles on gas hydrate formation with CH ₄ and CO ₂ gases.	18
Table 2.2: Summary of adsorbents utilized in the formation of CH ₄ and CO ₂ gas hydrates.....	20
Table 2.3: Adsorbents that are utilized with additives in the formation of CH ₄ and CO ₂ hydrates.	24
Table 3.1: Experimental techniques utilized in hydrate measurements (Babee, 2015; Croeser, 2017)	39
Table 3.2: Summary of equipment designs utilized for CH ₄ -CO ₂ replacement reaction without porous media.....	44
Table 3.3: Summary of experimental apparatus and techniques used for the CH ₄ -CO ₂ replacement reaction with porous media.	47
Table 4.1: Specification and description of chemical utilized in the study.....	51
Table 4.2: Summary of the source of uncertainty for variables reported in this study.	54
Table 4.3: Induction time for carbon dioxide hydrate system with additives.	61
Table 4.4: Induction time for methane hydrate formation with additives.	72
Table 4.5: Kinetic results obtained at a pressure of 4.66 MPa and different initial temperatures over 100 minutes.....	73
Table 4.6: Kinetic results obtained at a pressure of 275.8K and different initial pressures over 100 minutes.....	74
Table 4.7: Summary of kinetic parameters obtained with CH ₄ gas and additives utilized in the study (Maximum & Minimum).	76
Table 5.1: TCD calibration results for CO ₂ and CH ₄ showing the maximum relative absolute errors with a first-order polynomial.	85
Table 5.2: Summary of the source of uncertainty for variables reported in this study	87
Table 5.3: Molar composition uncertainty due GC Calibration adapted from (NIST et al., 1994).....	87
Table 5.4: Molar composition uncertainty due Gas mixture preparation.....	88
Table 5.5: Methane- hydrate formation and replacement analysis with CO ₂ /N ₂ gas mixtures.	94
Table 5.6: Carbon dioxide encapsulation in the replacement process with CO ₂ /N ₂ gas mixtures.	95
Table 5.7: Methane- hydrate formation with graphene nanoplatelets and SDS balance.....	101
Table 5.8: Carbon dioxide encapsulation in the replacement process with CO ₂ , and CO ₂ /N ₂ gas mixtures.	102
Table 6.1: Summary of the source of uncertainty for variables reported in this study.	119
Table 6.2: Reactor conditions and feeding specifications.....	121
Table 6.3: Methane hydrate formation with silica sand main parameters.....	125
Table 6.4: CO ₂ addition for CH ₄ replacement main parameters.	130
Table 6.5: Efficiency of CH ₄ replacement and CO ₂ sequestration ratio.....	133

Nomenclature

AA	Anti-agglomerates
AC	Activated carbon
BGHS	Base gas hydrate stability
CBG	Compressed biomethane
CCS	Carbon capture and storage
CLC	Chemical looping combustion
CMG	Computer Modelling Group
COP	Coefficient of Performance
CuO	Copper oxide
D	Diffusion coefficient
DEA	Diethanolamine
DEPG	Dimethyl ether of polyethylene glycol
DMCH	Dimethylcyclohexane
DTA	Differential Thermal Analysis
EGHR	Enhanced Gas Hydrate Recovery
GACR	Geothermal-assisted CO ₂ replacement
GHBS	Gas hydrate bearing sediments
GC	Gas Chromatography
GO	Graphene oxide
GPN	Graphene nanoparticles
HBGS	Hydrate-based gas separation
HBL	Hydrate bearing layer
HP-DSC	High-pressure Differential scanning Calorimetry
HPF	Hydrate pack factor
HEC	Hydroxyl ethyl cellulose
HS	Hollow silica
HyRes	Hydrate Reservoir simulator
IGCC	Integrated Gasification Combined Cycle
K	Kelvin
KI	Kinetic inhibitors

LBG	Liquefied biomethane
LDHI	Low dosage hydrate inhibitors
LNG	Liquefied Natural Gas
MEA	Monoethanolamine
MRI	Magnetic resonance imaging
MTBE	Methyl tert-butyl ether
MWCNTs	Multi-walled carbon nanotubes
NGH	Natural gas hydrates
OMWCNTs	Oxidised multi-walled carbon nanotubes
PSNS	Polystyrene nanosphere
PCM	Phase change materials
PRT	Platinum resistance thermometer
PXRD	Powder X-ray diffraction
QAS	Quaternary ammonium salts
QCM	Quartz crystal microbalance
QMD	Quantum mechanics molecular dynamics
RCB	RetrasoCodeBright
SEC	Specific energy consumption
SDS	Sodium dodecyl sulfate
SNP	Synthesized silver nanoparticles
STAR	Steam, Thermal and Advanced Process Reservoir Simulator
SUGAR	Submarine Gas Hydrate Reservoirs
TCD	Thermal conductivity detector
THF	Tetrahydrofuran
TBAB	Tetrabutylammonium bromide
TBACl	Tetrabutylammonium chloride
TBPF	Tetrabutylphosphonium bromide
UNEP	United Nations Environmental Policy
US	United States
ZIF	Zeolite Imidazolate framework

List of Symbols

Symbol	Description	Unit
A	area	m ²
C	concentration	g/cm ³
°C	degrees celcius	
G	Gibbs free energy	
<i>f</i>	fugacity	Pa
K	Kelvin	
K _{app}	apparent rate constant	Mol.G/molW.Pa.min
K _d	dissociation rate constant	
n	moles	mol
n _d	moles dissolved in water	mol
n _w	moles of water	mol
P	pressure	Pascals
R	universal gas constant	J/mol-K
S _g	gas saturation	
S _h	water hydration	m ³ /m ³
S _w	water saturation	m ³ /m ³
T	temperature	K
<i>t</i>	time	s
<i>u_c</i>	combined standard uncertainty	
V	volume	m ³
V _{cell}	volume of cell	m ³
V _{pores}	pore volume	
X	hydration number	mol/mol
Z	compressibility factor	

Greek Alphabet

Symbol	Description	Units
Δ	Change in property	-
η	Efficiency	-
μ	Chemical potential	J/mol
ρ	Density	-
β	Empty hydrate phase	-
γ	Activity coefficient	-
θ	Cage occupancy	-
\emptyset	Fugacity coefficient	-

Chapter 1

1 Introduction

High atmospheric carbon dioxide (CO₂) levels have exacerbated climate change (Ravanchi et al., 2021). These emissions are caused by a significant dependence on fossil fuel-generated power for electricity and automobiles in our modern civilization (Solomon et al., 2007; Gambelli et al., 2021). Sources of atmospheric CO₂ are divided into two sectors. The first source is due to the naturally occurring processes, such as respiration and decomposition, which account for most of the CO₂ emissions in the atmosphere and are balanced out by natural carbon dioxide sink. The second source of CO₂ is due to human activities, including fossil fuel combustion in automobiles and industrial processes (Songolzadeh et al., 2012). Coal is a significant contributor to global carbon emissions, contributing approximately 38% of the total CO₂ emissions (Naquash et al., 2022).

The largest CO₂ emitters in South Africa are Eskom and Sasol. Eskom is the sole producer of thermal electricity from coal-fired furnaces and is reported to produce 224.7 million tonnes of CO₂ annually. Sasol an integrated energy, and chemical company, is the second-highest emitter, at 61.77 million tonnes of CO₂ per year (Flak, 2011). Under the Kyoto Protocol, all signatory countries were expected to reduce the discharge of greenhouse gases (by 5% by the year 2012 relative to the 1990 emission levels) and reduce the use of global warming substances (Breidenich et al., 1988). Also, according to the Paris Agreement, CO₂ emissions need to be reduced by 45% by 2030 and reach net zero by 2050 (UNCA, 2022). Bound by this agreement, South Africa is obligated to reduce its greenhouse emissions (UNEP, 2022). In this regard, Sasol South Africa (SA) is implementing renewable energy sources such as solar, hydro, and wind as alternatives (Makgalemele, 2015, Sasol, 2021). However, there is a need to address the current stack emissions.

Various techniques have been applied to capture and sequester CO₂ from process emissions. The main carbon capture methods can be classified as carbon capture and recycling (CCR) and carbon capture and storage (CCS) (Budinis et al., 2018). To date, no single sustainable solution has found a wide-scale application. Research studies continue to explore alternative or improved technologies for CO₂ capture. Carbon dioxide removal from coal power plants has been studied extensively via pre-treating fossil fuel, oxy-fuel, and post-combustion capture (Khalik and Behzad, 2018). The oxyfuel combustion process utilises oxygen instead of air thus reducing thermal NO_x. Pre-combustion consists of pre-treating the fuel (coal or natural gas)

before combustion. The pre-treatment for coal is carried out in a gasifier with limited oxygen forming syngas which consists of CO and H₂. The post-combustion process removes CO₂ from the flue after combustion has taken place by employing adsorption and absorption separation technologies. Adsorption uses a solid absorbent to bind CO₂ to its surface, with typical sorbents being activated carbon, zeolites, calcium oxides, hydrotalcites, molecular sieves and lithium zirconate (Wall, 2007). Absorption is another method implemented in the industry as means of CO₂ capture. Chemicals such as methyl diethanolamine (MDEA), monoethanolamine, dimethyl ether of polyethylene glycol (DEPG), dialkyl imidazolium cations, 1-butyl-3-methylimidazolium tetrafluoroborate, and propylene carbonate have been studied for improving the absorption capacity of carbon dioxide (Cowdhury et al., 2013, Leung et al., 2014; Mai et al., 2018, Einloft, 2020).

Hydrate-based separation has shown promising results in CO₂ capture along with technologies such as mixed matrix membrane, chemical-looping combustion, integrated gasification combined cycle (IGCC), and enzyme-based separation applied for carbon dioxide capture from flue gases (Mondal et al., 2012; Wang et al., 2020). Chemical looping combustion (CLC) is an alternative method utilising a metal oxide as a solid oxygen carrier. The metal oxide reacts with a solid, liquid, or gaseous fuel in the fluidised bed combustor producing solid metal particles and a mixture of carbon dioxide and water vapour (Herzog et al., 2004). Integrated Gasification Combined Cycle (IGCC) plants have been installed for fossil fuel-powered stations which results in lower emissions of sulfur dioxide, particulates, mercury, and carbon dioxide (Cousins et al., 2015). The products from these stations are CO₂ and H₂ produced via a shift reaction in the ratio of 40 and 60 % respectively (Castellani et al., 2014). Mixed matrix membranes (MMMs) are composite materials made up of a polymeric matrix and inorganic or organic fillers, such as zeolites, metal-organic frameworks (MOFs), or carbon nanotubes. The incorporation of these fillers can enhance the gas separation properties of the membrane by creating additional gas transport pathways, increasing surface area, and modifying the surface chemistry (Li et al., 2018). Enzyme-based separation has emerged as a promising technology for CO₂ capture due to its potential for high efficiency and low energy consumption. Here are some examples of research papers related to enzyme-based separation in CO₂ capture (Al-Mamun et al., 2019).

The development of CCS technologies enables the electricity demand to be met with a small carbon footprint. Several CCS projects have been initiated; most of these plants are based in America. These have been utilized in the enhanced oil recovery process in the primary storage

for the captured CO₂ (Mai et al., 2018; Arlota et al., 2021). Geological sequestration of CO₂ in deep aquifers or depleted oil and gas reservoirs is a mature technology (Gentzis et al., 2000). Furthermore, the sequestration of CO₂ in permeable and porous underground rock at the Sleipner West gas field in the North Sea has been demonstrated to be safe, secure, and acceptable by the public (Holloway et al., 2003). Sasol Italy and Sonatrach Raffina have partnered with Polytechnic University of Turin to size a plant to capture and use CO₂ to produce liquid fuels and synthesize gas (syngas) (Environmental, 2021). The South African government has published a hydrogen roadmap that seeks to utilize renewable energy sources to produce green hydrogen, reducing fossil fuel usage. This strategy seeks to decarbonize the economy, foster economic growth and fully utilize its mineral resources to encourage a transition away from coal (Hydrogen society roadmap for South Africa, 2021; CSIS, 2022).

The conversion of CO₂ to renewable fuels and valuable chemicals (CCR) is a promising solution for reducing greenhouse emissions (Perathoner et al., 2009). This process has been researched to mitigate CO₂ emissions. One of the reactions involves the conversion of CO₂ to methanol through homogenous catalysis, heterogenous catalysis, photochemical, photoelectrochemical, and electrochemical conversion. In addition, the conversion of CO₂ into value-added chemicals such as formic acid, ethanol, and methanol has also been reported (Karame et al., 2018).

Under 2050 net zero emissions Sasol SA has envisaged a fossil-free future. Therefore, it has reinvented Secunda and Sasolburg operations away from coal-produced carbon and hydrogen to biogenic and green hydrogen, hence mitigating CO₂ emissions (Sasol Limited, 2021). In addition, Sasol and ArcelorMittal SA have signed a pact to develop a carbon capture technology to produce sustainable chemicals and fuels. In this partnership, “green steel” (steel manufactured without using fossil fuels) will be produced from green hydrogen. Furthermore, Sasol has partnered with Freeport Saldanha industrial development to develop a green hydrogen hub within Saldanha Bay (Energy Africa, 2022, Steyn, 2022).

The discovery of the ability of carbon dioxide to replace the methane molecule from its hydrate has opened a promising channel to solve the CO₂ emission-to-atmosphere problem. This can be achieved by extracting carboniferous fuel from natural hydrates while substituting methane (CH₄) with CO₂ (Seo et al., 2013). The German gas hydrate initiative under the Submarine Gas Hydrate Reservoirs (SUGAR) project was initiated in 2008 and is coordinated by GEOMAR Helmholtz Centre for Ocean Research Kiel. The SUGAR project was set up to combine natural

gas production with the safe sequestration of CO₂ in hydrates below the sea floor (Haeckel et al., 2004). The potential energy stored in natural gas hydrates introduces a form of closed-carbon dioxide cycle energy that can help reduce the CO₂ emission problem. Naturally occurring CH₄ beds under the earth's surface are shown in Figure 1.1. The figure shows two areas where a large portion of natural gas occurs. These are the permafrost region and the sea beds on the sea floor. The large volumes of CH₄ found in permafrost regions and on sea beds are stored in a matrix of silica sand and water molecules (Hassanpouryouzband et al., 2020). In South Africa, vast natural gas hydrates beds exist on the continental margin on the West Coast area (Petroleum Agency SA). Research investigations have reported methane extraction from natural silica beds and CO₂ storage efficiency (Englezos et al., 2008, Wang et al., 2021, Amon., et al., 2022, Fan et al., 2022).

Thus, silica sand is actively being investigated to increase gas storage in hydrate form. These investigations are motivated by the natural occurrence of natural gases in silica sand matrices in sea beds. Moreover, other porous media such as glass beads, activated carbon, and silica mixtures (simulating natural ground layers) are being investigated in hydrate formation to increase gas storage (Perrin et al., 2003, Zanota et al., 2005, Belosludov et al., 2007).

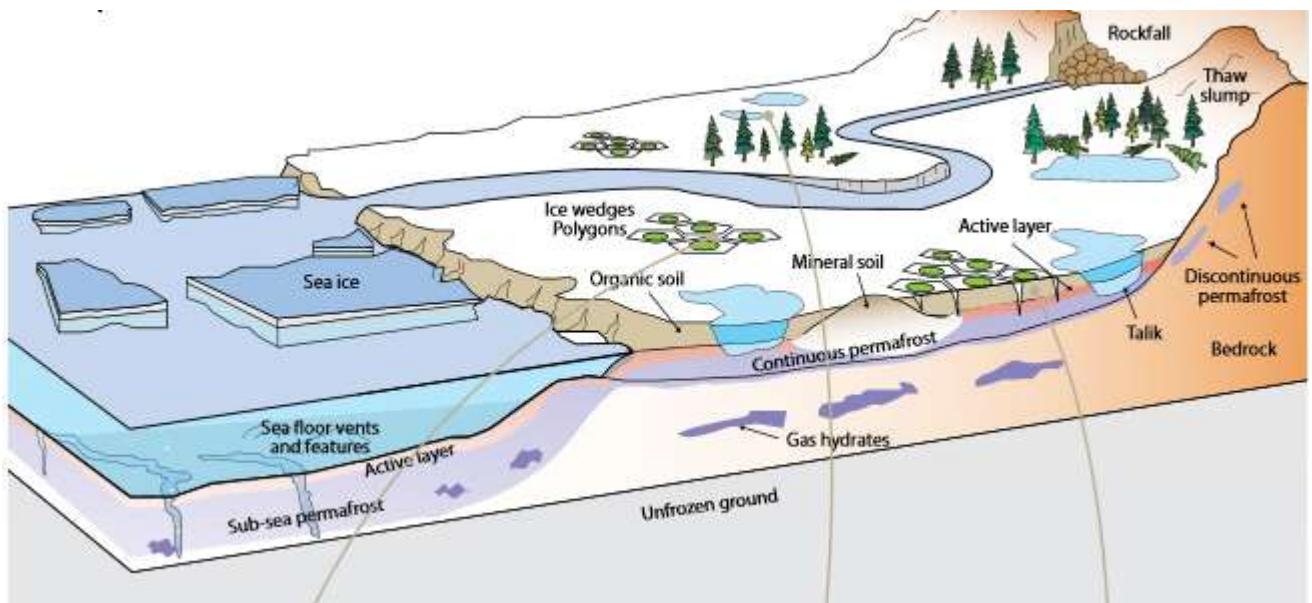


Figure 1.1: Natural occurring methane gas in natural gas hydrates in various areas underground (Machens, 2006).

Hydrate formation was discovered in the 1800s characterized by the transformation of water into a solid crystalline structure using a former gas encapsulated in water spaces. This occurred at temperatures higher than the freezing point of water (Makogon et al., 2007, Sloan and Koh, 2008). Studies on hydrate formation and characterization took an upswing in the 21st century

due to their occurrence in blocking natural gas transmission pipelines and terrestrial environments (Wan et al., 2019). Gas hydrates are non-stoichiometric compounds. They are composed of water molecules and small gas molecules such as methane, carbon dioxide, and propane trapped in the hydrate lattice with approximately 85% water and 15% gas (Lovedy and Nelmes, 2007, Siazik et al., 2017). Gas molecules are attached to water by a physisorption process which can be easily reversed by a change in temperature or pressure since the interaction is only physical (van der Waals) with no chemical interactions (McGrail et al., 2007). This mechanism allows the selective separation of gases with different molecular sizes by subjecting them to a gas hydrate formation environment (Babu et al., 2014).

The ability of CO₂ to form hydrates at pressure conditions lower than those of other gases in a flue gas mixture (approximately 1.2 MPa at the temperature of 273 K) makes hydrate technology a promising candidate method for CO₂ capture in the treatment of flue gas (Belandria, 2002). The hydrate formed from flue gases is expected to be rich in carbon dioxide. Thus, hydrate-based separation is based on the selective partitioning of components between the hydrate and gas phases (Demirbas, 2010). Although nitrogen, oxygen, and other component gases in the flue gas can form hydrates, these components only form hydrates at high pressure, allowing CO₂ capture into the hydrate at lower pressures (Xu et al., 2014). The formation pressure of nitrogen hydrate at 273 K is approximately 16 MPa, significantly above the hydrate formation pressure for CO₂ at this temperature (Belosludov et al., 2018).

Ongoing research on gas hydrate is perceived as a potential source of revenue for the future with the development of innovative technology processes. Moreover, gas hydrates can be a source of energy in the supply of natural gases for the future. An in-depth study of gas hydrate formation and dissociation is essential for drilling oil and production applications (Lee et al., 2011, Belosludov et al., 2018, Sa et al., 2019). The direction of gas hydrate research has changed from earlier studies that concentrated on preventing pipeline obstructions caused by hydrate development. The present emphasis is investigating the circumstances and chemical additions that encourage hydrate development (Herslund, 2013). Advances have been made in studying fuel gas (hydrogen) storage using hydrates. (Zhou, 2005, Davoodabadi et al., 2021) and gas separation (Tajima et al., 2004, Kang et al., 2013). Furthermore, it has been studied in the encapsulation of noble gases (Mondal and Chattaraj, 2014), natural gas/methane storage (Malagar et al., 2019), and natural gas hydrate deposits as a possible source of energy (Cannone et al., 2021). It has also been investigated in environmental safety (stability of seafloor and climate change), gas transportation, treatment of vinasse, gas separation and purification from

mixtures, desalination of seawater, subsea flow assurance and juice concentration (Xuab and Li, 2014, Croeser, 2017, Babu et al., 2020, Fakir et al., 2021).

Additives have long been applied in hydrate formation to improve the kinetics and thermodynamics of hydrate formation and gas storage (Kumar et al., 2004, Linga et al., 2009, Zanjani et al., 2012). Promoters such as tetra-n-butylammonium fluoride (TBAF), cyclopentane, quaternary ammonium/phosphonium, and neohexane exhibit great thermodynamic effectiveness in the formation of the hydrates (Zheng et al., 2017). Sodium dodecyl sulfate (SDS) can be added to reduce the surface tension of liquid water (Zhang et al., 2013), thus enhancing the dissolution of the hydrate former in the liquid. The presence of 1.0 mol% tetrahydrofuran (THF) substantially reduces the hydrate formation pressure from a flue gas mixture (CO₂/N₂) and allows capturing CO₂ at medium pressures. Hydrate formation was observed to preferentially form on the surface area of silica due to presence of SDS (Englezos et al., 2008). The use of nanoparticles in hydrate studies has yielded some positive output in enhancing gas storage and improving the kinetics of hydrate formation. Nanoparticles provide a suitable heterogeneous nucleation site for gas hydrate formation and growth. Moreover, the nanoparticles' motion and movement reduce film resistance in the gas/water interface. This leads to a better mass transfer which increases gas dissolution in the liquid phase (Ataei et al., 2013, Aliabadi et al., 2015).

1.1 Aim and Objectives

This study aims to develop an approach for capturing and storing CO₂ via substituting the methane in a methane clathrate and simultaneously releasing methane gas for use in energy applications. To achieve this, several objectives are proposed:

- i. Experimentally measure the thermodynamic and kinetic behavior of carbon dioxide/methane with suitable storage material and nanoparticles and sodium dodecyl sulphate (SDS) as an additive.
- ii. Measure methane and carbon dioxide hydrate formation with different additives and silica sand.
- iii. Report the storage capacity, induction time, and rate of hydrate formation based on kinetic measurements

- iv. Evaluate the experimental technique of capturing and substituting carbon dioxide into the methane hydrate using a laboratory scale high pressure apparatus
- v. Repeat CH₄-CO₂ replacement measurements with synthesized flue gas systems (CO₂/N₂) with thermal stimulation.

While many studies have been performed using hydrates to capture and encapsulate CO₂ (Hosseini et al., 2015), this project uses methane hydrates as a medium of carbon dioxide sequestration. The CO₂ captured from stack emissions can be compressed, transported from the point of generation using pipelines, and stored or buried underground. South Africa reportedly has methane hydrates beds off the west coast (Bronwyn 2014). The CH₄/CO₂ replacement technique uses the phase equilibrium difference between CO₂ hydrate and natural gas hydrate (mainly CH₄) to replace CH₄ from the natural gas hydrate with CO₂ gas. This method enables natural gas hydrate exploitation, CO₂ storage, and stabilization of the reservoir (Wang et al., 2021; Ndlovu et al., 2022).

This project aims to address the problem arising from the release of CO₂ in emissions from such industries by proposing a method for CO₂ sequestration in natural gas hydrates. This proposal is an alternative route for CO₂ mitigation methods that are being explored, such as direct CO₂ extraction from the atmosphere (Daniel, 2019) and conversion of CO₂ to methanol and various chemicals (Honeywell, 2022). The results from this study will inform the possible design of a carbon capture storage system using suitable porous media hence a gas storage medium. Moreover, the study seeks to increase the storage capacity and improve the kinetics of gas hydrate formation by applying silica sand and chemical additives in the hydrate formation process.

1.2 Thesis Overview

This thesis consists of eight chapters, including Chapter 1, an introductory chapter. The contents of the seven Chapters are described herein. Chapter 2 contains the literature review on hydrates technology, while Chapter 3 summarizes the equipment utilized in the study of gas hydrates. Chapters 4 to 6 detail the equipment, experimental procedure, and results of the three separate experimental studies performed to meet the set objectives. The results have been presented in three chapters. This format is deemed to be suited for the presentation of different equipments used and experimental work performed in this study. The objective of this work is to carry out experimental measurements of CH₄ gas replacement with CO₂ gas from the CH₄ gas hydrates. The main challenge with gas hydrate applications is the slow rate of formation

thus kinetic studies with the application of nanoparticles were performed in order to improve the rate of hydrate formation and replacement reaction. Since gas hydrates form in the presence of porous media in sea beds and permafrost areas. Hence CH₄ gas hydrates were formed in the presence of silica sand and nanoparticles were added to improve the hydrate formation process. To improve the encapsulation of CO₂ gas in the CH₄ gas hydrates, nitrogen gas was injected and thermal stimulation was applied. Finally, the conclusions of the entire study are detailed in Chapter 7. Chapter 8 lists the recommendations for further studies. The entire contents of each chapter are outlined below;

Chapter 2: Contains a literature review on carbon capture technologies, hydrate structure, and hydrate formation kinetics in the presence of various additives. It also details the CH₄-CO₂ replacement reaction, focussing on the various parameters affecting the replacement rate.

Chapter 3: Presents a review of various equipment utilized in hydrate studies with the main focus on the CH₄-CO₂ replacement reaction.

Chapter 4: Presents equipment description, experimental procedure, and modelled kinetics data for methane and carbon dioxide with selected nanoparticles and microparticle additives in the presence of Sodium dodecyl sulphate (SDS).

Chapter 5 Presents the equipment description, experimental measurements, and results on CH₄-CO₂ replacement without porous media.

Chapter 6: Presents replacement with porous media from the design of the replacement vessel to the CH₄-CO₂ replacement reaction experimental procedure and results.

Chapter 7: Concluding statements for the entire study.

Chapter 8: Recommendations made from the study.

References: Literature sources obtained are listed at the end of the study, with the Author(s) listed first, then the year and the title.

Appendices: This section contains all the supporting data and information utilized in the above chapters.

Chapter 2: Literature Review

2 Introduction

A review of CH₄ and CO₂ hydrate formation in the presence of additives such as nanoparticles and porous media is presented in this chapter. An explanation of the use and performance of kinetic and thermodynamic promoters is provided in this chapter. The first part focusses on the structure of gas hydrates structure and formation kinetics. The technique of hydrate formation by CH₄ and CO₂ in the presence of silica sand and other additives is detailed. This is followed by a summary of the CH₄-CO₂ replacement studies reported in the literature. Then hydrate technology application in Carbon Capture, and Storage (CCS) is discussed. Lastly, the application of hydrates in energy storage and various technologies in solid gas storage.

2.1 Hydrates Structure

Gas hydrates or clathrates are ice-like crystalline solid structures made from water and gas molecules. The water molecules are the host, forming a cage-like hydrogen-bonded structure that physically encapsulates the gas molecule, the guest inside, and the encased gas molecules, exerting a multi-directional force to keep the cage-like structure rigid and intact (Sum et al., 2009). The hydrate structure can be formed by various host molecules that take on different structures. Under favorable conditions of temperature and pressure, these hydrate structures are stable. Depending on the guest molecules' composition and size, the resultant gas hydrate can have one of the three cells depicted in Figure 2.1.

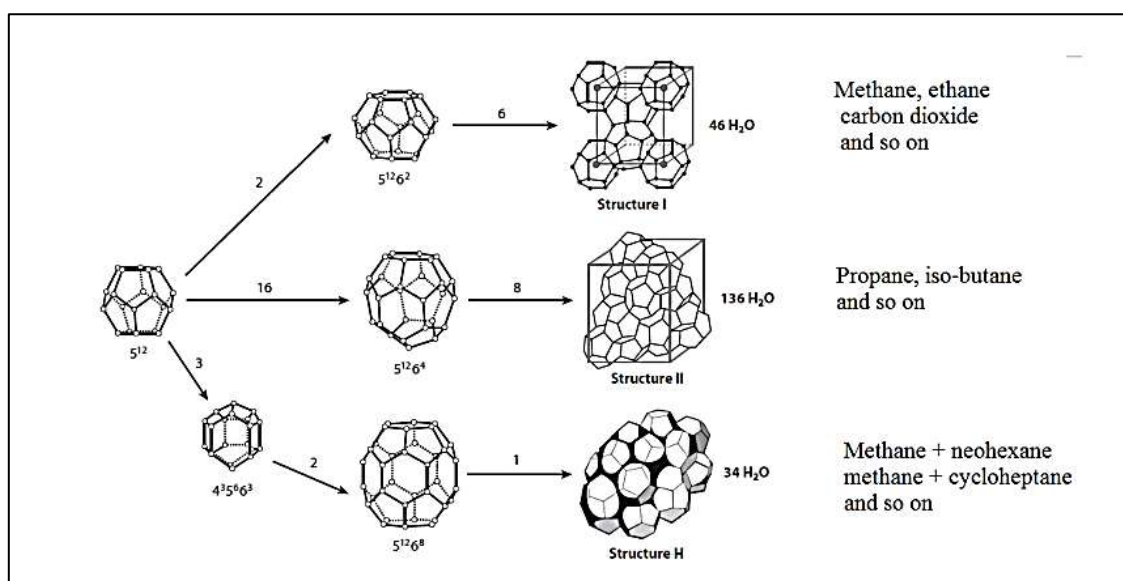


Figure 2.1: The three hydrate unit crystals and their cavity arrangements (Koh et al., 2011).

The number above the arrow in the structure represents the number of each respective cavity that make up a unit cell of a specific hydrate structure. The nomenclature used for describing hydrate structure is n_i^{mi} , where “n” is the number of edges in face type “i” and “mi” is the number of faces with n_i edges (Sloan and Koh,2008). The three structures are cubic structure I (sI), cubic structure II (sII), and hexagonal structure H (sH). The structure I have a unit cell, a body-centred cubic lattice constituted by two small cages and six large cages. The small cage is a pentagonal dodecahedron and has a notation 5^{12} which indicates that the cage has twelve pentagonal faces. The large cage is a tetra-decahedron with 14-faces and has a notation of $5^{12}6^2$. Methane and carbon dioxide form the sI structure. The unit cell structure II is a face-centred cubic lattice that comprises 16 small cages and eight large cages ($5^{12}6^4$). The sII large cage is larger than the sI cage, thus, the sII structure can fit bigger guests such as propane, isobutane, and other molecules. Each sII unit cell comprises 136 water molecules and 24 guest molecules in the complete occupancy configuration. The hydrates of structure H are a recent discovery and are less common than sI and sII. Its unit structure is more complex than those of sI and sII. Hydrates of the sH structure are always double hydrates, as they require two formers to be present for their formation, a small molecule and an sH former. Thus, sH contains 36 water molecules and forms three 5^{12} , two $4^35^66^3$, and $5^{12}6^8$ in a one-unit cell. Natural gases consisting of quest gases such as methane, hydrogen sulphide, propane, and butane form 5^{12} , $4^35^66^3$, $5^{12}6^4$, and $5^{12}6^8$ cavities (Koh et al.,2011; Caroll, 2014; Nashed et al., 2014; Nguyen, 2017).

2.1.1 Gas Hydrates Formation Kinetics

Gas hydrates occur naturally in environments with conducive conditions for their formation. This occurs in permafrost regions and marine sediments with water depths of over a hundred meters (Bohrmann et al., 2006). Interestingly, CO₂ hydrate formed rapidly when injected in liquid form directly onto the ocean floor at 3 650 m (Brewer et al., 1999). However, the kinetics of gas hydrate formation remains unclear as hydrate formation is stochastic (pattern cannot be precisely predicted). Thus, accurately reproducing hydrate kinetics in different laboratory apparatuses is difficult. Time-dependent kinetics pose the highest challenge in gas hydrate research. A clear macroscopic understanding of hydrates has been made, but the molecular picture of gas hydrate formation remains controversial and not fully understood. The most common theory of hydrate formation is the Labile cluster theory shown in Figure 2.2. It considers gas hydrate nucleation commencing from forming locally structured water clusters around dissolved gas molecules (hydration shells). The hydration shells transform into gas hydrate cages in the hydrate-forming zones. These cages agglomerate into hydrate nuclei.

When the nuclei size exceeds a critical value, the nuclei proliferate into a large hydrate mass (Sloan and Koh, 2008).

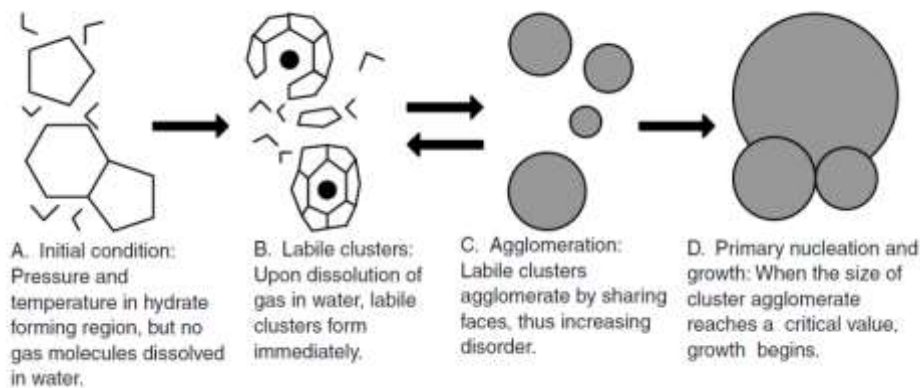


Figure 2.2: Mechanism of formation of gas hydrates formation from the labile theory (Extracted from Sloan and Koh, 2008).

The formation of gas hydrates usually begins at the gas-water interface. This is a critical occurrence in hydrate formation as it suggests that the interface-active agents can affect hydrate formation more than bulk-active ones. The occurrence of a thin film at the guest-water interface supports the interfacial formation of gas hydrates. The growth of the film becomes diffusion-resistant, thus preventing mass transfer across the interface (Taylor et al., 2007). The mechanism for hydrate formation at the $\text{CH}_4\text{-H}_2\text{O}$ interface is shown in Figure 2.3. hydrate structures (Koga et al., 2010).

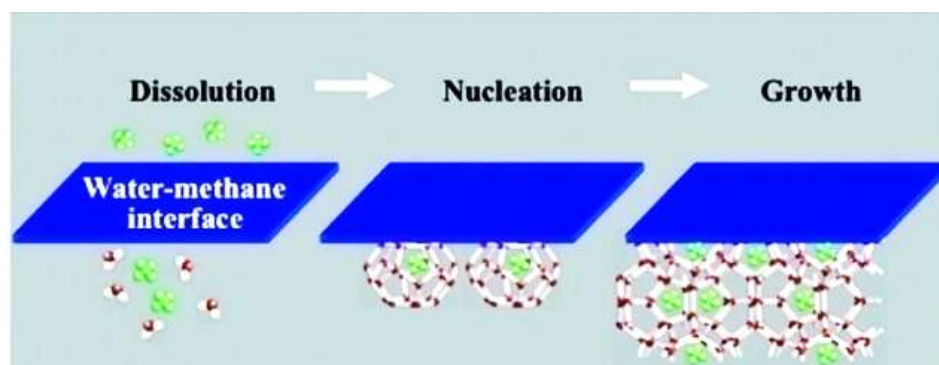


Figure 2.3: Pictorial view of three steps of CH_4 hydrate formation at the $\text{CH}_4\text{-H}_2\text{O}$ interface (Koga et al., 2010).

Initially, the CH_4 molecules transfer across the gas-water interface into the liquid phase. Then the hydrate cages form around the dissolved CH_4 gas molecules close to the water interface. The final step is the cage agglomeration into a hydrate crystal. The hydrate formed prevents the dissolution of CH_4 into water. Thus, hydrate growth under the interface is suspended. Hence, in this system, only the hydrate film is formed. In an agitated system, the turbulence

breaks the film, and the convection flow conveys the hydrate nuclei into the bulk, which grows into a larger hydrate structure (Koga et al., 2010).

2.1.2 Thermodynamics

Hydrate phase diagrams are plotted from PT values over a specific range. Understanding the phase diagram of different components in different phases is essential in predicting the hydrate formation and dissociation conditions. Moreover, these are essential in applying hydrate in various processes and understanding the behavior of different hydrates formed from numerous components such as additives and promoters. Figure 2.4 shows the hydrate phase boundary for CO_2 , N_2 , and CH_4 , flue gas (14.6% and 85.4%), and flue gas mixture with CH_4 . Increasing the system's pressure above the predicted phase boundaries can lead to hydrate formation. Also, adding different additives can shift the phase boundary (Farahani et al., 2021).

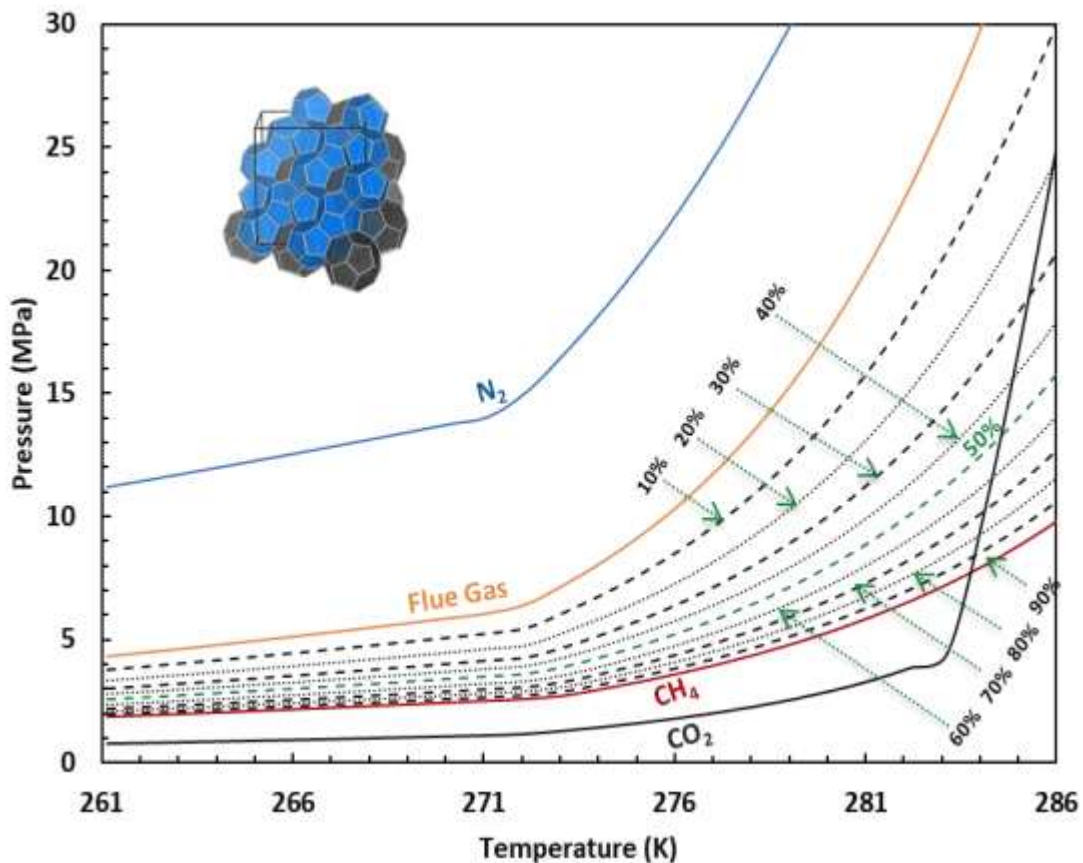


Figure 2.4: Phase diagram for CH_4 , CO_2 , N_2 flue gas (85.4% N_2 and 14.6% CO_2) and mixtures of flue gas with CH_4 (broken line) with respect to temperature (Hassanpouryouzbznd et al., 2019).

2.2 Hydrate promoters and inhibitors

Hydrate promoters and inhibitors are chemical substances that affect the gas hydrate formation and dissociation rate, respectively. The promoter effect increases the temperature or reduces

the pressure at which the hydrate forms, whereas the inhibitors have the opposite effect (Croeser 2017). Gas hydrate promoters can be classified according to their effect on the structure into two categories; (i) additives that do not change the structures of the water hydrogen-bonded networks, e.g., tetrahydrofuran (THF), anionic/non-ionic surfactants, cyclopentane, propane, acetone and so on. (ii) additives that take part in the structure of the ordinary water cages in the clathrates networks, such as quaternary ammonium salts; these include tetra-n-butylammonium salts (TBAB) and tetra-n-butylammonium borohydride (Eslamimanesh et al., 2012). THF is a thermodynamic promoter that can reduce the hydrate formation pressures of CO₂ hydrate (Lee et al., 2012). In comparison, SDS is a kinetic promoter that has been observed to increase the separation of CO₂ by hydrate formation (Kashkouli, 2015). Surfactants are another class of hydrate formation promoters that enhance the water-gas interface by forming micelles (supramolecular assembly of surfactants) encompassing the gas and the water molecules (Zhong and Roger, 2000). In Figure 2.5, SDS and micelle-SDS are shown to promote CH₄ hydrate formation.

Cyclopentane has been utilized as a promoter in the presence of TBAB, improving the gas uptake, CO₂ separation efficiency, induction time, and hydrate formation under different conditions (Li et al., 2011). Cyclohexane and methylcyclohexane are other heavy hydrocarbons utilized as thermodynamic promoters (Zhong et al., 2012). The quaternary ammonium/phosphonium salts (QAS/QAP), such as tetra butyl ammonium/phosphonium salts (TBAX/TBPX), where X represents halogen elements that are bromine, chlorine, and fluorine are common thermodynamics promoters. These substances can decrease the hydrate formation pressure as they form part of the structure of the hydrogen-bonded networks (Karmran-Pirzaman et al., 2013). For an in-depth study on promoters, the reader is referred to the work of (Herslund, 2013; Kashkouli, 2015 and Nasir et al., 2020).

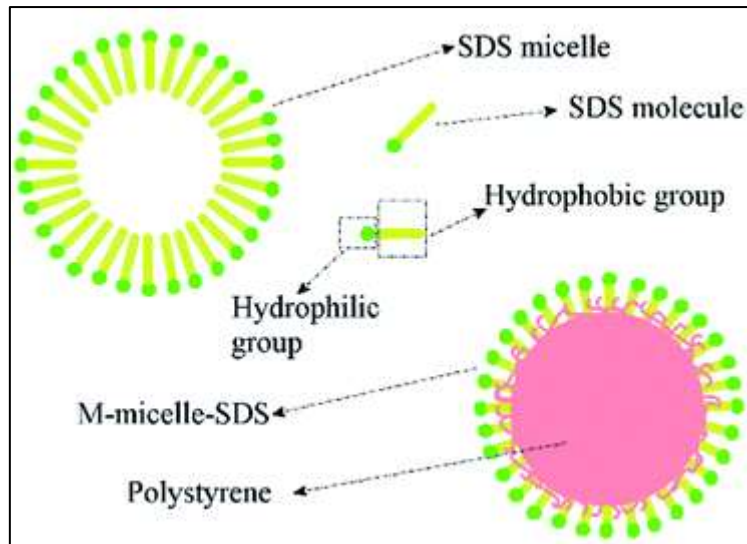


Figure 2.5: Schematic view of structures of SDS micelles and M-micelles promoting hydrate formation (He et al., 2019).

Thermodynamic inhibitors prevent hydrate formation by shifting the equilibrium conditions to high pressure or lower temperatures, thus making it difficult for the hydrate to form. Inhibitors are classified as thermodynamic (such as salts, glycols, and alcohol) and the low dosage hydrate inhibitors (LDHI). Under LDHI there are kinetic inhibitors (KI) and anti-agglomerates (AA). Kinetic inhibitors reduce the rate of hydrate nucleation and delay the rate of hydrate growth. The anti-agglomerates delay the agglomeration of hydrate crystals (Croeser, 2017).

2.3 Hydrate formation in porous media

A porous medium consists of pores that can fill with a gas or a liquid. Porous media application in hydrate formation has become common in recent years. Four types of hydrate growth have been reported in gas hydrate formation with porous media. The development and growth of the gas hydrate within the interstitial space of porous media and the hydrate are known as growth habits. The physical properties of the sediment layer are greatly affected by the presence of the gas hydrate in the pore space. Electrical conductivity, seismic velocity, and hydraulic permeability have been studied extensively (Priegnitz, 2015). Figure 2.6 shows the different types of hydrate growth habits in porous media. These are grain coating, cementing, pore filling, and load bearing

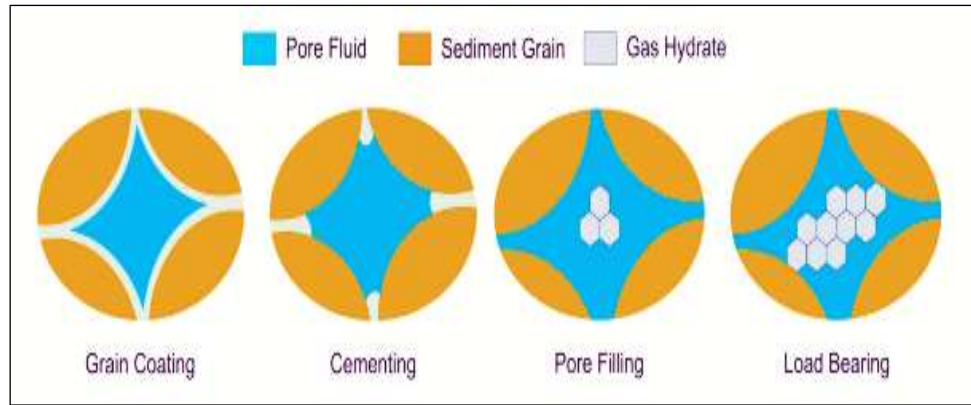


Figure 2.6: Schematic illustration of the four types of gas hydrate growth habits in porous media (Priegnitz, 2015).

Grain coating is prevalent in sediments that are not completely saturated with water. The water required is provided by the water initially attached to the sediment grains. Initially, hydrates form a shell around the grains, clog the pore, and cut the pore space from the interconnected pore networks. The hydrate “cements” itself on the grain surface. The wetting water provides the required water phase on the sediment grains with the pores, which are not fully water-saturated. Cementing process increases the hydrate strength leading to an increase in seismic velocity. Pore filling occurs in water fully saturated with methane gas. The hydrate forms in the middle of the pore without any contact with the surrounding sediment grain. The developing hydrate phase is considered to be part of the pore fill. With the growth of the formed hydrate cluster, the surrounding sediment grains are adjoined to increase the mechanical strength of the sediment floor. The interconnectivity of the pore space decreases with increasing hydrate saturation, a process referred to as load-bearing hydrate growth (Kashiev et al., 2002; Minagawa et al., 2005; Priest et al., 2009; Kumar et al., 2010; Siangsai et al., 2015; Dai et al., 2021). This process propagates hydrate growth by providing a stable structure and frame for hydrate stability.

According to experimental studies, hydrate formation kinetics improves as the particle size of the porous media decreases (Klauda et al., 2001; Mekala et al., 2014). This is caused by a smaller grain size generally being more regularly packed, resulting in more interconnectivity of the pores and greater surface area for the interaction of water and gas. However, in sediments with different particle-sized grains, hydrate formation occurs at the centre of the pores and not on the surface of the particles. This is caused by the preferential wetting of the grain with water rather than gas (Bhattacharjee et al., 2015). Hence, hydrate formation is possible when a gas guest molecule is present. The water molecules go to the interstitial area where the gas molecule

is stationed, causing the hydrate to develop. The observation was accurate for large grain sizes (>0.0313 mm), while for smaller particle sizes (<0.070 mm), gas hydrate crystals were formed around the particles of the porous media. Figure 2.7 is an illustration of this process.

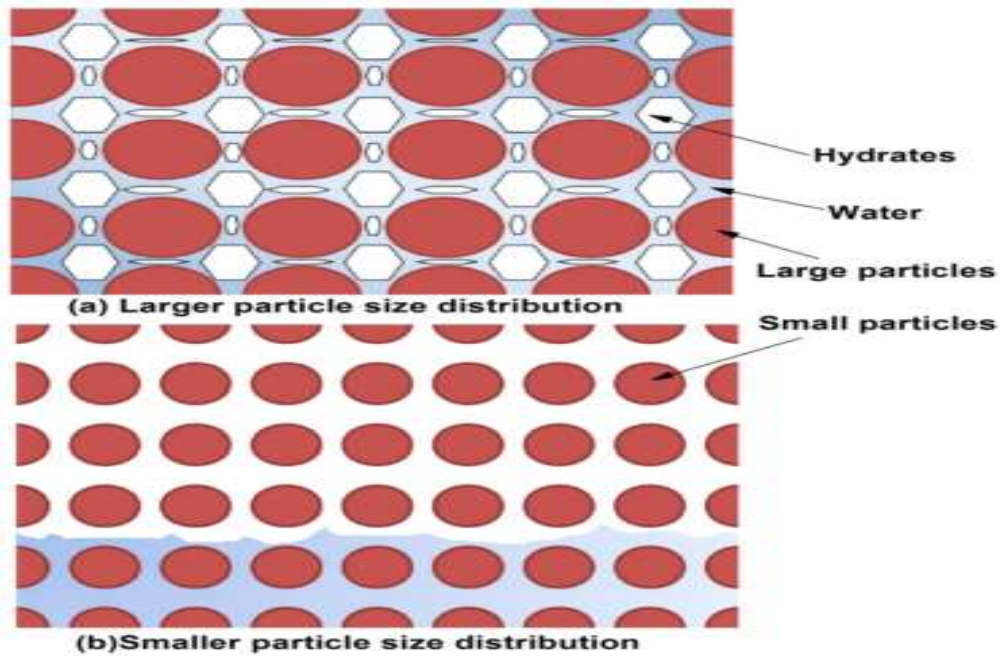


Figure 2.7: Hydrate formation in porous media with different particle sizes (Bhattacharjee et al., 2015).

Li et al., (2020) investigated gas hydrate formation at the pore scale in an etched high-pressure glass plate. It was noted that natural gas hydrates are formed in three stages, i.e., the instability period of gas-liquid dissolution, followed by hydrate formation and growth. The hydrate growth has three distinct stages: gas-liquid cluster and nucleation stage, gas-liquid film formation, and crystallization stage. Two different types of changes in the porous media interact with hydrate development. First, the contact between the gas and liquid seems hydrophobic, and the dissolving process exhibits repeated disorder. The orderly expansion of the current hydrate interface as it progresses into the depth of the pores indicates the hydrophilic nature of hydrates. As a result, the formation of hydrates in the pores adheres to an already present ordered hydrate interface. It can be inferred that hydrophobic materials encourage the development of gas hydrates because they raise the density of the former gas at its liquid contact. However, due to deformed water structures and insufficient gas density at the liquid-gas interface, hydrophilic materials prevent the formation of gas hydrates (Nguyen et al., 2020).

2.4 Hydrate formation with nanoparticles

The utilization of nanoparticles in hydrate studies has yielded promising results in enhancing gas storage and improving the kinetics of hydrate formation. Nanoparticles considerably enhance mass and heat transmission between gases, the hydrate phase, and liquids because of their small particle size (less than 100nm). In turn, this increases the transfer of the former gas to the hydrate phase and the heat generated in hydrate formation, thus significantly improving the volume of gas consumed and the rate of hydrate formation (Said et al., 2016). Nanoparticles provide suitable heterogeneous nucleation sites for the formation and growth of gas hydrate. Moreover, the motion and movement of nanoparticles reduce film resistance in the interface between water and the gas, thus leading to an improved mass transfer which increases gas dissolution in the liquid phase (Ataei et al., 2013; Aliabadi et al., 2015).

SDS and CuO nanoparticles were observed to lower the surface and interfacial tension of immiscible fluids, thus enhancing the solubility of CH₄ in CuO nanofluid compared to pure water (Moraveji et al. 2013). Silver nanoparticles reduced the induction time for hydrate formation in the silver nanofluid. The induction time, by definition, is the period from introducing the gas into the cell to the commencement of gas hydrate formation. It also increased the hydrate crystals' storage capacity (Arjang et al., 2013). Consequently, a kinetic study of CH₄ hydrate formation was carried out in 300 ppm SDS, and silver nanoparticles (SNPs) were synthesized. The addition of SDS and SNPs enhanced the storage capacity, gas uptake, and water into hydrates (Mohammandi et al., 2017). To determine the effects of Al₂O₃, Ag, Cu and SiO₂ nanoparticles on CH₄ and CO₂ gas hydrate formation, kinetics studies were carried out with pure water containing 0.1, 0.2, and 0.3 wt.% of each nanoparticle. The addition of nanoparticles had a positive effect on the study. SiO₂ of 0.3 wt.% had the highest CO₂ gas consumption, while Cu and Al₂O₃ nanofluids of all concentrations studied notably improved gas consumption during the dissolution stage (Said et al., 2016). Park et al., (2012) used a novel approach of adding MWCNTs (multi-walled carbon nanotubes) and OMWCNTs (oxidized multi-walled carbon nanotubes) to improve CH₄ adsorption during gas hydrates formation. The amount of CH₄ absorbed in the oxidized carbon nanofluid was approximately 4.5 times higher than in distilled water. A summary of research on the impact of nanoparticles in CH₄ and CO₂ hydrate formation is provided in Table 2.1, beginning from more current studies to earlier ones.

Table 2.1: Studies on effects of nanoparticles on gas hydrate formation with CH₄ and CO₂ gases.

Reference	Additive	Hydrate Former	Observation and resultant effect
Liu et al., (2020)	Al ₂ O ₃ nanoparticles	CO ₂	(Average diameter of 30 nm) influence of Al ₂ O ₃ nanoparticles on the formation of CO ₂ depends on the particle size and surface functional groups. The decrease in carbonate carbon, C-H carbon, and total carbon on the nanoparticles surface inhibited the kinetics of formation. Al ₂ O ₃ nanoparticles have a negligible impact on the CO ₂ hydrate phase equilibrium. The particle size and surface functional groups of the nanoparticles determine whether they have a promoting or inhibitory effect. Al ₂ O ₃ nanoparticles can more readily diffuse in deionized water due to their hydrophilicity.
Pahlavanzadeh et al., (2019) Pahlavanzadeh et al., (2016)	CuO nanoparticles	CH ₄ , CO ₂	High concentrations (0.0157M and 0.157M) are more effective in increasing CH ₄ consumption. Solutions (CuO + H ₂ O) remained stable for ± 6 days, and then sedimentation occurred.
Yu et al., (2016)	Graphite nanoparticles	CO ₂	The formation pressure rises in these suspensions compared to deionized water at a particular temperature, and the inhibitory impact is independent of the amount of graphite nanoparticles present.
Said et al., (2016)	Al ₂ O ₃ nanoparticles	CO ₂ , CH ₄	Improved gas consumption.
Najibi et al., (2015)	CuO nanoparticles and SDS	CH ₄	Increased CH ₄ consumption. Increased % mole of H ₂ O to hydrate conversion.
Mohammadi et al., (2014)	Silver nanoparticles and SDS	CO ₂	At high pressure, using the same SDS and Silver nanoparticles increases the consumption of CO ₂ , storage capacity, H ₂ O to hydrate conversion and rate of hydrate growth.
Zhou et al., (2014)	Graphite nanoparticles	CO ₂	The induction time decreases, and the CO ₂ consumption increases.
Choi et al., (2014)	Al ₂ O ₃ nanoparticles	CO ₂ , THF	Enhanced the hydrate formation rate due to increased heat transfer and Al ₂ O ₃ has a different surface potential according to the variation of pH, hence the CO ₂ ion is easily captured by the nanoparticles.
Arjang et al., (2013)	Ag nanoparticles	CH ₄	The induction time decreased by 85 and 73.9% with the amount of CH ₄ gas encapsulated in the hydrate structure improved by 33.7 and 7.4% at pressures of 4.7 MPa and 5.7 MPa, respectively.
Moraveji et al., (2013)	SDS and CuO nanoparticles	CH ₄	SDS was found to accumulate at the interface of immiscible fluids, which was reported to diminish surface and interfacial stresses. Additionally, nanoparticles with a high effective surface area had better solubility.

It can be concluded from Table 2.1 that the addition of nanoparticles improves the hydrate formation kinetics of the system. The main observation reported was the increase in gas consumption and a reduction in induction time due to the presence of nanoparticles. The presence of SDS reduced the surface tension of the liquid, thus increasing the solubility of nanoparticles in the solution.

2.5 The effect of porous media on CH₄ and CH₄/CO₂ hydrate formation

A microscopic pathway of gas hydrate formation on porous materials was discovered with two notable processes. The first stage is replacing water adsorbed on the carbon surface by the gas and replacing water in the pore with gas accompanied by gas condensation. The second stage is the growth of gas hydrate crystals out of the pore. These observations provided the theory for gas hydrate formation on porous materials and a guideline for further application of gas hydrates in gas separation (Liu et al., 2019). In a separate study, Wan et al., (2019) investigated the decomposition characteristics of methane hydrate confined inside nanoscale silica gel pores below 273.15 K. Strong hydrogen bonds between the pore water molecules were observed.

Numerous studies have demonstrated that most porous medium speed up hydrate formation while shortening the induction period, resulting in higher water to hydrate conversion (between 74-98 %) than pure water. Water conversion to CH₄ hydrate was also improved, and water saturation was reduced. Furthermore, it was discovered that adsorbates such as C₂H₆, CO₂, and CH₄, might substitute for preloaded water for hydrate formation on porous surfaces. Particle size and pore space had a significant impact on how the CH₄ hydrate formed. The effects of porous media on CH₄ and CO₂ formation have been published, and the reader is referred to Ndlovu et al., (2022). Table 2.2 summarizes the adsorbents used in forming CH₄ and CO₂ hydrates from early studies to more recent investigations.

Table 2.2: Summary of adsorbents utilized in the formation of CH₄ and CO₂ gas hydrates.

Reference	Reactants and Reaction conditions	Adsorbent	Hydrate Former	Formation Details
Perrin et al., (2003)	T = 274.15 K P = 10 MPa	Activated carbon (100-200 μm)	CH ₄	Water to activated carbon ratio was very close to one. The requirements for hydrate production were discovered to be high pressure (3 MPa) and temperature around 273.15 K. Here, the storage kinetics are very low.
Zanota et al., (2005)]	T = 274.15 K P = 1-8 MPa	Activated Carbon	CH ₄	When water is added up to a certain ideal value, CH ₄ storage is enhanced but decreases as more water is added. A pressure of between 6- 7 MPa was required to form the methane hydrate which can remain intact without disintegrating to a pressure of 4 MPa at a temperature of 274.15 K.
Linga et al., (2009)	T = 273.15-280.15 K	Silica sand particles (150-630 μm)	CH ₄	Due to the numerous nucleation sites observed, the conversion of water to hydrate was between 74.1 and 82.4 % at 273.15 and 277.15 K, however, at 280 K, the conversion was 10.5 or 11 %. The initial growth rate was slow, the rapid until 43-53 % water was converted to hydrate. The final conversion was between 74-98 %.
Seo and Kang., (2010)	T = 274.15 K P = 6.0-9.2 MPa	Silica gel (100 nm)	CO ₂ and H ₂	Analysis of the composition reveals that 96.5–98.7% of the CO ₂ was trapped. At pressures between 6.5 and 8.9 MPa, high CO ₂ is encapsulated in the hydrate phase, and this CO ₂ concentration decreases with an increase in pressure.
Zanjani et al., (2012)	T = 265.1 - 313.1 K P = 6.20 MPa	Silica-based porous media with amine& hydroxyl.	CO ₂ , H ₂ , and N ₂ CH ₄ /C ₂ H ₆ /C ₃ H ₈ (82.88/16.41/0.71 mol%)	Compared to the bulk system, the amount of gas trapped in the hydrate phase increased (by up to 44%) in the presence of porous materials. Precisely 0.118 mol gas/mol more water was consumed in the presence of the porous media compared to the bulk system. Heavier gas mixture components exhibited a stronger affinity to enter hydrate crystals as they grew. As a result, the equilibrium phase for the mixture in contact with the hydrate shifted to a lower temperature because the layer of gas close to the hydrate surface had lighter components.
Chari et al., (2015)	T = 277 K P = 7.5-10 MPa	Hollow silica and solid silica	CH ₄	Stirring affected the hydrate systems containing solid silica and water system, while no influence in the hydrate systems with hollow silica. The hollow silica yield was similar in both the stirred and unstirred experiments. When compared to a non-stirred reactor, the conversion of CH ₄ into methane hydrate in a solid silica and pure water system was ten times higher in the stirred reactor. Hollow silica turned out to be the best-performing silica for the storage and transportation of methane gas in the form of methane hydrate.

Table 2.2: Summary of adsorbents utilized in the formation of CH₄ and CO₂ gas hydrates. (*continued*)

Reference	Reactants and Reaction conditions	Adsorbent	Hydrate Former	Formation Details
Rungrussamee et al., (2018)	T = 277.15-294.15 K P = 8 MPa	Hollow Silica Activated carbon	CH ₄	Compared to activated carbon, hollow silica improved the conversion of water to hydrates and the consumption of methane. Decomposition was done through thermal simulation at 294.15 K porous material. With hollow silica and activated carbon, water conversion was 79.79 and 67.27%, respectively, without any noticeable difference in CH ₄ recovered.
Ge et al., (2019)	T = 277.15 K P = 8 MPa	Silica sand	CH ₄	Reduced H ₂ O saturation led to an increase in the conversion of water to CH ₄ hydrates, and 70% water saturation was the optimal saturation for CH ₄ hydrate formation. At 70% water saturation, the maximum gas absorption was attained with tiny particles (0.18–0.25 mm). With small particle sizes, the rates of hydrate formation, gas uptake, gas recovery, and hydrate dissociation were all high.
Wan et al., (2019)	T = 223-293 K P = 0.101 MPa	Nanoscale Pores of Silica Gel (15-20 nm)	CH ₄	The decomposition of CH ₄ hydrate is accompanied by a reformation of the hydrate phase. When the pressure at the equilibrium phase is lower, the reformation happens more frequently and the decomposition temperature decreases. The silica gel is more likely to regenerate under a higher pre-decomposition pressure before decomposing. As a result, reformation, which is caused by the structure of the pore water, is the primary cause of CH ₄ hydrate disintegration in nanoscale pores below 273.15 K.
Liu et al., (2019)	T = 273 K P = 1.52-2.53 MPa	Mesoporous carbon CMK-3 Irregular porous activated carbon.	CO ₂	Adsorbates like CO ₂ , CH ₄ , and C ₂ H ₆ could replace the preloaded water during the production of gas hydrates on porous surfaces. Low packing density is a barrier to gas storage for porous materials. Low packing density is overcome by combining gas storage in the pore with gas hydrate production in the space. It would considerably increase the ability of the porous materials to store gas.

2.6 The effects of additives utilized with adsorbents in CH₄ and CO₂ hydrate formation

CO₂ capture efficiency in gas hydrates increases with improved hydrate formation rate and reduced hydrate formation pressure (Gielen,2003). THF is a water-miscible solvent that can form solid clathrate hydrate structures with water at low temperatures. It facilitates hydrate formation and is frequently used as a thermodynamic promoter for hydrate formation. Englezos et al., (2008) observed that the presence of 1.0 mol % THF substantially reduces the hydrate formation pressure from a flue gas mixture (CO₂/N₂) and offers the possibility to capture CO₂ at medium pressures. Ganji et al., (2007) used 500 ppm of SDS and reported that the formation rate was increased by a factor greater than 35 and storage capacity doubled compared to pure water.

Furthermore, hydrate stability decreased with little starch or xanthan below the ice point, decreasing the hydrate dissociation rate. Nguyen et al., (2007) conducted a series of experiments using TBAB to reduce the crystallization pressure in the CO₂ capture process from a steel industrial gas mixture via hydrate crystallization. It was concluded that continuous crystallization is possible when optimum contact between the gas and the liquid phase is achieved. The adsorption of graphite to CH₄ was shown to improve the mass transfer efficiency. The large specific surface avails numerous heterogeneous nucleation sites. The hydrophobicity can make the molecular orientation arrangement in the SDS solution to provide a mass transfer channel for CH₄ to enter into the solution. The excellent heat transfer performance of graphite and the heat generated by the reaction can be quickly transferred to enhance hydrate formation, as shown in Figure 2.8.

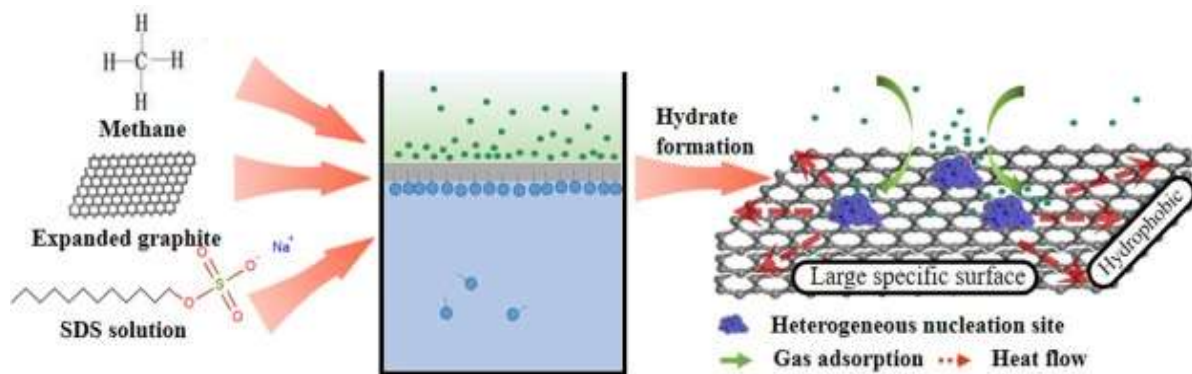


Figure 2.8: Methane hydrate formation on graphite in the presence of SDS (Deng et al., 2021).

For in-depth details on additives utilized with adsorbents CH₄ and CO₂ gas hydrate formation, the reader is referred to Chen et al., (2019); Ndlovu et al., (2022). Reports on various hydrate formation tests studies utilizing adsorbents with additives are shown in Table 2.3. Beginning with the most current findings and moving backward in time, investigations on silica and various porous materials are described in this table.

Table 2.3: Adsorbents that are utilized with additives in the formation of CH₄ and CO₂ hydrates.

Reference	Conditions T(K)/ P(MPa)	Hydrate former	Additives	Observation and results
Silica				
Pan et al., (2018)	T= 275.15 P = 7	CH ₄	Silica sand and SDS	Both 50 and 100% saturated sand, larger particle size exhibited a better methane storage capacity. SDS enhanced the hydrate formation process and weakened the effect of particle size on the hydrate formation rate.
Dicharry et al., (2013)	T=278.2-279.2 P = 3.8	CO ₂	Silica gel (30 & 1000 nm) and SDS	Saturated at 80% pore volume with pure water, sodium dodecyl sulfate (SDS), or polyoxyethylene sorbitan monooleate at a concentration of 100 ppm (Tween). Only SDS, one of the two surfactants utilized, was discovered to have a favorable impact on both the hydrate formation kinetics and the quantity of hydrate created.
Yang et al., (2013)]	T = 291.55 P= 3.04	CO ₂	Silica sand and SDS/THF	1000 mg/L SDS was shown to be a viable option for hydrate-based CO ₂ capture. Also, the CO ₂ hydrate equilibrium pressure was significantly reduced by 3mol% THF.
Various Porous Media Materials				
Shihui et al., (2017)	T = 278 P = 8.31	CH ₄	Saturated CuSO ₄ , Na ₂ SO ₄ , MgSO ₄ , and NH ₄ HCO ₃	The largest hydrate formation rate observed was with Na ₂ SO ₄ , which was 386 times greater than in deionized water and gas storage capacity being increased by ten times.
Yang et al., (2017)	T=285.15 P=3-4	CO ₂	THF	To lower equilibrium conditions and speed up hydrate formation, 19% of THF was used. It was discovered that hydrate production was enhanced by the higher temperature.
Raman et al., (2016)	T = 288.15		Cyclopentane, crude oil, and solid particles (Aerosil R974, fumed silica particles)	The induction time for hydrate formation was reduced by the presence of solid particles which provided nucleation sites. Compared to emulsions generated using surfactants, hydrate-forming emulsions produced with solid particles showed a higher viscosity.
Wang et al., (2015)	T = 343.15 P = 6	CH ₄	Sodium dodecyl sulfate (SDS) attached on the surface of polystyrene nanospheres termed (SDS@PSNS)	Compared to SDS, SDS@PSNS had a quicker induction time for hydrate production. Hydrates mostly generated near the bottom of the cell when SDS@PSNS was used as the promoter.
Liu et al., (2015)	T = 279.15		Porous media, THF, Natural gas	The findings suggested that memory effects and intense subcooling could shorten induction times. As particle size rises increases, the average induction time decreases.
Park et al., (2012)	T= 274.15 P = 3-7.	CH ₄	two types of multiwalled carbon nanotubes: unoxidized and oxidized.	In the oxidized carbon nanofluid, methane gas consumption during hydrate formation was around 4.5 times greater than in pure water.
Lee et al., (2007)		CH ₄	THF	THF was found to possess the capacity to regulate hydrate concentration and speed up the process by which hydrates are produced from aqueous phase methane in sediments.

2.7 Replacement of CH₄ with CO₂ from its Hydrate

The abundance of methane gas trapped in gas hydrates in subsea sediments has been reported (Zhu et al., 2018; Maeck et al., 2013; Kvenvolden, 1988). Several methods have been suggested for CH₄ recovery from hydrates in sediments such as thermal stimulation, inhibitor injection, depressurization, and CO₂ replacement (Kvenvolden, 1999; Maria, 2018). For the latter, injected CO₂ can aid in dissociating the CH₄ hydrates while replacing the CH₄ within the hydrate structure. This encapsulation can assist in the global control of carbon dioxide while simultaneously tapping into methane reserves. Consequently, CO₂ sequestration and CH₄ exploitation provide significant economic opportunities (Xu, 2014; Qorbani et al., 2017). Gas hydrates are stable within a specific temperature and pressure range known as the hydrate region. Thus, chemical equilibrium is essential for hydrates to remain intact. In the case of methane and carbon dioxide, the equilibrium pressure for methane hydrate dissociation is higher than carbon dioxide hydrate dissociation at a constant temperature (Goel, 2006). Thus, methane molecules can be exchanged with carbon dioxide in their hydrate due to this thermodynamic property. CH₄ hydrates have a higher chemical potential than CO₂ hydrates. This process creates the driving force for the replacement reaction of methane gas by carbon dioxide (Ohgaki et al., 1996).

The replacement reaction can be split into two stages, the fast surface reaction and a gradual process caused by a layer of mixed CO₂ hydrate and CH₄ that inhibits CO₂ diffusion to the underlying CH₄ gas hydrate (Zhao et al., 2015). Numerous kinetic and thermodynamic models which have been generated to study the CH₄-CO₂ replacement process are stated in Appendix A.

2.7.1 Factors affecting replacement reaction

The CH₄-CO₂ replacement technique uses the phase equilibrium difference between the CO₂ hydrate and natural gas hydrate (mainly CH₄ hydrate) to replace CH₄ molecules from the natural gas hydrate structure with CO₂ gas molecules. This method enables natural gas hydrate exploitation, CO₂ storage, and stabilization of the reservoir (Wang et al., 2021; Ndlovu et al., 2022). Zhang et al. (2017) stated that the CH₄/CO₂ replacement reaction occurs in two steps: (1) a fast surface exchange reaction followed by (2) slower diffusion-limited transport because of the formation of a mixed hydrate layer in the preceding step. It has been reported that an impervious CO₂ layer forms on the surface of the CH₄ hydrate, acting as a physical barrier between CO₂ gas and CH₄ thus hindering the perpetual release of CH₄ from the underlying

hydrate (Chatti et al., 2005; Zhou et al., 2008). This was due to the weakening of the force driving the reaction. Similar observations were also reported by (Pan et al., 2020).

Furthermore, all the replacement reactions were performed above the CH₄ hydrate and CO₂ hydrate equilibrium curve to ensure that release of methane was due to CO₂ replacement rather than dissociation of the methane hydrate. The fugacity difference between the fluid and hydrate phases significantly affects the CH₄-CO₂ replacement reaction (Ota et al., 2007). Additionally, the gas hydrate must dissociate for the replacement, enabling the released gas to interact with dissociated water and reconstruct the gas hydrate. The system temperature, pressure, and the amount of salts or other additives in the gas mixture affect how quickly the gas hydrates develop. Numerous analytical tools and quantitative techniques have been created to study the replacement of CH₄ with CO₂ (Gupta, 2009; Matsumoto et al., 2014; Musakaev et al., 2018; Liu et al., 2019). The variables and factors influencing the CH₄-CO₂ replacement reaction are listed in Table A.1.

2.7.2 Limitations in the replacement process

The challenges encountered in the replacement experiments at the laboratory scale are the low methane output and slow replacement rate due to an impenetrable barrier of CO₂ hydrate formed on the CH₄ hydrate surface, thus making the process economically unviable. Pressure reduction and chemical techniques (addition of promoters) are postulated to overcome the mass-transfer barrier. However, few studies have been done in this regard. Another challenge is the annealing process which is the dissociation and reformation of the hydrate several times in the porous media (Yousif et al., 1991). Poor interfacial contact between water in porous media and dissolved carbon dioxide results in an extended formation time (Tohidi et al., 2001). Numerous factors affect hydrate formation in porous media, such as pore size, the temperature at which dissociation experiments were initiated, and the volume of the headspace above the porous medium in the testing cell (Wilder et al., 2001).

There are inconsistencies among the resultant data reported on hydrates regardless of the similar procedures employed in preparing the reactants and using similar porous media in the experiments and conditions (Kleinberg et al., 2003). Therefore, researchers in this field must pay careful attention to the techniques (pressure and flowrate techniques) utilized to add the replacement gas mixture and use transparent equilibrium cells or view windows to visualize the replacement process stepwise.

2.8 Hydrates as a Carbon capture and storage (CCS) technology

There are three main CO₂ capture routes: post-combustion, pre-combustion, and oxy-combustion capture. These processes are shown in Figure 2.9. More details on carbon capture technologies are contained in the following sources (Mondal et al., 2012, Rhodes et al., 2012; Nandi et al., 2014; Wang and Song, 2020).

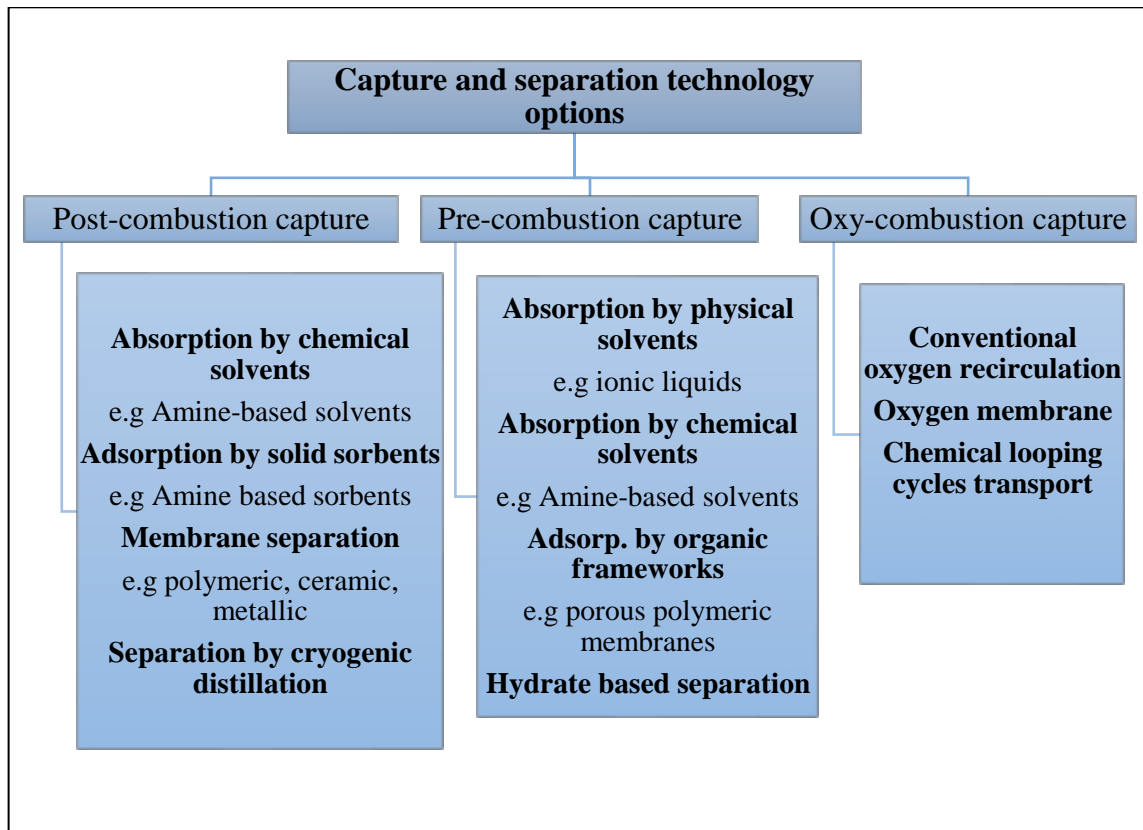


Figure 2.9: Overview of Carbon capture Technologies (Adu et al. 2019).

Due to environmental concerns, integrated gasification combined cycle (IGCC) plants have been installed for fossil fuel-powered stations, resulting in lower emissions of sulphur dioxide, particulates, mercury, and carbon dioxide (Cousins et al., 2015). The products from these stations are CO₂ and H₂ produced via a shift reaction of 40 and 60 %, respectively. The resultant H₂ can be utilized in fuel cells or gas turbines with CO₂ directed for capture and sequestration (Castellani et al., 2014).

2.8.1 Commercial CO₂ Capture Technologies

Little progress has been made in commercializing CO₂ sequestration technologies. In Norway, Equinor, a company that extracts natural gas, pumps CO₂ from the process back into the seabed. Approximately 90 tons per hour of CO₂ is stored permanently in the seabed (DW Documentary, 2021). In Canada, the Weyburn and Midale projects capture CO₂ emissions in North Dakota

and utilize them to enhance oil recovery (EOR) operations (Partoon et al., 2015). In Iceland, a process known as CarbFix captures CO₂ from a single source, such as a power station. The technology involves scrubbing the flue gas stream with cold water resulting in a carbon dioxide-laden stream pumped underground and reacting with the rock to produce new stones. A Swiss company called Clime Works developed a technology to absorb CO₂ straight from the atmosphere. It has a filter system that captures CO₂ through a chemical reaction and stores it in tanks with 50 tons capacity (Daniel, 2019). Carbon Engineering has a CO₂ capture pilot plant in British Columbia where process fans are employed to draw air wherein CO₂ reacts with a solution containing calcium, resulting in pellets of CaCO₃, which can be buried underground (Barnard, 2019).

2.8.2 Hydrates in CO₂ capture

Hydrates have proven to have the capacity to store large amounts of gas, thus, it has drawn much attention as a potential avenue for capturing CO₂. (Lovedy and Nelmes, 2007). The hydrate separation/capture method is also considered an offsite method as it is costlier to incorporate it directly into the existing flue gas stream networks (Shifeng et al., 2010; Lijith et al., 2019; Arooa et al., 2021). Hydrate technology has the advantage of a small energy penalty (6–8 %) compared to other technologies, such as electrostatic precipitation. The energy consumption of CO₂ capture via hydrate could be as low as 0.57 kWh/kg-CO₂ (Elwell and Grant, 2006).

The major challenge in implementing gas hydrate technology is its slow formation rate and high-pressure dissociation conditions leading to high capital costs (Zhang et al., 2022). In most cases, thermodynamics promoters are added to lower the formation pressure, thus enhancing the gas encapsulation in the hydrate formation (Lederhos et al., 1996; Zhang et al., 2021).

Gas hydrates form in the presence of a gas molecule, a hydrate former, and a large amount of water under high-pressure conditions and low temperatures. During the hydrate formation process, the crystal structure of the hydrate determines the type of guest molecule that can be trapped in the lattice. Hydrate-based capture has been selected as the process of choice in this study as it is one of the promising technologies in carbon dioxide capture.

In an experimental study, Seo and Kang, (2010) successfully captured CO₂ in the hydrate phase from a gas mixture of CO₂ and H₂ using silica gels to form hydrates. Composition analysis showed that 96.5 – 98.7 % of CO₂ was captured at a pressure range of 6.0-9.2 MPa at 274.15 K in 100 nm silica gel. Carbon-13 NMR spectra supplemented the phase composition analysis

and suggested that CO₂ occupied 93 % of the small cages and 100 % of the large cages in the hydrate phase. Li et al., (2011) in investigating the effects of temperature fluctuations on the hydrate-based CO₂ separation from IGCC syngas, observed that approximately 30 % more CO₂ gas was consumed with temperature fluctuation during the period of hydrate formation. This was achieved by increasing the temperature from 277.15 to 281.15 K during hydrate formation for 30 minutes before returning it to its initial value. It was concluded that CO₂ separation efficiencies were improved with temperature fluctuations. Moreover, Hassanpouryouzband et al., (2018) invested in the thermodynamic process by which CO₂ in flue gas or CO₂-N₂ mixture was captured as a hydrate through conducting a series of experiments. These experiments investigated the dependence of CO₂ capture efficiency on the reservoir conditions. Pressures ranging from 2.6-23.8 MPa and hydrate reservoir temperatures from 273.2 to 283.2 K were utilized. Results showed that more than 60 % of the CO₂ in the flue gas was captured and stored as CO₂ hydrate in this study.

In an experimental study, Linga et al., (2008) demonstrated that hydrate crystallization can be employed to separate CO₂ from flue gases in the presence of THF. Torre et al., (2011) performed an experimental kinetic study of CO₂ hydrate formation in a high-pressure batch reactor using THF and SDS, which proved very efficient in promoting CO₂ capture. Studies on storage capacity and induction time of CO₂ hydrate with SDS and THF additives revealed that SDS did not significantly affect the storage capacity compared to CH₄. In contrast, a mixture of SDS and THF reduced induction time significantly (Lirio et al., 2013). Also, utilizing SDS, Choi et al., (2014) performed an experimental study to develop new adsorbents to form CO₂ hydrate under atmospheric pressure. The effects of SDS and nanoparticles such as Al₂O₃ additives and THF surfactants on the formation rate and induction time of CO₂ hydrate were studied. Results indicate that adding THF, SDS, and Al₂O₃ increases the hydrate formation rate. In a separate study, the effects of THF/SDS additives mixture on CO₂ hydrate formation and dissociation in porous media were investigated experimentally. It was observed that 1000 mg/L SDS was the best additive, reducing the induction time and resulting in higher hydrate saturation than at other concentrations. Further, 3 mol% THF aqueous solution reduced the hydrate phase equilibrium pressure. The hydrate equilibrium temperature was 291.55 K in an aqueous phase with 3 mol % THF at 3.04 MPa, the highest equilibrium temperature in the investigation (Yang et al., 2013).

Galfre et al., (2014) demonstrated through experiments that the hydrate formation pressure for CO₂ can be reduced to atmospheric pressure. The CO₂ capture was enhanced with cyclopentane

as an additive however, using TBAB CO₂, the capture was increased to 100%. Moreover, it was physically impossible to find a thermodynamic additive to drop the operative pressure without dropping the storage capacity (Zhong et al., 2014). Similarly, Ma et al., (2016) reviewed using promoters such as quaternary ammonium salt application in CO₂ hydrates to reduce the hydrate equilibrium pressure and enhance the hydrate kinetics and stability.

Veluswamy et al., (2016) studied the kinetics of CO₂ hydrate formation in the presence of THF, at different temperature and pressure conditions. THF did not improve the kinetic/gas uptake in CO₂, but rapid hydrate formation kinetics were achieved in the CH₄ study. It was conclusive that the type of guest gas highly influences hydrate formation kinetics in the presence of the THF. Linga et al., (2012) investigated the rate of hydrate formation in a fixed bed column filled with sand and a stirred vessel using several gas mixtures for CO₂ capture. The storage results showed that the rate of hydrate formation in the fixed bed column was significantly improved, resulting in higher water conversion to hydrate in a shorter space. Babu et al., (2013) investigated a hydrate-based gas separation process with silica gel and silica sand to capture CO₂ from a fuel gas mixture. Variables investigated were the water-to-hydrate conversion, hydrate rate of formation and gas consumption. The study observed that the water conversion was 36% with silica sand, while that for silica gel was 13%. The gas consumed (mol/mol of H₂O) was 0.0404 and 0.0185 for silica sand and silica gel, respectively. Partial recovery was achieved at the dissociation of the hydrate thus, a combination of depressurization and thermal simulation was employed for the complete hydrate dissociation. Ho et al., (2013) investigated the separation of CO₂ from a pre-combustion gas mixture using a hydrate-based gas separation (HBGS) process with (7.5, 15, and 22 ml) cyclopentane and (100, 300, and 1000 ppm) SDS as a promoter in an unstirred reactor. No improvement was observed in the process due to the presence of the promoter. The kinetics yielded better results using an unstirred reactor than the stirred one utilized in a separate study.

Babu et al., (2014) incorporated propane as a co-guest in hydrate formation with silica sand in CO₂ capture and seawater desalination. An unusual behavior was exhibited where propane drew water dispersed in the silica sand bed to the hydrate formation zone. Water migration was reported to have led to enhanced hydrate formation for CO₂ capture and desalination. Moreover, Partoon et al., (2015) designed a semi-batch hydrate crystallizer for carbon dioxide capture from a gas stream with reduced induction time, increased formation rate and solution for heat problems. In the analysis of the experimental data, it was noted that the rate of gas

hydrate formation for the CO₂/CH₄ system is affected mainly by the pressure and gas phase composition.

Yang et al., (2014) investigated the capture of CO₂ with HBGS. THF and SDS were added to accelerate hydrate formation and to lower the equilibrium conditions in the presence of a porous media. Results showed that THF promoted solution concentration as the solution rarely moved and the distribution of the solution was homogenous and in hydrate formation and dissociation. Zhou et al., (2018) built a high-pressure flow loop apparatus to investigate the effects of four parameters, flow rate, liquid loading, temperature, and initial pressure on CO₂ hydrate formation. Results revealed that gas consumption increased with pressure yet decreased with an increase in temperature, flow rate and liquid loading.

2.9 Hydrates as an Energy Resource

Hydrate deposits are estimated to occupy 99% of the reserves in the world both onshore and offshore. The prevailing temperature and pressure for hydrate formation at the seabed are at a depth of 300-800 m, sufficient to stabilize the hydrate (Bai et al.,2012). On the mainland, hydrates occur in areas of permafrost, which are the long-term frozen surface areas with year-round temperatures below zero degrees as shown in Figure 2.10.

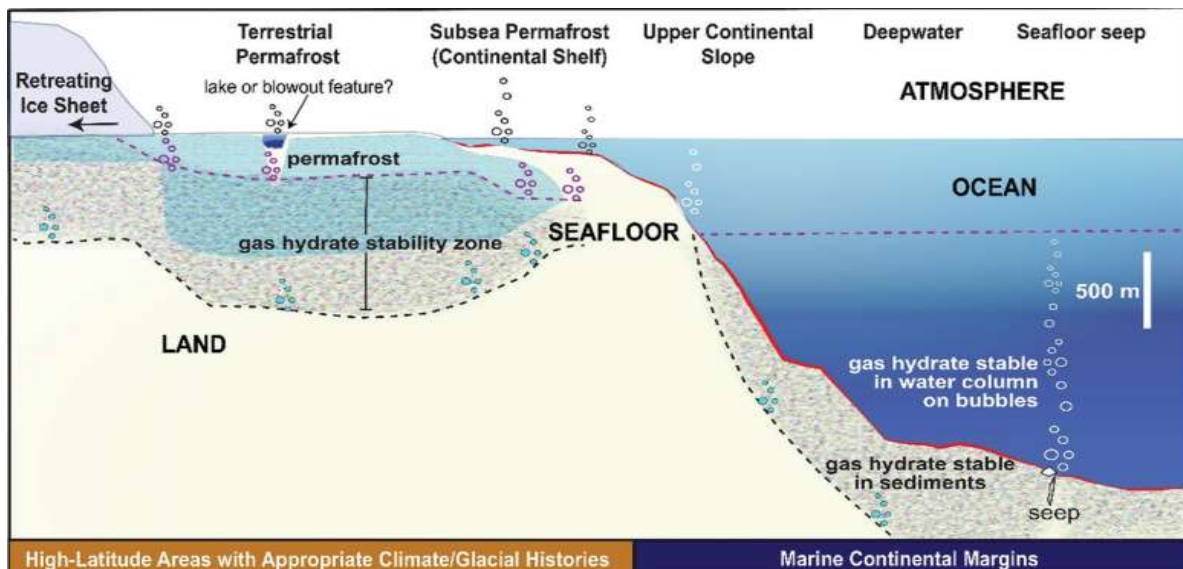


Figure 2.10: Pictorial representation of terrestrial and marine occurrences of hydrates (Hassanpouryouzband et al., 2020).

Hydrates have a large storage capacity (one cubic meter of hydrate can store up to 150 m³ of natural gas) under safe conditions. Furthermore, it was shown that energy storage in hydrates is potentially more operable and safer than compressed natural gas or liquid natural gas (Ruffine,2005; Zheng et al., 2020). These serve as natural energy stores, which motivated

studies in improving energy storage in hydrate clathrate as artificial energy stores. Geophysical explorations include seismic surveys, borehole logging and the technologies categorized based on the dissociation techniques involved, such as thermal stimulation methods, inhibitor injection, and depressurization methods. Production techniques for gas exploration require extensive knowledge of the geotechnical characteristics of hydrate reservoirs (Joseph et al., 2015). Natural gas hydrate exploration is detailed in Appendix A.2.

Excellent progress has been accomplished in studying clathrate hydrate as a storage medium for gases, with hydrogen being the most considered in numerous types of research. Several promoters have been successfully utilized to improve clathrate hydrates' storage capacity. Raman spectroscopic, diffraction, and gas analysis methods have successfully measured and confirmed the resultant structures' storage capacity (Davoodabadi et al., 2021; Gupta et al., 2021; Walsh et al., 2011). Recent studies by Ghaani et al., (2019) reported the effects of microbial stabilization and kinetic enhancement of marine methane hydrates. Extracytoplasmic porin produced by a marine methylotrophic bacterium culture was observed to provide the basics for kinetic enhancement and stabilization of methane hydrates under conditions simulating the seabed environment. It was concluded that there is an existence of microbe-based stabilization of marine hydrates. Filarsky et al., (2018) developed an absorption process for gas storage in its hydrate form. In a gas mixture containing methane, ethane and propane, methane was separated and stored as a gas hydrate while the natural gas remained in the gas phase. High formation rates, separation efficiencies and high storage conditions were achieved with 5.56 mol % THF as a promoter at a pressure of 0.8 MPa and temperatures between 287.15 to 282.15 K.

Hydrates have been applied to the automobile sector as well as other applications. Yevi and Rogers. (1996) studied fuel storage in hydrates for natural gas, which was considered a possible replacement for liquid petroleum-based fuels due to environmental concerns. Results showed up to 143 - 159 (v/v) of gas that could be stored. In addition, they observed that controlled decomposition of the hydrate could be utilized in feeding an automobile vehicle. Arca et al., (2011) investigated the feasibility of using hydrate technology as a storage media for biogas, a renewable energy source with low environmental impact. Biogas is a mixture of CH₄, CO₂, and H₂S, which can be converted into renewable electric power. Results showed that biogas could be upgraded to biomethane with two different cost-effective approaches, whereas Ruppel. (2011) reported on the feasibility of using methane as a reliable energy source for domestic and

commercial applications. It was noted that methane produced from gas hydrates was not utilized for domestic or commercial purposes. Nazari et al., (2011) studied batch production of natural gas hydrates at 10 MPa and 277 K. Hydrate stabilization tests were carried out for hydrate storage and transportation. Gas-rich-dry hydrate was obtainable by heating-cooling the hydrate in the metastable zone leading to ice melting and the hydrate cages being occupied by liquid water converted to a hydrate. The presence of SDS promoter and hydroxy ethyl cellulose (HEC) stabilizer increased the gas storage capacity of the hydrate, thus enhancing the hydrate formation rate and stabilizing the hydrate for lower pressure storage and transportation. In addition, Khot and Sanjay. (2017) investigated an energy storage system for automobiles to reduce fuel prices. Methane hydrate with solar energy as a heat source for the hydrate dissociation was feasible for automobile fuel systems with eliminating regasification costs. Approximately 6.15 kg of methane was released daily using solar energy from 45.92 kg of hydrate. Furthermore, Kezirian and Phoenix. (2017) presented a design for producing, storing, and transporting natural gases. The production scheme was designed to cater to natural gases in deep oceans and to address hazards associated with conventional means of transporting natural gases. However, this method does not cater to energy release for domestic use. Also, in a study on the transportation of biogas and biomethane as compressed biomethane (CBG) or liquefied biomethane (LBG), a comparison of energy performance and climate impact of two gas hydrate scenarios was made. Results showed that the distribution of biomethane as gas hydrates had lower energy performance and higher climate impact than compressed biomethane distribution (Moghaddam et al., 2021). A summary of studies on utilizing hydrates as energy storage media is presented in Table A.2 in Appendix A.

2.10 Gas storage in solid systems

The common technologies utilized in gas storage are pressure gas tanks (Hua et al., 2011), porous media (Xia et al., 2013), metal hydrides (Li et al., 2014) and gas hydrates (Nguyen et al., 2020). The technologies employ different techniques, mechanisms and physical principles to store gases hence they have different storage capacities.

The storage of these gases in solid form is currently being researched intensively. There are several reasons to support gas storage inside a solid material rather than in a storage tank or cylinder. Firstly, more gas can be stored in a given solid volume than in a tank under relatively high pressure, increasing the gas storage density. Additionally, storing gas in solid encapsulations is advantageous for safety reasons such as the risk of high-pressure explosion

and minimization leakages. Thirdly when gases are required in small quantities, it is easier to scale storage to a small amount of solid material (Robert et al., 2009).

2.10.1 Various Gas Storage Technologies

The United States Department of Energy (US DOE) has set a target for CH₄ storage systems at 180 v(STP)/v(STP) (STP equivalent of methane per volume of adsorbent material storage system). Under 35 bar and near ambient temperature. Al-soc-MOF-1 has been developed for CH₄, O₂ and CO₂ storage in a highly porous aluminum-based metal-organic framework. MOF-5 with a BET surface area of 3800 m²/g and a volumetric storage capacity of 66 g/L for H₂ gas (Kaye et al., 2007). IRMOF-6 absorbed 155 v(STP)/v (or 240 cm³/g) CH₄ at 298 K and 36 atm, much higher than zeolite material or any other porous MOF 9. The addition of a phenyl ring improved the storage of this MOF dubbed PCN-14, with an absolute uptake capacity of 230 v(STP)/v (excess: 220 v(STP)/v) 28% higher than the US DOE target, at 290 K and 35 bars. PCN-14 currently holds the record for CH₄ storage and represents the first case surpassing the US DOE targets for porous MOFs (Ma, and Zhou, 2010).

A Germany company Badische Anilin- und Sodafabrik (BASF) constructed a pilot plant that used ZnO and ethylene MOFs for gas purification and storage. It was reported that the structure allowed maximum gas storage per volume (Research News, 2005). The industrial application of Basolite Z377 pellets-based MOFs system for H₂ storage on a pilot scale study showed that storage capacity was comparable to 70 MPa compressed H₂ gas. The adsorbent offered advantages in terms of the volumetric and gravitational capacities (Dailly et al., 2011). The UiO-66 and Al-fumarate MOFs were applied in a pilot-scale heat pump. It was observed that the MOFs outperformed commercial silica gel under standard conditions with stability over numerous cycles. The performance of the MOFs was affected by mass transfer limitations caused by the organic binders (Farrusseng et al., 2018).

Magnesium metal hydrides have been investigated extensively in the storage of H₂ gas. Mg₈₀Y₅Ni₁₅ hydride has been reported to have high H₂ absorption of 4.2 wt.% at 200°C (Xu et al., 2019). This method is advantageous in that it is compact. However, the high costs incurred in producing alloys for the operation and the slow dehydrogenation kinetics are the main challenges in its application (Stamatakis et al., 2018). An H₂ gas purification prototype based on LiNi₃ hydride has been commissioned to absorb 100 cm³/min of gas and H₂ recovery of over 95% (Borzzone et al., 2017). However, most porous materials have low capacity due to

their packing density, and their storage capacity depends on the molecules' geometric structure (Alezi et al., 2015).

High-pressure tanks are much simpler in application and can take up large volumes of gases but require a durable construction material to withstand compressed gas at a pressure of up to 20 MPa (Dagdougui and Ouammi, 2018). Moreover, gas tanks are potentially explosive. An economic analysis of CO₂ capture using cryogenic packed-bed anti-sublimation technology showed an estimated cost of 34.5 pounds/ton of CO₂ (Moreno et al., 2019). Cryogenic techniques such as controlled freeze zone and anti-sublimation have been applied in biogas upgrading with estimated energy consumption of 0.31-0.35 kWh/Nm³ (Popov et al., 2019; Naquash et al., 2022). In Japan, a company known as Kawasaki heavy industries is utilizing cryogenic cooling of hydrogen to a temperature of minus 253 °C. This results in the phase change from gas to liquid and volume reduction, improving storage and transportation efficiency (H₂ Bulletin, 2021). The main challenge of this method is the cost associated with the cooling and compression of the system (Zohuri and Zohuri, 2019). In Australia, a pilot plant-based cryogenic condensation with the formation of hydrates was constructed for CO₂ capture and storage in power plants. Continuous condensed CO₂ and CO₂ hydrate production were achieved with approximately 70 mol% CO₂ capture (Surovtseva et al., 2011).

Compared to other gas storage methods discussed in this section, the hydrate technique is advantageous because it is a safer method (uses water and hydrate forming gas), inflammable and environmentally friendly in that it does not leave a carbon footprint or pollutant by-products. Additionally, hydrate dissociation is rapid and requires minimum energy for decomposition (Ozaki et al., 2014; Veluswamy et al., 2014). A major challenge with the hydrate system is requiring a continuous cooling system to maintain the hydrate within the hydrate stability zone. Moreover, any abrupt failure in the cooling system can have catastrophic consequences as the hydrate would decompose and release large amounts of gas quickly. The feasibility of continuous gas hydrate production is another critical concern with two pilot plant operations documented in the literature. These included a 5t per day hydrate production pilot plant which used water and bubble column, constructed in 2008 by Mitsui Engineering and Shipbuilding (MES) (Watanabe et al., 2008). And secondly, a plant commissioned by the Korea Institute of Industrial Technology (KITECH) was built in 2012 (Veluswamy et al., 2018). No further reports have been recorded on the commercial use of the two technologies in recent years.

2.10.2 Current trends in South African Energy Sector

Hydrogen is classified as green, blue or grey depending on the raw materials and production route. Grey hydrogen is obtained from reforming fossil fuels or steam reformation of natural or shale gas (Sazali et al., 2020). When carbon emissions are captured and stored, hydrogen is referred to as blue hydrogen (IEA, 2019). When renewable energy sources such as wind and solar are utilized to produce hydrogen, it is designated green. It is obtained mainly through water-splitting or dehydrogenating hydrogen carrier molecules (Wang et al., 2019). The abundance of renewable resources in Africa as well as the developed energy sector, makes it a key candidate in producing renewable energy at a low cost. The key component in this energy map is low-cost green hydrogen which gives Africa a clear competitive edge as a clean hydrogen hub (Bowyer, 2022). The global hydrogen market is set to expand from 70 million tonnes in 2019 to over 120 million tonnes in 2024 (Safari and Dincer, 2020). Morocco and South Africa are the notable Africa nation to create the hydrogen sector. Morocco has already set up a National hydrogen commission and currently developing its national road map. South Africa, on the other hand, has published its hydrogen roadmap/strategy. Hence, South Africa is focussing on green hydrogen as it has identified it as a critical component in its energy transition and global commitment towards a decarbonized economy (Green hydrogen Organisation, 2021). In addition, South Africa is targeting to become a major global producer and exporter of green hydrogen, with a 4% share of the global market by 2025 (CSIS, 2022). This current study focussed on gas hydrates to store gas in solid form and can be considered portable green hydrogen storage.

In conclusion, in this chapter, various aspects which affect the rate of CO₂ or CH₄ hydrate formation, structure, and CO₂/CH₄ hydrate storage studies available in the literature have been presented. Moreover, the replacement of CH₄ with CO₂ from the CH₄ hydrates for CO₂ sequestration and CH₄ release was presented. Lastly, the storage of gas in solid systems was presented as well as green hydrogen potential utilization in the global energy sector. In the subsequent chapter, techniques of hydrate formation and the equipment utilized for hydrate equilibrium measurements will be presented. Furthermore, the apparatus used in the replacement reactions will be detailed.

Chapter 3: Review of equipment and experimental techniques for CH₄-CO₂ replacement

3 Introduction

The design and specifications of hydrate equipment have evolved over the years from the basic hand-blown glass to highly sophisticated high-pressure reactor vessels allowing for the hydrate's withdrawal of hydrate of solution/gas. The most common apparatus applied in hydrate measurements consist of a high-pressure reactor cell, an agitation device, data logging systems, sampling mechanisms, and heating and cooling devices. This chapter focuses on equipment designs and experimental techniques applied specifically in methane-carbon dioxide hydrate systems incorporating porous media. Modifications to the existing hydrate equipment for CH₄-CO₂ replacement reactions and techniques are also presented.

3.1 Principles of equilibrium apparatus and technique development

Three principles were established to serve as a blueprint for the development of succeeding apparatuses and techniques in investigating hydrate behavior (Sloan and Koh, 2008).

- For total water transformation into hydrate phase, vigorous agitation is required - it was observed in early experiments that agitation resulted in a decreased the quantity of water molecules in the hydrate. There are three reasons why agitation is essential: to prevent water occlusion and expose liquid to the hydrate former for surface renewal. As Hammerschmidt reported (1934), agitation is required to start hydrate formation and shorten the metastability stage.
- The hydrate equilibrium point is determined using hydrate dissociation – Caillet, (1877) observed that pressure should increase beyond the hydrate equilibrium point and the formation of hydrates resulted in a relaxation of the metastable pressure. For hydrate dissociation, slow heating or depressurization did not result in metastability. Although the hydrate dissociation endpoint was repeatable, it was interpreted as a sign of the upper limit of formation metastability.
- A sudden drop in pressure or rise in temperature in a constant volume device denotes hydrate formation. – early researchers observed a decrease in the pressure as the gas was encapsulated in the hydrate. On the other hand, the disappearance of the final hydrate crystal coincides with a decrease in the pressure-temperature trace during dissociation with heating. Thus the hydrate equilibrium can be obtained without visual

observation but by measuring at the point of the cooling and heating isochors intersects (Sloan and Koh, 2008).

3.1.2 Classification of techniques and equipment

The experimental methods can be classified into two categories depending on how the equilibrium is attained (Richon, 1996). The dynamic (open circuit) and static (closed circuit) methods are used. In the dynamic method, equilibrium is achieved without mechanical agitation since one of the phases is circulated until equilibrium is attained. This method is associated with a relatively high cost of maintenance. In the static method, internal stirring or agitation is employed to reduce the required time for the system to attain equilibrium without recirculating the fluid phases (Raal and Mühlbauer, 1998). Another way of classifying different experimental measurements is according to their means of composition analysis of the equilibrium phase. This includes analytical methods or measurements of an actual synthesized charge. These methods are analytical or synthetic (Dohrn et al., 2010). Another postulated method (Schroeter et al., 1983) is based on whether a visual or non-visual hydrate technique is employed. This method is based on observing the hydrate as it forms in an equilibrium cell, hence it requires an optically clear cell or optical window. It is only practically applicable above the freezing point of water as the ice can cloud or obscure the visualization of hydrate formation. This is a distinguishing feature in most static apparatus for hydrate studies.

The widespread method of obtaining phase equilibria data is monitoring the hydrate phase indirectly. Parameters that can be observed are associated with pressure decrease or increase in temperature in the fluid phase. A visual inspection is the only direct evidence of the formation of the hydrate phase. Measuring the quantity of hydrate phase formed is imperative, with homogenous hydrate formation indicated by macroscopic phase equilibria data and guest size. In contrast, microscopic (spectroscopy/diffraction) measurements of the hydrate phase show a heterogeneous hydrate composition (Sloan and Koh, 2008).

3.2 Techniques for determination of dissociation point measurement

Three techniques have been reported in hydrate formation experiments. These include isobaric, isothermal, and isochoric techniques, as summarized in Table 3.1. Hydrate formation above 273 K proceeds in one of the three static modes mentioned above. Hydrate formation point is dependent on various factors such as stirring rate, initial temperature, the water quality and its history whether it has been previously used for hydrate formation hence it is not unique and cannot be referenced. A critical point of note is hydrate dissociation, a repeatable

thermodynamic equilibrium point regardless of the equipment utilized. It is also known as the condition of temperature and pressure where the last hydrate crystal dissociates (Tohidi et al., 1997).

Table 3.1: Experimental techniques utilized in hydrate measurements (Babee, 2015; Croeser, 2017)

Method	Characteristic	Hydrate Formation	Hydrate Dissociation
Isothermal non-visual	Constant Temperature	Decreasing pressure	Increasing pressure
Isothermal visual	Constant Temperature	Observed visual (increasing pressure)	Observed Visual (decreasing pressure)
Isobaric	Constant Pressure	Sudden significant fluid (gas or liquid) injection from an external source	Visual observation of gas disappearance
Isochoric	Constant Volume	A sharp decrease in pressure	Cooling curve and heating curve intersection

In the *isothermal method*, the hydrate gas and liquid are set at a pressure value higher than the hydrate formation point. An external reservoir controls the system pressure by adding and withdrawing hydrate-forming fluid. After hydrate formation, pressure is gradually reduced, and the equilibrium pressure is noted through visual observation of the disappearance of the hydrate crystal (Fakir et al., 2021). In a non-visual isothermal method, the system is stabilized at a certain temperature and pressure value. Hydrate formation begins once the sample is stable and is indicated by a pressure decrease in the system. Gas ventilation decreases the system pressure below the expected equilibrium value once the pressure is close to an equilibrium value. The previously formed hydrate dissociates, causing a pressure increase in the system, thus approaching the equilibrium value (Sloan and Koh, 2008, Croeser, 2017).

In *isobaric operation*, gas exchange with an external reservoir keeps the system pressure constant. At the onset of the experiment, the equilibrium cell is pressurized with the hydrate former and allowed to reach equilibrium. Then pressure decreases and the consumed hydrate former is recharged into the system to maintain constant pressure. At the end of hydrate formation, the system reaches steady conditions, and the temperature is slowly increased at constant pressure maintained by withdrawing the former to dissociate the hydrate. Temperature increment is affected until the last hydrate crystal dissociates. This point is the equilibrium hydrate dissociation temperature at constant pressure (Sloan and Koh, 2008).

The *isochoric method*, is a non-visual method where a constant volume high-pressure vessel is utilized for hydrate measurements. This method is shown in Figure 3.1 by the temperature-pressure trace. This method was selected for use in this work due to its ease of application and repeatability. The initial experiment condition is indicated by point A, which is the liquid and gaseous hydrate former. The gradual cooling leads to pressure decrease until point B is reached, where hydrate formation commences, and a sharp pressure decrease is observed as the hydrate grows and encapsulates more of the gas. Point C is reached when the constant temperature and pressure of the system over show the hydrate formation process. The temperature is increased slowly until point D is reached, where the heating curve intersects or flattens to run parallel to the cooling curve. This is known as the hydrate equilibrium point or final dissociation point (Sloan and Koh, 2008). This method was utilized throughout this study for the hydrate dissociation data measurement.

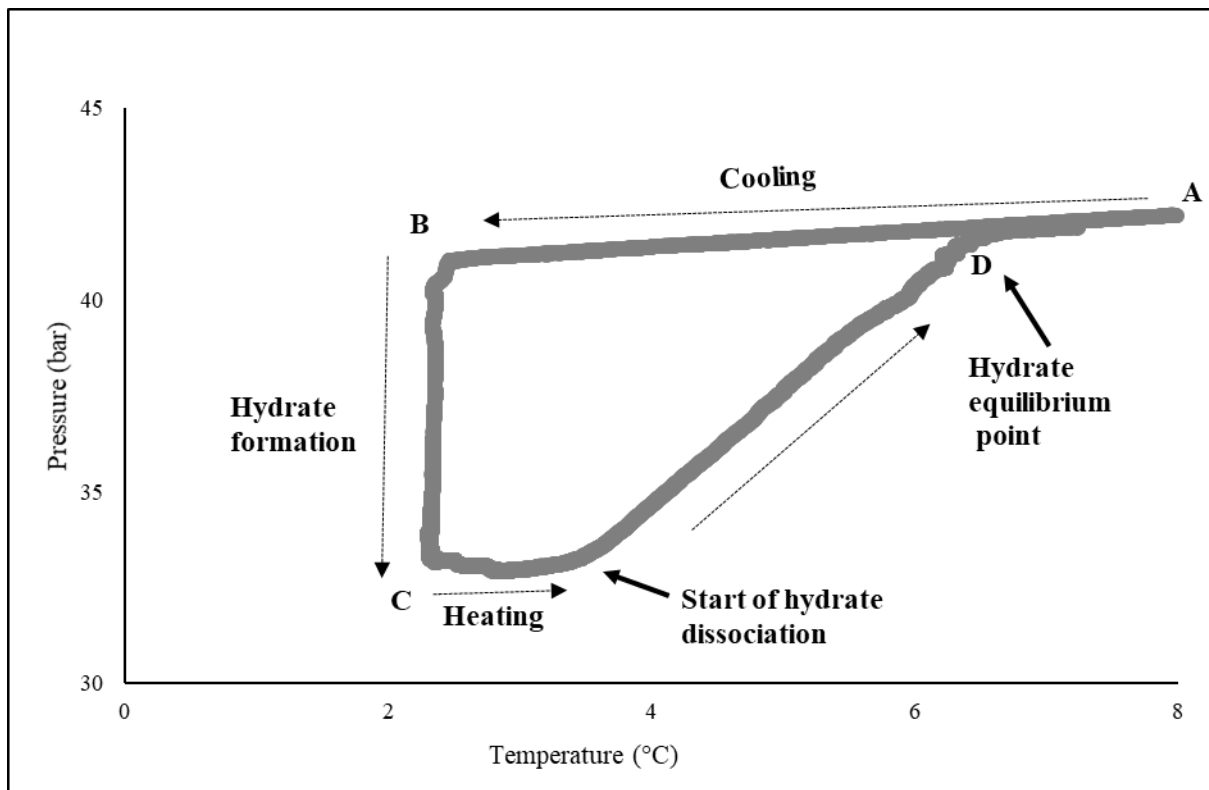


Figure 3.1: Pressure-Temperature plot utilizing the isochoric method for methane hydrate (figure produced in this work).

3.3 Apparatuses utilized in hydrate phase equilibrium measurements

It is imperative to produce precise hydrate equilibrium data for the equipment design of hydrate processes. Therefore, a reliable hydrate apparatus is essential. The current apparatuses have evolved from Deaton and Frost (1937), who designed this static equipment and investigated

gas hydrate equilibria. The following types of equipment have been developed and applied in hydrate studies as *Quartz crystal microbalance* (QCM) (Mohammadi et al., 2003), *Sapphire equilibrium cell* (Dholabhai et al., 1996), *differential thermal analysis* (Fournaison et al., 2004), *differential scanning calorimeter* (Delahaye et al., 2006), and *Cailletet apparatus* (Peters et al., 1993). Improvements and changes to the design of hydrate phase equilibria apparatuses have incorporated modern auxiliary components which allow for the improvement in uncertainty measurement, an extension of pressure operating ranges, and improvement in the data acquisition. This section presents a brief description of the hydrate phase equilibria apparatuses. A summary of the equipment is given in this section with the schematic is provided in Appendix B.

3.3.1 Summary of equipment utilized in hydrate phase equilibrium

The *high-pressure Rocking cell* reported by Deaton and Frost, (1937) was the first piece of equipment to be documented in hydrate investigation. It had a view window on the equilibrium cell to visually observe hydrate formation, a valve to regulate gas flow in and out of the cell, thermocouples, and a pressure transducer (Bourdon tube gauge). It was applied above the freezing point of the hydrate former. (Sloan and Koh, 2008).

Kobayashi developed the *high-pressure Ball Mill hydrate apparatus* in the 1950s following the work begun by Katz et al., (1959). The setup consisted of a high-pressure non-visual, stainless-steel cylinder rotating about its axis. Galloway et al., (1970) modified the equipment by inserting a stainless-steel ball inside the cylinder for surface area renewal upon rotation to convert water to hydrate. Further equipment modifications were carried out by Aoyagi and Kobayashi (1978) so that gas could be recirculated through the cell in a semi-batch operation (Sloan and Koh, 2008).

The *Cailletet apparatus* is a high-pressure apparatus with a transparent wall, a pressure range of 0.35-15 MPa, and a temperature range of 250-450 K (Peters et al., 1986, Peters et al., 1993). It had a pressure gauge with an accuracy of 0.0025 MPa, and a platinum resistance temperature probe with an accuracy of 0.01 K. Its main features are a 500 mm thick-walled Pyrex glass tube (Cailletet tube) used as an equilibrium cell with an inner diameter of 3 mm and an outer diameter of 10 mm. The upper end of the tube was closed, with the lower end with a conical thickening enabling the tube to be mounted in an autoclave. The *sapphire equilibrium cell* is made of a sapphire tube with a pressure limit of 15 MPa fitted with 316 stainless steel as the

top and bottom flanges with a Ruska piston pump employed to vary the volume of the equilibrium cell tapping from the mercury reservoir (Dholabhai et al., 1993; Sabil, 2009).

One of the modern apparatuses assembled is a *Quartz crystal microbalance*. It was first published and utilized in hydrate measurements by Mohammadi et al., (2003), with a thin disk of quartz placed between two electrodes that conducted an electric current that caused the quartz disk to oscillate at a specific frequency. The *Differential Thermal Analysis (DTA) apparatus* was designed to distinguish the thermal behavior of binary and ternary mixtures for the phase diagram of CO₂ hydrate mixtures and measurement of heat transfer, as could be inferred from its name (Fournaison et al., 2004). It comprises two symmetric transparent glass cells, one containing an experimental solution and the other with an inert solution.

The *high-pressure Differential Scanning Calorimeter (DSC)* was designed and successfully employed for hydrate phase equilibria data and thermal property data (Delahaye et al., 2006). A *Micro-DSC analyzer in conjunction with high-pressure Differential scanning Calorimetry (HP-DSC)* has two pressure-controlled cells, a sample cell containing the experimental solution and an empty reference cell. No stirring mechanism was installed in the apparatus due to the nature of the system. It has been utilized by various researchers (Dalmazzone et al., 2002; Martinez et al., 2008, Mayoufi et al., 2009).

3.3.2 Equipment for investigating the hydrate structure

Various apparatus have been developed to measure different hydrate properties. *Setaram* with the *DSC 111, BT2-15 calorimeter, micro-DSC VII* have been utilized to measure the thermal properties of gas hydrates (Sloan and Koh, 2008). High-accuracy calorimetric measurements were obtained from a modified *Setaram BT Tian-Calvet calorimeter* for pressures. A laser scattering method was applied to measure changes in hydrate particle size distribution during hydrate formation or decomposition, which is focussed on the beam reflectance method. Yang et al., (2004) and Taylor (2006) used a *micromechanical force apparatus* to measure the adhesive forces between hydrate particles or between a hydrate particle and a surface directly. Hydrate transport properties (thermal conductivity, permeability, and thermal conductivity) and kinetics properties (density profiling of the hydrate, gas, and water phases) were determined by *X-ray computed tomography* (Kneafsey et al., 2005, Gupta et al., 2009). *Magnetic resonance imaging (MRI)* was utilized by Moudrakovski et al., (2004) to study real-time hydrate growth from ice particles, water droplets, and particle morphology. These

instruments are essential as they measure different hydrates properties which are imperative in application of gas hydrates.

3.4 Equipment used for CH₄-CO₂ replacement reactions without porous media

Unique equipment designs have been utilized in replacement reactions. Acute modification, including a buffer cell, gas booster, and ISCO syringe pump for pressurizing CO₂ gas, has been carried out on the reactor vessel and the equipment designed to suit the experiments (Ota et al., 2005, Kang et al., 2014). The types of equipment that have been developed to investigate replacement reactions mainly focus on the innovative mechanism of substituting CO₂ for CH₄ in methane hydrates. For effective hydrate formation and dissociation, stirring, bubbling, and spraying are necessary for effective gas and water mixing. A summary of the equipment designs used in the substitution of CH₄ with CO₂ without a porous media is presented in Table 3.2, going from older to most recent investigations.

Table 3.2: Summary of equipment designs utilized for CH₄-CO₂ replacement reaction without porous media.

Reference	Equipment Description	Operating Conditions	Design Advantages
(Hirohama et al., 1996)	A 3.2 dm ³ reactor with a cooling jacket A view window Mechanically sealed stirrer, driven by compressed air The feeding system consisted of a water vessel, air pump to feed water, a mass flow meter	P – 7 MPa T – 274 - 283 K	Sampling balloon for gas collection Wet gas meter to determine the quantity of CH ₄ and CO ₂ in the gas phase and liquid phase
(Ota et al., 2005) (Ota et al., 2007)	A high-pressure cell with an internal volume of 129.8 cm ³ An expansion tank with an internal volume of 7.40 cm ³ Three high-pressure glass windows at the top and sides magnetic agitator inside to enhance hydrate formation Two buffer cells of internal volume of 150 cm ³ Raman spectrometer or gas chromatograph was used to follow the reaction profile	P – 3.26-6.0 MPa T – 273.2 K	Three high-pressure view glass windows Buffer cell could be detached to determine the amount of gas by weight change
(Lee et al., 2012)	A pressure cell (170 ml) made of stainless steel pressure Gas supply vessel (23 ml) back pressure regulators for pressure control A gas booster pressurizes gaseous CO ₂ Ruska pump (500ml in volume) to generate liquid CO ₂ A gas purifier filled with silical gel and sodium chloride	P – 10.34 MPa T- 263 – 275 K	Gas booster for pressurizing gaseous CO ₂
(Kang et al., 2014)	Equilibrium cell with a volume of 50 ml Quartz view window A 500 ml reservoir cell placed in the same temperature bath as the equilibrium cell ISCO syringe pump model 260D to increase gas pressure A back pressure regulator to maintain constant pressure (XRD/HRPD, Raman) and Gas chromatography was used for gas analysis	P – 20.0 MPa T- 263 – 288 K	Use of a syringe pump (ISCO, model 260D for increasing pressure of the feed gas Incorporation of a buffer to regulate the temperature of the incoming gas

Table 3.2: Summary of equipment designs utilized for CH₄-CO₂ replacement reaction without porous media. (Continued)

Reference	Equipment Description	Operating Conditions	Design Advantages
(Zhou et al., 2015)	High-pressure reactor with an Internal volume of 5.3 L Cooling jacket coated outside that was made of 316 stainless steel Agitator- anchor-type stirrer gas chromatography for gas analysis Gas booster Installed gas sampler	P – 6.2 MPa T – 230-273.9 K	Analysis of the hydrate structure and the gas phase by Raman spectroscopy and gas chromatography
(Partoon et al., 2018) (Partoon et al., 2015)	A 5250 mL stainless steel 316 reactor The water line sprayer quenched in the middle where there is heat generated as gas hydrate form A gas analyzer checked the gas-phase composition	P – 3.0 -5.0 MPa T - 263-300 K	A four-stage gas compressor achieves high pressure. A reactor controlled by an Omron PLC along with a PC

3.5 Equipment Designs for CH₄-CO₂ dioxide replacement with porous media

In the investigation of methane replacement with carbon dioxide in the presence of porous media from a methane hydrate, various modifications and novel designs have been applied and widely published in the literature. Notable changes were in the reactor design, thermocouples orientation and a buffer tank or a reservoir vessel were incorporated and placed in the same temperature bath as the reactor vessel (Zhou et al., 2008, Zhang et al., 2017). One noticeable difference in the apparatus used in the presence of porous media is the absence of stirring devices or mechanisms. This is due to the nature of the fixed bed of porous media, which does not permit agitation. Hydrate formation and growth in porous media occur in the interstitial or sediment pore space through any of the four methods mentioned in Chapter 2. The gas is bubbled through the equilibrium cell to enhance contact between the hydrate former and the porous media which acts as a nucleation site. For a more detailed description of the apparatuses, the reader is referred to the literature for the apparatuses summarized in Table 3.3 starting with earlier to recent studies.

The techniques and equipment design discussed in this chapter informed the design of the equipment utilized in this study. Three different high-pressure vessels were utilized in this study, with a new apparatus designed specifically for the CH₄/CO₂ replacement experiments in the presence of porous media. The details and schematic of the equipment are presented in Chapter 4 (kinetic measurements), Chapter 5 (replacement without porous media), and Chapter 6 (replacement in the presence of porous media).

Table 3.3: Summary of experimental apparatus and techniques used for the CH₄-CO₂ replacement reaction with porous media.

Reference	Equipment description	Replacement Technique	CO ₂ addition procedure
Zhou et al., (2008)	A stainless-steel equilibrium cell - internal dimensions of 36 mm, diameter height of 200 mm with inner volume of 350 mL PTFE inner sleeve for insulation, internal cooling jacket Four thermocouples 60 mm apart Data collector Mass flow meter for gas flow measurement Gas chromatography for gas analysis	Replacing CH ₄ with another gas in a quartz sand-containing hydrate Use of Carbon dioxide-in-water emulsion	After methane hydrate formation temperature was reduced to 271.2 K A flow meter measured the amount of free CH ₄ that was discharged CO ₂ was used to purge the cell Then liquid or emulsion or CO ₂ was injected into the cell controlled at 281.2 K and 5 MPa
Yuan et al., (2013)	An equilibrium cell with a height of 100 mm and an inner diameter of 300 mm with a maximum pressure of 16 MPa Sixteen thermocouples were inserted into the reactor to measure the temperature during hydrate formation Each group includes four thermometers distributed at the same depth but a different radius of 132 mm, 99 mm, 66 mm, and 33 mm from the centre of the reactor, respectively. The depths of four groups of thermometers were 82 mm, 58 mm, 34 mm, and 10 mm respectively	Recovery of CH ₄ from natural gas hydrate in porous sediment Use of pressurized liquid CO ₂	After CH ₄ formation, the pressure was gradually reduced to the equilibrium pressure of CH ₄ hydrate at the experimental pressure Then CO ₂ was continuously pumped into the reactor. The free CH ₄ molecules in the gas phase were replaced with CO ₂
Zhou et al., (2015)	Stainless steel reactor with an inner volume of 288 ml, a diameter of 50mm and a height of 130 mm Temperature and pressure measurements using a signal converter, a system to supply gas Mass analyzer to analyze the composition of the gas Viewing windows made of quartz on either side Reactor had four temperature sensors are attached its walls	Combined replacement and depressurization	When the absolute pressure had decreased to 50 kPa CO ₂ /N ₂ gas mixture was then added to prevent decomposition of the CH ₄ hydrate temperature was dropped to 273.9 K Gas injection was terminated when the pressure dropped to between 0.02 and 0.5 MPa below the desired level. The temperature was not allowed to increase beyond 270 K during the injection to prevent the dissociation of the CH ₄ hydrate

Table 3.3: Summary of experimental apparatus and techniques used for the CH₄-CO₂ replacement reaction with porous media (*continued*)

Reference	Equipment description	Replacement Technique	CO ₂ addition procedure
Jinhai et al., (2017)	Cylindrical stainless-steel cell with a movable piston, 75 mm diameter, 300 mm in length, and volume of 800cm ³ The piston was utilized to change the cell volume Quizix pump Platium resistance thermometer (PRT) Druck pressure transducer Linear variable differential transmitter (LVDT) installed on the piston, Gas chromatograph for gas analysis	Injection of flue gas into gas hydrate reservoirs The usage of simulated flue gas containing 14.6 mol% CO ₂ and 85.4 mol% N ₂	Purge pressure was set at 0.7 MPa higher than the dissociation pressure of the flue gas hydrate to reduce CH ₄ hydrate dissociation Returning the piston expanded the cell capacity, lowering the cell pressure quickly to the required level without the need for fluid reduction
Zhang et al., 2017	A stainless steel reactor Two quartz viewing windows on either side A gas supply system, Gas chromatography Data acquisition system, Two high-pressure 260D ISCO pumps Two refrigerated circulators ranging from 245 K to 473 K	Thermal stimulation in the CH ₄ /CO ₂ replacement	The temperature of glycol bath was reduced from 273.65 to 268.15 K to preserve the hydrate The vessel was evacuated using a vacuum pump to remove excess CH ₄ from the pores of the porous medium CO ₂ is quickly pumped into the reaction cell using a high-pressure pump until the pressure reaches a predetermined level The temperature was raised to 273.65K
Pan et al., 2020	316L stainless steel reactor, - 18cm high, a diameter of 6 cm -an internal volume of 509 mL The small cylinder is used to store CH ₄ for methane hydrate formation. Two platinum resistance thermometers (pt100), vertically arranged within the reactor, Single pressure sensor	CH ₄ from hydrate-bearing clay sediment CO ₂ /N ₂ gas mixture utilized	The CO ₂ /N ₂ was introduced into the reactor through a cooled pipe (5m pipeline placed in glycol bath) up until the desired pressure of the was reached The replacement gas was injection through the six-way valve and it was 30s long The temperature was set at 274.2 K for gas replacement. 100ml withdrawn and analyzed

Chapter 4: Kinetics Studies, Measurements, Modeling and Results

4 Introduction

The hydrate encapsulation kinetic studies of carbon dioxide (CO₂) and methane (CH₄) in the presence of copper oxide (CuO), aluminum oxide (Al₂O₃) nanoparticles, and graphene nanoplatelets are presented in this chapter. The results from kinetic studies of graphite powder, magnesium nitrate hexahydrate (MgN₂O₆.6H₂O) crystals and Zinc oxide (ZnO) microparticles are presented. The effects of varying concentration, temperature and pressure on the hydrate formation kinetics were investigated. The data obtained from experimental studies were entered into a kinetic model to produce the following kinetic parameters; induction time, storage capacity, rate of gas consumption, and water-to-hydrate conversion. In addition, CO₂ and CH₄ hydrate dissociation studies were carried out. Ngema et al., (2014) designed and assembled the equipment utilized.

4.1 Apparatus

The experimental apparatus utilized in the study is shown in Figure 4.1. It was designed and first utilized in a hydrate study by Ngema et al., (2014). The equipment consists of a 316L stainless steel equilibrium cell with a working volume of 52 cm³, with an effective volume of 36.5 cm³, and a maximum pressure limit of 10 MPa. Stirring was accomplished by a Heidolph RZR 2041 motor gear system connected to the shaft with a magnetic tip turning a magnetic lined stirrer inside the cell. A WIKA pressure transducer model P-10 with an operating range of 0-10 MPa gauge pressure and with an accuracy of 0.025 MPa was used to monitor pressure during the reaction. A TDGC2 model, a variac voltage regulator, was utilized to maintain the temperature of an aluminum block that housed the pressure transducer. A WIKA Class A thermocouple temperature probe with an accuracy of 0.03 K was utilized for temperature measurement. Temperature and pressure data were logged every 5 seconds by a 34972A Agilent data acquisition unit. A Polyscience TXF200 programmable temperature controller with an operating temperature in the range of 243.15 to 323.15 K was used to maintain a water/ethylene glycol water bath temperature with an external dimension of 595 x 460 x 360 mm. A mechanical jack was used to lower and raise the water bath when placing the cell in the water bath. An RV12 rotary vane vacuum pump was utilized to evacuate the system. For the full description of the equipment, the reader is referred to Appendix C.1.

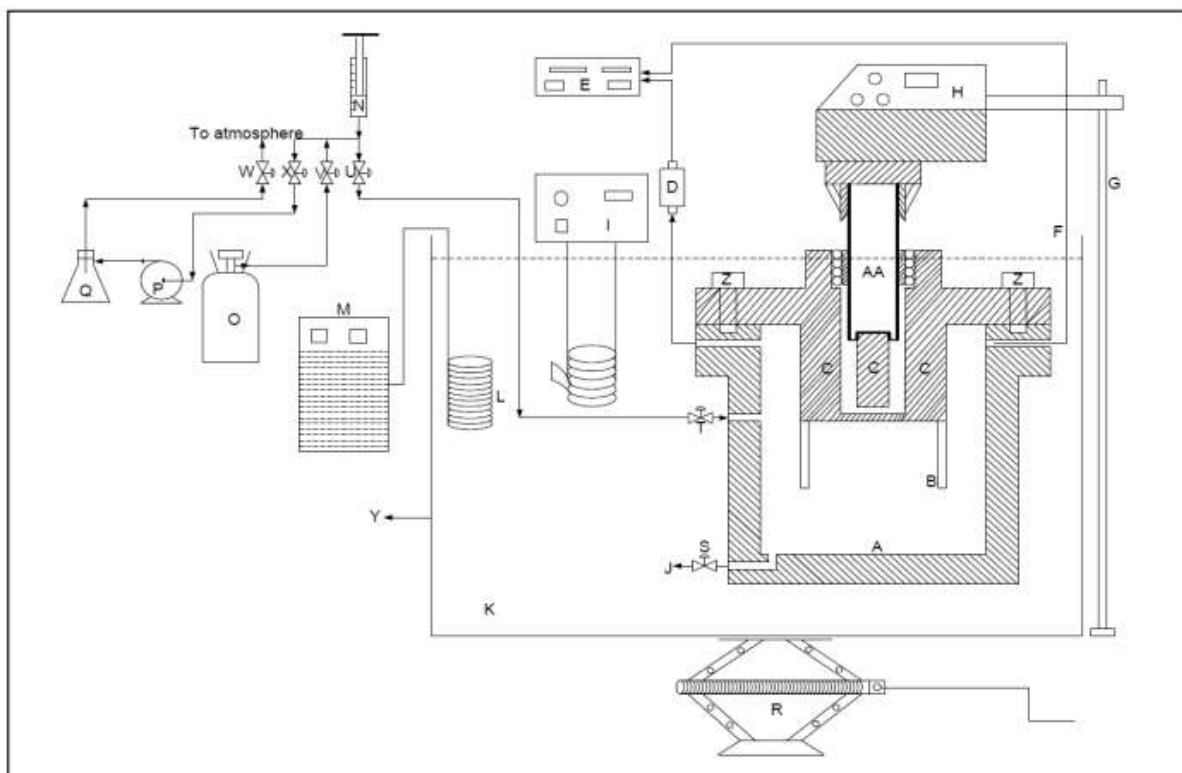


Figure 4.1: A schematic of the experimental setup:

A, equilibrium cell; B, Impeller; C, Neodymium magnet; D, Pressure transducer; E, Data acquisition unit; F, Pt-100; G, Stainless steel stand; H, Overhead mechanical stirrer; I, Temperature programmable circulator; J, Drain line; K, Chilling fluid; L, Cooling coil; M, Cold finger; N, Liquid syringe with an aqueous solution; O, CO₂/CH₄ cylinder; P, Vacuum pump; Q, Vacuum flask; R, Mechanical jack; S, Drain valve; T, Inlet valve; U, Loading valve; V, Gas valve, W, Vent valve to the atmosphere; X, Vacuum valve; Y, Water bath and Z, Stainless steel bolts. (Ngema et al., 2014).

4.2 Materials

The chemicals utilized in the study are specified in Table 4.1. These chemicals were used as provided and not purified or altered. Deionized water with a conductivity of 0.64 mS/cm was prepared in the laboratory. The conductivity was indicated on the Elgar deionization machine.

Table 4.1: Specification and description of chemical utilized in the study.

Chemicals	Description	CAS number.	Formula	Supplier	Purity (vol%)
Carbon dioxide	gas	124-38-9	CO ₂	Afrox	>99.9
Methane	gas	74-82-9	CH ₄	Afrox	>99.9
Copper oxide	<50 nm nanoparticles	1317-38-0	CuO	Sigma-Aldrich	>99.0
Aluminium oxide	<50 nm nanoparticles	1344-28-1	Al ₂ O ₃	Sigma-Aldrich	>99.9
Zinc oxide	5µm powder	1314-13-2	ZnO	Sigma-Aldrich	>99
Graphene	>25 µm nanoplatelets	7782-42-5	C (GPN)	Sigma-Aldrich	>90
Graphite	< 20 µm powder	7782-42-5	C-C	Sigma-Aldrich	>90.0
Magnesium nitrate hexahydrate	crystals	13446-18-9	MgN ₂ O ₆ .6H ₂ O	Sigma-Aldrich	>99.99
Sodium dodecyl sulfate	220-350 nm	151-21-3	CH ₃ (CH ₂) ₁₁ OSO ₃ Na (SDS)	Sigma-Aldrich	>99.0
Water	**	7732-18-5	H ₂ O		

*Not provided by the supplier.

** Deionised water with a conductivity of 0.64 mS/cm

4.3 Experimental method

This section presents the calibration procedure for the temperature and pressure sensors used in this work, followed by leak testing and kinetics measurements.

4.3.1 Calibration of Sensors

Two parameters are imperative in hydrate kinetics studies. These are the system's temperature and pressure, which were measured by a temperature probe and a pressure transducer in this study.

4.3.1.1 Temperature Calibration

A CTH 6500 WIKA-certified standard temperature probe was utilized to calibrate the temperature sensor employed in the replacement study. A silicon oil bath was used to maintain a constant temperature for the standard and the sensor. The temperature sensor and the standard probe were tied together with a string and dipped into the oil bath. The temperature of the silicon oil bath was raised in 10 K increments from 273.15K to 373.15K, allowing the sensor's temperature to stabilize before readings could be taken. The Agilent logged the temperature of the Pt-100 sensor, while the standard probe Agilent logged the temperature of the Pt-100 sensor. The standard temperature probe readings were plotted against temperature readings of

the experimental probes in excel. The results produced a linear plot that was fitted to a first-order polynomial shown in Figure 4.2. The maximum temperature calibration error is reported as the maximum deviation of the measured values to the calibration polynomial shown by a red color in Figure 4.2.

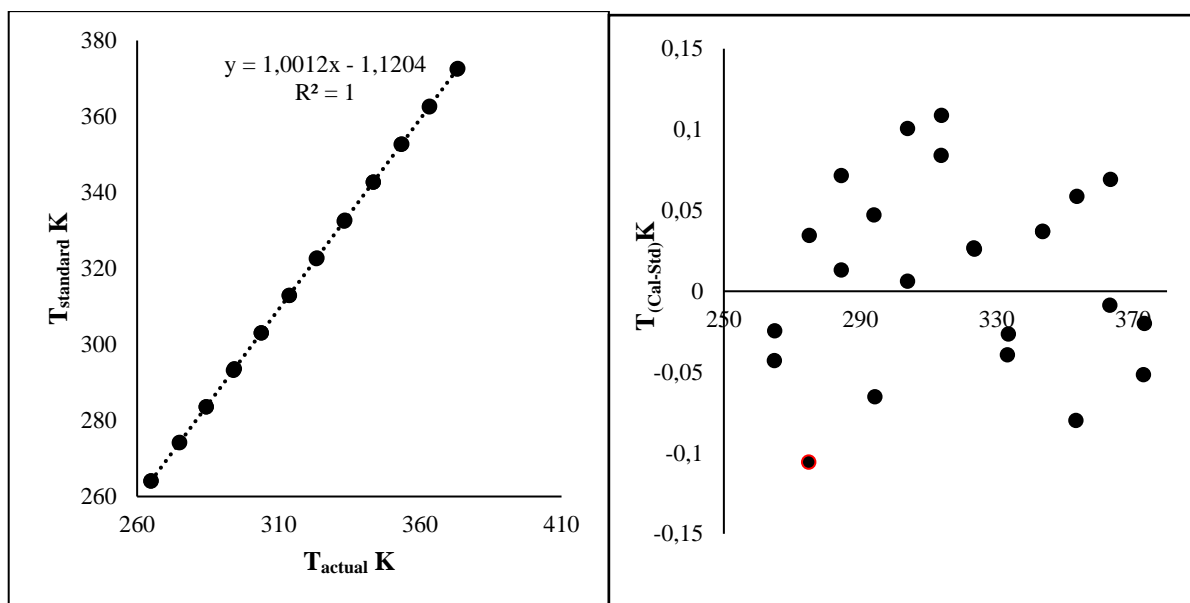


Figure 4.2: Temperature calibration chart for and uncertainty scatter for the temperature probe for the kinetics cell.

4.3.1.2 Pressure Calibration

The pressure calibration was performed using a CPH 6000 pressure Mensor standard on the pressure transducers. A vacuum pump was utilized to evacuate the cell at the beginning of the calibration process. A nitrogen gas cylinder was connected to the standard pressure Mensor unit and then to the equilibrium cell to which the pressure transducer is connected. The temperature in the equilibrium cell was maintained at a constant temperature of 293.15K with a water bath to eliminate the effects of the external environment on the pressure readings. The pressure was varied from 0 to 10 MPa on the Mensor, and the corresponding pressure of the transducer was logged on the Agilent data logging system. The pressure stabilized at each set value before recording and adjusting the pressure. This was carried out step-wise from low to high pressures, then vice versa. The data logger takes a reading every 5 seconds therefore several values would have been recorded after five or more minutes. An average value was computed and used as the reading at the stabilized set point. The data obtained were fitted to a first-order polynomial resulting in a straight-line plot. The calibration trend obtained is shown in Figure 4.3, along with the pressure deviations of the sensor from the standard reading. The pressure difference is between the standard pressure and the pressure indicated by the pressure

transducer. The maximum pressure calibration error is reported as the maximum deviation of the measured values to the calibration polynomial shown by a red color in Figure 4.3.

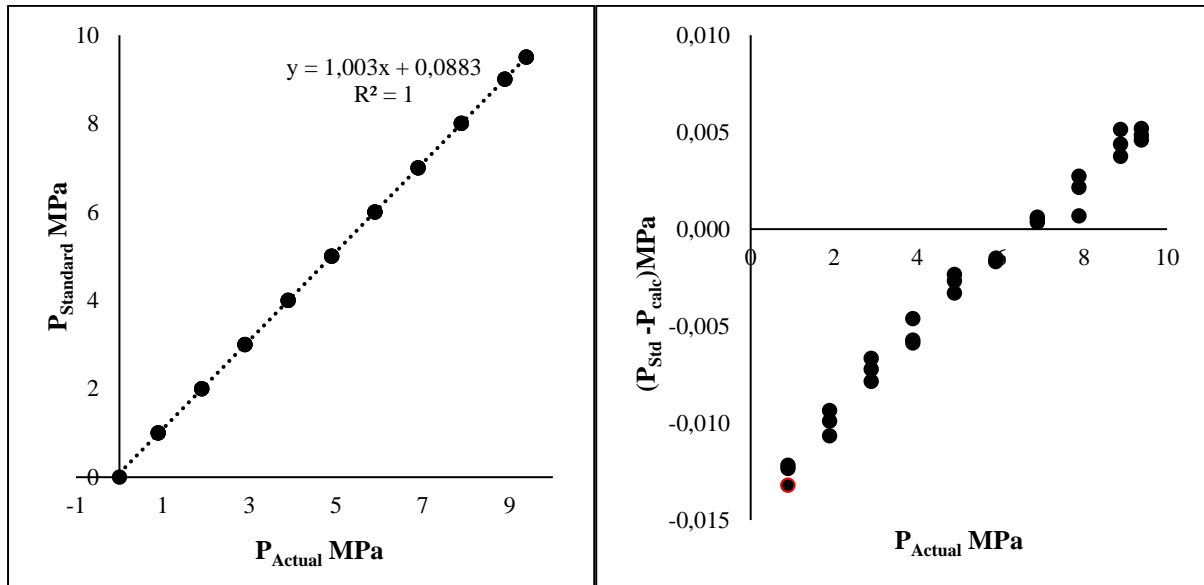


Figure 4.3: Pressure calibration chart and uncertainty scatter for the pressure probe of the equilibrium cell utilised in kinetic measurements.

4.3.3 Uncertainty in measured variables

The combined standard uncertainty (CSU) of measurement is obtained by combining the individual standard uncertainties by the propagation of error of type A and type B uncertainties using the method of combined deviations. To sum up the combined standard uncertainty, the root of the sum of the square mean method was applied. The manufacturer-stated instrument, standard calibration correlation, and calibration uncertainty contributed to the uncertainties.

The combined standard uncertainty has a confidence interval of approximately 95%. (NIST) (Taylor et al 1994). The expanded uncertainty intends to improve the confidence that a reported datum is within a stated uncertainty interval. It is obtained by multiplying the CSU by the coverage factor, k , with a typical value of 2 to give combined expanded uncertainty represented by $U(x)$. For further explanation on uncertainty computation, the reader is referred to Appendix D.1. Contributing uncertainties considered in computing the combined expanded uncertainty for temperature and pressure are shown in Table 4.2. The concentration uncertainty was 0.06%. The concentration calculations are detailed in Appendix D.2

Table 4.2: Summary of the source of uncertainty for variables reported in this study.

Uncertainty source	T (K)	P (MPa)
Manufacturer stated instrument error \mathbf{u}_{instr}	± 0.03	± 0.025
Standard calibration correlation error \mathbf{u}_{corr}	± 0.05	± 0.002
Calibration error, \mathbf{u}_{calib}	± 0.07	± 0.0015
Combined standard uncertainty, $U_c(x)$	± 0.06	± 0.007
Combined expanded uncertainty, $U(x)$	± 0.1	± 0.01

4.4 Experimental Measurements

After temperature and pressure calibrations, methane and carbon dioxide dissociation points measurements were measured. The dissociation points measurements where experiments were carried out to verify the calibrations, prove the suitability for use in these types of equilibrium cell measurements, and confirm the purity of the gases utilized in the study. The temperature range selected covers the experimental conditions.

4.4.1 Leak Testing

Leak testing is imperative in this experimental work as this was a pressure-varying procedure. Its main purpose was to determine the final dissociation point defined by two variables, i.e., pressure and temperature. The hydrate cell was pressured to 9 MPa at 303.15 K and monitored on the Agilent for 48 hours. The absence of leaks in the system was identified with the decrease of pressure from a set point of 9 MPa over the leak test period. If the pressure of the cell decreased from the set point, the leaks in the system were identified using liquid Snoop® applied on the joints, valves connections, and all fittings. For the section of the equipment submerged in the water bath, leaks were detected by the appearance of water bubbles from the leaking spots. While for the section outside the water bath, a leak was detected by observing the occurrence of foam as a result of gas escaping from a specific point. Leaking joints were tightened or reinforced with thread tapes before further tightening. The equipment was deemed leak-tight when it held pressure for 48 hours without any pressure loss.

4.4.2 Preparation of the equilibrium cell

The equilibrium cell was cleaned with distilled water, rubbed with a sponge and then rinsed with acetone. The cell top flange used to close the cell was fitted back and closed, then pressure tightened using six -3 mm bolts and nuts. Then the cell was placed in a water bath containing ethylene glycol-water solution. The cell was connected to a connecting line and then vacuumed

for 10 minutes to a pressure of 0.0002 kPa using an Edwards vacuum pump model RV3. This was done to remove any trapped air in the cell or feeding line that could tamper with the composition of the feed. With the pump still on, a 20 cm³ of distilled water was drawn into the equilibrium cell from a 50 cm³ syringe. Thereafter the equilibrium cell inlet valve and vacuum inlet line valve was shut, and the system was observed for 30 minutes to ensure that no rapid pressure increase occurred within the cell. Subsequently, the cell was pressurized for hydrate formation.

4.4.3 Sample preparation

Sodium dodecyl sulfate (SDS) was dissolved in deionized water in a 2000 ml volumetric flask to make a 0.05 wt.% SDS solution. This solution was utilized to produce nanofluids of different nanoparticle concentrations of (0.1, 0.2, 0.5, 1.0, and 1.2 wt.%). An OHAUS PA4202C top pan balance with an accuracy of 0.0001 g was used to measure the mass of the nanoparticle. Then it was added into a 50 ml sterile centrifuge tube and mixed in a vortex mixer for five minutes to ensure the complete mixing of the solution with the nanoparticles.

SDS was added to all the samples utilized in the study to reduce the surface tension between water and the additive and enhance fluid mixing. Graphene nanoplatelets had a larger particle size than the CuO and Al₂O₃ nanoparticles. In contrast, H₁₂MgN₂O₁₂ crystals had large crystals, while graphite and zinc oxide were in powder form. Dissolution of the additives in the solvent was assumed to occur normally until the saturation point.

4.4.4 Hydrate formation measurements

At the beginning of each experiment, the cell was opened and cleaned then a new sample of 20 cm³ of pure water/additive solution was introduced into the cell. The top flange was replaced and tightened using six bolts and nuts to produce an air-tight seal. The cell was placed in the water bath (293.15K) and then evacuated using an Edwards vacuum pump for two minutes to eliminate air and incondensable impurities. The hydrate former gas was introduced into the equilibrium cell by a one sixteenth inch line, and the cell was pressurized to the desired value, 4.66 MPa for CH₄ and 3.41 MPa for CO₂. During this process, the pressure was measured using a pressure transducer. The pressure conditions were selected to ensure that the kinetic studies occurred in the CH₄ and CO₂ stability zone. The Heidolph RZR 2041 overhead stirrer was switched on to 220 rpm (moderate stirring speed) then the data logger was turned on to log in the data during the reaction. The temperature dropped to 275.15 K in the hydrate region to allow hydrate formation. The reaction was stopped when pressure readings became constant.

4.4.5 Shutdown procedure

At the end of the hydrate, the experimental data was transferred from the Agilent software into an excel sheet on the computer connected to the experimental setup. Afterward, all the electric devices were switched off, beginning with the mechanical stirrer, chiller unit, temperature controller and Agilent data acquisition system. The valve on the drain line was opened and the aqueous solution was collected in a waste bottle. The water bath was lowered using a mechanical jack to elevate the equilibrium cell out of the water bath. The cell was disconnected from the gas line then opened and cleaned in preparation for the next experimental run.

4.5 Kinetic Model

The kinetic models applied in this study have been utilized by Babae et al., (2015) and Fakir et al., (2021). The parameters estimated from the kinetic measurements were the amount of CH₄ gas consumed, the water-to-hydrate conversion, storage capacity (SC), rate of hydrate formation, and the apparent rate constant. An extensive description of the kinetics model is presented in Appendix E.1. This section presents equations utilized to determine key kinetic parameters.

The rate of gas consumed $r(t)$ during hydrate formation is defined using the equation shown below (Babae, 2015)

$$r(t) = \frac{n_{gas,i-1} - n_{gas,i+1}}{(t_{i+1} - t_{i-1})n_{wo}} \quad 4.1$$

where $n_{gas,i-1}$ and $n_{gas,i+1}$ are the number of moles of carbon dioxide or methane in the gas phase at t_{i-1} and t_{i+1} respectively which are calculated using the real gas law and n_{wo} is the initial number of moles of water.

The following equation was used to estimate the apparent rate constant of the reaction during hydrate formation (Babae et al., 2015).

$$k_{app} = \frac{r(t)}{f_{gas}^G - f_{equilib}^G} \quad 4.2$$

Where $f_{equilib}^G$ is described as gas fugacity at the hydrate equilibrium pressure ($P_{equib.}$) and initial temperature conditions. $f_{equilib}^G$ can be calculated using the thermodynamic model for gas hydrate equilibrium conditions.

The storage capacity (SC) is defined as the standard volume of gas stored per hydrate volume. The equation below can be used to calculate SC (Babaei et al., 2015).

$$SC = \frac{V_{STP}}{V_H} = \frac{n_{gas}RT_{STP}/P_{STP}}{V_H} \quad 4.3$$

The subscript STP stands for standard conditions and V_H is the volume of gas hydrate (Babaei et al., 2015).

The water-to-hydrate conversion is defined as the number of moles of water converted to hydrate per mole of feed and is given by the following equation (Babaei et al., 2015).

$$\text{Water to hydrate conversion} = \frac{M \times \Delta n_{gas}}{n_{wO}} \quad 4.4$$

4.6 Results and Discussions

This section discusses test systems, commencing with the calibration procedures and outcomes, and experimental as well as kinetic model results of CO₂ and CH₄.

4.6.1 Test systems

Hydrate dissociation measurements for known systems were measured as a test system before the commencement of the kinetic measurements. Hydrate dissociation measurements of CO₂ and CH₄ gas were conducted. This was done to test the reliability of the experimental equipment and the procedure. The measured data for CO₂ + water was compared to data found in the literature of Deaton and Frost, (1946), Englezos and Hall, (1994), and Mohammadi et al., (2005). The temperature vs. pressure plot is shown in Figures 4.4 and Ln P vs 1/T was plotted to show the linear relation between data measured in this study and literature data. Tabulated literature data for CO₂ and CH₄ with the pressure difference between measured and literature data are provided in Table E.2. and Table E.3, respectively.

Since the equipment was utilized for CH₄ kinetics measurements, it was also imperative to carry out CH₄ + water dissociation points measurements. The obtained results were compared to Deaton and Frost, (1946), Roberts, (1940), and Gallowing et al., (1970). The temperature vs pressure and Ln P vs 1/T plots obtained are shown in Figure 4.5. For both systems of CO₂ and CH₄ shown in Figures 4.4 and 4.5 good correlation was demonstrated between literature data and results obtained in this study. Hence the equipment and the experimental procedure were deemed suitable for this study.

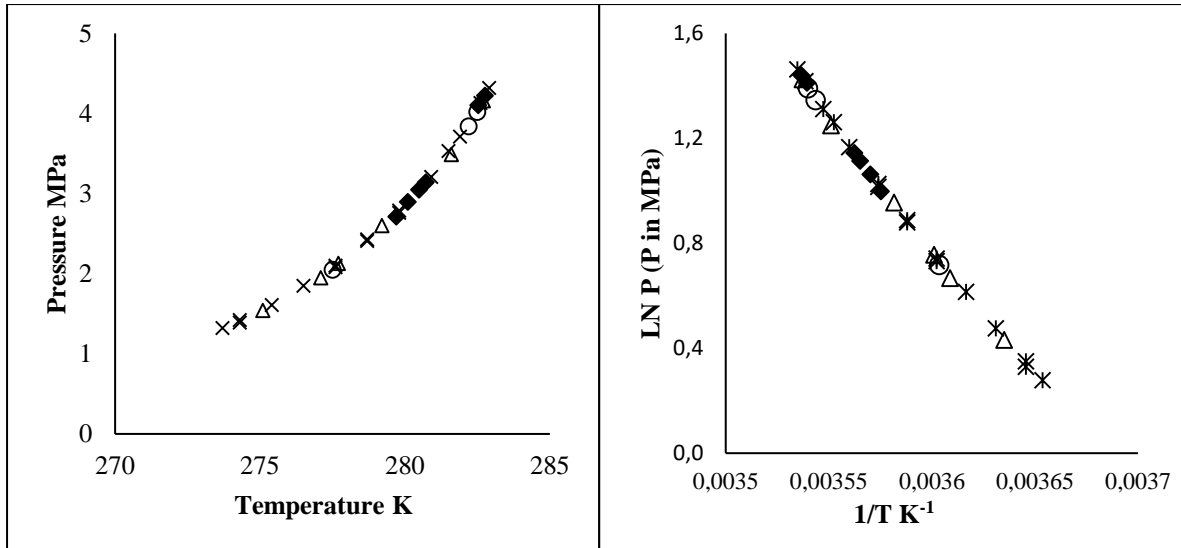


Figure 4.4: Hydrate dissociation points for the CO₂ and water system:(♦) Kinetics cell (*) Deaton and Frost, (1946); (Δ) Englezos and Hall, (1994); (○) Mohammadi et al., (2005).

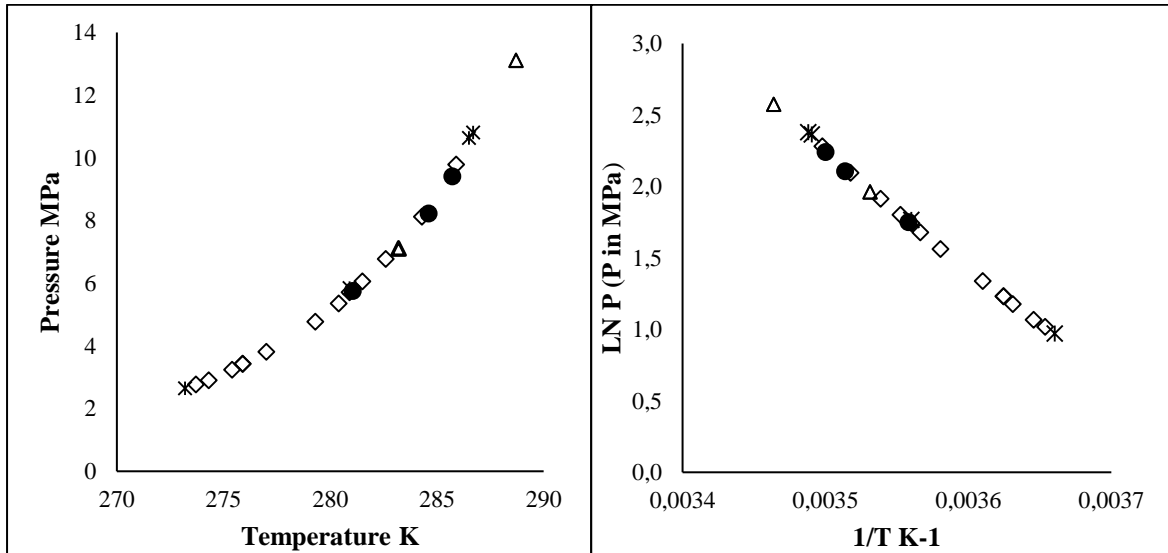


Figure 4.5: Hydrate dissociation points for the CH₄ and water system:(●) Kinetics cell (◇) Deaton and Frost, (1946); (*) Roberts, (1940); (Δ) Gallowing et al., (1970).

4.7. Carbon Dioxide Kinetics Results

4.7.1. Kinetics of Hydrate Formation

A solution of 0.1 wt.%, 0.2 wt.%, 0.5 wt.%, 1.0 wt.%, and 1.2 wt.% of each additive with 0.05 wt.% SDS was utilized in hydrate formation. Sodium dodecyl sulfate (SDS) was added to reduce the surface tension of liquid water (Zhang et al., 2013). Moreover, 0.05 wt.% SDS was reported to reduce surface and interfacial tensions by accumulating at the interface of immiscible fluids in the study of the effects of CuO nanoparticles on the dissolution of CH₄ in water (Moraveji et al., 2013).

In reporting the kinetics of carbon dioxide hydrate formation, the following parameters were considered, i.e., initial temperature, initial pressure, and stirring rate. These were determined as specified in the hydrate formation procedure. The experimental results were used to determine water-to-hydrate conversion, gas consumption, rate of gas uptake, and hydrate storage capacity. Values utilized in pressure and temperature investigations are specified in the subsequent sections.

The initial and hydrate equilibrium pressure difference is defined as the degree of subcooling or driving force for gas hydrate formation. As shown in Figure 4.6, increasing the initial pressure of CO₂ leads to a higher degree of subcooling, increasing the hydrate formation rate.

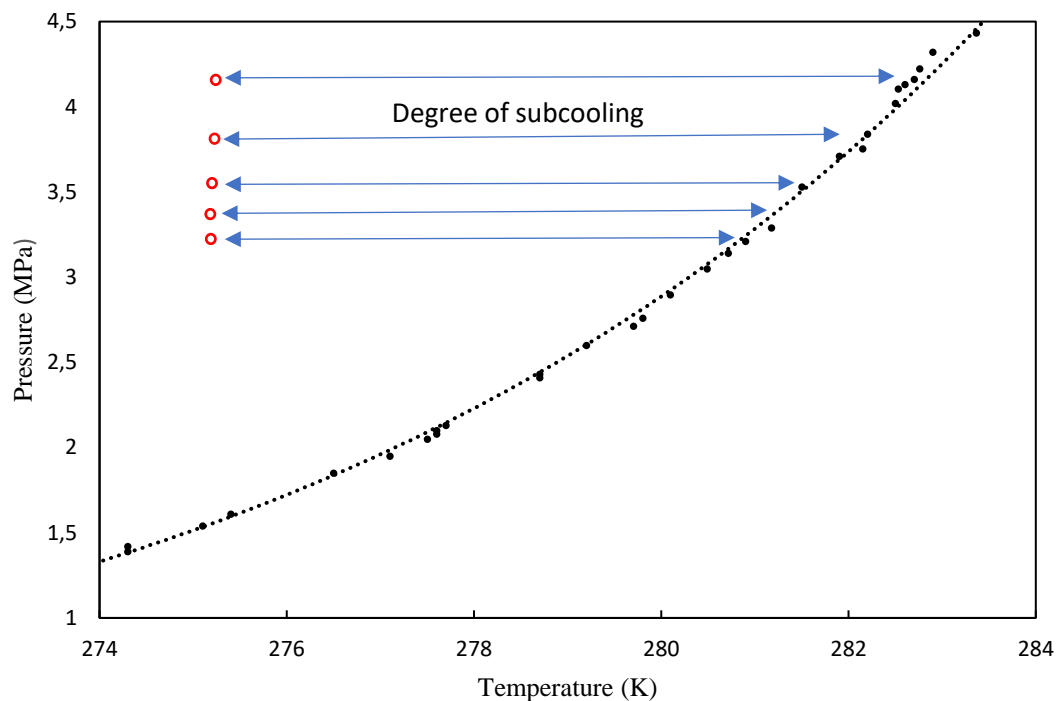


Figure 4.6: The driving force between the initial kinetic experimental conditions and CO₂ hydrate equilibrium line (○) initial pressure, (●) dissociation points for CO₂.

4.7.2. Induction time

Hydrate formation occurs in three stages: gas dissolution, followed by the induction period, then hydrate growth (Said et al., 2016). Hydrate formation is an exothermic process hence the presence of nanoparticles aids in heat dissipation as the nanofluid has a higher heat transfer coefficient enhancing the rate of hydrate nucleation. Moreover, the heterogeneous nucleation rate is less energy-intensive than homogenous nucleation (Aliabadi et al., 2014). Due to their particle size (less than 100nm), nanoparticles have a high specific surface area which significantly improves mass and heat transfer between gas hydrate and liquid phase. This, in

turn, increases the transfer of the former gas to the hydrate phase and the heat generated in hydrate formation, thus significantly improving the amount of gas consumed and the rate of hydrate formation (Gambelli et al., 2022). Thus, the presence of nanoparticles in water and CO₂ systems enhances the rate of hydrate nucleation. The gas dissolution stage is the first part of the graph, where the pressure decreases at a constant temperature. During this period, gas dissolves into the liquid solution and is dependent on the rate of agitation of the system. This reduces the liquid surface tension to enhance mass transfer at the phase interface. The point at which stable crystals form and grow is the turbidity point. This point marks the end of the induction period, demarcated by a sharp rise in the temperature profile. The induction time is the period from the introduction of the gas into the cell to the initial formation of gas hydrate. The essential parameter in the hydrate nucleation process is the induction time. The induction time is shown by a sharp increase in the temperature plot and a slight drop in the system's pressure as gas is incorporated into the hydrate. This is illustrated clearly in Figure 4.7 in a CO₂ system containing 1.2 wt.% graphene nanoparticles and 0.05 wt.% SDS solution where the induction time was 32.67 minutes.

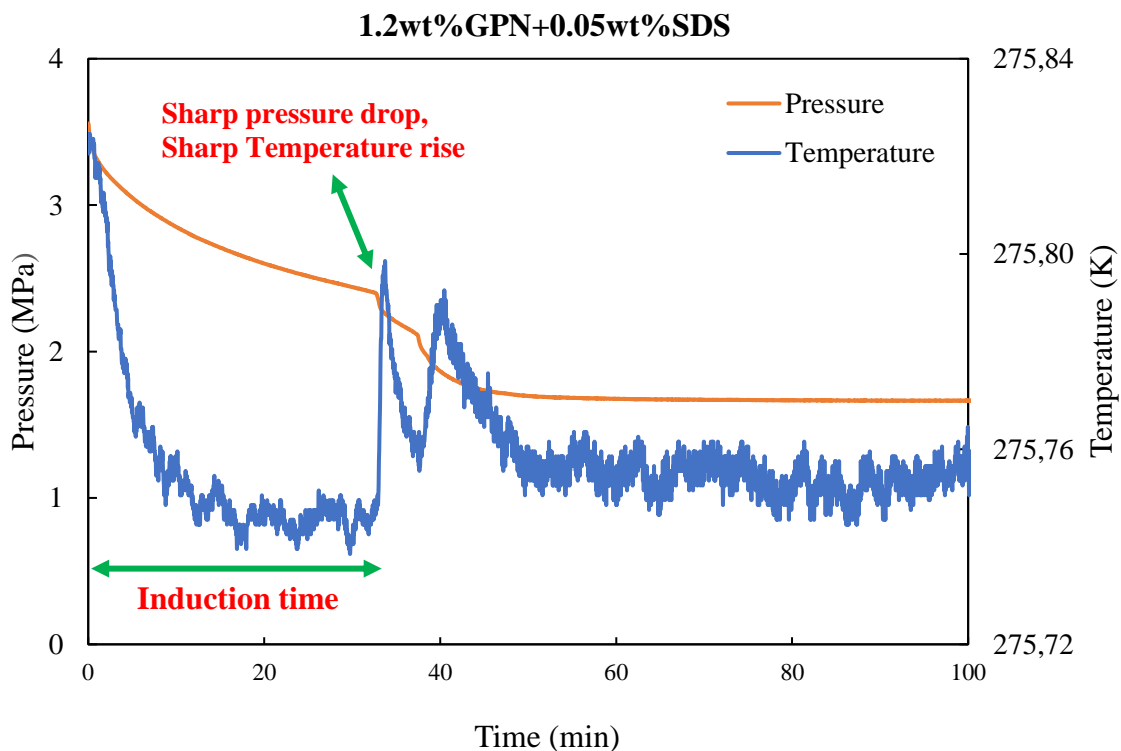


Figure 4.7: Illustration of determination of induction time from a temperature - pressure vs. time plot.

Table 4.3 contains the induction time for all the systems investigated in this study with CO₂ gas. The induction time for most of the nanofluid solutions was, on average, one minute, while for systems with ZnO and H₁₂MgN₂O₁₂, the times were longer than 10 minutes.

The hydrate formation process is exothermic. Carbon dioxide has low solubility in water hence the hydrate formation on the hydrate surface is dominated by the mass transfer of the former gas to the hydrate surface. Moreover, the hydrate growth is also affected by the same process. Due to their particle size, nanoparticles have a high specific surface area, significantly improving mass and heat transfer between gases and hydrate phase and liquids. This, in turn, increases the transfer of the former gas to the hydrate phase and the heat generated in hydrate formation, thus significantly improving the amount of gas consumed and the rate of hydrate formation (Said et al., 2016).

Table 4.3: Induction time for carbon dioxide hydrate system with additives.

Solution	Concentration of Additives (wt.%)					
	0	0.1	0.2	0.5	1	1.2
	Induction time (min)					
Water	8.97	----	----	----	----	----
Water + CuO + 0.05 wt.% SDS	----	0.01	0.70	0.93	0.53	0.63
Water + Al ₂ O ₃ + 0.05 wt.% SDS	----	1.70	0.87	1.03	0.73	2.03
Water + GPN + 0.05 wt.% SDS	----	0.03	0.47	0.40	38.67	32.67
Water + C-C + 0.05 wt.% SDS	----	0.01	0.10	0.93	0.77	0.83
Water + ZnO + 0.05 wt.% SDS	----	12.3	1.43	0.70	0.80	0.50
Water + H ₁₂ MgN ₂ O ₁₂ + 0.05 wt.% SDS	----	0.67	1.53	0.7	52.13	6.23

Uncertainty $U(T) = \pm 0.1 K$, $U(P) = 0.01 MPa$ $U_{concentration} (wt\%) = 0.06\%$ $U(t) = 0.01s$.

*The concentration was varied from 0.1 to 1.2 wt.%

The concentration of the nanoparticles has to be within defined limits to be effective for hydrate growth and to affect the rate of hydrate formation. There is a lower limit where additives have a negligible effect on hydrate formation and an upper limit where agglomeration may occur,

hindering the mass and heat transfer necessary for hydrate formation. These limits differ from one additive to another. This can be used to explain the drastic change in the induction time for graphene nanoplatelet system due to increasing the graphene concentration from 0.5 to 1.0 wt.%.

4.7.3 Temperature Variations

The effects of temperature variations on CO₂ gas hydrate formation were assessed at a pressure of 4.07 MPa. This pressure was selected to improve the low performance in hydrate formation observed in pressure variation, as discussed below. The temperature varied from 275.25 to 276.26 K, and it was observed that the performance at 275 and 276.26 K was the same. It can be seen from Figure 4.8a to 4.8d that hydrate formation kinetics improved with a decrease in temperature, with the best performance obtained at the lowest temperature of 275.25 K.

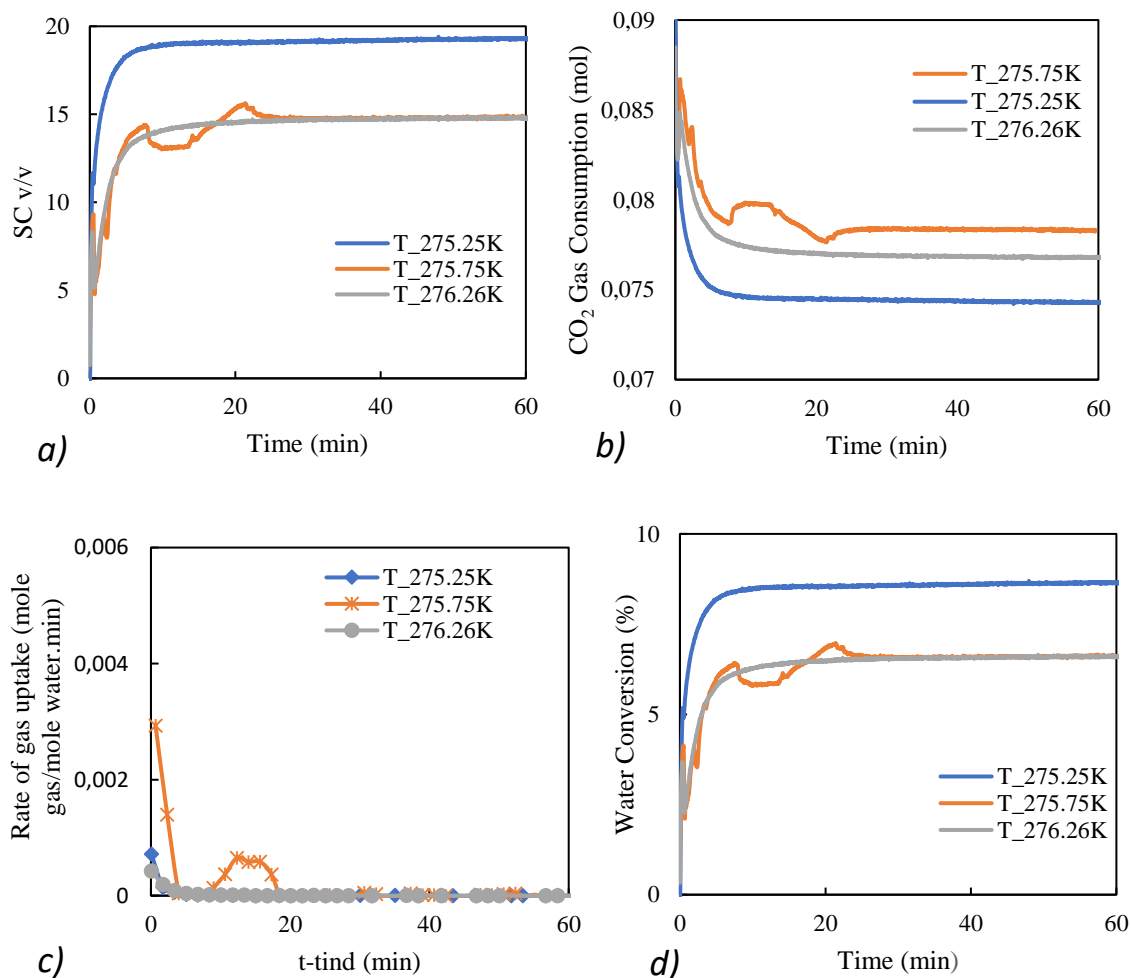


Figure 4.8: Effects of temperature variation on a) storage capacity, b) gas consumption, c) mol of gas consumed to mole of water, d) water consumed in CO₂ hydrate formation at a pressure 4.07 MPa. Uncertainty $U(T) = \pm 0.1$ K, $U(P) = 0.01$ MPa $U_{concentration}$ (wt%)=0.06% $U(t)$ =0.01s.

In Figure 4.8 *a*, it can be seen that a maximum storage capacity (SC) of 19.26 (v/v) was obtained with the lowest value of 14.76 (v/v) obtained at a temperature of 275.75 and 276.26 K. Gas consumption presented in Figure 4.8*b* shows that a maximum gas consumption of 0.01 moles was obtained at 275.25 K. The gas consumption at 275.75 K is unexpectedly lower than that obtained at 276.26 K, this anomaly might have been caused by the fact that there is a small temperature difference between these two values. The lowest gas consumption was obtained at 275.75 K. Figure 4.8*c* shows the ratio of moles gas consumed to moles of water with a temperature of 275.25 K, giving the best result. The water conversion percentage shown in Figure 4.8*d* was less than 10% for all investigated temperatures, showing poor hydrate formation.

4.7.4 Pressure Variation

This section reports the effects of pressure on the kinetics of CO₂ hydrate formation. Four factors were investigated: storage capacity, gas consumption, the ratio of moles of gas to moles of water, and water conversion percentage. Initially, five different pressures of 3.32, 3.41, 3.55, and 3.74 MPa were utilized at a temperature of 275.8 K. Distilled water with no additives was used for CO₂ hydrate formation during the pressure variation stage. For all four parameters studied, it can be observed in Figures 4.9*a* through 4.9*d* that favorable results were obtained for the parameter under investigation as pressure increased from 3.32 MPa to 3.74 MPa. Thus, as reported in literature studies gas hydrate formation was observed to be favoured by high pressures (Ganji et al., 2007). However, gas hydrates formation at high pressures is uneconomic for hydrate application as it requires durable materials. Hence additives are required to improve hydrate formation at low pressure. In Figure 4.9*a*, it can be seen that a maximum of 59.7 (v/v) was obtained at a pressure of 3.74 MPa and the lowest was 44.65 MPa obtained at a pressure of 3.32 MPa. The storage capacity increased as pressure increased from 3.32 MPa to 3.74 MPa. Thus, as pressure increases, the gas molecules are forced closer together and become more densely packed within the hydrate lattice. This increases the amount of gas that can be stored in the same volume of gas hydrate.

Gas consumption was comparable for the four pressure values considered. A maximum of 0.05 moles of gas were consumed at pressures between 3.32 and 3.74 MPa. Figure 4.9*c* shows the ratio of moles of gas to moles of water. A maximum of 0.05 mol/mol was achieved at 3.74 MPa, a similar trend was obtained with moles increasing as pressure increased from 3.32 to 3.74 MPa

The water conversion percentage is shown in Figure 4.9d; a maximum of 28.9% of water was converted to hydrate at 3.74 MPa, with a minimum conversion of 21.23% achieved at 3.32 MPa. The water consumption in gas hydrates tends to increase with increasing pressure, at least over a certain range of pressures (Zhang et al., 2017). In an investigation of the effects of starting pressure on water consumption during gas hydrate formation from water-in-oil emulsions. Water consumption was found to increase with pressure which was attributed to an increase in gas solubility and a reduction in the driving force for water uptake as the pressure increased (Liu et al., 2016). To investigate the effects of chemical additives in this study, 3.41 MPa was selected to ascertain the effects of additives on hydrate formation.

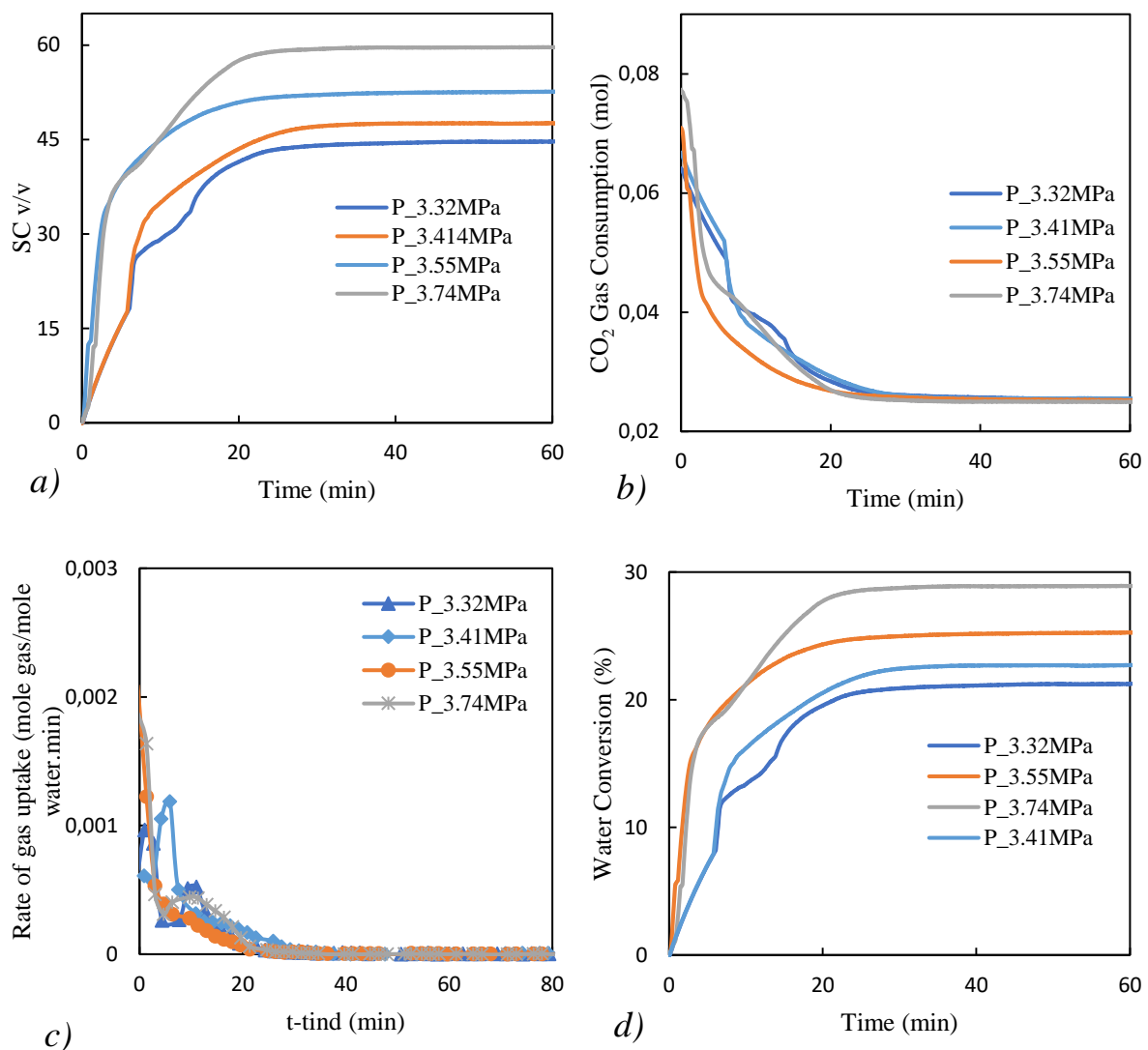
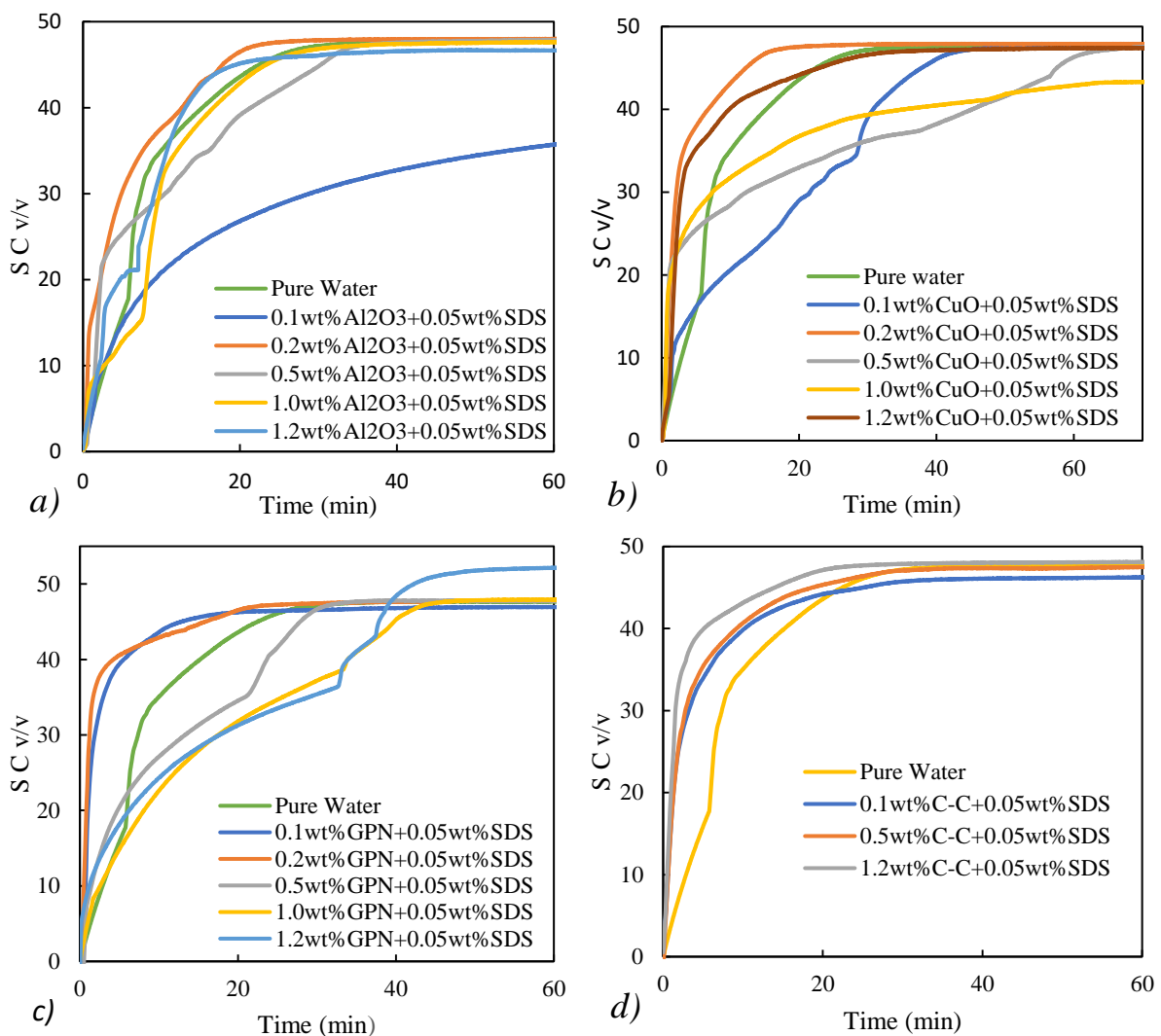


Figure 4.9: Effects of pressure variation on a) storage capacity, b) gas consumption, c) mol of gas consumed to mole of water, d) water consumed in CO₂ hydrate formation at a temperature 275.8K. Uncertainty $U(T) = \pm 0.1 \text{ K}$, $U(P) = 0.01 \text{ MPa}$, $U_{\text{concentration}} (\text{wt}\%) = 0.06\%$, $U(t) = 0.01 \text{ s}$.

4.7.5 Storage Capacity

The storage capacity of the CO₂ hydrate in the presence of additives utilized in the study as a function of time is shown in Figure 4.10a through 4.10f for Al₂O₃ nanoparticles, CuO nanoparticles, graphene nanoplatelets, graphite powder, ZnO powder, and magnesium nitrate hexahydrate. This is a critical factor in the study of gas hydrates for carbon capture or gas storage as it indicates the amount of gas a hydrate clathrate can accommodate in its lattice structure. A maximum storage capacity of 51 (v/v) was obtained with 1.2 wt.% GPN + 0.05 wt.% while all the other systems tested, an average storage capacity of 46 (v/v) was obtained. Thus, the addition of nanoparticles proved to be favorable for CO₂ storage as they increased the capacity of the hydrate lattice compared to that of pure water, H₁₂MgN₂O₁₂, and ZnO systems.



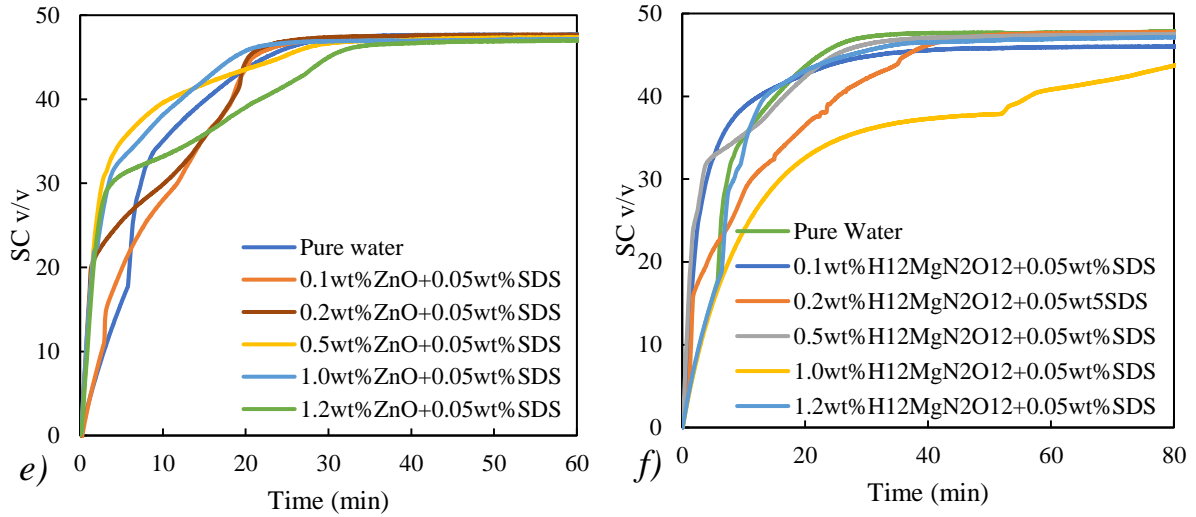
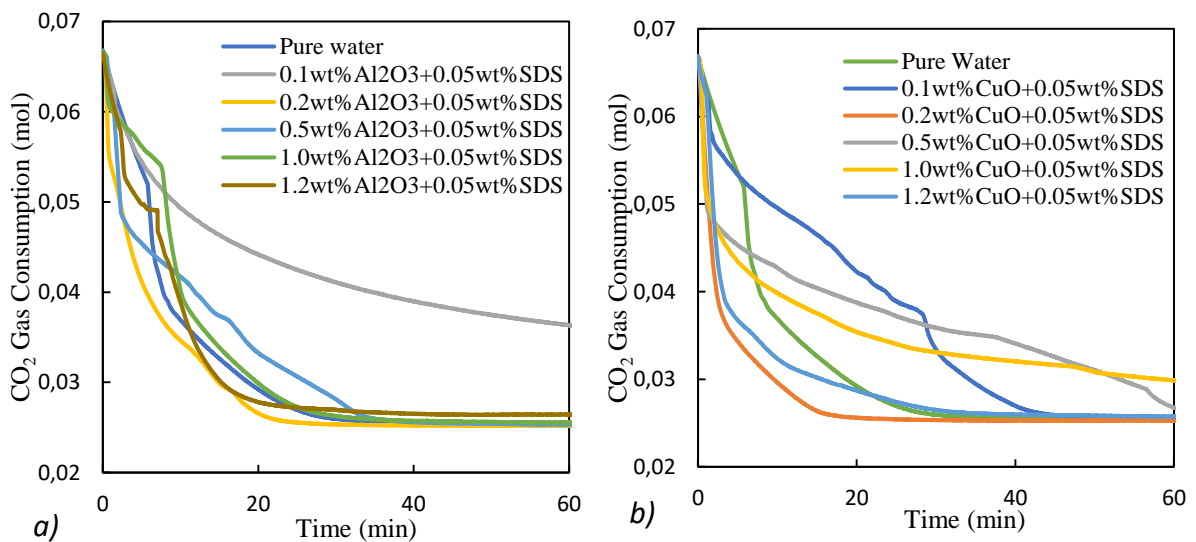


Figure 4.10: Storage capacity of CO₂ hydrate formation for a) aluminium oxide (Al₂O₃) nanoparticles, b) copper oxide (CuO) nanoparticles, c) graphene (GPN) nanoplatelets, d) graphite (C-C) powder, e) zinc Oxide (ZnO) powder, f) magnesium nitrate hexahydrate (H₁₂MgN₂O₁₂) crystals at 275.8 K and 3.41 MPa in concentrations specified. *Uncertainty $U(T) = \pm 0.1$ K, $U(P) = 0.01$ MPa $U_{concentration}$ (wt%) = 0.06% $U(t) = 0.01$ s.*

4.7.6 Gas Consumption

In this study, gas consumption during CO₂ hydrate formation was computed by calculating the amount of gas decrease from the gas phase with time. This parameter also indicates the crystallization rate as the hydrate crystal formation proceeds with the incorporation of gas molecules into the hydrate structure. Gas consumption with different additives in hydrate formation are shown in Figure 4.11a through Figure 4.11f.



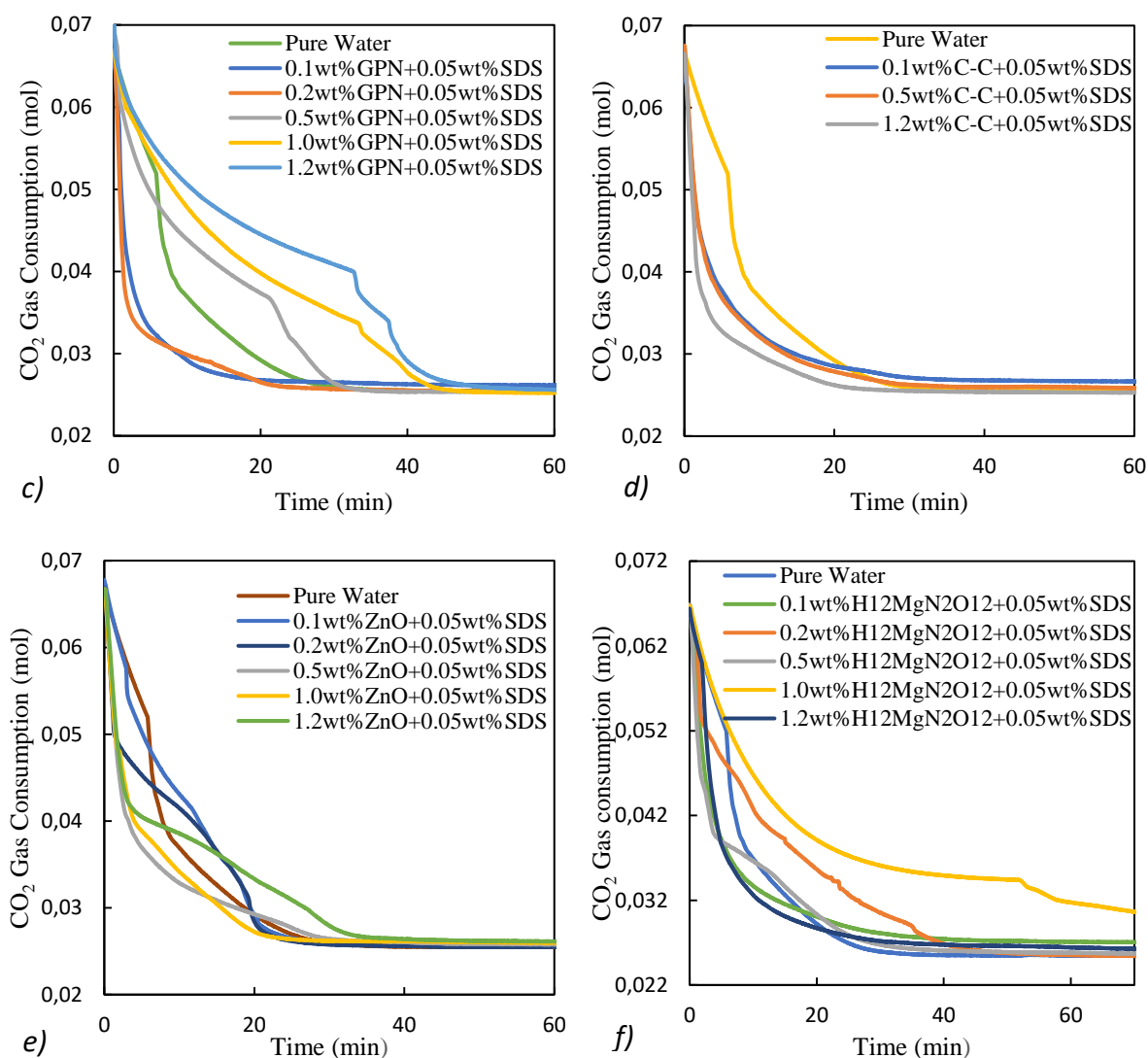


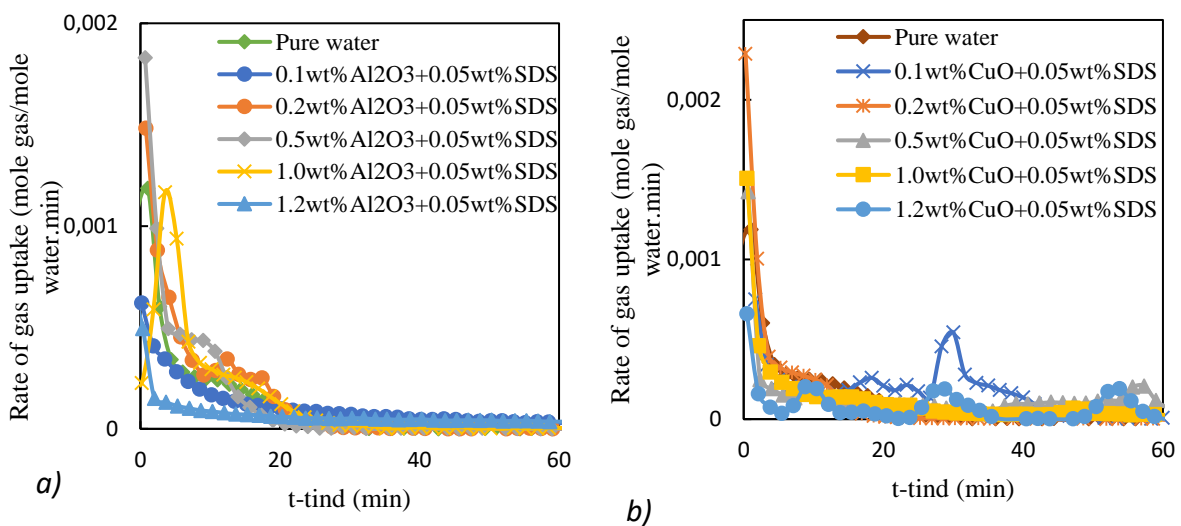
Figure 4.11: Carbon dioxide consumed in hydrate formation for a) aluminium oxide (Al_2O_3) nanoparticles, b) copper oxide (CuO) nanoparticles, c) graphene (GPN) nanoplatelets, d) graphite (C-C) powder, e) zinc Oxide (ZnO) powder, f) magnesium nitrate hexahydrate ($\text{H}_{12}\text{MgN}_2\text{O}_{12}$) crystals at 275.8 K and 3.41 MPa in concentrations specified. *Uncertainty* $U(T) = \pm 0.1 \text{ K}$, $U(P) = 0.01 \text{ MPa}$ $U_{\text{concentration}} (\text{wt}\%) = 0.06\%$ $U(t) = 0.01 \text{ s}$.

Figure 4.11a is a system of Al_2O_3 nanoparticles with 0.05 wt.% SDS. From 0.2 wt.% to 1.2 wt.% Al_2O_3 , there is a gradual increase in gas consumption rate at the beginning of the reaction. In all Al_2O_3 concentrations, the gas was consumed faster than pure water except for the 1.0 wt.% Al_2O_3 system, though the final gas consumption was 0.0389 moles for all the concentrations. An anomaly was obtained with 0.1 wt.% Al_2O_3 where the storage of 0.025 moles was obtained. Figure 4.11b shows the trends obtained with CuO nanoparticles, an average of 0.0382 moles was obtained in all the concentrations studied. The reaction rate was faster than that with Al_2O_3 nanoparticles as shown by the difference in the gradients of the graphs.

Graphene nanoplatelets had the best performance with an average gas consumption of 0.0437 moles obtained. Also, its reaction rate was faster than that of Al_2O_3 and CuO nanoparticles. The gas consumption rate decreased as the concentration of the nanoplatelets increased in the solutions. The best performance was obtained with 0.2 wt.% graphene nanoplatelets. This reaction had a faster reaction rate than that of pure water. The gas consumption of 0.5 wt.% graphene was comparable to pure water, while 1.0 wt.% and 1.2 wt.% graphene platelets reacted slower than pure water. This might have been due to the saturation of the solution with the nanoplatelets leading to a reduced hydrate formation rate. In Figure 4.11d the gas hydrate formed with graphite powder is shown with all the gas being consumed faster than water in all concentrations, and an overall conversion of 0.039 moles was obtained. Zinc oxide and magnesium nitrate hexahydrate gas consumption are shown in Figures 4.11e and 4.11f. The average gas consumption for both systems was 0.038 moles, and they exhibited better performance than water.

4.7.7 Rate of gas uptake

In Figure 4.12a through to Figure 4.12f the rate of gas uptake as a ratio of moles of gas consumed to moles of water is plotted against time with nanofluids and selected chemical additives in weight percentages varied from 0.1 to 1.2 wt.% with 0.05 wt.% SDS.



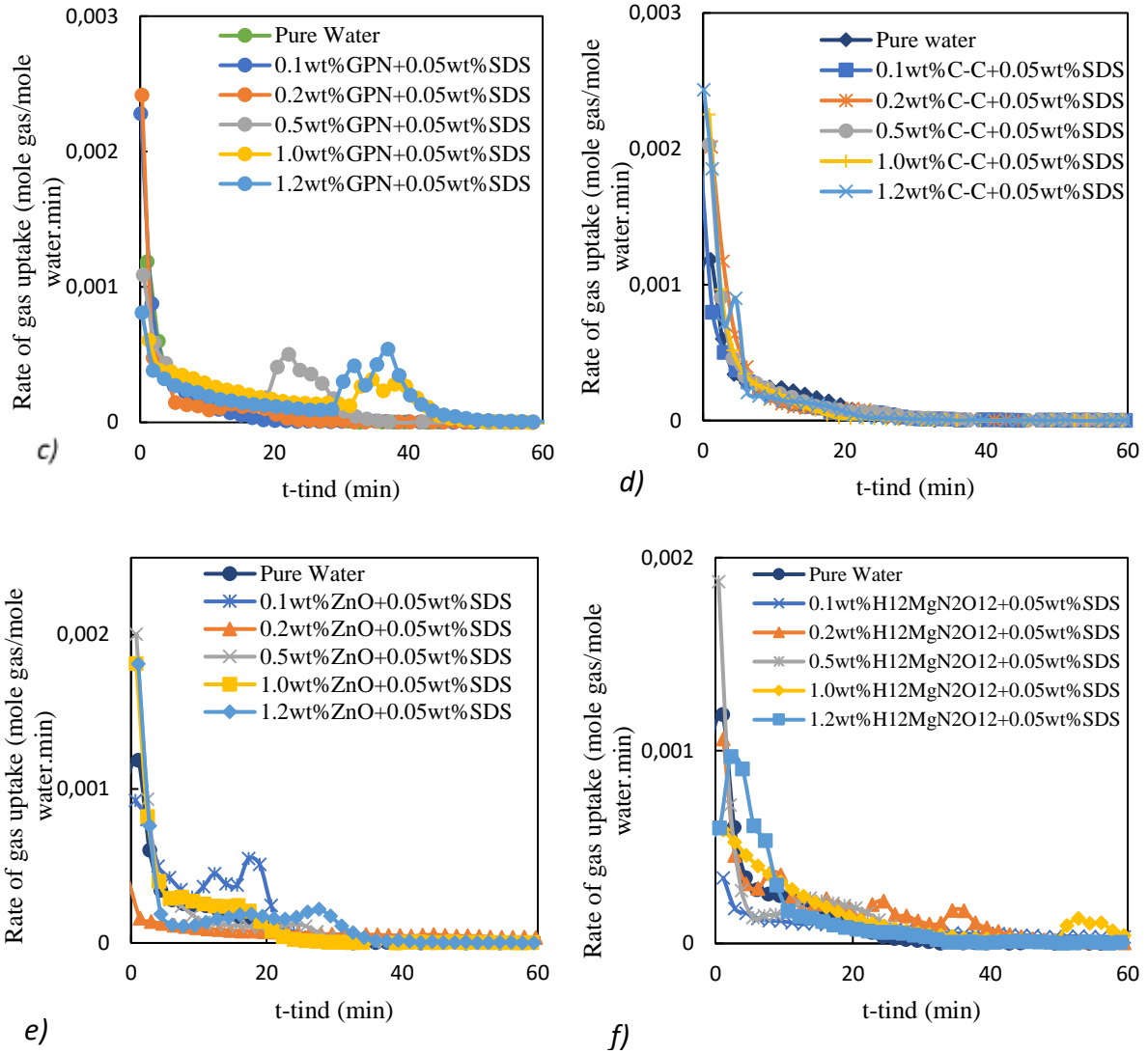


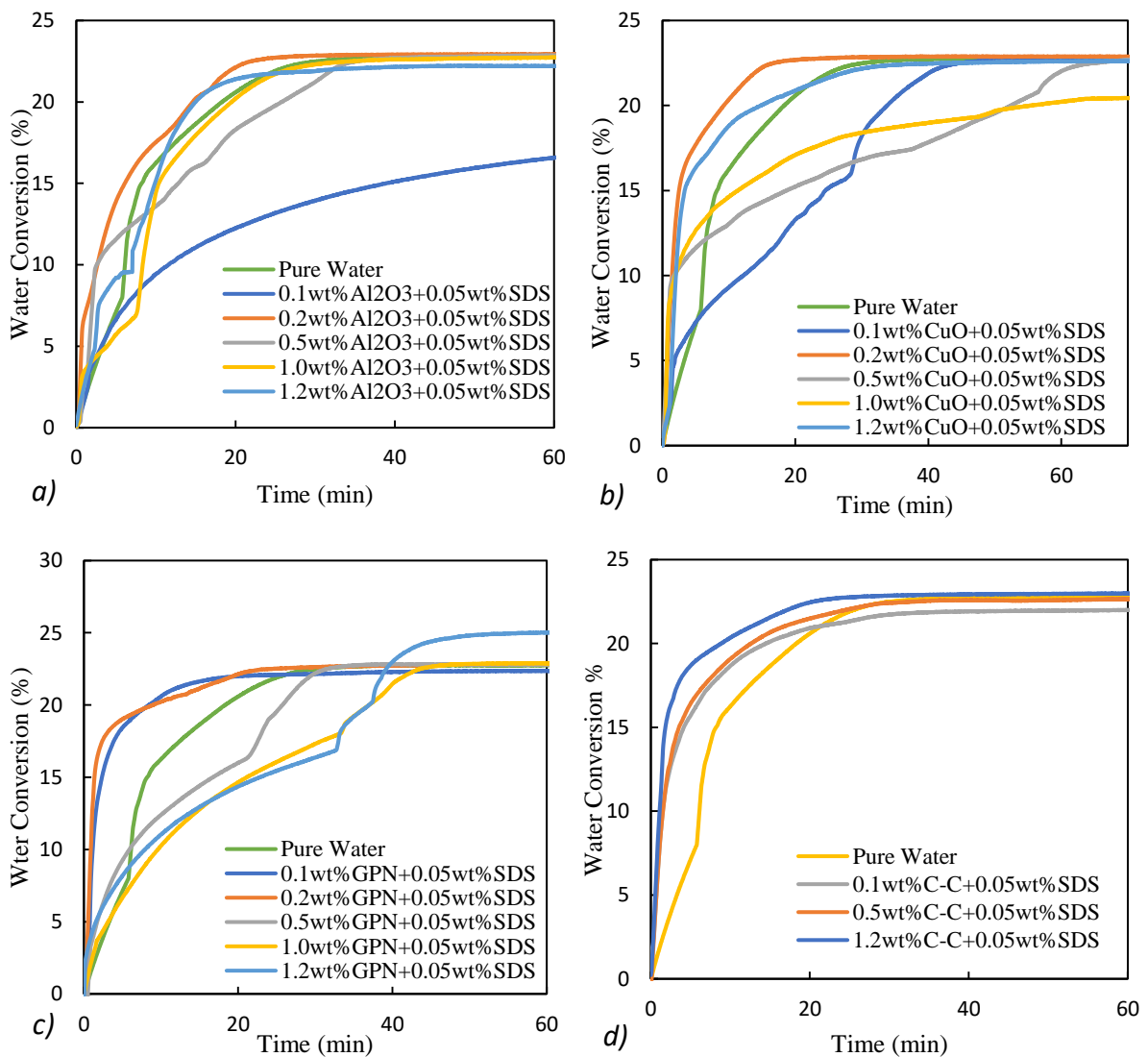
Figure 4.12: Rate of CO₂ consumption during hydrate formation for a) aluminum oxide (Al₂O₃) nanoparticles, b) copper oxide (CuO) nanoparticles, c) graphene (GPN) nanoplatelets, d) graphite (C-C) powder, e) zinc Oxide (ZnO) powder, f) magnesium nitrate hexahydrate (H₁₂MgN₂O₁₂) crystals at 275.8 K and 3.41 MPa in concentrations specified. *Uncertainty* $U(T) = \pm 0.1$ K, $U(P) = 0.01$ MPa $U_{concentration}$ (wt%) = 0.06% $U(t) = 0.01$ s.

In all the systems tested, the gas was consumed at a faster rate than that for pure water. The highest values show this were obtained at the beginning of the reaction as the concentration of the reactants was high. The nanoparticles had a higher gas uptake rate than other systems with chemical additives. The highest value obtained was $2.44 \times 10^{-3} \text{ mol}_G \text{ mol}_W^{-1} \text{ min}^{-1}$. This was obtained with 0.2 wt.% GPN + 0.05 wt.% SDS. As shown in Figure 4.12a to 4.12c, nanoparticles had a rate constant higher than $2.0 \times 10^{-3} \text{ mol}_G \text{ mol}_W^{-1} \text{ min}^{-1}$ except for Al₂O₃ nanoparticles. ZnO and H₁₂MgN₂O₁₂ had lower rate of gas uptake with their highest value less than $2.0 \times 10^{-3} \text{ mol}_G \text{ mol}_W^{-1} \text{ min}^{-1}$. The rate of gas uptake was higher at lower concentrations of the nanoparticles, that is 0.1 and 0.2 wt.% and became lower as the weight percent was

increased. This was attributed to the saturation of the solution, thus hindering effective contact between the reactants. In Figure 4.12f magnesium nitrate hexahydrate showed a fast reaction rate than expected, and the overall consumption was comparable to the obtained with nanoparticles.

4.7.8 Water to hydrate conversion percentage

The trends for the water conversion percentage of the nanoparticles and chemical additives are shown in Figure 4.13a through Figure 4.13f. It can be seen that these are similar to the trends obtained in storage capacity investigations.



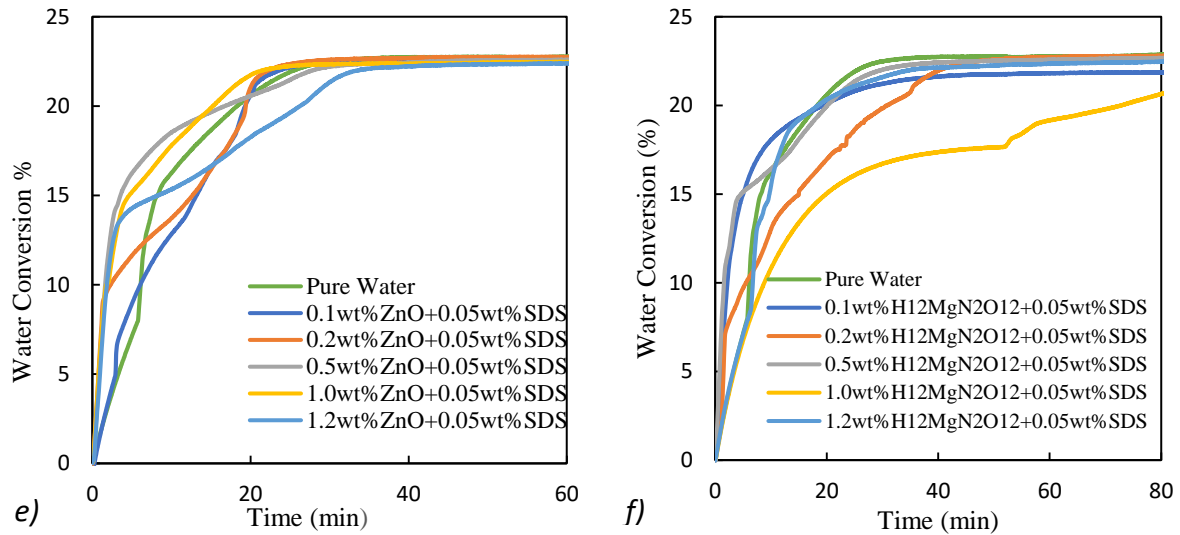


Figure 4.13: Percentage of water conversion in CO₂ hydrate formation for a) aluminium oxide (Al₂O₃) nanoparticles, b) copper oxide (CuO) nanoparticles, c) graphene (GPN) nanoplatelets, d) graphite (C-C) powder, e) zinc Oxide (ZnO) powder, f) magnesium nitrate hexahydrate (H₁₂MgN₂O₁₂) crystals at 275.8 K and 3.41 MPa in concentrations specified. *Uncertainty* $U(T) = \pm 0.1$ K, $U(P) = 0.01$ MPa $U_{additive}$ (wt%)=0.06% $U(t)$ =0.01s.

All the systems investigated had an average of 22.72% water conversion, except for 1.2 wt.% GPN+0.05 wt.% SDS system where water conversion of 25% was achieved. By definition, gas hydrates are non-stoichiometric compounds composed of water molecules and tiny gas molecules trapped in the hydrate lattice with approximately 85 % water and 15 % gas (Loveday et al., 2008). Thus, a large volume of gas is absorbed when the conversion of water to hydrate is also high.

4.8 Methane Gas Kinetics

In reporting the hydrate formation kinetics, the initial pressure, initial temperature, and additives effects were investigated in different concentrations with the stirring rate maintained constant. The experimental results were used to determine water-to-hydrate conversion, gas consumption, rate of gas uptake, and hydrate storage capacity. To investigate the effect of pressure on the CH₄ hydrate formation kinetic, the following initial pressures were utilized: 6.16 MPa, 5.61 MPa, 5.11 MPa, and 4.66 MPa at a constant temperature of 275.8 K. Whereas, in the investigation of the effects of initial temperature, the following initial temperature values were utilized: 275.77 K, 276.25 K, 276.77 K, 277.30 K, and 277.74 K at a constant pressure of 4.66 MPa. In all the investigations, a stirring rate of 220 rpm (optimum stirring speed which did not interfere with effects of the effects of parameters being investigated) was employed. The graphs obtained in this study are presented in Appendix E.2 and the remaining results and

tables for the effects of temperature and pressure are displayed in sections 4.8.2 and 4.8.3, respectively.

4.8.1 Induction Time

Induction times for all the CH₄ systems in the study are shown in Table 4.4. Generally, the system with nanoparticles had a lower induction time than other systems in the study. This is due to numerous nucleation sites in the solution, thus lowering the time required for the hydrate to form. The induction time for pure water was 18.4 minutes while adding 0.05 wt.% SDS reduced the induction time to 7.9 minutes.

Table 4.4: Induction time for methane hydrate formation with additives.

Solution	Concentration of Additives (wt.%)					
	0	0.1	0.2	0.5	1	1.2
	Induction time (min)					
Water	18.40	----	----	----	----	----
Water + 0.05 wt.% SDS	7.90	----	----	----	----	----
Water + *CuO + 0.05 wt.% SDS		1.0	1.80	3.30	2.30	7.40
Water + *Al ₂ O ₃ + 0.05 wt.% SDS		6.30	10.70	24.70	5.80	1.10
Water + *GPN + 0.05 wt.% SDS		0.90	2.50	4.10	0.10	0.30
Water + *C-C + 0.05 wt.% SDS		7.87	1.63	0.90	0.77	2.57
Water + *ZnO + 0.05 wt.% SDS		1.30	13.10	5.20	19.10	20.70
Water + *H ₁₂ MgN ₂ O ₁₂ + 0.05 wt.% SDS		12,43	12,07	10,87	2,23	1,67

Uncertainty $U(T) = \pm 0.1 K$, $U(P) = 0.01 MPa$ $U_{concentration} (wt\%) = 0.06\%$ $U(t) = 0.01s$.

**The concentration was varied from 0.1 to 1.2 wt.%*

The addition of nanoparticles into the solution of SDS further decreased the induction time thus, hydrate formation occurred quickly and hydrate growth. As shown in Table 4.4, an average of 2 minutes was the induction time obtained with nanoparticles. The induction time of one minute was obtained for the solution of 0.1 wt.% CuO+0.05 wt.% SDS had the lowest induction time in this study. Al₂O₃ had longer induction times than the other nanoparticles studied. This trend observed with the Al₂O₃ system might have been due to the saturation of

the solution, which inhibited nucleation and hydrate formation. Similar results were reported in a study on CH₄ kinetics with 500 ppm SDS and CuO nanoparticles with weight percentages between 0.01 and 1.0 %. In the study, 0.01 wt.% CuO had the lowest induction time while 1.0 wt.% had the highest (Aliabadi et al., 2015).

4.8.2 Effects of temperature variation on kinetic parameter

The amount of CH₄ moles consumed during hydrate formation increases with decreasing temperature, as shown in Table 4.5. The lowest gas consumption of 0.001 moles was obtained at the highest temperature of 277.74 K utilized in this set of measurements. The highest gas consumption of 0.021 moles was obtained at a temperature of 275.77 K, the lowest temperature utilized in this study. The maximum storage capacity of 25.62 (v/v) was achieved at a minimum temperature of 275.77 K however, the lowest storage capacity of 2.81 (v/v) was obtained at a temperature of 277.74 K. It is evident that storage capacity decreases as the temperature increases due to the increase in the driving force with movement into the hydrate stable region as temperature decreases. For water to hydrate conversion it can be seen from Table 4.5 that the trends obtained are similar to the ones obtained for storage capacity. This is caused by the incorporation of the gas into the hydrate structure, thus a specific amount water is consumed. The rate of gas uptake decreases with temperature as shown in table 4.5.

Table 4.5: Kinetic results obtained at a pressure of 4.66 MPa and different initial temperatures over 100 minutes.

Temperature/K	275.77	276.25	276.77	277.30	277.74
Gas consumption (moles)	0.021	0.018	0.012	0.009	0.001
Storage Capacity(v/v)	25.62	22.48	15.61	12.02	2.81
Water to Hydrate Conversion (%)	11.67	10.19	7.02	5.34	0.71
Rate of gas uptake (mol of gas consumed/mol of water. min) ×10 ⁴	2.99	2.70	1.29	0.77	0.314

Uncertainty $U(T) = \pm 0.1$ K, $U(P) = 0.01$ MPa $U_{concentration}$ (wt%)=0.06% $U(t)=0.01$ s

The highest rate of gas uptake was 2.99×10^{-4} mol_G mol_w⁻¹min⁻¹ obtained at a temperature of 275.77 K. The lowest value obtained was 3.14×10^{-5} mol_G mol_w⁻¹min⁻¹ obtained at 277.77K. The rate of gas uptake decreased as temperature increased. This was due driving force for hydrate formation decreasing as temperature increases.

4.8.3 Effects of pressure variations on kinetic parameter

The results obtained with pressure variation on the CH₄-water hydrates are shown in Table 4.6.

Table 4.6: Kinetic results obtained at a pressure of 275.8K and different initial pressures over 100 minutes.

Pressure/MPa	4.66	5.11	5.61	6.61
Gas consumption (moles)	0.0196	0.0198	0.021	0.043
Storage Capacity(v/v)	25.48	25.48	28.32	50.63
Water to Hydrate Conversion (%)	11.67	11.67	12.92	23.68
Rate of gas uptake (mol of gas consumed/mol of water. min) ×10 ⁴	1.80	2.4	2.4	3.17

Uncertainty $U(T) = \pm 0.1$ K, $U(P) = 0.01$ MPa $U_{concentration}$ (wt%)=0.06% $U(t)=0.01$ s

The maximum gas consumption of 0.043 moles was achieved at a pressure of 6.16 MPa and a minimum of 0.0196 moles was attained at the pressure of 4.66MP, which was the lowest pressure utilized in this study. From the values presented in Table 4.6, it can be noted that there is little variation in the amount of gas consumed between the pressure of 4.66 MPa and 5.61 MPa. The highest storage capacity of 50.52 (v/v) was obtained at 6.16 MPa. The storage capacity obtained at 4.66 - 5.61 MPa was in a comparable range with an average value of 26.5 (v/v) for all systems. Generally, the storage capacity was directly proportional to pressure. In water-to-hydrate conversion, the highest percentage value of water-to-hydrate conversion obtained was 23.68%. It was obtained at a pressure of 6.61 MPa. As with storage capacity, a similar trend was observed in water-to-hydrate conversion. For pressure values between 4.66 – 5.61 MPa the average percentage for water-to-hydrate conversion was 12%. The rate of gas uptake decreases as pressure decreases as shown in Table 4.5. The highest rate of gas uptake of $3.17 \times 10^{-4} \text{ mol}_G \text{ mol}_W^{-1} \text{ min}^{-1}$ was obtained at 6.16 MPa, while the lowest value obtained was $1.80 \times 10^{-4} \text{ mol}_G \text{ mol}_W^{-1} \text{ min}^{-1}$ at 4.66 MPa as shown in Table 4.5

4.8.4 Kinetic Parameter with Additives

The kinetic parameters investigated in CH₄ hydrate formation with chemical additives utilized in the study are shown in Table 4.7. of the concentration of additives utilized was 0.1, 0.2, 0.5, 1.0, and 1.2 wt.% in the presence of 0.05 wt.% SDS. In the table only the maximum and

minimum values are presented. For the graphical trends of all the concentrations utilized in the study the reader is referred to Appendix E.2

4.8.4.1 Gas Consumption

The maximum and minimum values for gas consumption obtained with different additives is shown in Table 4.7. The highest gas consumption of 0.0238 moles was obtained with 0.1 wt.% CuO +0.05wt.% SDS while the lowest was 0.0184 moles obtained with 0.2 wt.% $\text{H}_{12}\text{MgN}_2\text{O}_{12}$ +0.05 wt.% SDS. However, in all the systems where nanoparticles were utilized, the moles consumption of CH_4 during hydrate formation was higher than that of water and SDS solution. The values obtained with graphene nanoplatelets were comparable to those obtained with other nanoparticles, even though graphene particles were nanoplatelets. Similarly, Aliabadi et al., (2015) reported the highest gas consumption at 0.3 wt.% CuO +500 ppm SDS. The amount of gas consumed was not dependent on the concentration of the additives.

It was observed that ZnO systems had long induction times, and the rate of hydrate formation was slower than in pure water in all cases, excluding the system containing for 0.1 wt.% ZnO + 0.05 wt.% SDS. The consumption rate for ZnO was lower compared to that of nanofluids. This is likely due to the large particle sizes for the ZnO microparticles. The values obtained with graphite powder were comparable to those of ZnO. This behavior is expected as both powders are microparticles. The magnesium hexahydrate crystals had lower values than all the systems investigated due to the size of its crystals.

Table 4.7: Summary of kinetic parameters obtained with CH₄ gas and additives utilized in the study (Maximum & Minimum).

	Gas consumption (moles)	Storage Capacity(v/v)	Water to Hydrate Conversion (%)	Rate of gas uptake (mol _G mol _w ⁻¹ min ⁻¹) × 10 ⁻⁴
Water	0.0198	23.98	10.92	2.06
0.05 wt.% SDS	0.0198	23.98	10.92	6.30
Copper Oxide (CuO)+0.05wt.% SDS	0.1 wt.% - 0.0238 1.0 wt.% - 0.0206	0.1wt.% - 28.50 1.2 wt.% -24.98	0.1 wt.% - 13.09 1.2 wt.% - 11.35	0.2 wt.% - 89.4 1.2 wt.% - 5.63
Aluminium Oxide (Al ₂ O ₃) + 0.05wt.% SDS	0.2 wt.% - 0.0210 1.0 wt.% - 0.0199	0.2 wt.% - 25.28 0.5 wt.% - 24.01	0.2 wt.% - 11.50 1.2 wt.% - 10.98	1.2 wt.% - 10.2 0.1 wt.% - 6.55
Zinc Oxide (ZnO) + 0.05 wt.% SDS	0.1 wt.% - 0.0204 1.0 wt.% - 0.0197	0.1 wt.% - 25.86 1.0 wt.% - 24.09	0.1 wt.% - 11.37 1.0 wt.% -10.92	0.1 wt.% - 6.79 1.0 wt.% - 5.79
Graphene (GPN) + 0.05 wt.% SDS	0.5 wt.% - 0.0207 1.0 wt.% - 0.0199	0.2 wt.% - 25.42 1.2 wt.% - 24.99	0.2 wt.% - 11.39 1.2 wt.% - 10.94	1.2 wt.% - 7.68 1.0 wt.% - 5.03
Graphite (C-C) + 0.05 wt.% SDS	0.2 wt.% - 0.0208 1.0 wt.% - 0.0196	0.2 wt.% - 25.64 1.2 wt.% - 24.09	1.0 wt.% - 11.84 1.2 wt.% - 11.45	1.2 wt.% - 20.4 0.1wt.% - 7.97
Magnesium nitrate hexahydrate (H ₁₂ MgN ₂ O ₁₂) + 0.05 wt.% SDS	0.1 wt.% - 0.0199 0.2 wt.% - 0.0184	0.1 wt.% - 24.33 0.2 wt.% - 23.88	0.1 wt.% - 10.92 0.2 wt.% - 10.55	0.5 wt.% - 18.7 1.2 wt.% - 3.40

Uncertainty $U(T) = \pm 0.1$ K, $U(P) = 0.01$ MPa $U_{concentration}$ (wt%)=0.06% $U(t)=0.01$ s.

4.8.4.2 Storage Capacity

The results presented in Table 4.7 were obtained by selecting different nanoparticles and chemical additives to increase the storage capacity of the CH₄ hydrate. A maximum storage capacity of 28.5 (v/v) was achieved with a concentration of 0.1 wt.% CuO + 0.05 wt.% SDS system. The minimum storage capacity of 24.98 (v/v) was obtained with 1.2 wt.% CuO + 0.05 wt.% SDS. The Al₂O₃ nanofluid systems did not show any significant difference in the amount of CH₄ gas stored at different concentrations. The highest storage obtained was 25.28 (v/v), with 0.2 wt.% Al₂O₃ + 0.05 wt.% SDS and the minimum was 24.01 (v/v) from 1.2 wt.% Al₂O₃ + 0.05 wt.% SDS. A similar trend was obtained with graphene nanoplatelets shown in Table 4.7 and Appendix E.2. The maximum gas storage of 25.42 (v/v) was obtained with 0.2wt.% GPN + 0.05 wt.% SDS and a minimum of 24.99 (v/v) was obtained from a 1.2 wt.% GPN +0.05 wt.% SDS. In all the systems containing nanoparticles, the storage capacity was observed to decrease as the concentration increased. This might be due to solution saturation with nanoparticles leading to slow hydrate growth.

The system comprised 0.2 wt.% H₁₂MgN₂O₁₂ + 0.05 wt.% SDS had the lowest storage capacity than any of the systems in this study of 23.88 (v/v). With microparticles, 0.1 wt.% ZnO + 0.05 wt.% SDS had the highest storage capacity of 25.86 (v/v). Good repeatability was obtained with 0.1 wt.% ZnO + 0.05 wt.% SDS as seen in ZnO storage capacity graph profile in Appendix E.2. Graphite, ZnO and graphene had comparable results as the maximum and minimum values from these systems were in the same range. The H₁₂MgN₂O₁₂ system had the lowest storage capacity compared to other systems utilized in the study as shown in Table 4.7. This was likely due to the nature of the solution formed between the H₁₂MgN₂O₁₂ crystals and the water, which did not favor extensive hydrate growth.

4.8.4.3 Water-to-Hydrate Conversion

The results of water-to-hydrate conversion for this study's additives are as a percentage in Table 4.7. The distilled water and 0.05 wt.% SDS system had the same water-to-hydrate conversion percentage, which was 10.92%. Thus, SDS's effects proved insignificant in converting water to hydrate. The nanoparticle system in this study had a higher conversion of water to hydrate. This was caused by the numerous nuclei sites in the form of nanoparticles which enhanced hydrate growth and, consequently, water consumption. The maximum conversion obtained was 13.09% which was obtained with 0.1 wt.% CuO + 0.05 wt.% SDS and the minimum was

10.94% obtained with 1.2 wt.% GPN + 0.05 wt.% SDS. In general, all the nanofluids had a higher conversion than pure water. The ZnO and graphite microparticles had comparable results for water-to-hydrate conversions. With these microparticles, the highest conversion of water to hydrate was 11.84%. It was obtained with 1.0 wt.% graphite + 0.05 wt.% SDS. The 1.0 wt.% ZnO + 0.05 wt.% SDS system yielded the lowest water-to-hydrate conversion of 10.92%. These values were expected to be lower than those obtained with nanoparticles due to the thermo-physical properties mentioned in Chapter 2. The system containing the $H_{12}MgN_2O_{12}$ crystals had the lowest percentage of water-to-hydrate conversion due to the crystal's large particle size, which does not improve hydrate formation.

4.8.4.4 Rate of gas uptake

As presented in Table 4.7, additives drastically improved the rate of gas uptake when compared to runs carried out with pure water. Considering the nanoparticles systems, the highest rate of gas uptake was $8.94 \times 10^{-3} \text{ mol}_G \text{ mol}_W^{-1} \text{ min}^{-1}$ obtained with 0.5 wt.% CuO + 0.05 wt.% SDS. While the maximum gas uptake value achieved with Al_2O_3 nanofluid was $1.0 \times 10^{-3} \text{ mol}_G \text{ mol}_W^{-1} \text{ min}^{-1}$ obtained with 1.2 wt.% Al_2O_3 + 0.05 wt.% SDS. The rate of gas uptake with 0.05 wt. % SDS was of $6.5 \times 10^{-4} \text{ mol}_G \text{ mol}_W^{-1} \text{ min}^{-1}$ this was the same for 1.0 wt.% CuO + 0.05 wt.% SDS system. Pure water had the lowest $2.0 \times 10^{-4} \text{ mol}_G \text{ mol}_W^{-1} \text{ min}^{-1}$. The ZnO microparticles had the highest value for the rate of gas uptake of $6.7 \times 10^{-4} \text{ mol}_G \text{ mol}_W^{-1} \text{ min}^{-1}$ with 0.1 wt.% ZnO + 0.05 wt. % SDS. The other ZnO concentration and 0.05 wt. % SDS had comparable values for the rate of gas uptake of about $6.0. \times 10^{-4} \text{ mol}_G \text{ mol}_W^{-1} \text{ min}^{-1}$. Graphite and magnesium hexahydrate showed comparable results as shown Table 4.7 with the highest value obtained with 1.2 wt.% C-C + 0.05 wt.% SDS and 0.5 wt.% $H_{12}MgN_2O_{12}$ + 0.05 wt.% SDS. The values obtained with ZnO, C-C, $H_{12}MgN_2O_{12}$ were lower than the values obtained with nanoparticles, proving that nanoparticles improve hydrate formation.

4.9 Summary

The results obtained in this study show desirable effects on the kinetics of the CO_2 and CH_4 hydrate formation. While nanoparticles improve the kinetics, higher concentrations do exhibit adverse effects on the hydrate growth. This was due to the saturation of the system which then hinders nucleation. For the CH_4 system, induction time was reduced from 18 minutes with deionized water to 1.0 minute when nanoparticles were added to the solution. The CO_2 system's induction time decreased from 8 minutes to 0.01 minutes. This attribute is very desirable in

employing hydrate for CO₂ capture as it ensures that the reaction time will be greatly reduced, making the process more efficient. For the CO₂ systems, 0.1 wt.% CuO + 0.05 wt.% SDS the induction time of 0.01s, while 1.0 wt.% H₁₂MgN₂O₁₂ + 0.05wt.% SDS has the longest induction time of 52. 13s. The 1.2 wt.% GPN + 0.05wt.% SDS had a storage capacity of 52.12 (v/v) and 46.70 (v/v) was the average storage capacity of CuO and Al₂O₃ nanoparticles. The 1.2 wt.% H₁₂MgN₂O₁₂ + 0.05wt.% SDS had the lowest storage capacity of 43.01 (v/v). The average value obtained was gas storage of 0.040 moles with CuO and Al₂O₃ nanoparticles. The maximum value of the rate of gas uptake obtained was $2.44 \times 10^{-3} \text{ mol}_G \text{ mol}_W^{-1} \text{ min}^{-1}$. this was obtained with 0.2 wt.% graphite powder + 0.05 wt.% while the lowest $3.34 \times 10^{-4} \text{ mol}_G \text{ mol}_W^{-1} \text{ min}^{-1}$. value obtained with 0.1 wt.% H₁₂MgN₂O₁₂ + 0.05wt.% SDS. For water conversion, 24.98% was the maximum obtained 1.2 wt.% GPN + 0.05wt.% SDS while, 20.46% obtained with 1.0 wt.% H₁₂MgN₂O₁₂ + 0.05 wt.%.

For the CH₄ system, the 0.1 wt.% CuO + 0.05 wt.% SDS system had the best performance in all the parameters investigated with gas consumption of 2.38×10^{-2} moles, a storage capacity of 28.50 (v/v), water to hydrate conversion of 13.09% and a rate of gas consumption $8.94 \times 10^{-3} \text{ mol}_G \text{ mol}_W^{-1} \text{ min}^{-1}$. The 0.2 wt.% H₁₂MgN₂O₁₂ + 0.05 wt.% SDS system had the lowest values in gas consumption, storage capacity and water-to-hydrate conversion which were 0.0184 moles, 23.88 (v/v) storage capacity, and 10.55%, respectively. CuO nanoparticles exhibited the best performance, followed by Al₂O₃ nanoparticles and graphene nanoplatelets. These were followed by microparticles (graphite and zinc oxide). The H₁₂MgN₂O₁₂ crystalline system exhibited the lowest performance of all the systems investigations. The improvement shown by nanoparticles in the storage capacity analysis is critical in ensuring that a large amount of CO₂ can be stored in carbon capture and storage applications or large amounts of CH₄ in energy storage applications.

Chapter 5: CH₄ replacement with CO₂ in CH₄ hydrates

5 Introduction

This chapter presents the experimental method and results for the replacement measurements of CH₄ with CO₂ from the CH₄ hydrate matrix without any porous media. Prior to experimental work, hydrate dissociation measurements were performed to assess the equipment and the calibration of the sensors on the equipment. The experimental method includes methane hydrate formation and methane recovery. For the latter, the CO₂ encapsulation into the clathrate structure is presented on the equipment available in the Thermodynamics research unit (TRU) research laboratories. For the formation of the methane hydrate, one method was utilized in all the experimental runs carried out in the study. Graphene nanoplatelets and sodium dodecyl sulphate (SDS) enhanced methane hydrate formation. Nitrogen gas was added as a secondary gas to improve the replacement. For the final experimental runs, the replacement temperature was increased during the replacement in a process known as thermal stimulation to effect higher CH₄ release. Argon was also utilized as a secondary gas to assess its performance. The results obtained are presented in Appendix F.3.

5.1 Apparatus

A schematic of the experimental apparatus utilized in the study is shown in Figure 5.1. The main reactor of the equipment is a 316L stainless steel equilibrium cell with a volume of 52 cm³ and a maximum pressure limit of 10 MPa. Stirring was accomplished by a Heidolph RZR 2041 motor gear system connected to the shaft with a magnetic tip turning a magnetic lined stirrer inside the cell. A WIKA pressure transducer with an operating range of 0-16 MPa gauge pressure and expanded uncertainty of 0.02 MPa was used to monitor pressure during the reaction. A WIKA model REB Pt-100 thermocouple temperature probe with an accuracy of 0.05 K was utilized for temperature measurement. Temperature and pressure data were logged every 5 seconds by the Agilent data acquisition system. A Polyscience TXF200 programmable temperature controller with an operating temperature of 243.15 to 323.15 K was used to maintain the water/ethyl glycol bath temperature. A 260D ISCO Syringe pump with a working pressure of 0.07-51.7 MPa was used for loading the gases into the equilibrium cell. An RV12 rotary vane vacuum pump was utilized to evacuate the system. The composition of the gas mixture was analyzed using an online Shimadzu 2014 gas chromatograph with a thermal conductivity detector (TCD) and Poropak packed column. A ROLSITM was used as an online sampling device. Full details of the apparatus details are given in Appendix F.1.

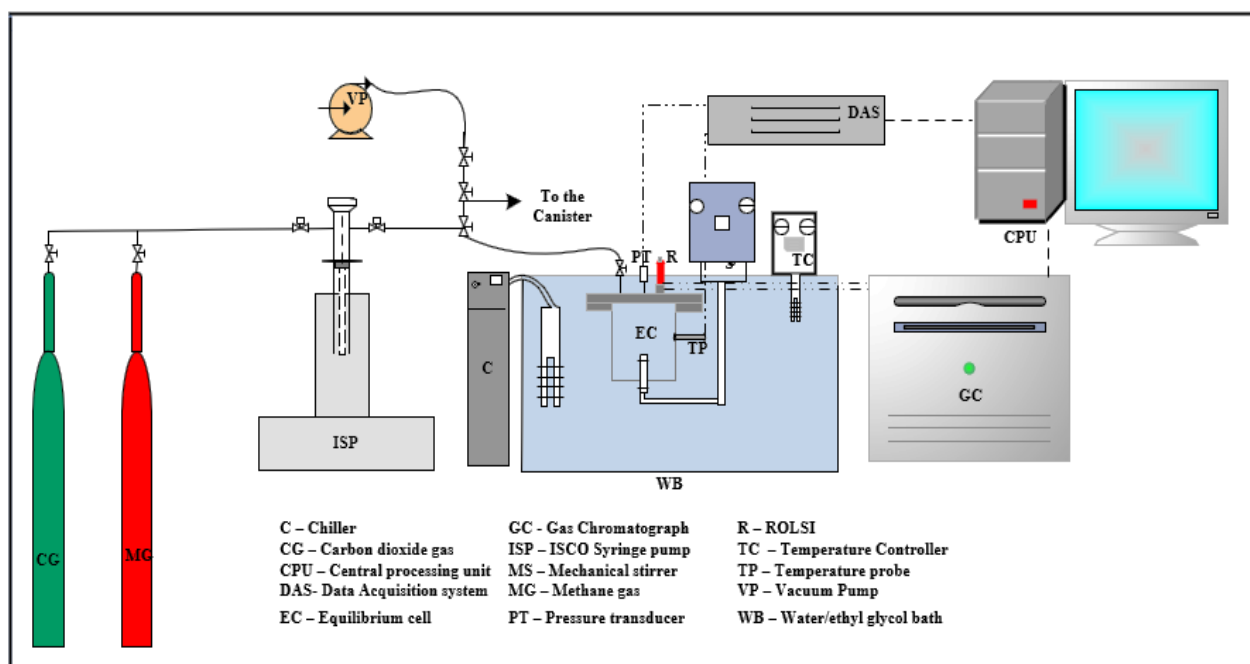


Figure 5.1: Schematic diagram of the experimental setup utilized in CH₄-CO₂ replacement without porous media.

5.2. Materials

Methane, nitrogen and carbon dioxide gas with a purity (vol%) of 99.9% was supplied by Afrox. Argon of purity (vol%) 99.8% was supplied by Air Liquide. Gas mixtures were prepared using an OHAUS PA4202C top pan balance with an accuracy of 0.0001 g. Distilled water with a conductivity of 0.64 mS/cm was obtained from the laboratory. Graphene nanoplatelets with over 90% carbon and SDS with purity greater than 99.0% were supplied by Sigma- Aldrich. A Full description of the graphene nanoplatelets is provided in Table F.2.

5.3 Experimental methods

This section presents the temperature, pressure, and gas chromatography calibration procedure and results. Moreover, the uncertainty in temperature, pressure and gas chromatography detection measurements is presented.

5.3.1 Calibrations of sensors

Calibrations were carried out for the temperature probe, pressure transducer, and gas chromatography detector. In this section, the calibration procedures followed for calibrating the instruments mentioned above are detailed, and the calibration outcomes are obtained. It was imperative to calibrate the devices mentioned above to ensure that accurate results were obtained and reported. The temperature and pressure calibration procedure are detailed in

subsection 4.3.1.1. In this section pressure and temperature calibration curve are presented along with graphy showing the deviations obtained.

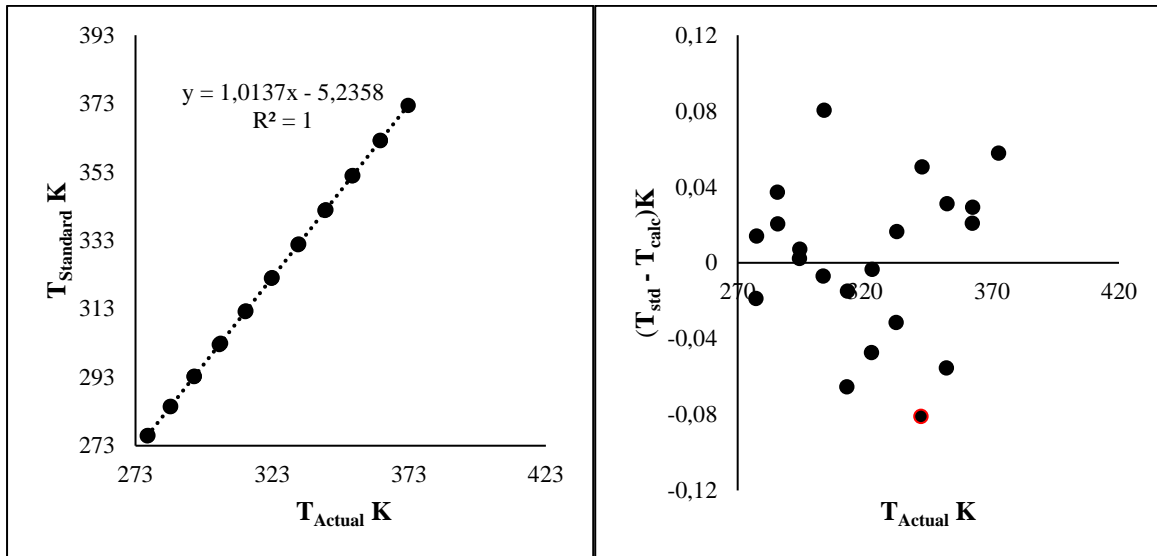


Figure 5.2: Calibration of the temperature probe (LHS) and plot of the temperature deviation (RHS) used for the temperature probe utilized in the equilibrium cell.

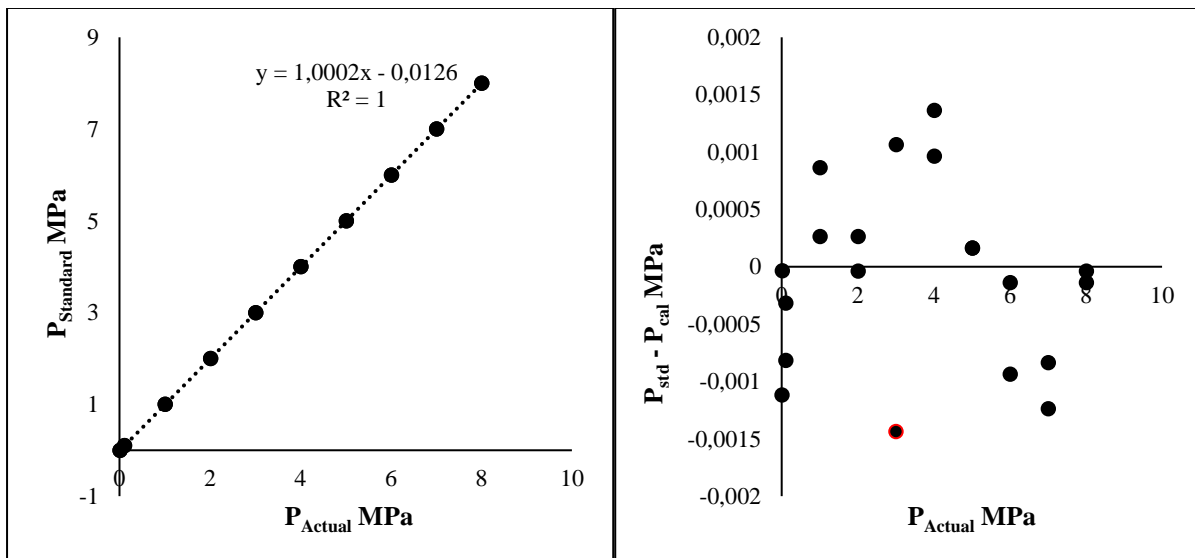


Figure 5.3: Calibration plot of the WIKA pressure transducer (LHS) and pressure deviation (RHS) used in a reactor vessel.

5.3.2 Gas Chromatography detector calibration

Gas chromatography (GC) was utilized to analyze and determine the different compositions of gases available in the cell at any given time. This is accomplished by obtaining peak areas by GC detector and then using the GC detector calibration curve to obtain molar ratios. This is possible as different gases have different resident times in the GC column. The quantitative

relationship between the response of the Shimadzu 2014 gas chromatography Thermal Conductivity Detector (TCD) for each compound and the composition of gas mixtures separated by gas chromatography was determined the composition of each compound. This study employed the direct injection calibration method, first published in detail by Raal and Mühlbauer, (1998), as its accuracy was acceptable. This method has been successfully applied by many researchers, including Naidoo (2004), Belandrin, (2012), Lubimbi, (2017), and Matizakurima, (2020). In this method, two SGE Analytical science 50 μ L and 250 μ L gas-tight syringes were used to inject known volumes of pure components and mixtures directly into the GC via the injection port. For the calibrations with the gas mixtures, the Gas Chromatograph conditions were optimized to distinguish the pure component GC peaks and their areas carefully and correctly integrated. The pure components present in the mixtures, such as N₂, CH₄, and CO₂ gases, were shown to produce separate peaks. Gas mixtures were prepared in a separate mixing vessel using the successive addition method using pressure and mass (the gas preparation procedure is provided in Appendix F.2). In contrast, pure gas samples were obtained from the supply gas cylinders through a septum by analytical syringes. The sample was injected into the GC

The TCD calibration plot for the gases was established by plotting the peak areas obtained from the chromatogram against the number of moles for pure gases. For the gas mixtures, the ratio of the peak areas was plotted against the molar ratios of the corresponding components. The calibration curve was fitted to the first-order polynomial for the pure gases and gas mixtures. The composition of a gas phase at a known temperature and pressure conditions is thus determined from the known GC peak area ratio of the unknown sample and the coefficients of the corresponding polynomial equation for each compound.

The response factor is defined as the proportionality constant between the number of moles passing the detector and the peak area A obtained from, e.g., an electronic integrator $n_i = A_i F_i$. Since Area (A) depends on the amount of sample injected, which is generally very reproducible thus, area ratios are used, as shown in equation 5.1;

$$\frac{n_1}{n_2} = \left(\frac{A_1}{A_2}\right) \left(\frac{F_1}{F_2}\right) = \frac{x_1}{x_2} \quad 5.1$$

Where x is the mole fraction, A is the peak area, F is the response factor, n is the peak area and response factor.

The response factor is obtained from a plot of $\frac{A_1}{A_2}$ vs $\frac{x_1}{x_2}$. When the inverse of this graph is plotted, the gradient is also expected to be inverse. The calibration graph involving the two components (CH₄ and CO₂) investigated in the study is shown in Figure 5.4.

For binary and ternary systems, the following relations were utilized to obtain the molar ratios of the gases;

$$\frac{y_i}{y_j} = \frac{A_i}{A_j} m + c \quad 5.2$$

$$y_1 + y_2 = 1 \quad 5.3$$

where y_i and y_j are the molar ratios of the pure gases, A_i and A_j are the peak areas obtained from the GC, C is the Y-intercept, and m is the gradient of the curve. Graphs of composition ratios $\frac{y_i}{y_j}$ plotted against the ratio of peak areas $\frac{A_i}{A_j}$ were utilized to obtain molar ratios. For a binary system equation, 5.3 was utilized to obtain molar ratios. For ternary mixtures, the following relations were utilized to obtain molar ratios.

$$\frac{1}{y_1} = 1 + \frac{y_2}{y_1} + \frac{y_3}{y_1} \quad 5.4$$

$$\frac{1}{y_2} = 1 + \frac{y_1}{y_2} + \frac{y_3}{y_2} \quad 5.5$$

$$y_i = \frac{1}{1 + \sum_{i=2}^n \left(\frac{y_j}{y_i}\right)} \quad 5.6$$

$$y_3 = 1 - (y_1 + y_2) \quad 5.7$$

5.3.2.1 Calibration results: Gas Chromatography Detector

Pure Gases- Figures 5.4 to 5.6 show the GC detector calibration curves obtained with pure gases CO₂ and CH₄, with respective deviations presented alongside both gases. The maximum deviation obtained for the two graphs was 0.048%.

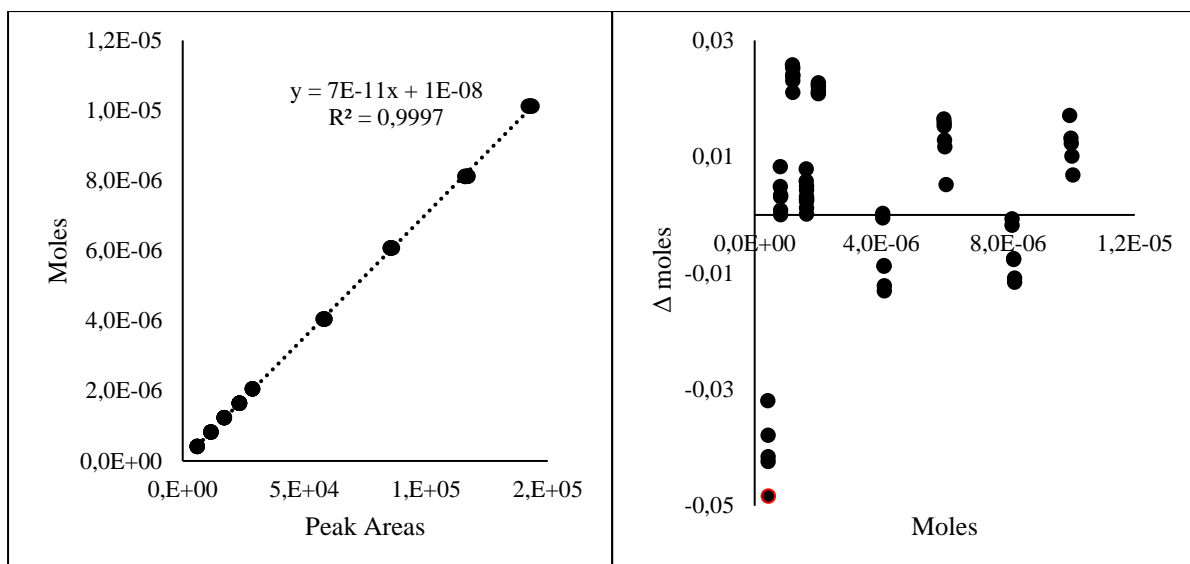


Figure 5.4: GC detector calibration curve for pure CO₂ (LHS) and deviations in measurements in the calibration (RHS).

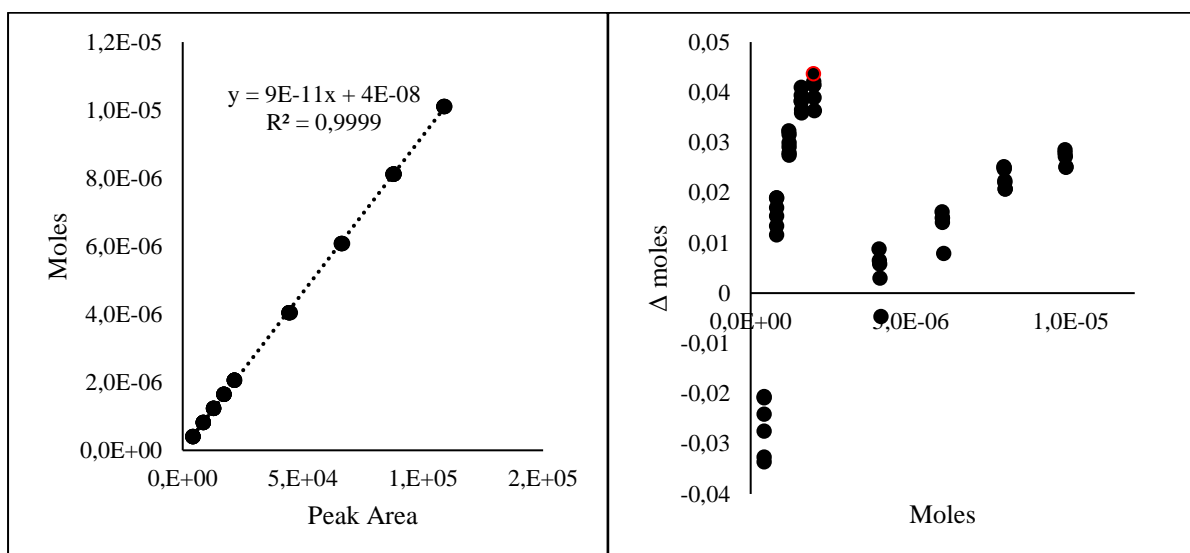


Figure 5.5: GC detector calibration curve for pure CH₄ (LHS) and deviations in measurements in the calibration (RHS).

Table 5.1: TCD calibration results for CO₂ and CH₄ showing the maximum relative absolute errors with a first-order polynomial.

Gas	Volume	$\Delta n/n$ (max)	Correlation	R^2
CO ₂	0 -250	0.048	$n_{\text{calc}} = 7 \times 10^{-11} + 1 \times 10^{-8}$	0.9997
CH ₄	0 -250	0.044	$n_{\text{calc}} = 9 \times 10^{-11} + 4 \times 10^{-8}$	0.9999

Binary gas mixture- The calibration of the binary mixture was compared to the pure gas ratios to validate the calibration procedure.

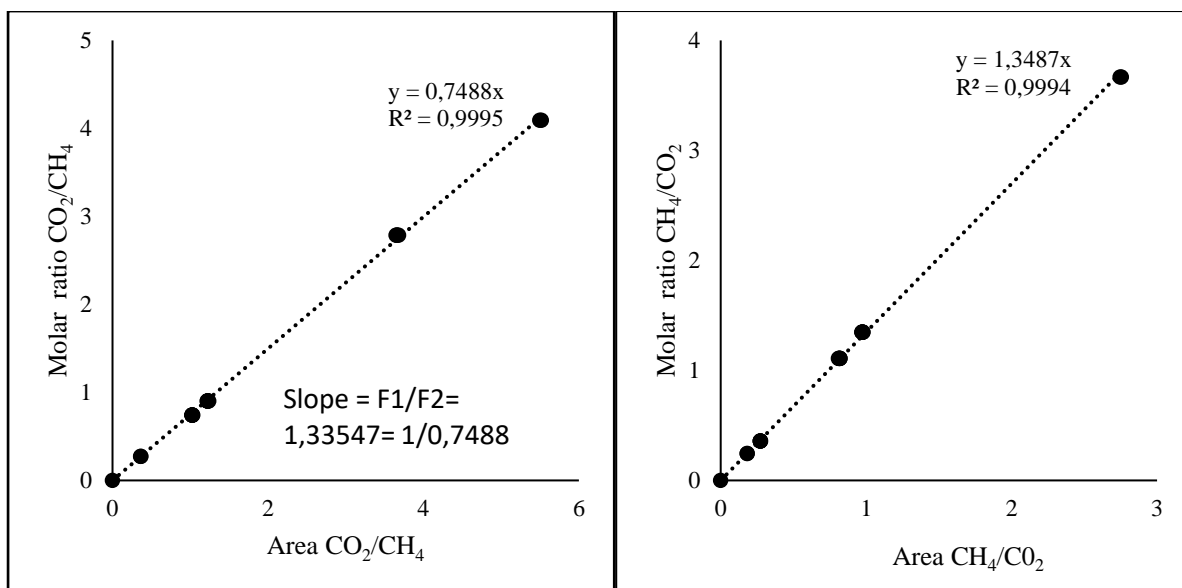


Figure 5.6: GC detector calibration of methane (2)/carbon dioxide (1) binary mixture (LHS) and methane (2)/carbon dioxide (1) binary mixture. (RHS).

The GC detector calibration was confirmed by plotting the calibration results obtained via two different methods, i.e., Pure components and gas mixtures alongside one another on the same graph. The resulting plot is shown in figure 5.7.

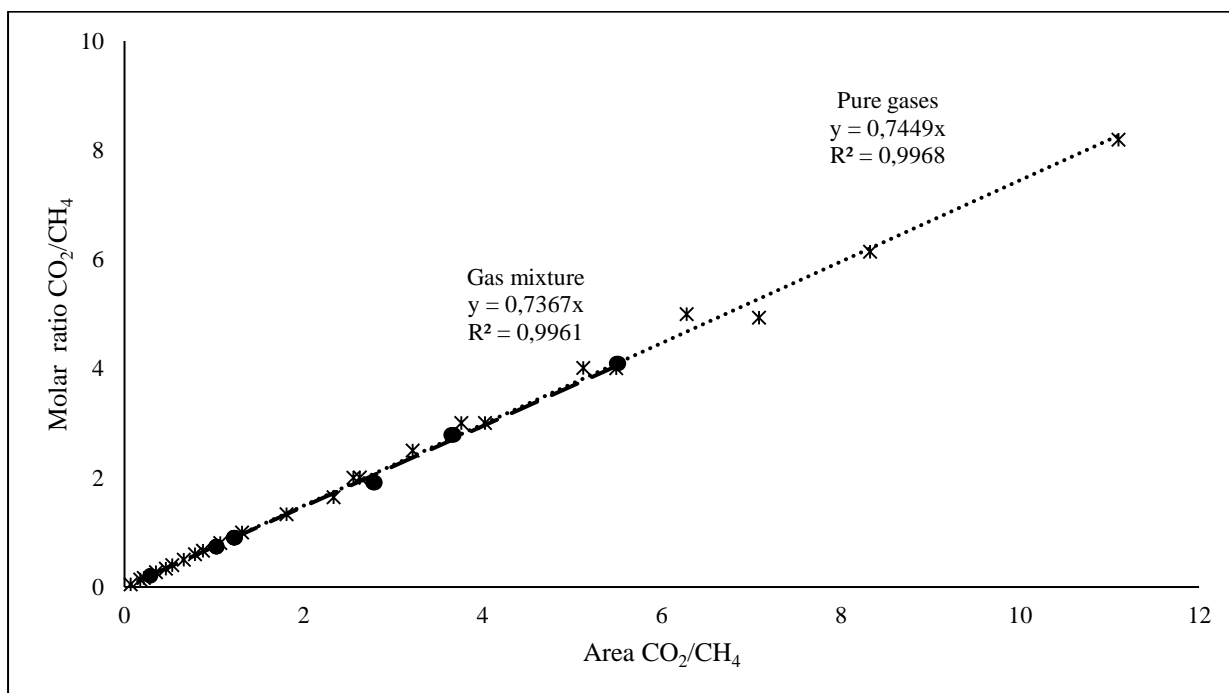


Figure 5.7: Comparison of GC detector response calibration curves for pure gases and binary mixture (*..... Pure gases, ● - - - - -Gas mixture).

Ternary Gas Mixtures - The GC detector calibration results obtained from a ternary gas mixture were fitted in the first polynomial and plotted in Figure 5.8.

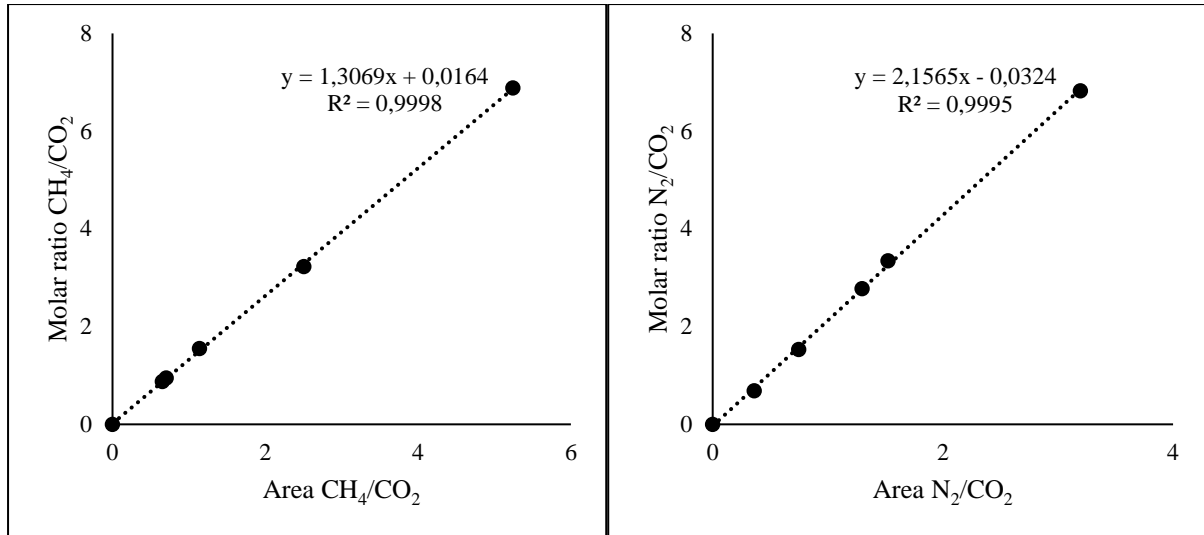


Figure 5.8: GC detector calibration for methane-carbon dioxide (LHS) and nitrogen-carbon dioxide (RHS) calibration curve for nitrogen-methane-carbon dioxide system.

5.3.3 Uncertainty in measurements

Contributing uncertainties considered in computing the combined expanded uncertainty for temperature, pressure, and molar composition are shown in Tables 5.2, 5.3 and 5.4. The formulas utilized in computing combined uncertainty are presented in Appendix D. The molar composition uncertainty was a summation of uncertainty due to GC calibration shown in Table 5.3 and uncertainty due to gas mixture preparations shown in Table 5.4.

Table 5.2: Summary of the source of uncertainty for variables reported in this study

Uncertainty source	T (K)	P (MPa)
Manufacturer stated instrument error \mathbf{u}_{instr}	± 0.03	± 0.005
Standard calibration correlation error \mathbf{u}_{corr}	± 0.04	± 0.008
Calibration error, \mathbf{u}_{calib}	± 0.05	± 0.0015
Combined standard uncertainty, $u_c(x)$	± 0.04	± 0.08
Combined expanded uncertainty, $u(x)$	± 0.09	± 0.02

Table 5.3: Molar composition uncertainty due GC Calibration adapted from (NIST et al., 1994).

	CO ₂	CH ₄
Standard uncertainty the ideal gas law: $\mathbf{u}_{ig} \mathbf{n}_x$	6.34338E-07	7.00862E-08
Standard calibration correlation error \mathbf{u}_{corr}	6.32859E-15	9.71637E-16
Standard uncertainty in the number of moles $\mathbf{u}(\mathbf{n}_x)$	6.39307E-07	7.67054E-08
Standard uncertainty repeatability, \mathbf{u}_{rep}	0.0027333	0.001938
Combined standard uncertainty, $u_c(\mathbf{n}_x)$	0.0027332	0.001937
Combined expanded uncertainty, $u(\mathbf{n}_x)$	± 0.005	± 0.004

Table 5.4: Molar composition uncertainty due Gas mixture preparation.

Uncertainty source	P (MPa)
Manufacturer stated instrument error \mathbf{u}_{instr}	± 0.0006
Standard calibration correlation error \mathbf{u}_{corr}	± 0.0135
Calibration error, \mathbf{u}_{calib}	± 0.0135
Combined standard uncertainty, $u_c(\mathbf{n}_x)$	± 0.0159
Combined expanded uncertainty, $u(\mathbf{n}_x)$	± 0.0317

5.4 Experimental Section

In this section, procedures for sample preparation and experimental measurements are discussed. The procedure for cell cleaning and leak testing applied before the commencement of experiments is detailed in section 4.4.

5.4.1 Sample preparation

Sodium dodecyl sulfate (SDS) was dissolved in deionized water in a 500 ml volumetric flask to make a 0.05wt.% SDS solution. This solution was utilized to produce 0.5wt.% GPN nanofluids. An OHAUS PA4202C top pan balance was used to measure the mass of the nanoparticle. Then it was added to a 50 ml sterile centrifuge tube. The solution was mixed in a vortex mixer for five minutes to ensure the complete mixing of the solution with the nanoplatelets. The solution was immediately added to the 50 cm³ syringe in preparation for addition to the cell.

5.4.2 Methane hydrate formation

The equilibrium cell and connecting lines were evacuated for 30 minutes using a vacuum pump to a pressure of 0.07 MPa before commencing each experimental run. Approximately 1.11 moles of water or solution-containing additives were transferred into the cell from a 50 cm³ syringe connected to the drain valve of the cell by a plastic pipe. The volume of the cell is 52 cm³, and the volume of water utilized was approximately 20 cm³. The vacuum pump was then switched off. After that, the cell was pressurized with CH₄ from an ISCO syringe pump to a pressure above 7.0 MPa. The pressure and temperature of the cell were noted and recorded. When the system parameters stabilized for approximately 5 minutes, the CH₄ hydrate formation process was initiated by turning on the stirrer and decreasing the temperature to between 276

and 273 K. The hydrate formation process proceeded for over 24-72 hours and was noted by a pressure drop at a constant temperature.

5.4.3 Purging of CH₄ in the gas phase

The temperature of the equilibrium cell was then decreased to a temperature of 273 K before the addition of replacement gas to preserve the hydrate from the temperature influence of the incoming gas stream. This was done to ensure that the temperature change from the incoming gas did not significantly alter the hydrate structure. The stirrer was turned off then the CH₄ gas remaining in the gas phase was evacuated into a canister through the feed valve. The reactor vessel pressure dropped to below 0.1 MPa in the process. The connecting lines were evacuated using the Edwards vacuum pump. The vacuuming was performed in less than 10 seconds to ensure that CH₄ hydrate remained intact. Immediately the equilibrium cell was pressurized with CO₂ to a set pressure value through the feed valve for replacement. The incoming gas was cooled to 273 K by a temperature control jacket of the ISCO pump utilized for gas injection into the equilibrium cell. Online sampling of the gas phase composition was monitored, and the process was discontinued when CH₄ area peaks were no longer detected by the GC detector or became insignificant (10^{-5}).

5.4.4 Preparation of Gas Mixtures

Gas mixtures utilized in the replacement reactions were prepared in the laboratory. An OHAUS PA4202C top pan balance was used to measure the mass of the gases. The gas mixtures were prepared in preselected molar ratios. A 669 ml canister was utilized for gas mixture preparations. With careful control, the gas was filled in the canister, which enabled the mass change to be recorded. With the canister on the mass balance, a second component was added, the mass of the gas was noted on the scale.

5.4.5 Replacement reaction procedure

After purging of CH₄ gas, CO₂ was fed into the reaction cell to a pressure of approximately 4.0 MPa. The temperature was either lowered or maintained at the application for CH₄ hydrate formation. Using the real gas law and GC calibration equations, the molar composition of gases at the beginning of the replacement reaction was computed. The stirrer was turned on, and the replacement reaction was allowed to proceed. The gas phase was analyzed at regular intervals during the replacement reaction to determine the composition of the gases as the replacement occurred. The reaction was stopped when there was no observable change in the peak areas in the gas phase for over 24 hours.

At the end of the replacement reaction, the gas phase was analyzed using the online GC then the gas contents were vented from the cell and collected in a canister. The number of moles of the collected gas was computed using the ideal gas law. The cell was then evacuated for thirty seconds to remove residual components from the gas phase. The temperature of the equilibrium cell was then increased by increasing the water bath temperature, causing hydrate dissociation. A pressure increase accompanied this. When the pressure and temperature stabilized at the new temperature setting, the moles of the gas trapped in the hydrate phase were computed using the ideal gas equation.

5.4.6 Shutdown procedure

At the end of the hydrate experimental measurements, the data on the Agilent software was saved on the computer connected to the experimental setup. The GC was stopped from running to allow the temperature to drop. Afterward, all the electric devices were switched off, starting with the mechanical stirrer, chiller unit, temperature controller and Agilent data acquisition system. The valve on the drain line was opened, and the aqueous solution was collected in a waste bottle. The water bath was lowered using a mechanical jack to elevate the equilibrium cell out of the water bath. The cell was disconnected from the gas line and then opened and cleaned in preparation for the next experimental run. When the GC detector had reached 50 °C it was switched off.

5.5 Calculation of CH₄ and CO₂ in the replacement

The following equations and balances were utilized in this study. The real gas equation computed the number of moles of CH₄ trapped in the hydrate:

$$n_{CH_4}^{initial} = \frac{P_i V_i}{Z_i R T_i} - \frac{P_e V_e}{Z_e R T_e} \quad 5.8a$$

$$n_{CH_4}^{initial} = n_{CH_4, Fed} - n_{CH_4, Gas-phase(vessel)} \quad 5.8b$$

P, T, and V are the gas pressure, temperature, and volume inside the equilibrium cell. Subscripts "i" and "e" denote the initial and end of the methane hydrate formation, respectively. Z is the compressibility factor calculated by the Redlich-Kwong Equation of state. $n_{CH_4}^{initial}$ were moles of methane initial trapped in the hydrate, $n_{CH_4, Fed}$ are moles of methane fed to the reactor, $n_{CH_4, Gas-phase(vessel)}$ Moles of methane remains in the gas phase after hydrate formation. The volume occupied by the gas was determined using the difference in volume in the cell:

$$V_t = V_{cell} - V_{water} \quad 5.9$$

Where V_{cell} is the volume of the cell and V_{water} is the volume of the water introduced in the cell. In this study, it was assumed that the solubility of CH₄ in water was negligible (Pruteanu et al., 2017). In addition, the volume change during hydrate formation was negligible as the density of CH₄ hydrate is near unity (Gabbitto and Tsouri, 2010). The density of CH₄ hydrate can vary depending on the temperature and pressure conditions at which it is formed, however at the temperature and pressure conditions investigated in this work, the density of CH₄ hydrate is near unity and volume change during the hydrate formation could be negligible.

The mole fractions of CH₄ and CO₂ in the equilibrium cell and canister were analyzed by a gas cylinder and were marked as $y_{CH_4, vessel}$, $y_{CO_2, vessel}$, $y_{CH_4, canister}$ and $y_{CO_2, canister}$, respectively. The mole amounts of CH₄ and CO₂ in the reactor vessel and gas canister were named; $n_{CH_4, vessel}$, $n_{CO_2, vessel}$, $n_{CH_4, canister}$ and $n_{CO_2, canister}$, respectively.

$$n_{CH_4, vessel} = y_{CH_4, vessel} * n_{gas, vessel} \quad 5.10$$

$$n_{CH_4, canister} = y_{CH_4, canister} * n_{gas, canister} \quad 5.11$$

$$n_{CO_2, vessel} = y_{CO_2, vessel} * n_{gas, vessel} \quad 5.12$$

$$n_{CO_2, canister} = y_{CO_2, canister} * n_{gas, canister} \quad 5.13$$

where $n_{gas, canister}$ and $n_{gas, vessel}$ are the moles gas in the canister and the reactor vessel after the free gas in the reactor vessel was discharged.

Mass balance of each component for CH₄ and CO₂ in the hydrate phase and after the replacement were computed by the following equations:

$$n_{CH_4, hydrate}^{end} = n_{CH_4, hydrate}^{initial} - n_{CH_4, canister} - n_{CH_4, vessel} \quad 5.14$$

$$n_{CO_2, hydrate} = n_{CO_2, fed} - n_{CO_2, canister} - n_{CO_2, vessel} \quad 5.15$$

where $n_{CO_2, fed}$ and $n_{CO_2, hydrate}$ are the total mole of injected CO₂ and the mole of CO₂ hydrate after the replacement reaction; $n_{CH_4, hydrate}^{initial}$ and $n_{CH_4, hydrate}^{end}$ are the moles of CH₄ in the hydrate phase before and after the methane hydrate formation, respectively, calculated by the ideal gas equation.

The replacement reaction had a dual purpose: to sequester CO₂ by exchanging CH₄ with CO₂ in the hydrate to release CH₄ from the hydrate. Therefore, CH₄ replacement efficiency and CO₂ sequestration ratio were two of interest in this reaction.

Methane replacement efficiency is the ratio of the molar quantity of CH₄ in the gas phase to the initial molar quantity of CH₄ in the hydrate phase. The CO₂ sequestrated ratio is the molar quantity of consumed CO₂ in the gas phase to the initial molar quantity of CO₂ after gas mixture injection (Maria, 2018).

$$\% \text{ CH}_4 \text{ replaced from hydrate} = \frac{n_{\text{CH}_4, \text{Canister}}}{n_{\text{CH}_4, \text{Hydrate}}} \times 100 \quad 5.16$$

$$\% \text{ CO}_2 \text{ sequestrated in the hydrate} = \frac{n_{\text{CO}_2, \text{vessel}}}{n_{\text{CO}_2, \text{feed}}} \times 100 \quad 5.17$$

5.6 Results and Discussion

The results for hydrate dissociation data and CH₄-CO₂ replacement reaction without porous media are presented in this section. A total of ten experimental runs were performed to replace CH₄ contained in the hydrate with CO₂. In the first four runs the hydrate was formed with CH₄ gas and H₂O only, whereas, in the last six runs SDS and graphene were added to improve the CH₄ hydrate formation process. The replacement process was carried out with the following gaseous compositions: in runs one and two, pressurized CO₂ was utilized, for runs three and eight 90 mol% CO₂/10 mol% N₂ was used and for runs four to seven, 20 mol% CO₂/80 mol% N₂ was utilized. The replacement reactions in experimental runs nine and ten were performed with pressurized CO₂ and applied thermal stimulation.

5.6.1 Test systems - hydrate dissociation data

Hydrate dissociation data points for CO₂ and CH₄ were measured and compared with published data to validate the experimental apparatus, technique, and calibration of sensors. For the CO₂ system, four data points were measured at different initial pressures, and a good correlation was obtained, as shown in Figure 5.9. For the CH₄ system, seven data points were measured and presented in Figure 5.10. The excellent agreement demonstrates the reliability of the isochoric pressure-search method for use in this study.

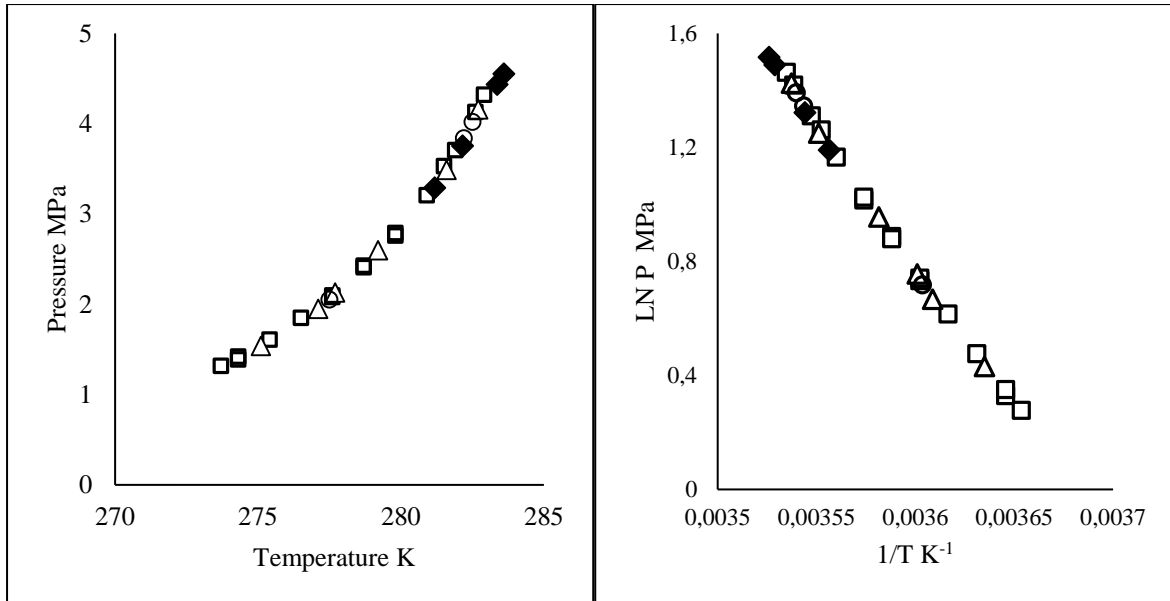


Figure 5.9: Hydrate dissociation points (LHS) and L.N. P vs 1/T correlation (RHS) for the CO₂ and water system: (◆) Exp, This work, (◻) Deaton and Frost, (1946); (△) Englezos and Hall, (1994); (○) Mohammadi et al., (2005).

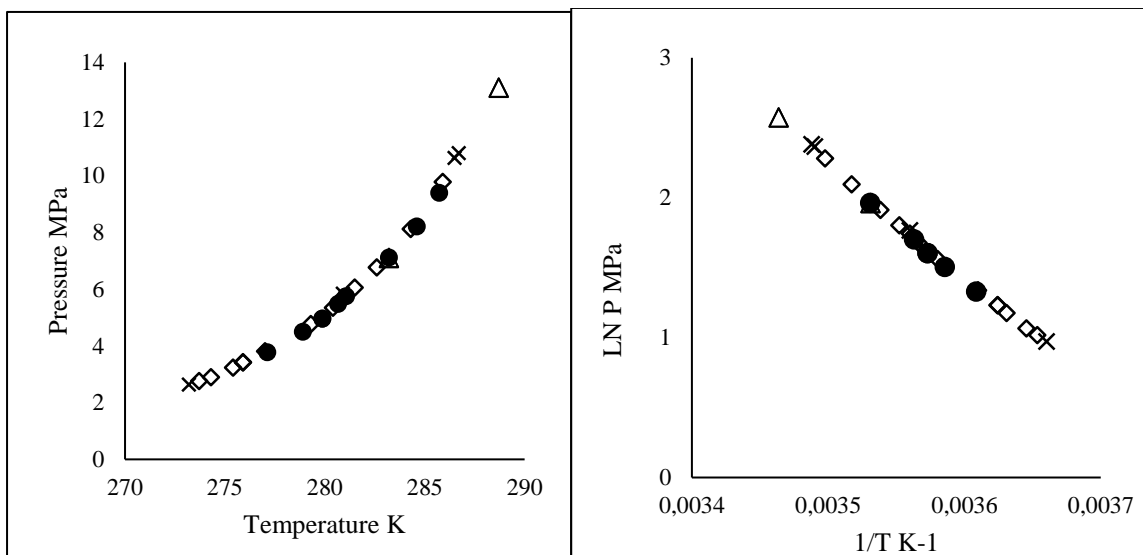


Figure 5.10: Hydrate dissociation points (LHS) and L.N. P vs 1/T (RHS) for the CH₄ and water system: (●) Exp, this work, (◆) Deaton and Frost, (1946); (×) Roberts, (1940); (△) Gallowing et al., (1970).

5.6.2 Replacement using pressurized CO₂

In this section, two experimental runs were performed with pressurized CO₂ and the other two with a CO₂/N₂ gas mixture to replace CH₄ from a CH₄-H₂O hydrate. Pure water was used to form the methane hydrate in this set of experimental runs. The summary of these experimental conditions and results is in Table 5.5 and 5.6.

Table 5.5: Methane- hydrate formation and replacement analysis with CO₂/N₂ gas mixtures.

Experimental run	1	2	3	4
Feed solution	water	water	water	water
Water fed (ml)	20	22	20	20
Temperature hydrate formation (K)	276.45	276.23	276.68	276.56
Pressure (MPa)	7.68	7.88	7.57	7.61
Pressure end of hydrate (MPa)	5.03	3.12	5.08	5.11
Duration of replacement (hour)	138.43	142.35	107.70	80.22
Stirring rate (rpm)	200	250	250	250
Moles CH ₄ charged	0.112	0.097	0.1059	0.1066
Methane balance				
(a) Initial CH ₄ moles in hydrate	0.0314	0.0460	0.0348	0.03513
(b) CH ₄ released from hydrate during replacement	0.0005	0.0006	0.0015	0.00133
% CH ₄ replacement efficiency	1.63	1.30	4.30	3.79

Combined Expanded uncertainties (k=2): $U(T) = \pm 0.09$ K, $U(P) = \pm 0.02$ MPa, $U(n_{CH_4}) = 0.005$

Table 5.5 summarizes the overall CH₄ hydrate formation and recovery efficiency, while Table 5.6 summarizes the replacement reaction process with CO₂ gas and CO₂/N₂ gas mixtures.

Considering experimental run 1 and 2 in Table 5.5 performed with pure water and gaseous CO₂, an average pressure drop of 4.0 MPa was obtained during the CH₄ hydrate formation. An average of 0.10 moles of CH₄ gas was charged into the replacement cell for the CH₄ hydrate formation, with approximately 0.04 moles consumed in hydrate formation. The moles of CH₄ gas remaining in the gas phase at the end of the hydrate formation phase were released into a canister analyzed. Figure 2 shows a picture of the methane hydrate formed in run 2 in the presence of only water.

Table 5.6: Carbon dioxide encapsulation in the replacement process with CO₂/N₂ gas mixtures.

	1	2	3	4
Feed for replacement	CO ₂	CO ₂	90CO ₂ mol%/ 10mol%N ₂	80N ₂ mol%/ 20mol%CO ₂
Replacement feed pressure (MPa)	6.69	3.56	4.12	6.28
Replacement reaction pressure (MPa)	5.39	3.49	3.64	6.15
Replacement temperature (K)	275.41	273.66	273.35	273.32
Carbon dioxide balance				
Moles Charged for replacement	0.2171	0.0534	0.0469	0.01048
Moles trapped in the hydrate	0.0781	0.0153	0.0049	0.00165
% CO ₂ sequestration ratio	35.99	28.74	10.57	15.75
Nitrogen balance				
Moles fed for replacement			0.0095	0.0768
Moles in the hydrate			0.0000	0.0000
% gas trapped in the hydrate			0.000	0.000

Combined Expanded uncertainties (k=2): $U(T) = \pm 0.09 \text{ K}$, $U(P) = \pm 0.02 \text{ MPa}$, $U(n_i) = 0.03$

As shown in Table 5.5, an average pressure decrease of 4.0 MPa was obtained during the CH₄ hydrate formation with optimal stirring. An average of 0.10 moles of CH₄ gas was charged into the replacement cell for the CH₄ hydrate formation, with approximately half of these moles consumed in hydrate formation. The moles of methane gas remaining in the gas phase at the end of the hydrate formation phase were purged. Figure 5.11 shows a picture of the methane hydrate formed in the presence of only water. The figure shows that the amount of CH₄ hydrate formed does not fill up the cell but formed where the blades of the stirrer are located and around the inner cell walls.



Figure 5.11: Picture of the cell showing CH₄ hydrate after formation without replacement reaction.

As shown in Table 5.5, the highest value of CH₄ replacement efficiency obtained with CO₂ gas was 1.63 %, while from Table 5.4 the highest carbon dioxide sequestration ratio was 35.99 % from run one. This study's amount of carbon dioxide sequestered was higher than the 18.74% reported by Hirohama et al. (1996), which was used as a benchmark. The high value of carbon dioxide sequestration could be attributed to the availability of free water during the replacement period, thus permitting carbon dioxide-water hydrate formation without any methane release. The CH₄ replacement efficiency obtained in this study was lower than the value reported by Hirohama et al., (1996) which was 21.04 %.

Due to slow reaction kinetics during the replacement step, the process could proceed for an average of 100 hours to maximize CH₄ recovery. By monitoring the molar ratios of the gas phase in the reaction vessel as the replacement reaction proceeded, it was observed that methane release and carbon dioxide capture was more prominent in the first 24 hours of the reaction this was due to the direct contact of the CH₄ hydrate with CO₂ replacement gas. This reaction trend is shown in Figure 5.12 for a CH₄-CO₂-H₂O system. Thus, the replacement was prominent at the beginning of the reaction and ceased after a certain period.

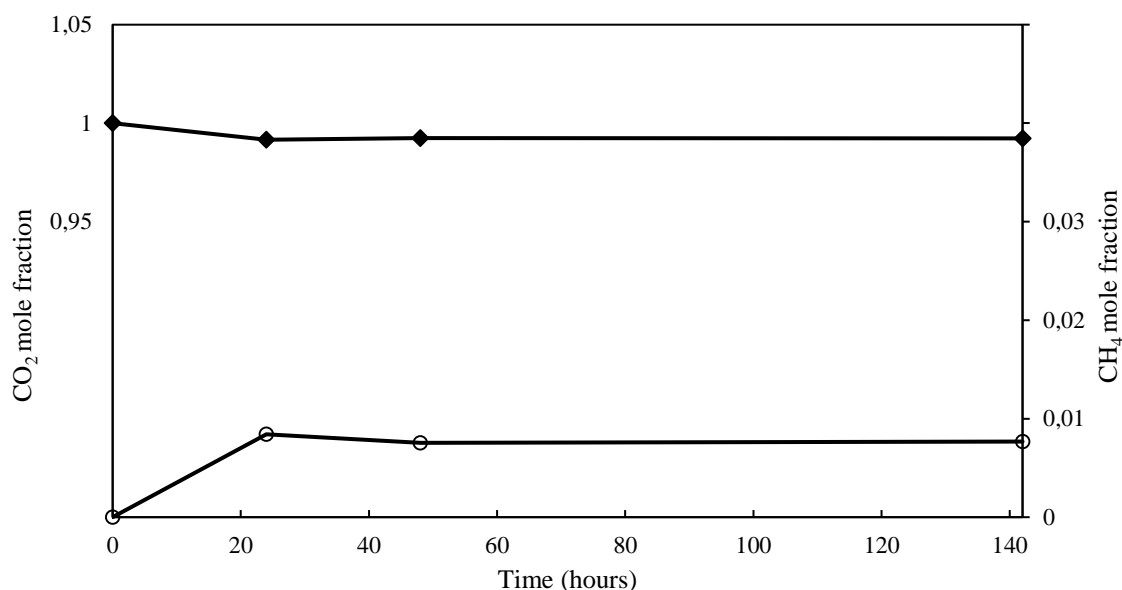


Figure 5.12: CH₄-CO₂ Replacement reaction profile for experimental run 2 (♦ CO₂, ○ CH₄) $U(n_i) = 0.005$.

The contents of the equilibrium cell were visually examined at the end of the replacement process as it dissociated due to a change in its equilibrium conditions. The picture is shown in Figure 5.13. It was noted that the surface or outer layer dissociated with a fizzing sound, whereas the middle part of the hydrate dissociated differently in a calmer manner. The fizzing was due to carbon dioxide, which was abundant in the outer layer because of CO₂ hydrate formation at the surface where there was free water. The contents within the hydrate were mainly composed of methane gas. Hence, different dissociation behaviors were observed for different hydrate layers.

5.6.3 Addition of a secondary gas in the replacement process

The use of a secondary gas in the replacement reaction was shown to yield favorable results Koh et al., (2016). Flue gas mainly contains CO₂ and N₂ gas mixture that has been proposed for replacement reactions. It was demonstrated through a spectral study that nitrogen gas attacks methane in the hydrate cages during the replacement reaction which leads to improved CH₄ recovery Park et al., (2006). Moreover, in the presence of a secondary gas the replacement reaction is enhanced by competitive adsorption and change in the hydrate stability of the hydrate structure. In competitive, the presence of N₂ increases the number gas molecules in the gas phase which can compete with CH₄ and CO₂ for adsorption sites in the hydrate lattice. Hence the competition for adsorption sites increases the rate of replacement reaction. With a change in hydrate stability, the presence of N₂ gas can modify the size and shape of the gas hydrate cage, making it more accommodating to CO₂ molecules. This effect can increase the

likely hood of CO₂ adsorption and hence the replacement of CH₄ (Matsui et al., 2020; Wang et al., 2021).



Figure 5.13: Photograph of the cell content showing the hydrate at the end of CH₄-CO₂ replacement reaction.

Thus, to improve the replacement efficiency of the reaction in this study, a secondary gas, nitrogen, was introduced. After over 24 hours of methane hydrate formation, the replacement gas mixture was introduced. Different mole ratios of the binary feed gas were utilized in the study to ascertain the effect of varying ratios of the gases on the replacement step. The experimental conditions and results are shown in Table 5.5 and 5.6, as experimental runs 3 and 4. In these experiments, the mole fraction of the secondary gas trapped in the hydrate was very low, with values of less than one percent. This means that replacement occurred between CH₄ and CO₂. This behavior follows the same observations reported by Ding et al., (2017), who stated that H₂, a secondary gas in that study, seemed not to be present in the final hydrate. Thus, it did not compete with CO₂ in the hydrate phase. Hence the presence of the N₂ gas which acted as a secondary gas served to improve the replacement of CH₄ by CO₂ though the microscopic level analysis of the reaction was not carried out in this study.

When using varying gas feed ratios, secondary gas had no noticeable effect on carbon dioxide sequestration. The addition of secondary gas was unfavorable for carbon sequestration as the gas phase is dilute, thus lowering carbon dioxide conversion to hydrate form, as seen from runs 3 and 4. A significant enhancement was apparent due to incorporating a secondary gas improving CH₄ release from the hydrate. This can be seen from the increase in the percentage of CH₄ realized from 1.63% in run one to 4.31% in run 4. The reaction profile of run 4 for CH₄ + 80 mol% N₂/20 mol% CO₂ gas mixture + H₂O profile is shown in Figure 5.14.

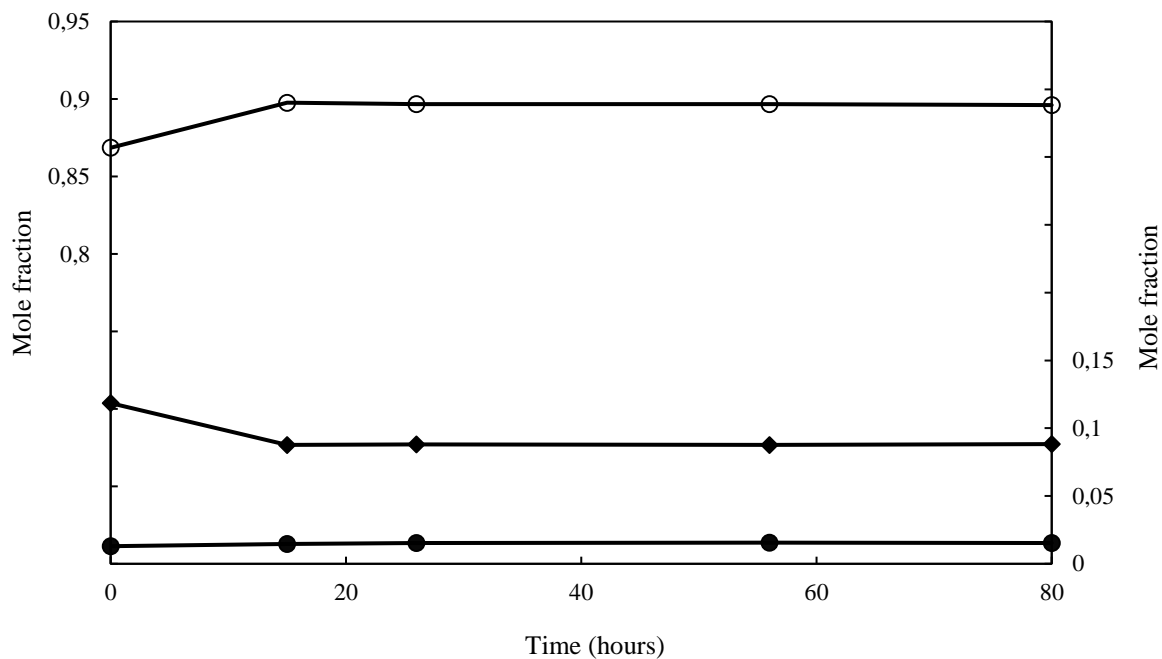


Figure 5.14: CH₄ + 80mol% N₂/20mol% CO₂ gas mixture + H₂O replacement reaction profile for experimental run 4 (◆ CO₂, ○ N₂, ● CH₄) ($U(n_i) = 0.03$).

The molar fraction of methane gas in the gas phase increased slightly as the replacement reaction proceeded. Molar fractions of CO₂ and N₂ increased slightly at the beginning of the replacement reaction due to rapid reaction at the beginning of the replacement.

5.6.4 Addition of Nanoplatelets

To improve hydrate formation and gas storage, graphene nanoplatelets with sodium dodecyl sulfate (SDS) were utilized in the methane hydrate formation process. The presence of nanoparticles or nanoplatelets in the CH₄-CO₂ can increase the replacement reaction through catalysis, increased adsorption, improved dispersion and increased adsorption capacity. They can also act as surfactants, reducing the surface tension between water and gas hydrates, hence

facilitating the replacement reaction. In a study of silica nanoparticles utilization for CH₄-CO₂ replacement in simulated gas hydrate reservoirs (Zhou et al., (2016a), it was found that silica nanoparticles significantly increased the rate of methane replacement and resulted in higher methane recovery rates. This was attributed to the ability of nanoparticles to reduce the surface tension between water and gas hydrates, thus facilitating the replacement reaction. In an investigation of the use of platinum nanoparticles as a catalyst for the replacement of methane with carbon dioxide in gas hydrates, it was observed that platinum nanoparticles significantly increased the rate of the replacement reaction and reduced the energy required to extract methane from gas hydrates. This was caused by the ability of platinum nanoparticles to dissociate carbon dioxide and facilitate its incorporation into the gas hydrate structure (Lee et al., 2006). Zhou et al., (2016b) investigated the use of copper nanoparticles to enhance the replacement of methane with carbon dioxide in gas hydrates. It was found that the copper nanoparticles significantly increased the rate of the replacement reaction and resulted in higher methane recovery rates due to the ability of copper nanoparticles to dissociate carbon dioxide and promote the formation of hydrate-like structures that can trap methane.

Six experimental runs were performed (run 5-10) in this study in the presence of graphene nanoplatelets and tabulated in Tables 5.7 and 5.8.

Table 5.7: Methane- hydrate formation with graphene nanoplatelets and SDS balance.

Reaction	5	6	7	8	9	10
Feed solution	0.05 wt.% SDS+0.2 wt.% GPN			0.05 wt.% SDS + 0.5 wt.% GPN		
Water fed (ml)	20	20	20	20	20	20
Temperature (hydrate formation) (K)	276.15	276.42	276.58	276.9	276.7	27.63
Pressure (MPa)	7.55	7.56	7.58	7.68	8.06	7.49
Pressure end of hydrate (MPa)	3.21	3.10	3.10	3.18	3.14	3.10
Duration of replacement (hour)	50.03	94.90	45.37	99.25	98.78	100.38
Stirring rate (rpm)	250	250	250	250	250	250
Moles CH ₄ charged	0.1056	0.1058	0.1062	0.1068	0.1124	0.0983
Methane balance						
(a) Initial CH ₄ moles in hydrate	0.0608	0.0625	0.0627	0.0623	0.0687	0.0550
(b) CH ₄ released from hydrate during replacement	0.0068	0.0106	0.0098	0.0048	0.0149	0.0158
% CH ₄ replacement efficiency	11.13	17.04	15.63	7.71	21.69	28.77

Combined Expanded uncertainties (k=2): $U(T) = \pm 0.09 K$, $U(P) = \pm 0.02 MPa$, $U(n_{iCH_4}) = 0.005$

Table 5.8: Carbon dioxide encapsulation in the replacement process with CO₂, and CO₂/N₂ gas mixtures.

Reaction	5	6	7	8	9	10
Feed for replacement	80 mol% N ₂ /20 mol% CO ₂			90 mol% CO ₂ / 10 mol% N ₂	CO ₂	
Replacement feed pressure (MPa)	5.18	4.77	4.46	4.43	4.58	5.66
Replacement reaction pressure (MPa)	5.20	5.34	4.86	4.01	3.81	4.91
Replacement temperature (K)	274.79	274.77	269.45	273.34	275.21	275.9
Carbon dioxide balance						
Moles charged for replacement	0.0076	0.0058	0.0063	0.0485	0.0717	0.0714
Moles trapped in the hydrate	0.0020	0.0018	0.0021	0.0232	0.0384	0.0407
% CO ₂ sequestration ratio	26.95	31.90	33.33	47.84	53.52	57.03
Nitrogen balance						
Moles fed for replacement	0.0609	0.0564	0.0545	0.0103		
Moles in the hydrate	0.0002	0.0006	0.0006	0.0003		
% gas trapped	0.40	1.04	1.12	2.69		

Combined Expanded uncertainties (k=2): $U(T) = \pm 0.09$ K, $U(P) = \pm 0.02$ MPa, $U(n_i) = 0.03$

Table 5.7 and Table 5.8 shows that the addition of secondary gas in this system improved the CH₄ replacement efficiency and the CO₂ sequestration ratio with run 6 producing. CH₄ replacement efficiency value of 17.04%, and 47.84% CO₂ sequestered. Thus, the presence of secondary gas in a CH₄-nanoparticle + SDS solution improves the replacement efficiency and CO₂ sequestration. A high amount of CO₂ (more than 83.7%) in the gas mixtures was observed to result in high values of CO₂ being stored in the hydrate.

The addition of the two additives (graphene and SDS) enhanced the hydrate formation process and the replacement thereof. Figure 5.15 demonstrates a methane hydrate formed from 0.05 wt.% SDS + 0.5 wt.% graphene nanoplatelets. From visual comparisons to Figure 5.11, which was formed in pure water, it is evident that adding these additives enhanced methane hydrate formation. Also, considering the number of moles reported in Table 5.7, an average of 0.06 moles of CH₄ were converted to the hydrate. Whereas, as seen in Table 5.5, in the absence of additives, an average of 0.035 moles of CH₄ were converted to the hydrate.

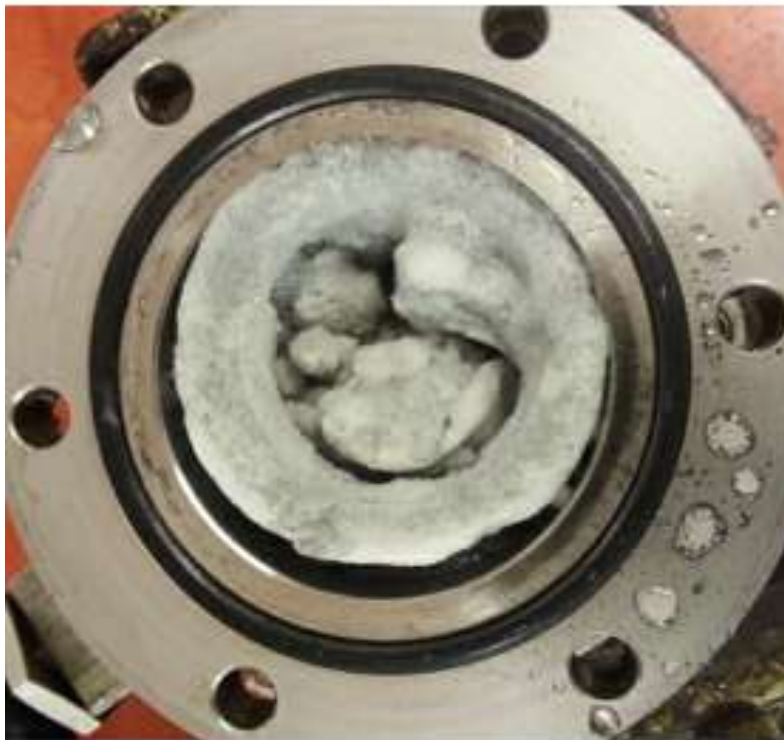


Figure 5.15: Picture of the cell contents showing the methane hydrate - 0.05wt.% SDS + 0.5wt.% graphene nanoplatelets solution hydrate.

Figure 5.16 shows the dissociation images of 0.05 wt.% SDS + 0.5 wt.% graphene nanoplatelets-CH₄ hydrate over 12 mins after opening the cell. It was deduced that the hydrate

remained intact for approximately 9, with dissociation occurring after 10 minutes. There was an improved yield for CH₄ replacement efficiency and carbon dioxide sequestration ratio in this set of experiments. The highest methane replacement efficiency was obtained with pressurized CO₂, sequestered carbon dioxide. Using a lower concentration of graphene nanoparticles yielded lower replacement efficiency and carbon dioxide sequestration. This is illustrated in runs 5 and 7, where 0.2 and 0.5 wt.% graphene was used, respectively as shown in Table 5.8. This reduction in the graphene concentration decreased CH₄ replacement efficiency from 17.04% to 11.13%, while the percentage of CO₂ sequestered dropped from 31.90% to 26.95%. This demonstrates the dependence of the reaction on the concentration of the additives in the solution.

The runs 7 to 9 presented in Tables 5.7 and 5.8 were synthesized to obtain a composition similar to flue gas streams. As seen in Tables 5.7 and 5.8, in run 6, 17.04% CH₄ replacement was obtained with a 31.90% carbon sequestration ratio. In run 7, 15.63% CH₄ replacement was obtained with 19.04% CO₂ sequestration reported. Satisfactory results were obtained with both runs, the difference being the time durations in the two runs. Run 7 occurred in half the time as for reaction run 6. Increasing the amount of CO₂ to 90 mol% in the replacement gas mixture only increased the amount of CO₂ sequestered to 47.84% while lowering the amount of CH₄ released to 7.71%.



Figure 5.16: Pictures of different views of the hydrate formed with 0.05 wt.% SDS + 0.5wt.% graphene nanoplatelets over 12 minutes time period in an open environment.

Figure 5.17 demonstrates a replacement profile for a CH_4 -0.05wt.%SDS + 0.05wt.% Graphene nanoplatelets hydrate system and 80mol% N_2 /20mol% CO_2 utilized in replacement. Figure 5.17 shows a sharp increase in CH_4 gas in the gas phase in the first six hours of the replacement reaction. After that, a gradual increment is observable in the next 48 hours of the reaction. This is in line with earlier observations where the reaction is rapid at the beginning and slows down to a final state as time progresses. The amount of carbon dioxide in the gas phase decreased gradually throughout the reaction, with nitrogen remaining constant after the initial pressure drop.

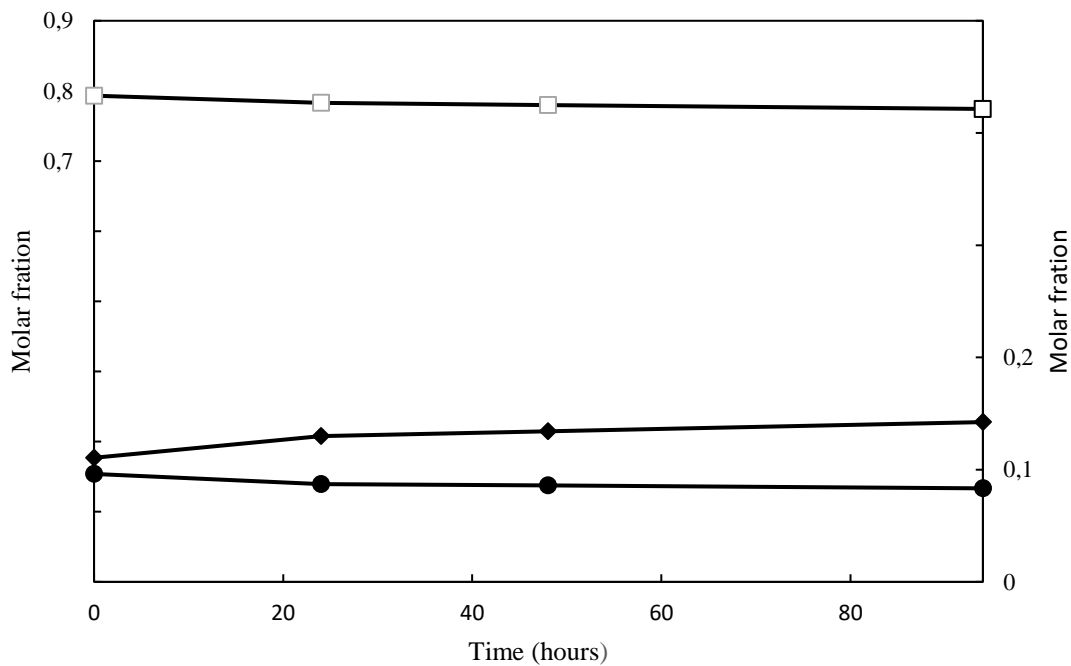


Figure 5.17: CH_4 + 80mol% N_2 /20mol% CO_2 + 0.05wt.% SDS+0.5wt.% graphene nanoplatelets replacement reaction profile for experimental run 7 (\blacklozenge CH_4 , \bullet CO_2 , \square N_2) ($U(n_i) = 0.03$).

The reaction profile for a system with a high 90 % CO_2 molar ratio and low 10 % N_2 molar ratio with 0.05wt % and 0.5wt % graphene nanoplatelets is shown in Figure 5.18. The CH_4 molar concentration increased gradually throughout the experiment to very minute proportions. A slight drop in the molar fraction of nitrogen was observed, which remained relatively constant throughout the experiment which might have been caused by the incorporation of the gas in the gas hydrate cages. The CO_2 molar ratio decreased as the reaction progressed as it was being absorbed into the hydrate cavities.

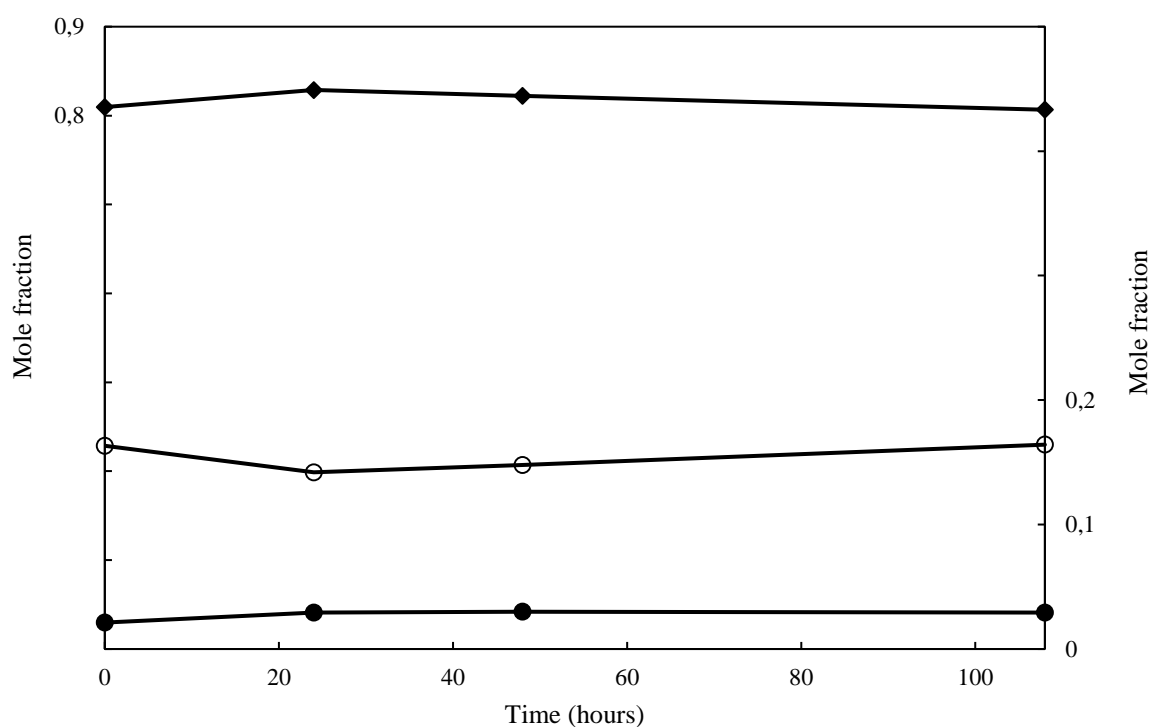


Figure 5.18: CH₄ + 90mol% CO₂/10mol% N₂ + 0.05wt.% SDS + 0.05wt.% graphene nanoplatelets replacement reaction profile for experimental run 8 (♦ CO₂, ● CH₄, ○ N₂). ($U(n_i) = 0.03$).

The pressure-temperature profiles for two replacement reactions are shown in Figures 5.19 and 5.20. The CH₄ hydrate formation stage was the first portion demarcated by a pressure and temperature drop. Both reactions form at the same temperature of 275 K, although different temperatures were utilized when feeding the CH₄ gas. This process takes an average of 1000 minutes for both experimental runs, as shown below. The pressure drop due to hydrate formation was different for the two runs due to the different feed for the CH₄ hydrate formation stage. For experimental run 6 the temperature dropped by 1.5 K just before the addition of the replacement gas. There was a dip in the pressure trend due to the release of methane gas in the gas phase for both runs. After adding the replacement gas mixture, the two experimental runs proceeded with different reaction pressure trends. Pressure behaviour was affected by two different elements, namely, CH₄ hydrate dissociation and CO₂ inclusion into the hydrate's clathrate. Experimental run 5 proceeded with a gradual pressure drop attributed to CO₂ inclusion in the hydrate, which exceeds the rate of CH₄ gas release.

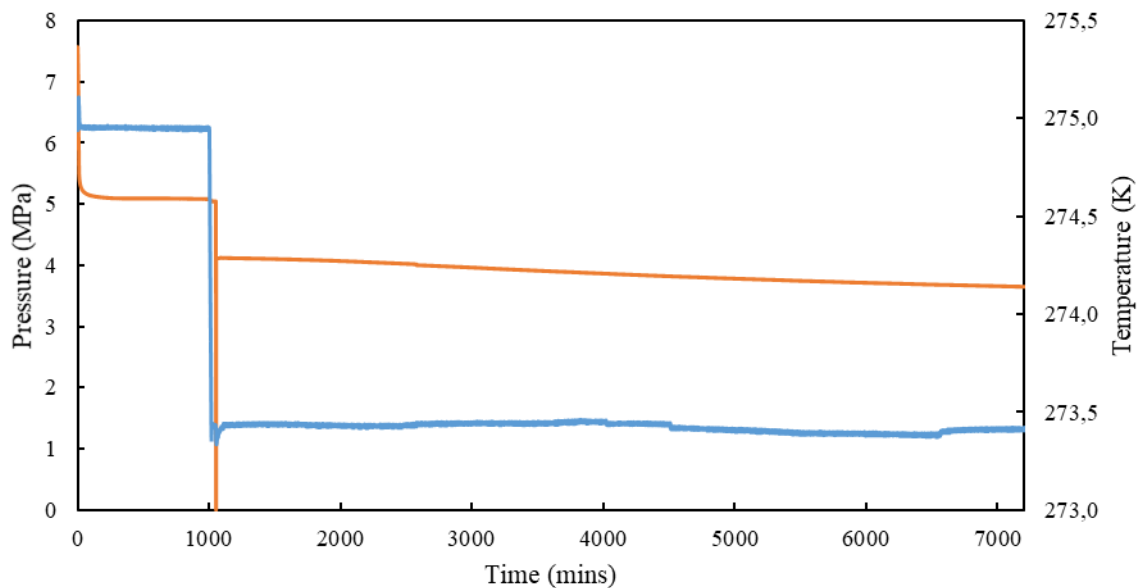


Figure 5.19: Temperature-pressure against time for run 5, carried out at 7.6 MPa and 275 K (-) pressure, (-) temperature.

Replacement reaction run 9 increased pressure due to a high percentage CH_4 release as the reaction occurred. Replacement periods for the two experimental runs were different due to the rate of CH_4 being released in the two reactions. The replacement period for run 5 was double that of run 9.

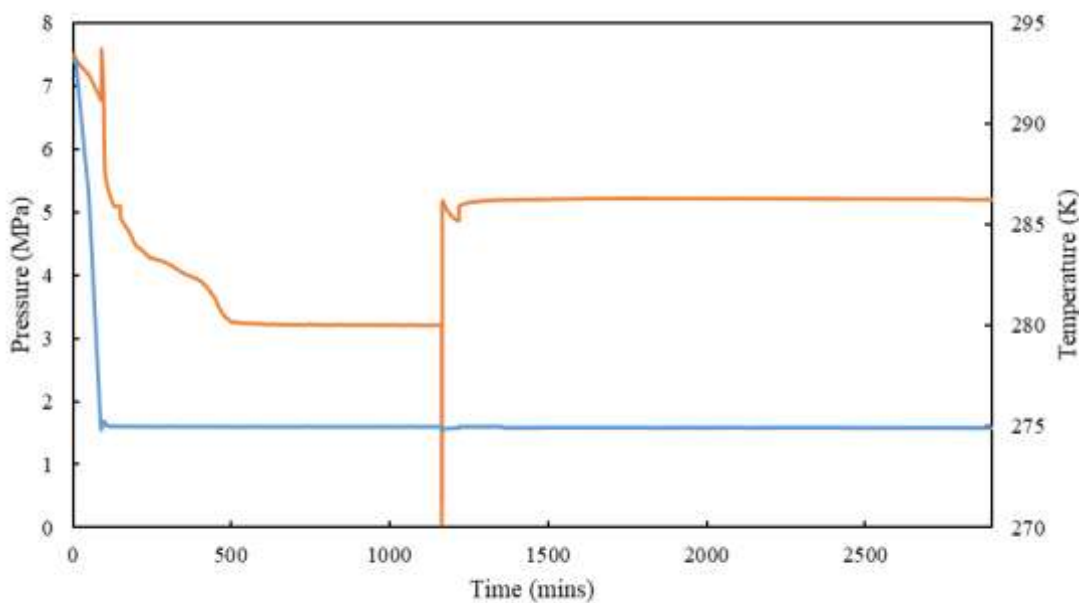


Figure 5.20: Temperature-Pressure against time for experimental run 9, 0.05 wt.% SDS + 0.5wt.% graphene at 7.5MPa and 275 K (-) pressure, (-) temperature.

5.6.5 Thermal stimulation

In experiments 9 and 10, the temperature of the replacement vessel was increased at constant pressure soon after adding CO₂ gas into the vessel temperature to affect a higher release of methane from the hydrate. This process has been applied to CH₄-CO₂ replacement reactions to improve the diffusion of CO₂ in the hydrate matrix while allowing CH₄ to be released. As can be seen from Tables 5.7 and 5.8, the highest amount of CH₄ released and CO₂ sequestered were 28.77% and 57.03%, respectively. The temperature increase was within the methane hydrate region to ensure that the hydrate core remained intact. The high CH₄ release was due to thermal energy exciting CH₄, thus enabling the gas to break away from the hydrate structure. The release of more CH₄ created space for more CO₂ to occupy the vacant cages in the hydrate lattice. These findings agree with numerous studies by Wang et al., (2021). The most improvement in CH₄ release effected by the application of this method was 21.06 to 63.13 % by Zhang et al., (2017). Figure 5.21 summarizes the main outcomes of this part of this study. It can be seen from the results of experimental runs 5 to 10 which are shown in Figure 7, that the addition of graphene nanoplatelets and SDS improved the CH₄ hydrate formation as well as the CH₄ replacement efficiency. While for CO₂ sequestration, the application of thermal stimulation was more effective than adding secondary gas in the CH₄-CO₂ replacement reaction as can be seen from comparing experimental runs 8 to 10 to runs.

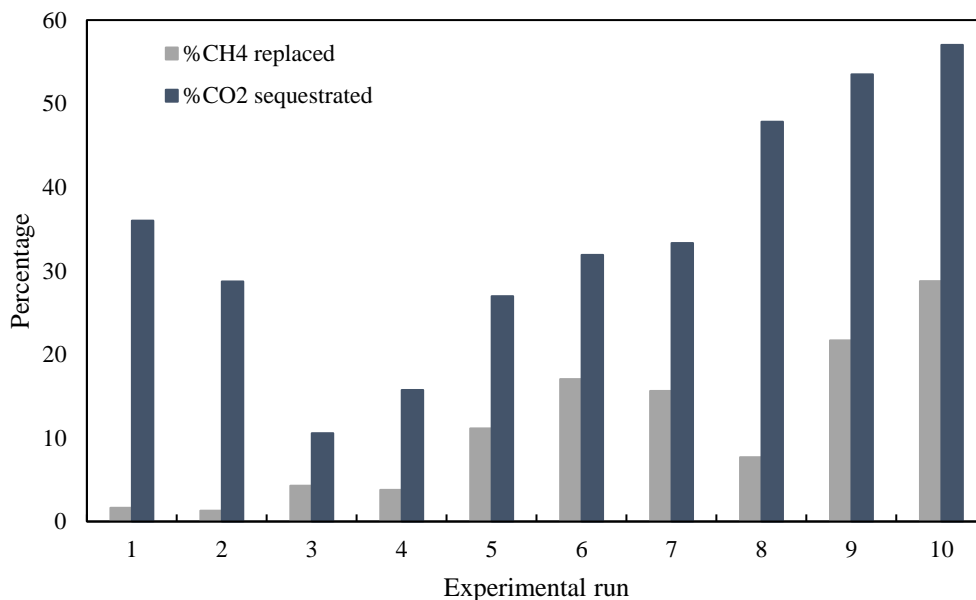


Figure 5.21: Comparison of the percentages of CO₂ sequestered and CH₄ replaced in all the runs carried out in the study.

* Liquid solution for CH₄ hydrate formation: water - for experimental runs 1 to 4; a solution of 0.05 wt.% SDS + 0.2 wt.% graphene solution - for experimental run 5; 0.05 wt.% SDS + 0.5 wt.% graphene solution - for experimental runs 6 to 10. Gas feed for replacement; for experimental runs 1 and 2 - CO₂ gas, for experimental run 3 - 90 mol% CO₂ + 10mol% N₂, for experimental runs 4 to 7 - 80 mol% N₂ + 20 mol% CO₂, experimental run 8 - 10 mol% N₂ + 90 mol% CO₂, and experimental runs 9 to 10 - pressurised CO₂ gas + thermal stimulation.

5.7 Summary

The experimental results in this section show that the addition of graphene nanoparticles to the solution had a significant effect on the CH₄ hydrate formation. This outcome is ideal for CH₄ hydrate utilization in energy storage as 44% increment in gas storage was observed. In CO₂ sequestration, using nitrogen as a secondary gas reduced CO₂ sequestration ratio though overall, a higher sequestration ratio of 47.84% was achieved with 0.5 wt.% graphene + 0.05 wt.% SDS. The highest carbon dioxide sequestration ratio was obtained with a solution pressurized CO₂, corresponding to the highest value of 57.03% of CH₄ release when applied thermal stimulation. It also resulted in the highest amount of CH₄ released which was 28.77%. This study has extended the understanding of CH₄ replacement and CO₂ sequestration in CH₄ hydrates in the application of thermal stimulation and in the presence of secondary gas. Thermal stimulation is a promising method for CH₄ production and CO₂ sequestration. Studying the effects of these additives and parameters in natural methane hydrate beds would be essential.

Chapter 6: CH₄- replacement with CO₂ in CH₄-silica sand hydrates

6 Introduction

This chapter assesses the viability of capturing and substituting carbon dioxide into a methane hydrate from a laboratory-scale experimental measurement in the presence of porous media. The first part of the chapter reports equipment description, including the design specification of the equilibrium cell. Calibrations of the pressure and temperature sensors and the experimental procedure follow. The final section presents the experimental results for the silica hydrate dissociation and results for the CH₄-CO₂ replacement reactions in CH₄-silica sand hydrate. To improve the CH₄-CO₂ replacement process, 0.5 wt.% GPN + 0.05 wt.% SDS was added to the silica sand. This additive was based on the results of the kinetic measurements, as using this additive, the best kinetic results were achieved and this additive has not been studied in this field of study. Moreover, N₂ gas was incorporated in the replacement mixture gas to produce 85 mol% CO₂/15 mol% N₂ and thermal stimulation was applied, with their effects on replacement monitored and assessed.

6.1 Equipment description

The equipment utilized in the study is shown in Figure 6.1. This apparatus was designed and assembled specifically for this study in the Thermodynamics Research Unit (TRU) as part of this project. This equipment design was adapted from the designs of the apparatus presented by Yuan et al., (2013), Zhou et al., (2015), Zhang et al., (2017), and Pan et al., (2020) as reviewed in Chapter 3. The main components of the equipment setup were:

- High-pressure stainless-steel reactor with approximately 300 cm³ internal volume
- Shimadzu 2014 Gas Chromatograph
- Keysight DAQ970A Data logging system
- Edwards Vacuum Pump
- PolyScience flow through chillers model KR-80A
- Grant TX200 digital temperature controller
- Swagelok (KPB Series) Pressure regulator and VAF_G1_01L Gas flowmeter
- WIKA model A-10 pressure transducer measuring of 0-15 MPa
- TR40 RTD temperature sensor
- 260D ISCO D-Series syringe pump
- 699 ml gas canister and 10 000 ml gas mixing canister

Equipment Design

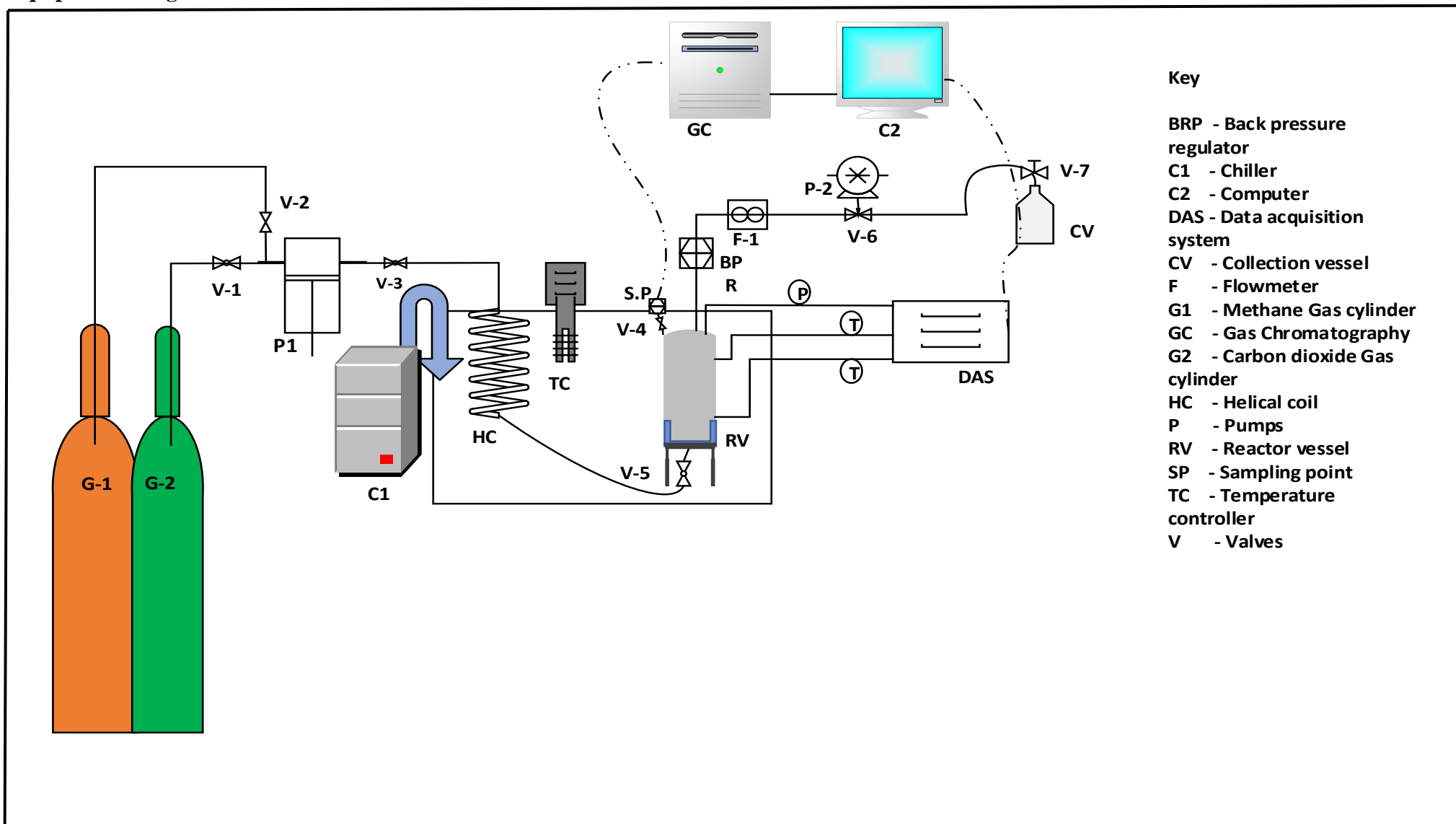


Figure 6.1: Equipment setup designed for use in this study for the CH₄ replacement CO₂ in the CH₄-silica hydrate.

6.1.1 Equilibrium cell

The equilibrium cell utilized in the study was constructed from stainless steel 316. The thermocouples for temperature measurement were attached at the side equilibrium cell thus, slight temperature changes needed to be detected as the hydrate formation reaction is exothermic. The design dimensions and cell outlay are shown in Figure G.1.

The cell had a working volume of 300 cm³, an internal height of 15 cm, and an internal diameter of 5 cm. Two 5 mm thick flanges were fastened with six bolts at the top and the bottom of the cell. An O-ring was positioned in a 2 mm wide groove on the bottom and top of the cell wall to ensure an airtight seal between the flanges and the cell. The bottom flange had a sparger welded to its centre. This served as an inlet for gas injected into the cell. The pictorial view of the cell is shown in Figure 6.2. The maximum allowable pressure was 10 MPa due to the limitation of the pressure transducer. The cell thickness design calculations are provided in Appendix G.1.

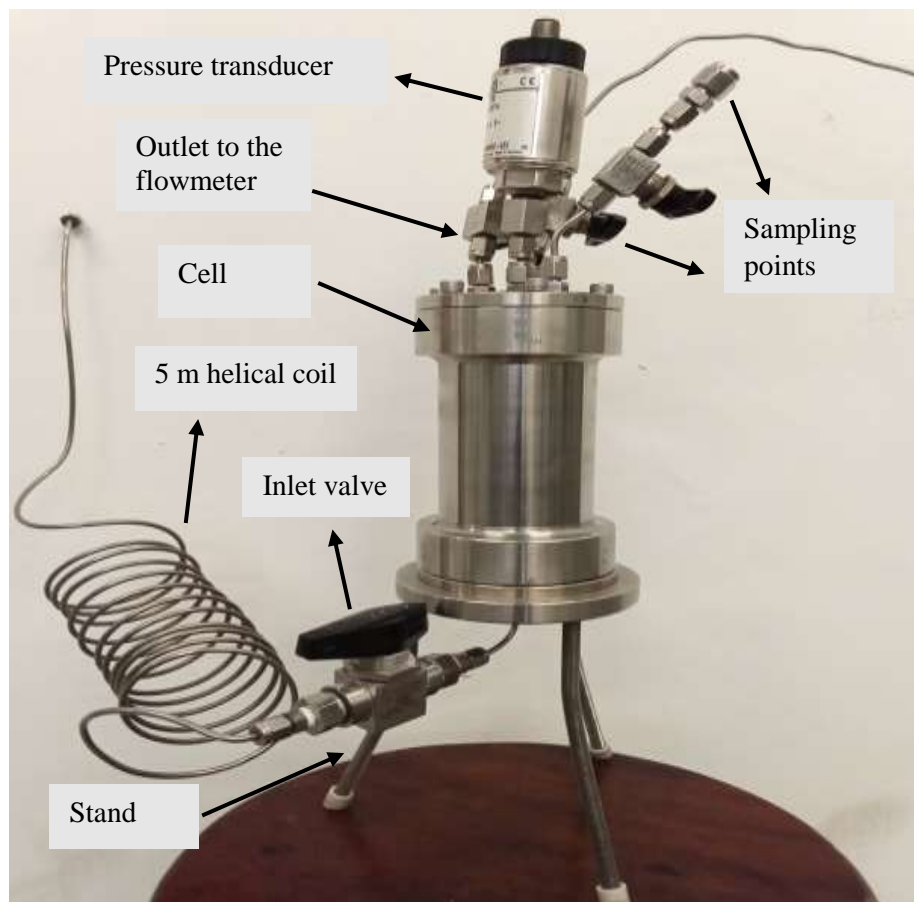


Figure 6.2: Pictorial view of the replacement cell with some of its auxiliary components.

The cell was placed on a three-legged stand to support and balance inside the water bath. A teflon material was placed at the bottom tip of the stand to reduce friction between the stand and the water bath. A helical coil made from a 5 m- $\frac{1}{4}$ stainless steel line was fixed before the cell inlet and placed in the same water bath as the cell to regulate the temperature of the incoming gas before it entered the cell. The gas flowed into the cell through a sparger fitted to the bottom and through the connecting line at the top of the cell.

6.1.2 Sparger design

The cell was designed to operate without any agitation device. The porous media and the sparger increased contact between the former gas and water, thus enhancing gas hydrate formation. A sparger was utilized for bubbling the gas through the porous media. The design specifications of the sparger are shown in Figure G.2. The sparger was positioned at the bottom flange's center and welded to the flange to produce an airtight seal. It was cylindrical with a height of 5 mm and a diameter of 20 mm. A tiny apertures of 0.1 mm diameter were drilled into the groove on the side of the sparger.

The groove was necessary in the design to prevent clogging of the sparger holes by the porous media or the resultant hydrate. Thus, the head of the sparger is a hollow space with holes on the side to release the gas. The photograph of the sparger is shown in Figure 6.3a with the operation of this unit displayed in Figure 6.3c.

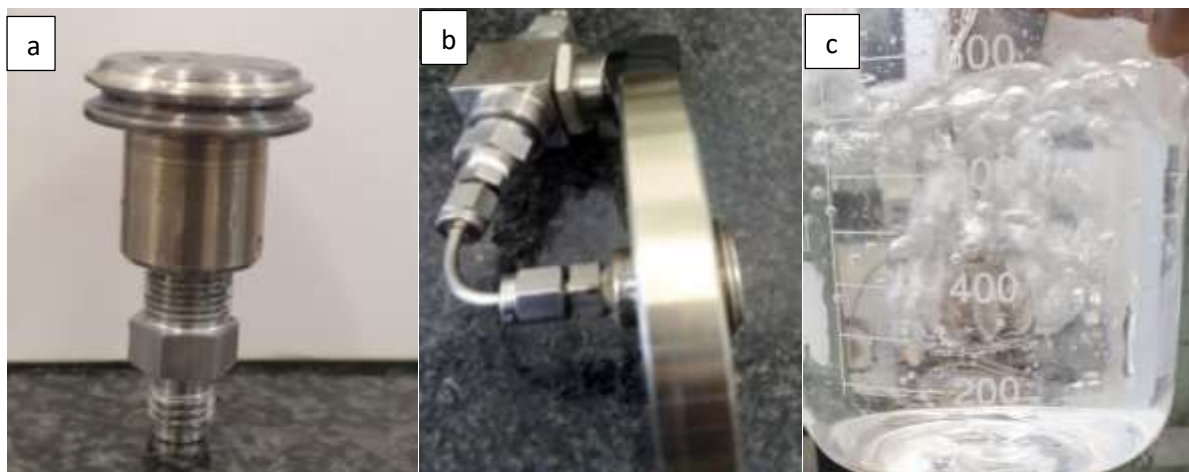


Figure 6.3: Pictorial view of a) sparger, b) bottom flange with the sparger c) testing of sparger in a beaker.

The sparger was fitted with a $\frac{1}{4}$ inch fitting which could be connected with a $\frac{1}{4}$ nut to the gas feed line, as shown in Figure 6.3b. A valve was installed close to the sparger inlet to prevent

backflow of the cell contents. Figure 6.3c shows gas bubbling through water in a beaker from the sparger in a 500 ml beaker.

6.1.3 Sampling points

Two sampling points were utilized for gas sampling. These gases were injected into the GC for analysis. Since there was no stirring in the vessel, it was imperative to have two sampling points to check for the possibility of gas pockets. As shown in Figure G.1, a valve allowed the gas to enter a chamber covered with a septum on the outlet port. Before a sample could be taken, the valve was opened to allow high-pressure gas into the chamber sealed by the septum, after which a 250 μ ml syringe took a sample. Approximately five repeatable samples were taken then an average was used in the analysis. Samples were also obtained from the gas canister using the same method. The GC utilized to obtain gas peak areas was a Shimadzu 2014 described in Chapter 5.

6.1.4 Gas vessels

A 699 cm^3 gas canister was used to collect the residual gas in the gas phase before adding CO_2 for replacements and was also used at the end of the replacement period. It had a stirring system to ensure the mixing of its contents and could withstand a pressure of up to 8 MPa. This vessel was utilized for making gas mixtures, as utilized in Chapter 5.

A 10 000 cm^3 stainless steel vessel was used to prepare the replacement reaction's gas mixtures. The procedure flowed in gas preparations as outlined in section 5.4.4 in Chapter 5. The vessel had an inlet port and an outlet port with a valve at which port to control the gas flow.

6.1.5 Keysight DAQ970A data logging system

A Bench Vue data acquisition control DAQ973A system with four-channel simultaneous digitizing with DAQ909A digitizer module was utilized for data logging. It has a time domain and frequency (FFT) Domain Chart Gadget with various waveform measurement operations the in-time domain chart. A DAQM901A multiplexer (2/4-wire) module and 20 channels with the ability to provide extensive data trace, measurement logging capabilities, and automation test flow. Data can be exported to MATLAB, or Microsoft Excel or Microsoft Word.

The DAQ970A data acquisition systems had high-quality switching, and an advanced six-and-half digit DMM built in that allows for accurate measurements. The built-in internal module calibration reduces thermal voltage offset errors. The key features are a nine switch, RF, and control plug-in modules, including a new 4-channel simultaneous sampling digitizer and up to

450 channel/s scan rate as well as up to 120 channels per system with a capacity of up to one million points scanning memory. It measures and converts 14 different input signals: temperature with the thermocouple, RTDs, and thermistor; dc/ac volts; 2- and 4-wire resistance; frequency and period; dc/AC, diode, and capacitance; direct strain and bridge strain. It was configured to measure pressure as well in this study.

6.1.6 Edwards Vacuum pump

An RV12 rotary vane vacuum pump was used to evacuate the system before and during the replacement reaction. The vacuum was utilized to remove air and any impurities in the system before the reaction

6.1.7 Pressure regulator

A spring-loaded back pressure regulator was utilized to ensure constant pressure flow to the gas flowmeter during the gas exchange phase of the replacement reaction. It is a medium to high-pressure Swagelok (KPB Series) piston sensing back pressure regulator. It is lightweight, compact, and mainly applied in gas and liquid applications. The body is made of stainless steel 316 SS with a nylon knob handle and 316 SS insert. It has a ¼" female NPT. Connection and a maximum working pressure of 27.5 MPa.

6.1.8 Gas flowmeter

A Swagelok gas flow meter was installed for metering gas flow during the replacement phase of the reaction. The model of the flow meter acquired was VAF_G1_01L_1-0. It had a measuring range of between 0.011 to 0.11 L/min. Its gasket was made of a fluorocarbon (FKM) standard.

6.1.9 Temperature sensors

Two TR40 cable RTD sensors (MI-cable) were installed on opposite sides of the reactor vessel to measure the temperature. The sensor was designed with lead wires with a temperature range of -200 to 600 °C. Its insertion length was 150 mm, i.e., the sensor's part that detected temperature changes. The probe diameter was 3 mm, the probe material was stainless steel 316 SS and the cable length was 3000 mm. The probe design was straight, with stripped leads at the cable end. The readings from the second probe were not used as the probe got damaged, resulting in inconsistent readings.

6.1.10 Pressure transducer

A WIKA model A-10 pressure transducer was utilized for pressure measurement with a measuring range of 0-10 MPa. The wetted parts were made of 316l, with a permissible working temperature of 0 – 80 °C and copper sealing connector. It has a specified accuracy of 0.5% BFSL. The current output was 4-20 mA, and the power supply was 8-30 V DC.

6.1.11 Temperature Controller

The bath temperature was controlled by a TXF200 Grant precision immersion circulator which operated over a temperature range of -15 to 200 °C with a temperature certainty of ± 0.05 °C and a maximum pressure rating of 530 mbar. It was designed to be operated with various liquids such as silicone fluid and 50% water, 50 % ethylene glycol (antifreeze) in a tank with a capacity of 5 to 38 liters. The front panel is a large bright full-color display with an option of five languages. The controller was secured on stainless steel bath through the hole bridge plate and aligned using the location threads. It had safety warnings on liquid levels and temperature ranges. It had a powerful integral pump for external fluid circulation.

A Thermo fisher scientific EK90 immersion cooler was employed to cool the water bath. It could not control the bath temperature and did not have a temperature display thus, it worked alongside the Grant precision immersion circulator. It could decrease the temperature of the liquid to -90 °C, though in the current set up it was not possible to reach this low temperature.

6.1.12 Water bath

The water bath housing the reactor cell, chiller, and the cooling coil was provided supplied by Laboquip. It was made from stainless steel coated with proofing paint. It had external dimensions of 250mm by 400 mm by 300 mm deep. The water bath was filled with 50% water and 50% ethylene glycol. The reactor cell was immersed in the water bath to ensure constant temperature during the reaction.

6.1.13 ISCO Syringe pump

The pump utilized in this study was 260D ISCO D-Series syringe pump. This pump was designed specifically for refilling under high pressure and pressure programming operations. Its maximum operating pressure is 51.7 MPa, and a flow rate range from sub-microliter to 100 mL/min. The pump was operated at either a fixed flow rate or set pressure. It operates on the same principle as that of a syringe, i.e., refilling and emptying. It had a temperature control jacket around its main chamber, which regulated the temperature of the fluid. The standard

material for cylinders, pistons, and caps was austenitic stainless steel with outstanding strength and corrosion resistance.

6.2 Materials

The materials presented in section 5.2 were utilized in these measurements with the addition of silica sand. The properties of the silica utilized are summarized in Table G.2. The parameters were specified by the supplier, Macherey Nagel. The sand was chosen based on its particle size range to represent the natural silica sand found in sea beds and on sea shore. Moreover, the sand used had all the necessary parameter needed to be able to compute the necessary calculations essential in the study.

6.3 Experimental methods

6.3.1 Calibrations of sensors

The procedure and standard equipment utilized in calibrating temperature and pressure sensors is detailed in section 4.3 in Chapter 4. In this section the temperature and pressure calibration graphs are presented.

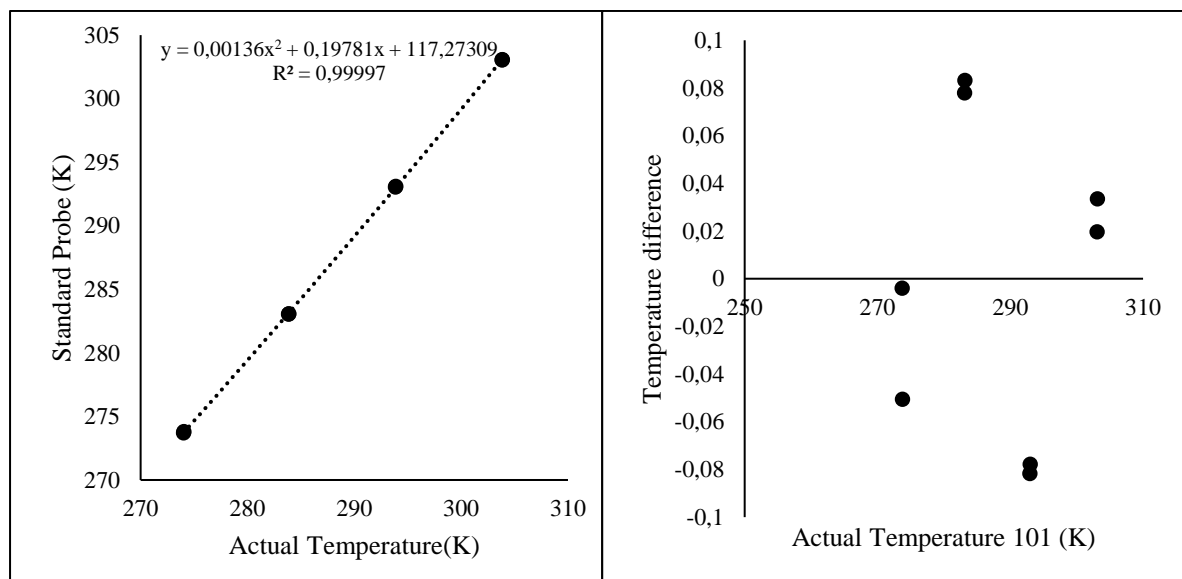


Figure 6.4: Calibration of the temperature probe 101 (LHS) and plot of the temperature deviation (RHS) used for the temperature probe utilized in the reactor vessel.

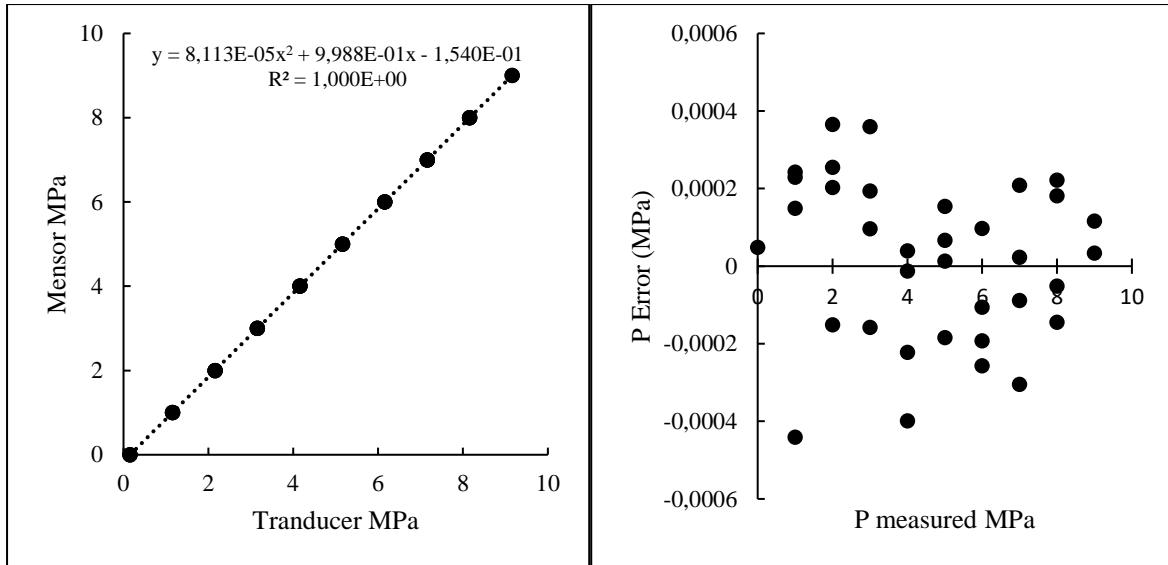


Figure 6.5: Calibration plot of the WIKA pressure transducer (LHS) and pressure deviation (RHS) used in a reactor vessel.

6.3.1.1 GC calibrations

The GC utilized in the replacement measurements in Chapter 5 was also utilized in this portion of the study. The calibration procedure and uncertainty in measurement are detailed in Appendix D. The calibration parameters are presented in Tables 5.2 and 5.3.

6.3.2 Uncertainty in measured variables

Contributing uncertainties considered in computing the combined expanded uncertainty for temperature, and pressure, are shown in Table 6.1. The concentration uncertainty was 0.08%. The concentration calculations are detailed in Appendix D.2.

Table 6.1: Summary of the source of uncertainty for variables reported in this study.

Uncertainty source	T P101 (K)	P (MPa)
Manufacturer stated instrument error \mathbf{u}_{instr}	± 0.03	± 0.025
Standard calibration correlation error \mathbf{u}_{corr}	± 0.04	± 0.0003
Calibration error, \mathbf{u}_{calib}	± 0.05	± 0.0029
Instrument uncertainty, \mathbf{u}_{instru}	± 0.02	± 0.002
Combined standard uncertainty, $U_c(x)$	± 0.06	± 0.002
Combined expanded uncertainty, $U(x)$	± 0.1	± 0.004

6.4 Experimental Procedure

The experimental procedure was divided into two sections: the methane hydrate formation in the porous medium and the CH₄ gas exchange with CO₂ in the CH₄ hydrate. Cell cleaning was carried out as outlined in Chapter 4, section 4.4.

6.4.1 Leak testing

Before the equipment setup could be utilized for hydrate measurements, leak testing was carried out. The procedure followed in leak testing is detailed in Chapter 4.

6.4.2 Preparation of the equilibrium cell

The equilibrium cell described in subsection 6.1.1 was cleaned with distilled water, rubbed with a sponge, and then rinsed with acetone. The bottom flange was blown with compressed air to remove any particles trapped in the apertures of the sparger. A vice grip was used to balance the cell, and then the bottom flange was fitted first with six 3.5 mm bolts. The top flange was fitted after the sample was added to the cell with six 3-mm stainless steel bolts. Then the cell was placed in a glycol-water bath by a tripod stand. The cell was connected to a connecting line and then vacuumed for 10 minutes to a pressure of 0.0002 kPa using an Edwards vacuum pump model RV3, with pressure monitored on the computer monitor. This was done to remove any trapped air in the cell or feeding line that could tamper with the composition of the feed. After that, the inlet valve was shut, and the system was observed to ensure no rapid pressure increase occurred within the cell. Subsequently, the cell was pressurized through the sparger for hydrate formation.

6.4.3 Sample preparation

A mass of 150g silica sand was weighed and placed in a beaker. An OHAUS PA4202C top pan balance measured the mass of silica sand. The silica sand was then transferred to the equilibrium vessel. Approximately 67.5 ml of water was added to the silica sand from the top of the open cell. In all the experiments, 60% silica pore saturation was attained. The mass of graphene utilized was 0.3375g to achieve 0.5 wt.% concentration relative to the volume of solution utilized. Silica sand and nanoparticles were mixed in a sealed plastic container on a shaker to even mix. Handshaking was also applied to enhance mixing. Afterward, the mixture was transferred to the reactor. The sand was filled to approximately three-quarters up in the cell in this study's experimental runs. The data permitting the reactor, contents specifications, and material volumes inside the reactor are shown in Table 6.2 below.

Table 6.2: Reactor conditions and feeding specifications.

Property	Value
Reactor volume	300. cm ³
Head volume	98.17 cm ³
Sand volume	202.24 cm ³
Sand mass	150g
Sand pore volume	0.75 ml/g
Water pore saturation	60%
Water volume	67.5 cm ³

6.4.4 Methane hydrate formation in porous media

The reaction cell was filled with clean, dry silica sand and uniformly saturated with deionized water. To ensure that silica sand was uniformly soaked, water was added from the top of an open equilibrium cell using a 50 ml syringe and the cell was left overnight to allow water to percolate the silica sand. For the preliminary run, the sand was taken out of the cell and physically scrutinised to ascertain whether water soaked all the silica in the sand. The vacuum pump was connected to one of the sampling points and turned on for 10 minutes to evacuate air and incondensable gases from the cell. Again, in the preliminary run the cell was opened after applying a vacuum to ensure that water distribution did not change due to evacuation of the cell. The same procedure was utilized for all the experimental runs. Then a specific amount of CH₄ gas was injected into the cell through a 5-m coil line and a sparger at the bottom of the cell using the ISCO Pump. The temperature of the glycol bath was reduced to between 274.15 and 276.15 K and maintained constant for methane hydrate formation. The hydrate formation was allowed to continue for more than 48 hours and was considered complete when temperature and pressure remained constant for more than 6 hours.

6.4.5 CH₄-CO₂ hydrate replacement

At the end of CH₄ hydrate formation, the purging valve at the top of the cell was opened to allow excess CH₄ gas to flow through the back-pressure regulator to a gas flowmeter and finally into a gas canister. The residual CH₄ gas was vacuumed out of the cell to ensure no CH₄ remained in the gas phase. Then CO₂ or CO₂/N₂ gas mixture was injected into the cell through the sparger until a set pressure value was reached. The gas phase composition was analyzed using a Shimadzu GC-2014 at the beginning of the replacement reaction. This was done by taking gas samples from two sampling valves with a 250 µml syringe and injecting them into the GC. The replacement reaction was allowed to continue for more than nine days (216 hours) to allow the replacement reaction to proceed to completion.

At the end of the replacement reaction indicated by no change in the pressure profile of the reaction (or after the time set for the reaction has elapsed), the gas phase was analyzed using the GC. The gas contents are vented from the cell and collected in a canister. The number of moles of the collected gas was computed using the ideal gas law. The cell was then evacuated for thirty seconds to remove residual components from the gas phase. The temperature of the water bath was increased to raise the temperature of the equilibrium cell for hydrate dissociation. A pressure increase accompanied this. When the pressure and temperature stabilized at the new temperature setting, the moles of the gas trapped in the hydrate phase were computed to determine the composition of gases in the hydrate.

6.4.6 Preparation of gas mixtures

The gas mixtures utilized in the replacement reactions were prepared in the laboratory. A DE150K2DL Kern floor standing (non-automatic balance) top pan balance was used to measure the mass of the gases. The gas mixtures were prepared in molar ratios. A 10-liter canister was utilized for gas mixture preparations. With careful control, the gas was filled in the canister, which enabled the mass change to be recorded. With the canister on the mass balance, a second component was added, and the mass of the gas was noted on the scale

6.5 Calculations of CH₄ and CO₂ in the Replacement Process

Equation 6.6 was utilized to determine the quantity of CH₄ in the hydrate phase using the ideal gas law modified via compressibility factor Z , calculated for system conditions using the Redlich-Kwong Equation of State (Smith et al., 1996). The derivation of equation 6.6 is shown below, and contributing terms are presented in equations 6.1 to 6.5. These equations were adapted from Fitzgerald, (2004).

$$n_g = \frac{PV_g}{ZRT} \quad 6.1$$

$$n_t = n_g + n_h + n_d \quad 6.2$$

$$V_g = V_{pore} - V_w - V_h \quad 6.3$$

$$V_w = (n_{wi} - n_h X) \frac{1}{\rho_w} \quad 6.4$$

$$V_h = n_h \frac{1}{\rho_h} \quad 6.5$$

Equation 6.6 was obtained by combining equations 6.1 to 6.5. Where n_h is the total moles of hydrate in the system. Here ρ_h is the molar specific volume of methane hydrate in units of [mol/m³] calculated using a hydrate density of 913.9 kg/m³ at 275.15 K and 3.2 MPa and a hydration number X , assumed to be 6. One CH₄ molecule resulted in a molar mass of 124.1 g/mol and hydrate molar density ρ_h was 7.369 mol/m³.

$$n_h = \frac{(n_t - n_d) - \frac{P}{ZRT} V_{pore} + \frac{P}{ZRT} n_{wi} \frac{1}{\rho_w}}{1 + \frac{P}{ZRT} \left(X \frac{1}{\rho_w} \right) - \frac{P}{RT} \left(\frac{1}{\rho_{hyd}} \right)} \quad 6.6$$

Where n_t is the total moles of CH₄ in the system occupying hydrate, gas and dissolved phase, n_{wi} is total moles of water in the system. n_d represents the moles of CH₄ dissolved in the water phase after hydrate formation assuming saturation values. V_{pore} is the total available pore space in the system including the head space above the sand pack. P is the system's pressure measured in the head space reported in Pascals. R is the ideal gas constant in SI units, T is the system temperature in unit K after the formation has completed, X is the hydration number and ρ_w is the molar density of water (Fitzgerald, 2004).

$$n_{hyd} = \frac{V_{pore} (P_i Z_f - P_f Z_i)}{\left(Z_f (RT - P_f / \rho_{hyd}) \right)} \quad 6.7$$

$$S_H = \frac{n_{hyd} \frac{1}{\rho_{hyd}}}{V_{pore}} \quad 6.8$$

Where S_H is the sand pores space saturation percentage, P_i , and P_f are pressure values at the beginning and at the end of CH₄ hydrate formation respectively. T_i , and T_f are temperatures at the beginning and end of hydrate formation respectively. V_{pores} is the total sand pores volume cm³. Z_i , and Z_f are the compressibility factors calculated by Redlich/Kwong Equation of State (Smith et al., 1996).

At 273K, natural gas hydrate has a density of 0.92 g/cm³ from computation by Takeya et al., (2006) and was calculated as 0.91 g/cm³ from the thermodynamic model developed by Sloan et al., (1998). In calculating CH₄ replacement efficiency and percentage of CO₂ sequestered, equations 5.16 and 5.17 in **Chapter 5** were used.

6.6 Results and Discussions

6.6.1 Test Systems- silica hydrate dissociation data

The test system carried out in this part of the study was the dissociation measurement for the CH₄-silica sand-water system. The results are presented in Figure 6.6, along with silica hydrate dissociation measurements from stirred equilibrium cells utilized to obtain results reported in Chapter 4 and 5 experimental measurements. Table G.1 in the Appendices section provides the tabulated results of the dissociation data. The silica-CH₄-H₂O system was compared to data on various porous media materials obtained from the literature.

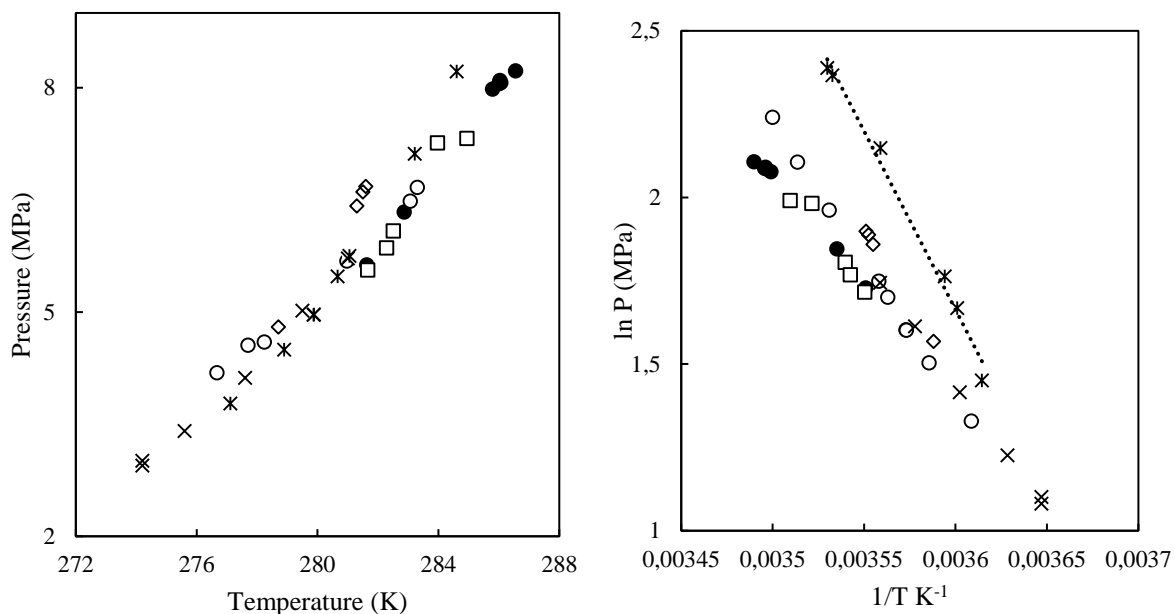


Figure 6.6: Hydrate dissociation points (LHS) and $\ln P$ vs $1/T$ (RHS) CH₄ -water system with different additives(*) CH₄ -water system in 52 ml cell, (o) 75-90 μm silica – CH₄-H₂O in 52 ml cell, (●) 280 μm silica -CH₄-H₂O in a 300 ml cell (utilized in this study), (□) 280 μm silica – CH₄-H₂O in 52 ml cell, (×) 100 nm porous glass (Uchida et al., 2002), (◇) 50nm porous glass (Uchida et al., 2002).

The temperature vs. pressure plot is shown in Figure 6.8 and $\ln P$ vs. $1/T$ was plotted to show a scatter plot for the system measured in this study. As seen in Figure 6.8, adding silica sand inhibits hydrate formation as the equilibrium curve for CH₄-silica sand-H₂O was lower than that for CH₄-H₂O. From the sizes of the silica sand particles, it can be seen that the silica sand's inhibition effect increases with the particle size. As reported by Uchida et al., (2002) a different porous material also showed this trend, glass beads.

6.6.2 Methane-silica hydrate formation

A total of seven experimental runs were carried out to form a CH₄ hydrate. The second stage of the experiment consisted of replacing CH₄ contained in the hydrates with CO₂. Two different systems were utilized in the formation of the CH₄ hydrate. The first four experiments were carried out with silica and water, while the last half was formed with silica - 0.5 wt.% graphene nanoparticle-water system. Table 6.3 summarises the experimental runs providing details for the CH₄ hydrate formation process and the results obtained. Three literature sources are presented in this section as a comparison of the results of this study. Maria et al., (2018) utilized a 949 cm³ reactor to study CH₄-CO₂ replacement in 50% saturated silica sand and applied thermal stimulation to enhance the replacement. Pan et al., (2020) investigated CH₄-CO₂ replacement in a 509 cm³ reactor with silica sand mixed with clay in the presence of N₂ gas. Lastly, Fan et al., (2022) utilized a gradual heating method of a silica hydrate in a 2 000 cm³ cell to enhance CH₄-CO₂ replacement.

Table 6.3: Methane hydrate formation with silica sand main parameters.

		Water-silica			Silica-0.5 wt.% graphene nanoplatelets solution				Maria , (2018)	Pan et al., (2020)	Fa et al., (2022)
Run no		1	2	3	4	5	6	7			
H ₂ O charged	mol	3.89	3.89	3.89	3.89	3.89	3.89	3.89	*	*	*
CH ₄ Initial Press	MPa	8.97	8.78	8.84	8.80	8.85	8.94	8.66	4.58	9.00	8.00
Hydrate formation Temp	K	277.45	277.45	273.44	274.43	275.26	274.77	274.25	275.50	274.20	275.15
CH ₄ charged	mol	0.65	0.52	0.66	0.82	0.71	0.94	0.91	0.605	*	*
CH ₄ Unused	mol	0.39	0.36	0.49	0.66	0.52	0.66	0.67	*	*	*
CH ₄ trapped in the hydrate	mol	0.27	0.16	0.17	0.15	0.19	0.27	0.24	0.234	*	*
H ₂ O remaining free	mol	2.30	2.96	2.87	2.96	2.74	2.25	2.43	*	*	*
% CH ₄ converted to hydrate± uncertainty	%	40.56±0.31	30.05±0.39	25.47±0.30	18.91±0.24	27.00±0.28	29.11±0.21	26.60±0.22	38.68	40.00	*

*values no specified

Combined expanded uncertainty $U(T) = \pm 0.1 K$, $U(P) = 0.006 MPa$ $U(n_{CH_4}) = 0.003$.

This study set the initial pressure between 8 - 9 MPa in all the experimental runs. The hydrate formation temperature varied between 273.44 and 277.45 K within the hydrate stability region. The amount of water used was 3.89 moles which were 60% saturation of the silica porous media. The moles of CH₄ gas injected at the beginning of the CH₄ hydrate formation process were between 0.5 and 0.94 moles, as listed in Table 6.3. It can be noted from the table that between 0.15 and 0.27 moles of CH₄ were trapped in the hydrate with an uncertainty of 0.003 moles. These values were determined by equation 6.7.

The CH₄ moles trapped in the CH₄ hydrate were between 0.15 and 0.27 moles. These were in the same range as the values reported by Maria, (2018), which were between 0.161 - 0.234 moles. The amount of CH₄ trapped in the hydrate was not necessarily dependent on the initial moles of CH₄ gas-charged. This observation was also noted by Zhao et al., (2016) and Maria, (2018). Also, in line with hydrate structure, Fitzgerald, (2004) observed that the hydrate formation may be delayed due to the system being mass limited, that is, insufficient fluids present in these locations to form hydrate. Thus, secondary hydrate formation occurs only when free water or gas is available. This might also be caused by developing a hydrate shell or skin around the sand particles, entrapping free water, which limits the exposure of the gas phase to the free water. If this outer layer cracks due to expansion associated with hydrate growth, free water is exposed to CH₄, resulting in more hydrate formation. Using temperature and pressure alone, it is difficult to conclude the nature of the process occurring accurately. Moreover, since the particles used in this study were not the same size but a range of sizes (0.071-0.063 mm), hydrate formation occurred in interstitial space (Bhattacharjee et al., 2015). This was confirmed by observing the hydrate at the end of the hydrate formation stage.

In addition, since 60% pore saturation was applied, hydrate formation and growth in the first four runs could have occurred through grain coating. In this process, hydrate growth clogged the pores and cut the pore space from the interconnected pore networks (Priegnitz, 2015). Therefore, the higher the number of nucleation points, the faster the rate of hydrate growth and gas consumption, whereas the fewer the nucleation points the lower the rate of hydrate growth hence the low amount of gas in the hydrate matrix. Hence the absence of stirring and the stochastic nature of this process account for the large range (0.15-0.27) of CH₄ moles converted into hydrate in this study.

The addition of nanoplatelets slightly stabilized the hydrate formation. The effects of nanoparticles were limited because there was no stirring hence the effects of nanoparticles were

not evenly distributed throughout the silica bed to produce uniform effects. In the presence of nanoparticles, hydrate formation occurred through a cementing process. Moreover, since hydrate formation occurs in the interstitial spaces, the presence of nanoplatelets might have led to the delay of nucleation hence allowing the movement of gas and water in a process known as "water migration" (Spangenberg et al, 2014; Wang et al., 2020). Moreover, in a separate study, Pan et al., (2020) observed that hydrate formation in silica sand decreased as the amount of clay added increased. The reduction in water activity reduced the hydrate growth due to geometric water constraints caused by the clay interlayer. Thus, it was concluded that clay content inhibited hydrate formation. Thus, similarly, in this study nanoparticles inhibited CH₄ hydrate growth. The average percentage conversion of CH₄ gas into the silica-CH₄ hydrate was 29.55%, while in the presence of nanoparticles, the average conversion was 25.41%. In experimental run two, the maximum percentage of CH₄ trapped in the hydrate phase was 40.56%, obtained with a silica-CH₄ water system. The minimum was 18.91% obtained with silica-0.5wt.% graphene nanoparticles in experimental run five. Good repeatability was observed in runs six to eight as the amount of CH₄ trapped in the hydrate phase was in the same range for these three experimental runs.

6.6.3 Analysis of silica-CH₄ hydrate

The silica sand soaked with water and graphene nanoparticles was used as an additive in the second set of runs. The cell filled with sand is shown in Figure 6.7a. At the end of the hydrate formation process, on opening the cell shown in Figure 6.7b to 7d, it seemed like the hydrate had swelled or expanded to fill up the whole vessel. However, on close analysis, it was observed that there was a hollow space at the top part of the hydrate. Thus, the sand did not expand but was instead displaced by the incoming pressure head of CH₄ gas.

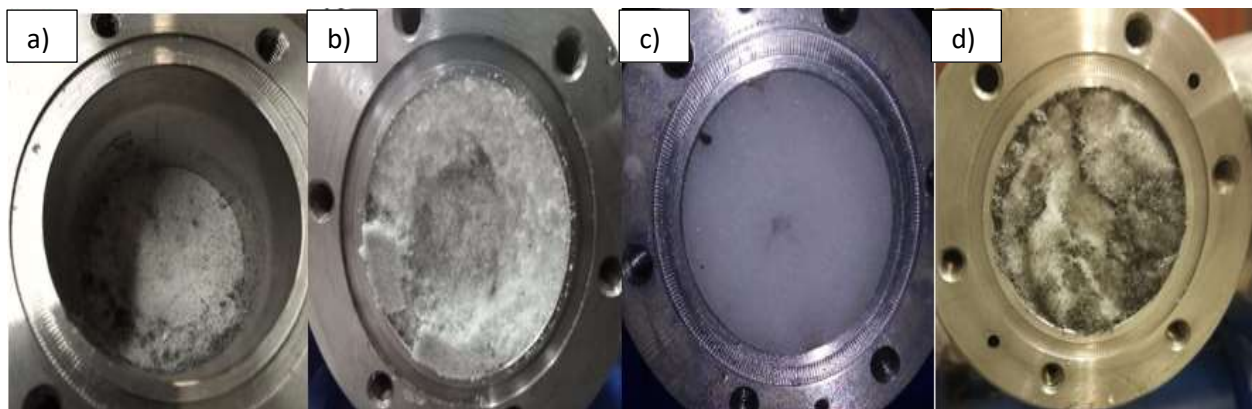


Figure 6.7: Photograph of silica sand in the cell a) before hydrate formation b) - c) after hydrate formation d) 0.5 wt.% graphene-silica sand-methane hydrate.

The absence of gas hydrate at the top of the hydrate bed confirms that the hydrate formed in the interstitial spaces. The structure and nature of the CH₄ hydrates obtained from this study are shown in Figures 6.8 (with silica only) and 6.9 (with silica and graphene nanoparticles). Figure 6.8a to 6.8f shows the pictorial view of the hydrate formed with the silica-CH₄ water system.

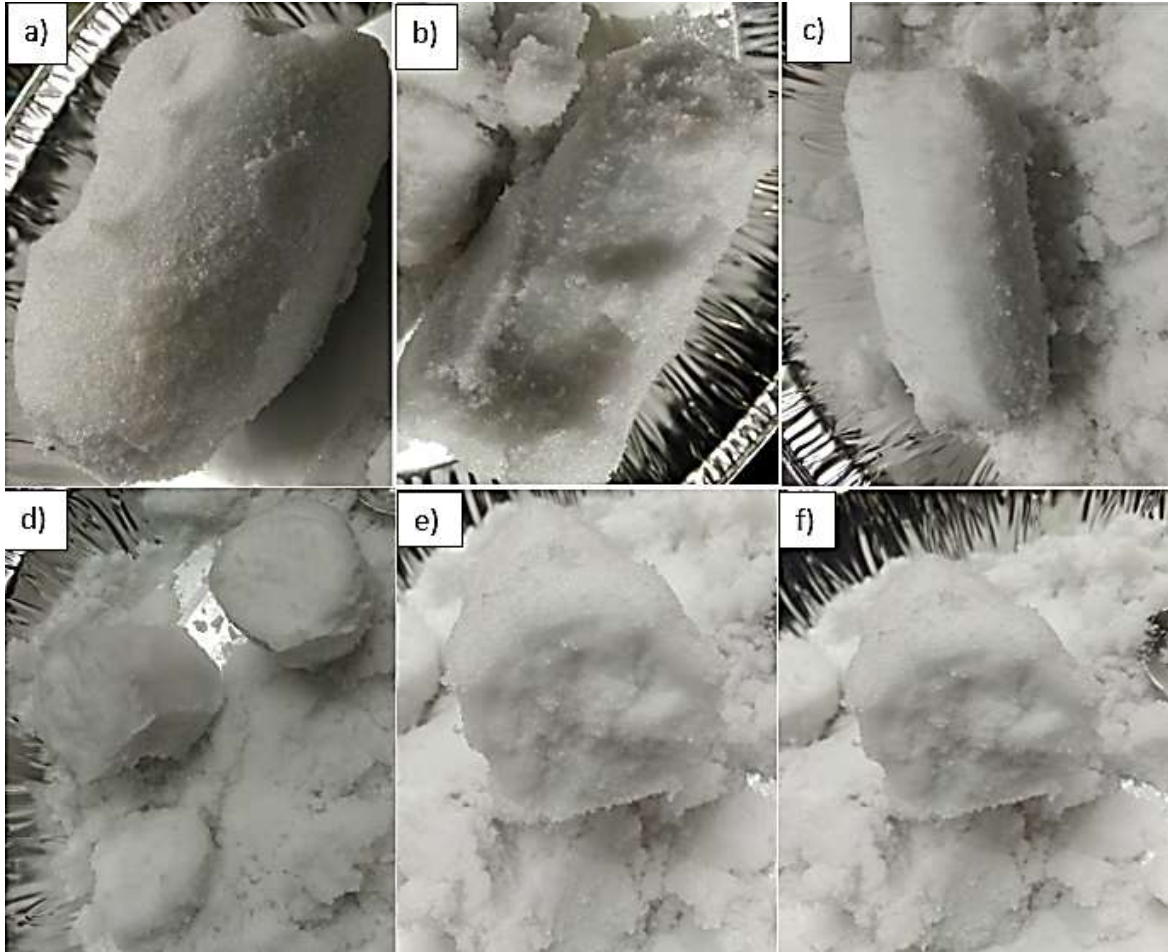


Figure 6.8: Photographs of hydrates formed with silica sand-methane gas-water examined from the surface to the core.

The outer layer of the hydrate was loosely packed. It was observed that the hydrate became rigid towards the centre, with the hydrate core being the firmest such that it could not be broken by hand. In Figures 6.8d to Figure 6.8f, two pieces of the hydrate are shown. On closer analysis of the hydrate core, it was observed that these were intact and more structured than the outer-lying parts. This might have been caused by water migration to the central part where initial nucleation occurred. However, this could not be validated as the cell had no viewing window. Moreover, the vacuuming step and CO₂ injection were too fast (in a few seconds) and could not affect the hydrate structure.

Figures 6.9a to 6.9d shows silica sand-CH₄ hydrate formed in the presence of 0.5 wt.% graphene nanoparticles. Figure 6.9b shows the top part of the hydrate formed in the presence of the nanoparticle. It can be seen that the hydrate matrix is spongy in its appearance. This might be opening the hydrate spaces to be occupied by more gas or a different gas for different cage occupancy. This outer layer shown in Figure 6.9c might explain why a high amount of CO₂ was trapped in the hydrate in all the experimental runs carried out in the presence of nanoparticles. However, the core of this hydrate was similar in appearance to the core without nanoparticles, as shown in Figures 6.9c and 6.9d. This observation was also made by Fitzgerald, (2004), who investigated hydrate formation in a large-scale reactor and reported that hydrate formation occurred in different locations, not in a uniform hydrate formation pattern observed in small-scale systems.

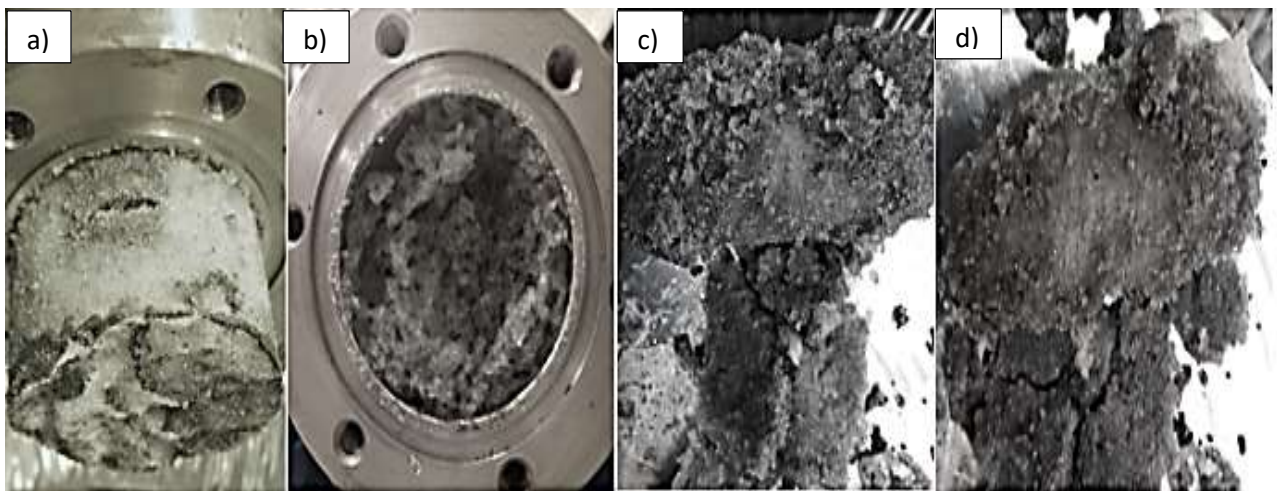


Figure 6.9: Photographs of hydrates formed with 0.5 wt.% graphene-silica sand-methane gas-water examined from the surface to the centre.

6.6.4 Addition of carbon dioxide

The conditions for the addition of replacement carbon dioxide are summarized in Table 6.4. Between 0.328 and 0.868 moles of CO₂ and 15% CO₂/85% N₂ mixture were utilized. In the replacement reaction, three factors were varied to enhance the replacement. These were the replacement's duration, the system's temperature, and the addition of a secondary gas (N₂).

Table 6.4: CO₂ addition for CH₄ replacement main parameters.

Soaking CH ₄ -hydrate in gas CO ₂	Pressurized Carbon dioxide						85% N ₂ /15% CO ₂		Maria, (2018)	Pan et al., (2020)	Fan et al., (2022)
	Run	1	2	3	4	5	6	7			
CO ₂ charged	mol	0.328	0.525	0.675	0.868	0.746	0.778	0.714	0.307	*	*
Duration of replacement	hrs	215	175	100	220	200	376	333	*	*	*
Beginning of replacement											
Pressure	MPa	4.02	7.01	7.65	8.00	8.49	8.06	7.40	3.35	8.19	3.30
Temperature	K	272.64	276.43	273.43	274.59	275.44	275.22	274.88	274.80	274.20	275.15
End of replacement											
Pressure	MPa	3.77	4.03	4.53	4.14	5.07	6.06	5.53	*	8.00	4.01
Temperature	K	274.40	276.44	274.09	274.42	277.47	277.37	276.06	279.75	274.2	280

Combined expanded uncertainty $U(T) = \pm 0.1 \text{ K}$, $U(P) = 0.006 \text{ MPa}$, $U(n_{CO_2}) = 0.004$, $U(n_{gmix}) = 0.032$

*no data provided in the literature

The replacement gas/gas mixture was introduced from the bottom of the cell through a sparger and allowed to penetrate the spaces in the hydrate matrix as it filled up the cell. This enhanced contact between the replacement gas and the CH₄ hydrate. The replacement reaction was allowed to continue for more than 100 hours to ensure enough time for the reaction to proceed to completion which was indicated by constant pressure readings for more than 24 hours. Three replacement reaction profiles are shown in Figure 6.10 through Figure 6.12. Three stages are labeled in replacement reaction run one, shown in Figure 6.10. The first one is CH₄ hydrate formation in the presence of silica sand it occurred for approximately 50 hours. After that, the temperature was reduced by 4 K to preserve the CH₄ before the injection of CO₂. This process was 50 hours long to ensure the hydrate formation process was complete, thus, the whole CH₄ formation process was over 100 hours. This procedure has been utilized extensively in replacement studies (Deusner et al., 2012, Lee et al., 2014, Pan et al., 2020, Heydari et al., 2020). The CO₂ was injected, and the replacement period was allowed to continue for 215 hours.

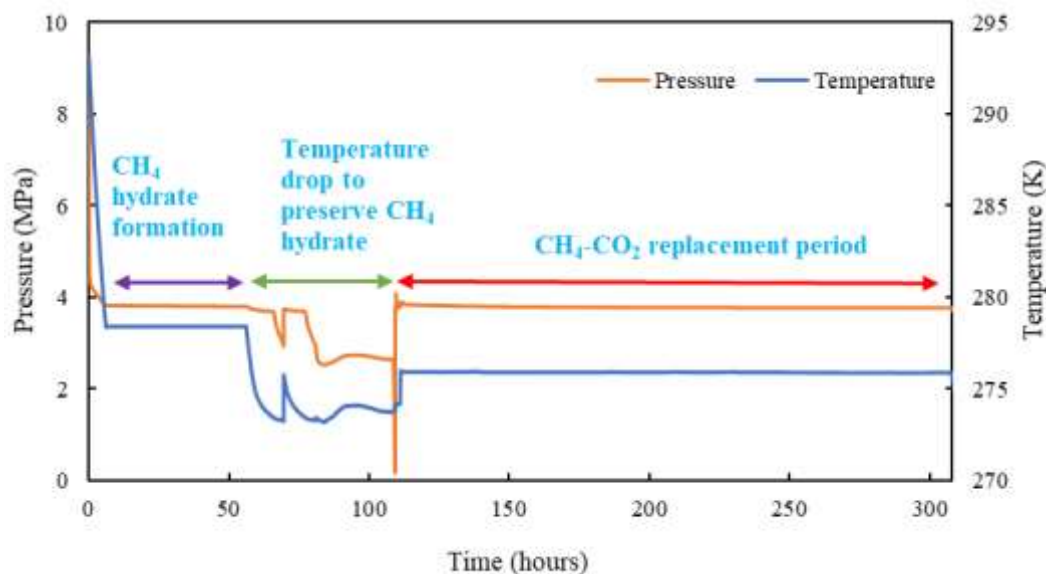


Figure 6.10: Replacement profile for an experimental run one between CH₄-silica-H₂O and CO₂.

The CH₄-CO₂ replacement profile carried out in the presence of 0.5 wt.% graphene nanoplatelets is shown in Figure 6.11. Two sharp temperature increments can be seen on the temperature profile corresponding with sharp pressure drops. This denotes the hydrate formation process which is exothermic. Excess gas was purged at the end of the CH₄ hydrate formation (as shown by the pressure drop to zero), and CO₂ gas was introduced. Then the next stage was the CH₄-CO₂ replacement process. The small spike in the pressure profile at the addition of CO₂ gas was due to the gaseous phase being converted to the liquid phase due to the equilibrium cell conditions.

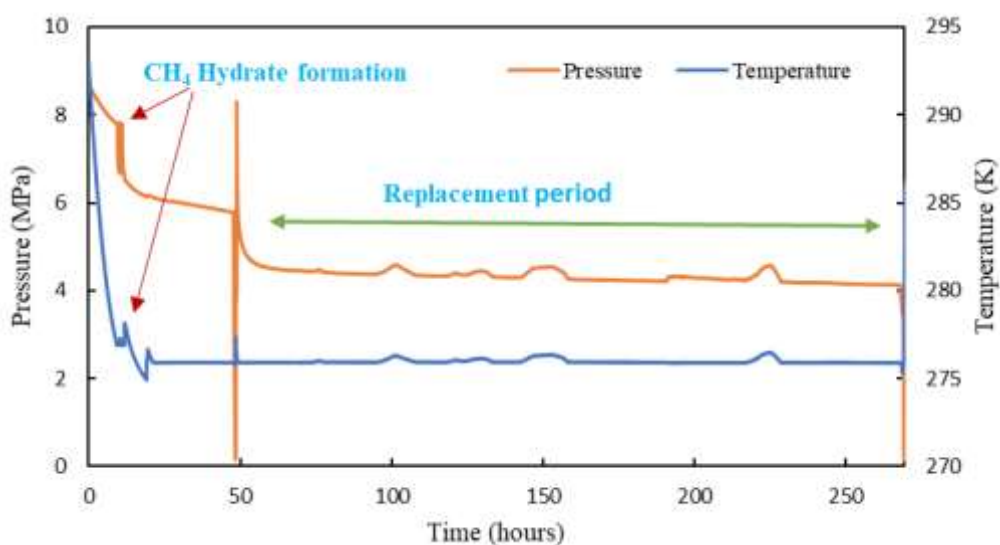


Figure 6.11: Replacement profile for experimental run 4 between CH₄-silica-H₂O and CO₂.

The CH₄-CO₂ replacement profile of CH₄ gas in 0.5 wt.% graphene nanoparticles and silica sand is shown in Figure 6.12. In this replacement, the reaction temperature was increased initially and toward the end to enhance the replacement reaction (thermal stimulation). The gas mixture used for the replacement was 85% N₂/15% CO₂. At the feed conditions, the CO₂ is in gaseous form when pumped from the cylinder but changes to liquid in the replacement cell, hence pressure drops suddenly soon after the injection of the replacement gas mixture. Temperature ramping was applied to enhance the hydrate formation and replacement process, as seen by the temperature and pressure profile peaks in Figure 6.12.

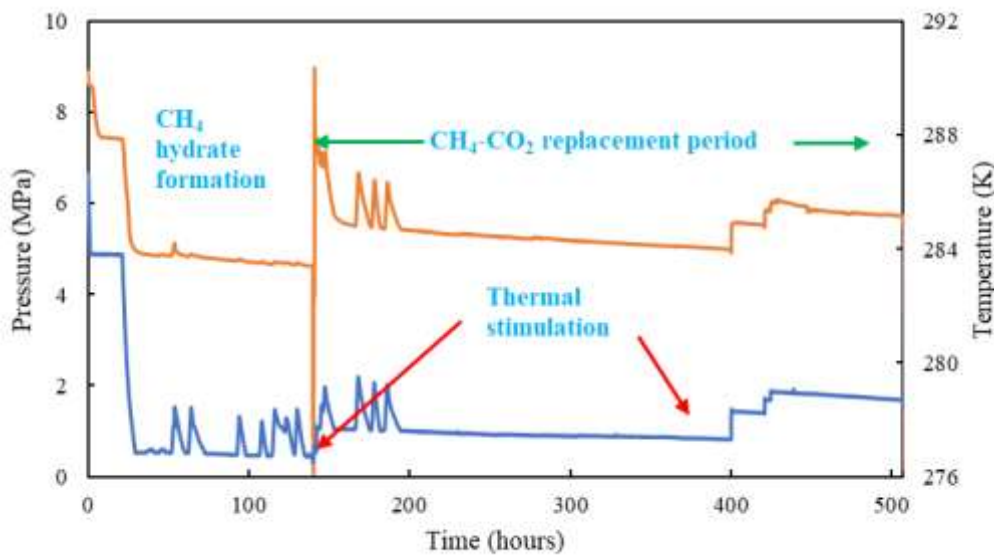


Figure 6.12: Replacement profile for experimental run 6 between CH₄-silica-H₂O and CO₂ (-) Pressure, (-) Temperature.

The content of the CH₄-CO₂ replacement vessel was examined at the end of the process; the photos taken are shown in Figure 6.13. As can be seen from Figures 6.13a and 6.13b, the silica gas hydrate seems to occupy the entire length of the cell however, the top part was hollowed with the hydrate formed equal to the initial volume of the silica and water added into the cell as shown in Figure 6.13e. The length of the hydrate was approximately 10.5 cm, equal to the height of the silica fed into the cell at the beginning of the reaction. The hydrate formed was rigid and could not be broken easily by hand, but the top layer was loosely attached to the hydrate, as shown in Figure 6.13f. Moreover, the effervescent sound was detected as the hydrate dissociated. The hydrate dissociation rate was prolonged, as the hydrate was still intact at the core 10 minutes after the cell had been opened. As time progressed, subsequent layers became loose as shown in Figures 6.13g and 6.13h, which were taken after 5 minutes intervals.

6.6.5 Analysis of CH₄-CO₂ replacement reactions

The key outcome parameters of this investigation are presented in Table 6.5 and Figure 6.14. The final parameters reported are the percentages of CO₂ sequestration and CH₄ replacement efficiency. The reactor was maintained in the CH₄ and CO₂ hydrates stability regions in all the experimental runs. Results from three literature sources are also presented in the table for comparison.

Table 6.5: Efficiency of CH₄ replacement and CO₂ sequestration ratio.

<i>Run</i>	1	2	3	4	5	6	7	Maria, (2018)	Pan et al., (2020)	Fan et al., (2022)
%CH₄ replacement efficiency	13.71 ±4.42	37.49 ±1.89	34.63 ±3.21	32.16 ±2.96	23.67 ±3.28	11.03 ±2.61	5.40 ±2.68	*	24	25.4 ±3.8
%CO₂ sequestration ratio	39.27 ±6.92	54.56 ±6.02	38.09 ±4.73	64.62 ±3.69	51.73 ±4.29	76.63 ±4.12	62.58 ±4.08	44	73.1	61.1 ±6.72

*not reported

Combined expanded uncertainty $U(T) = \pm 0.1 K$, $U(P) = 0.006 MPa$ $U(n_{gmix}) = 0.032$.

Experimental runs one to four were carried out with silica and equal water. It should be noted that CO₂ sequestration is a sum of CO₂ gas dissolved in the free water and the amount of water captured in the hydrate matrix. Run two gave the best CH₄ replacement and CO₂ sequestration results, which were 37.49% and 54.56%, respectively. Considering run two and three, it can be seen that the resultant CH₄ efficiency was higher than the values obtained from other runs in the study. The reason for this observation is the relatively short replacement period which prevented the reformation of the CH₄ hydrate which consumes CH₄ gas from the gas phase. The low value of CO₂ sequestered in run three was caused by a relatively short period of 100 hours for the replacement process.

Experimental runs four to seven were carried out in the presence of 0.5 wt.% graphene nanoplatelets. As can be seen from Table 6.6, the CO₂ sequestration percentage was greater than 51.73% in runs four to seven. This observation validates that adding nanoplatelets favors CO₂ storage more than CH₄ release. In this set of runs, the highest CH₄ replacement efficiency

was obtained in run four which was 32.16%, whereas the percentage of CO₂ sequestration was 64.62%. This experimental run's high CH₄ replacement efficiency was due to the "optimum" replacement duration. The assumption underlying this conclusion is that the CH₄ -CO₂ replacement process was stopped before the CH₄ hydrate reformation process had begun, thus resulting in high CH₄ gas in the gas phase. Replacement reactions in runs one to five occurred in the time range of between 100-220 hours.

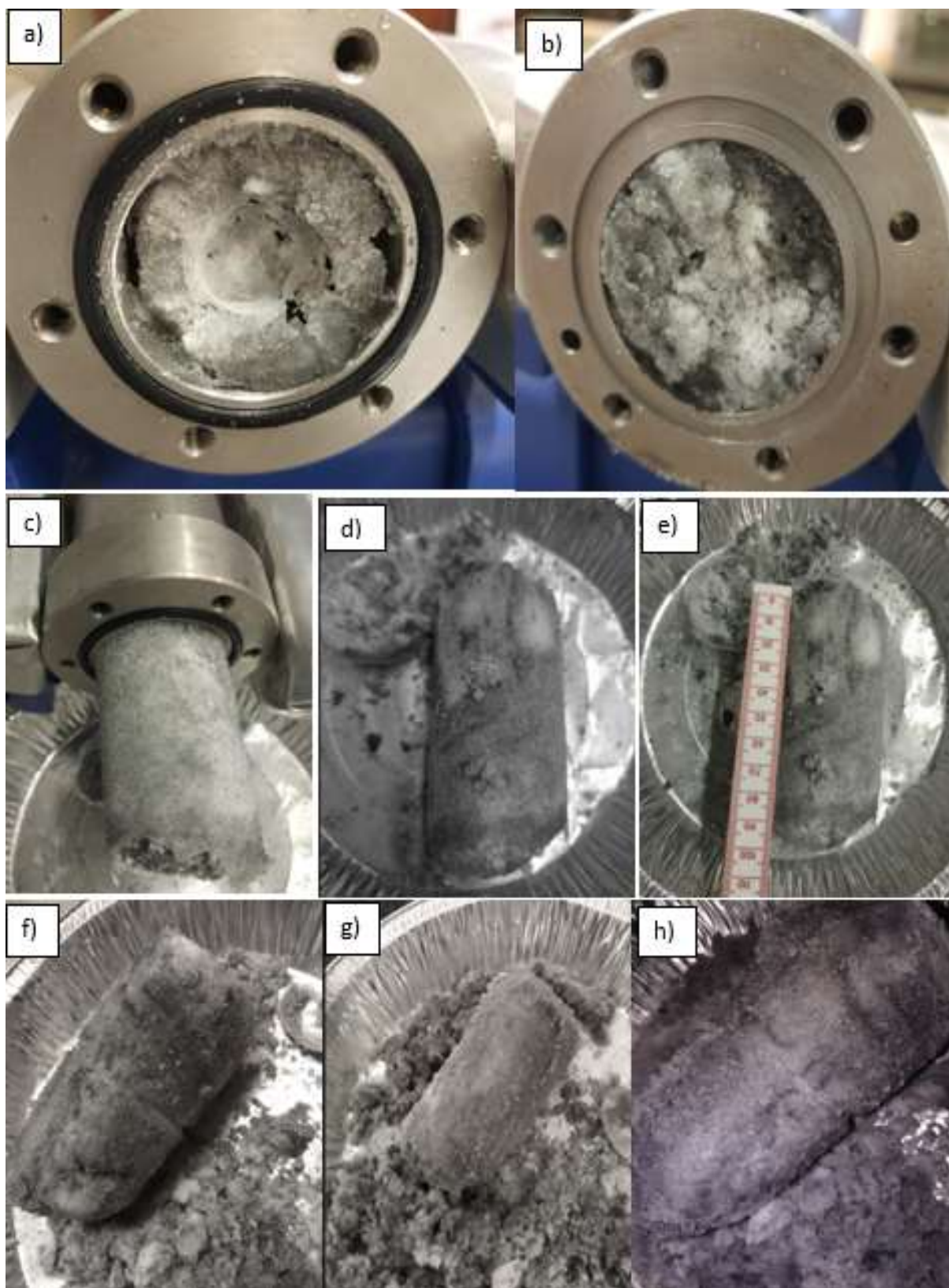


Figure 6.13: Photograph obtained from $\text{CH}_4\text{-CO}_2$ replacement reaction in the presence of 0.5 wt.% graphene nanoplatelets a) bottom view b) top view c) & d) side view of the hydrate, e) length of the gas hydrate, f) side view of the hydrate with the top layer scraped off g) side view of the gas hydrate after 5 minutes of cell opening h) side view after 10 minutes of cell opening.

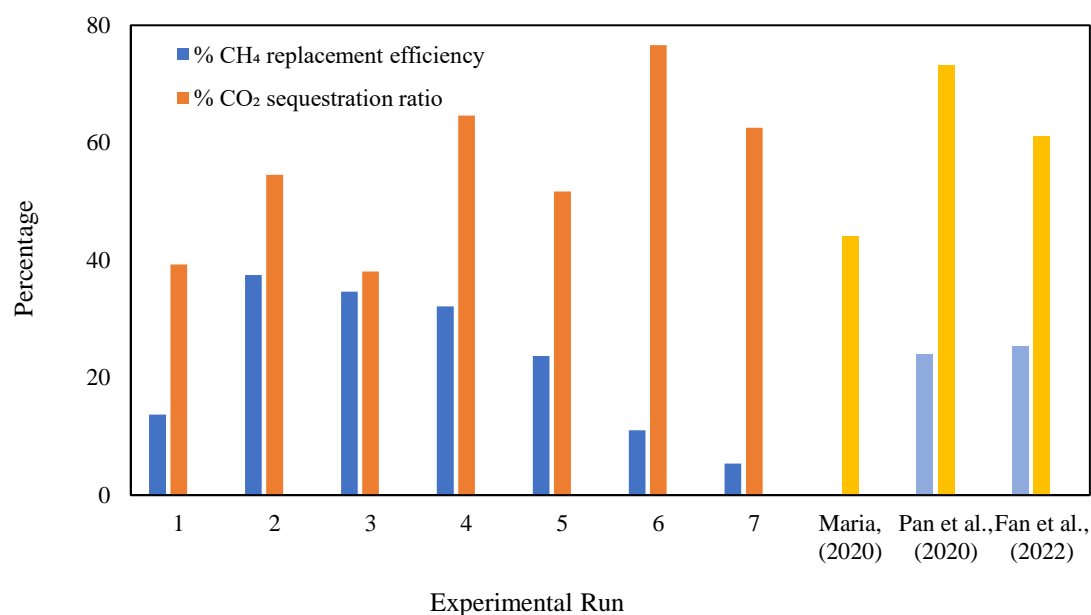


Figure 6.14: Percentages of CO₂ sequestrated and CH₄ replacement efficiency.

*Feed CH₄ hydrate formation for runs 1-3 was Silica sand-water system, runs 4-7 was Silica sand -0.5 wt.% graphene nanoplatelets solution. Feed for replacement runs 1-5 was pressurized CO₂ and for runs, 6-7 was 85% N₂/15% CO₂ gas mixture + thermal stimulation.

These sets of runs had the highest percentage of CH₄ released. The replacement runs carried outside this period had a lower portion of CH₄ replaced. Thermal stimulation was applied to experimental run five, and no significant change was observed in the percentage of CH₄ replaced or CO₂ sequestrated. A combination of thermal stimulation and the addition of a secondary gas (85% N₂ /15% CO₂) was applied in runs six and seven. Consequently, the amount of CO₂ sequestrated increased, whereas the amount of CH₄ replaced decreased. The incorporation of CH₄ into the mixed hydrate caused a decrease in the overall amount of CH₄ released in the gas phase. This was due to the reformation of the CH₄ hydrate with CH₄ initially released from the hydrate. This explains the low quantity of CH₄ obtained from the two-replacement reactions, which occurred over 300 hours. Moreover, Maria, (2018) reported that as the percentage of CO₂ sequestrated increased, the amount of CH₄ replaced decreased.

The highest value of CO₂ sequestrated recorded in this study was 76.63%, and it was obtained in an experiment run seven where thermal stimulation and secondary gas were used. The secondary gas utilized in the study did not occupy hydrate spaces as shown in the full results of the replacement provided in Table G.2. The values obtained for CO₂ sequestration in this study were higher than those reported by Castellani et al., (2016), Pan et al., (2020), Maria,

(2018) and Fan et al., (2022) by 15.52% relative to the highest value reported by these researchers. Compared with the three literature sources presented, the results from this study showed higher CH₄ recovery and CO₂ sequestration. Thus, combining the secondary gas approach and thermal stimulation is a viable avenue to consider in the CH₄-CO₂ replacement reactions.

6.7 Summary

This section proposes a method of gas storage in a solid form without hydrate form in the presence of porous media. But thermal heat injection enhanced replacement in the sedimentary layer. The results also showed an inhibition effect due to nanoparticle addition to the silica sand, which is a viable route for energy storage. The use of the silica sand as a porous media proved effective in promoting nucleation hence hydrate formation in the absence of an agitation device. This is evidenced by the CH₄ formation and CH₄-CO₂ replacement results obtained from the study compared to the literature data. Gas bubbling and the use of porous media in the absence of stirring proved to be an effective means of enhancing hydrate formation and CH₄ replacement with CO₂ gas from the CH₄ hydrates. The porous media can form gas hydrates in a system where it is impossible to install agitation devices. Moreover, the absence of mechanical agitation devices lowers the operation cost due to the gas hydrate formation process

The use of nanoparticles stabilizes the hydrate formation process with an inhibition effect. The replacement reaction between the CH₄ hydrate in porous sand and CO₂ gas yielded the highest amount of CH₄ released, 37.49% and 54.56% CO₂ sequestered. Application of N₂, a secondary gas, and thermal stimulation improved the percentage of CO₂ sequestered to 76.63% while the amount of CH₄ released was lowered to 11.03%. Thus, the storage of CO₂ in CH₄ gas hydrate is a promising avenue for CO₂ sequestration with the release of CH₄ gas. A critical step in applying hydrates is managing and controlling the rate of hydrate dissociation to provide gas energy at a controllable rate. The sequestration of CO₂ in natural CH₄- silica hydrates was aided by thermal stimulation and N₂ gas addition. Energy recovery was possible, though the rate of recovery and the amount of CH₄ obtained was very low with a maximum recovery of 37.92% achieved.

Chapter 7: Conclusions

Hydrate formation kinetics for CH₄ and CO₂ gas were experimentally investigated in a 52 cm³ equilibrium cell in the presence of SDS, nanoparticles, and microparticles. The experimental results were used in a kinetic model to determine gas consumption, rate of gas uptake, water-to-hydrate conversion, and hydrate storage capacity. Induction time was determined from the experimental results using temperature and pressure profiles. The replacement of CH₄ with CO₂ from the CH₄ hydrate in the presence of graphene nanoparticles enhanced by secondary gas and thermal stimulation. Also, the effects of graphene nanoparticles on hydrate formation were compared in the presence and absence of porous media. Gas hydrate dissociation measurements were performed for CH₄ and CO₂ with pure water and in the presence of nanoparticles, microparticles, and silica sand. A 300 cm³ equilibrium cell was designed and fabricated with a sparger to bubble the gas into the cell. Silica sand was utilized as a porous media for CH₄ hydrate formation without stirring in the 300 cm³ vessel.

In the kinetic studies for the CO₂ system, the 1.2 wt.% GPN + 0.05 wt.% SDS had the highest storage capacity of 52.12 (v/v). The highest rate of gas uptake obtained was $2.44 \times 10^{-3} \text{ mol}_G \text{ mol}_W^{-1} \text{ min}^{-1}$. This was obtained with 0.2 wt.% graphite powder + 0.05 wt.%, and a maximum conversion of 24.98% was obtained with 1.2 wt.% GPN + 0.05 wt.% SDS. For the CH₄ system, 0.1 wt.% CuO + 0.05 wt.% SDS system had the best performance in all the parameters investigated with gas consumption of 0.0238 moles, a storage capacity of 28.50 (v/v), water to hydrate conversion of 13.09%, and a rate of gas consumption of $8.94 \times 10^{-3} \text{ mol}_G \text{ mol}_W^{-1} \text{ min}^{-1}$. However, for both CO₂ and CH₄ systems. 0.5 wt.% GPN + 0.05 wt.% SDS had the optimal performance. Hence this concentration was selected for to be utilized in the CH₄-CO₂ replacement reaction. The equilibrium curves obtained with pure water were within the experimental uncertainty of literature data. Silica sand inhibited hydrate formation, with the inhibition effect increasing as the particle size of the silica sand increased.

The nanofluid produced from a solution of nanoparticles improved thermal properties, reduced induction time, and improved hydrate formation hence nanoparticles can be applied to improve gas hydrate formation and growth. The kinetic studies showed that gas hydrates in the presence of nanoparticles could be utilized to store CO₂ gas as the kinetics had higher output values than CH₄. Storage capacity is of paramount interest as it determines the amount of gas captured and stored.

In the CH₄-CO₂ replacement without porous media, adding 0.5 wt.% graphene + 0.05 wt.% SDS enhanced the replacement reaction by over 50% compared to the system without additives. This was attributed to the nanoparticles which have excellent thermodynamic properties. Physical viewing of the cell context showed that replacement mainly occurs on the outer surface, with CO₂ absent in the hydrate's inner matrix. The addition of nitrogen improved the replacement efficiency, with the secondary gas not occupying any space in the hydrate. In CO₂ sequestration, using a secondary gas reduced the CO₂ sequestration ratio though overall a higher sequestration ratio of 47.84% was achieved with 0.5 wt.% graphene + 0.05 wt.% SDS while with pressurized CO₂ 57.03% of CO₂ gas was sequestered. The highest CH₄ replacement efficiency obtained was 28.77% obtained with pressurized CO₂.

The sparger improved CH₄ replacement with CO₂ in the presence of silica sand and nanoparticles by increasing the contact between the gas and the porous media during the CH₄-CO₂ replacement in the 300 cm³ cell. It was observed that adding silica sand did not increase the storage capacity of CH₄ gas in the silica system. Also, the addition of graphene nanoplatelets in the absence of silica sand improved gas storage in CH₄ hydrate, while the effects of graphene nanoplatelets in the presence of silica sand were not significant. This observation confirmed that hydrate formation in the presence of graphene nanoplatelets in pore spaces occurred through grain cementing and not by pore filling. In the sequestration of CO₂, silica sand exhibited excellent CO₂ storing capacity with substantial CH₄ gas release. In the presence of silica sand, the addition of nanoparticles inhibited the CH₄ formation while the hybrid of thermal stimulation and the addition of secondary gas improved the CO₂ sequestration from 51.73% to 76.63%.

7.1 Implications

The techniques investigated in Chapter 4 can be used to pelletize CO₂ from the waste CO₂ gas stream into a hydrate form in the presence of nanoparticles. Furthermore, improvement in CH₄ gas hydrate formation in the presence of nanoparticles can be used to store small CH₄ gas pockets. Careful consideration is essential regarding the CH₄ release.

The production of CH₄ from natural gas beds needs to be carefully studied with a critical evaluation of all the factors affecting CH₄ gas release. The results and findings from this study confirmed that the application of thermal stimulations could enhance the replacement of CH₄ in the CH₄ beads.

Chapter 8: Recommendations

To improve the replacement of CH₄ with CO₂ in the gas hydrate structure, the following recommendations are made from this study:

- Further investigation of the relationship between time and CH₄ release as gas hydrate reformation was observed to hinder the recovery of natural gases.
- For molecular investigation of the CH₄-CO₂ replacement reaction, specialized equipment such as Raman spectroscopy has to be utilized to understand the process's microscopic nature.
- It is also advised to investigate the period for CH₄ removal from the equilibrium cell to prevent released CH₄ from reincorporating into the hydrate.
- Another study area is the thermal influence on CO₂ sequestration as it was observed that CO₂ sequestration improved with thermal stimulation. Moreover, scale-up of this process for use in natural hydrate beds is essential.
- Investigating the microscopic analysis of the effects of nanoparticles in the hydrate formation and replacement reaction is also imperative.
- The technique of introducing the replacement gas to the CH₄ hydrate needs to be improved further to enhance contact between the two reactants.
- Utilization of the equilibrium cell design for this study to form CO₂ composites in the presence of various metal silicates.
- The exact mechanism of how the secondary gas improves replacement has not been fully understood. Thus, it is imperative to study replacement in different N₂/CO₂ gas mixtures to fully understand the mechanism of gas exchange in the hydrate cages.
- Development of a simulation model which incorporates all the parameters associated with natural sea bed such as salty water, various ions and different landform to study the CH₄-CO₂ replacement reactions.
- As the South African government commits to a hydrogen society, gas hydrates could be investigated as hydrogen gas storage mediums because gas hydrates possess a large storage capacity that can be increased further.

References

- Adams, E., & Caldeira, K., 2008. Ocean storage of CO₂. *Elements*, 4(5):319–324. <https://doi.org/10.2113/gselements.4.5.319>
- Adibi, N., Mohammandi, M., Ehsani, M.R., Khanmohammadian, E. 2020. Experimental investigation of using combined CH₄/CO₂ replacement and thermal stimulation methods for methane production from gas hydrate in the presence of SiO₂ and ZnO nanoparticles. *Journal of Natural Gas Science and Engineering*, 84:103690.
- Adu, E., Zhang, Y., Liu, D., 2019. Current Situation of Carbon dioxide capture, storage, and enhanced oil recovery in the oil and gas industry. *The Canadian Journal of Chemical Engineering*, 97:1048-1076.
- Alezi, D., Belmabkhout, Y., Suyetin, M., Bhatt., P.M., Weselinski, L.J., Solovyeva, V., Adi, K., Spanopoulos, I., Trikalitis, P.N., Emwas, A.H., Eddaoudi, M. 2015. *Journal of American Chemical Society*, 137(41) 13308-13318.
- Aliabadi, M., Rasoolzadeh, A., Esmailzadeh, F, and Alamdari, A. 2015. Experimental Study of Using CuO Nanoparticles as a Methane Hydrate Promoter. *Journal of Natural Gas Science & Engineering* 27:1518-1522.
- Allison, E., & Boswell, R. 2009. Overview of the United States Department of Energy's Gas-hydrate research program: 2000 to 2005. in T. Collett, A. Johnson, C. Knapp, and R. Boswell, eds., *Natural Gas Hydrates—Energy resource potential and associated geologic hazards: AAPG Memoir*, 89:146-219.
- Almenningen, S., Graue, A., Ersland, G. 2021. Experimental Investigation of critical parameters controlling CH₄-CO₂ exchange in sedimentary CH₄ hydrates. *Energy & Fuels*, 35(3):2468-2477.
- Al-Mamun, M. R., Ding, Y., Khan, M. R., & Chow, C. W. K. 2019. Enzyme-based capture of carbon dioxide from flue gas: A review. *Renewable and Sustainable Energy Reviews*, 104, 62-71.
- Amon, D. J., Gollner, S., Morato, T., Smith, C. R., Chen, C., Christiansen, S., Currie, B., Drazen, J. C., Fukushima, T., Gianni, M., Gjerde, K. M., Gooday, A. J., Grillo, G. G., Haeckel, M. , Joyini, T., Ju, S. J., Levin, L. A., Metaxas, A., Mianowicz, K., Molodtsova, T. N., Narberhaus, I., Orcutt, B. N., Swaddling, A., Tuhumwire, J., Palacio, P. U., Walker, M., Weaver, P., Xu, X. W., Mulalap, C. Y., Edwards, P. E. T. and Pickens, C. 2022. [Assessment of scientific gaps related to the effective environmental management of deep-seabed mining](#). *Marine Policy*, 138.
- Arca, S., Poletti, L., Poletti, R., Alessandro, E.D. 2011. Upgrading of Biogas Technology through the application of Gas Hydrates in: S.-B. sn., (Ed.), 7th International Conference on Gas Hydrates (ICGH 2011) Edinburgh, United Kingdom.
- Aregbe, Z.C. 2017. Gas-hydrate-Properties, formation and benefits. *Open Journal of Yangtze Oil and Gas* 2(1):27-44.
- Arjang, S., Manteghian, M., Mohamma, A. 2013. Effects of synthesized silver nanoparticles in promoting methane hydrate formation at 4.7 MPa and 5.7 MPa. *Chemical Engineering Research and Design*, 9:1050 – 1054.

Arlota, C., Costa, H.K.M. 2021. Climate change, carbon capture and storage (CCS), energy transition, and justice: where we are now, and where are (should be) we headed? Carbon Capture and Storage in International Energy Policy and Law.

Ataei, S., Fakhroei, Z., and Vatani, A. 2013. Effect of nanoparticles in facilitating gas hydrate. Second national Iranian conference on gas hydrates., Department of chemical, oil and gas engineering of Semnan university, Iran.

Aroora, A., Kumar, A., Bhattacharjee, G., Balomajumder, C., Kumar, P. 2021. Hydrate-Based Carbon Capture Process: Assessment of various packed Bed systems for Boosted Kinetics of Hydrate Formation. *Journal of Energy Resource Technology*, 143(3):033005.

Babaei, S. 2015. Hydrate Phase Equilibrium Studies for Xe , Ar , Kr , and CF₄ In the presence of Aqueous Solutions. PhD Thesis. University of Kwazulu Natal, Durban, South Africa.

Babaei, S.; Hashemi, H.; Mohammadi, A. H.; Naidoo, P., Ramjugernath, D. 2015. Kinetic and thermodynamic behaviour of CF₄ clathrate hydrates. *Journal of Chemical Thermodynamics*. 81, 52-59.

Babaei, S., Hashemi, H., Javanmardi, J., Eslamimanesh, A., Mohammadi, A.H. 2012. Thermodynamic model for prediction of phase equilibria of clathrate hydrates of hydrogen with different alkanes, alkenes, alkynes, cycloalkanes or cycloalkene. *Fluid phase equilibria*, 336:71-78.

Babu, P., N. Abhishek, Z. R. Chong, ZDaraboina, N, Mohammad, A., Bamaga O.A., and Linga, P. (2020). Hydrate-based desalination (HyDeal) process employing a novel prototype design. *Chemical Engineering Science*, 218: 115563.

Babu, P., Linga, P., Kumar., R., Englezos., R. Wang, S. 2015. A review of the hydrate-based gas separation (HBGS) process for carbon dioxide pre-combustion capture. *Energy*, 85:261-279.

Babu, P., Yang, S.H.B., Dasgupta, S., and Linga P., 2014. Methane Production from Natural Gas Hydrates via Carbon Dioxide Fixation. *Energy Procedia*, The 6th International Conference on Applied Energy 61: 1776 – 1779.

Babu, P., Kumar, R., Linga, P. 2013. Pre-combustion capture of carbon dioxide in a fixed bed reactor using the clathrate hydrate process. *Energy*, 50:364-373.

Babu, P., Kumar, R., Linga, P. 2004. Unusual behaviour of propane as a co-guest during hydrate formation in silica sand: Potential application to seawater desalination and carbon dioxide capture. *Chemical Engineering Science*, 117:342-351.

Bai, D., Zhang, X., Chen, G., Wang, W. 2012. Replacement mechanism of methane hydrate with carbon dioxide from microsecond molecular dynamics simulations. *Energy & Environmental Science*, 5:7033.

Barnard, M. 2019. Best Carbon Capture Facility In World Emits 25 Times More CO₂ Than Sequestered. <https://cleantechnica.com/2019/06/12/best-carbon-capture-facility-in-world-emits-25-times-more-co2-than-sequestered/>. *CleanTechnica*, June 12th, 2019.

Beauchamp, B. 2004. Natural gas hydrates: myths, facts, and issues. *C.R Geoscience* 336: 751-765.

Belandria, V. 2012. Hydrate Phase Equilibria Study of CO₂ Containing Gases in Thermodynamic Promoter Aqueous Mixtures (Issue 2012ENMP0018) PhD Thesis. Paris Institute of technology. <https://pastel.archives-ouvertes.fr/pastel-00718604>.

Belosludov, V. R., Bozhko, Y.Y., Subbotin, O.S., Belosludov, R.V., Zhdanov, R.K., Gets, K.V., Kawazoe, Y. 2018. Influence of N₂ on formation conditions and guest distribution of mixed CO₂+CH₄ gas hydrates. *Molecules* 23(12): 336.

Belosludov, V. R., Bozhko, Y.Y., Gets, K.V., Subbotin, O.S., Kawazoe, Y. 2018. Clathrate hydrate for energy storage and transportation. *IOP Conf. Series: Journal of Physics: Conf. Series* 1128: 012031.

Belosludov, R. V., Subbotin, S.O., Krupski, S.D., Belosludov, V.R., Kawazoe, Y., Kudoh, J.2007. Physical and Chemical Properties of Gas Hydrates: Theoretical aspects of energy storage application. *Material Transactions* 48: 704-710.

Bhattacharjee, G., Kumar, A., Sakpal T., Kumar, R. 2015. Carbon dioxide sequestration: Influence of porous media on hydrate formation kinetics. *Sustainable Chemistry & Engineering*, 3(6):1205-14.

Bohrmann, G., and Torres, M.E. 2006. Gas Hydrates in Marine Sediments, in *Marine Geochemistry*, H.D. Schulz and M. Zabel, Editors. Springer Berlin Heidelberg: Berlin, Heidelberg. p. 481-512.

Bowyer, N., McNulty, B. 2022. Africa's competitive edge as a clean hydrogen hub. *Energy Notes*, 4 October 2022. Herbert Smith freehills.

Borzone, E.M., Baruj, A., Meyer, G.O. 2017. Design and operation of a hydrogen purification prototype based on metallic hydrides. *Journal of Alloys and Compounds*, 2190-2198.

Breidenich, C., Magraw, D., Rowley, A., Rubin, J.W. 1988. The Kyoto Protocol to the United Nations framework convention on climate change. *The American Journal of International Law* 92: 315-331.

Brewer, P.G., Friederich, G., Peltzer, E., Orr, F.M. 1999. Direct experiments on the ocean disposal of fossil fuel CO₂. *Science*. 284(5416): p. 943-945.

Bronwyn, K. S. 2014. Investigation into potential gas hydrate and gas zones off the South African coastline. *Chemical Engineering*. Cape Town, South Africa, University of Cape Town. Master of Science.

Budinis, S., Krevor S., Dowell N.M., Brandon, N., Hawkes, A. 2018. An assessment of CSS cost, barriers, and potential. *Energy Strategy Reviews* 22:61–81.

Cannone, S. F., Lanzini A., Santarelli, M. 2021. A Review on CO₂ capture Technologies with Focus on CO₂-Enhanced methane recovery from hydrates. *Energies* 14: 387.

Carroll, J. 2014. *Natural Gas Hydrates: A Guide for Engineers* (3rd edition). Gulf Professional Publishing.

Castellani, B., Rossetti, G., Tupsakhare, S., Rossi, F., Nicolini, A., Castaldi, M.J. 2016. Simulation of CO₂ storage and methane gas production from gas hydrates in a large-scale laboratory reactor. *Journal Petroleum Science Engineering*, 147:515-527.

Castellani, B., Morini, E., Filippini, M., Nicolini, A., Cotana, F., Rossi, F. 2014. Engineering, and process aspects of hydrate-based technology for energy applications, 14th CIRIAF National Congress: Energy, Environment and Sustainable Development, Perugia, Italy.

Chapoy, A., Anderson, R., Tohidi, B. 2007. Low-Pressure Molecular Hydrogen Storage in Semi-Clathrate hydrates of Quaternary Ammonium Compounds. *Journal of American Chemical Society Communications*, 129:746-747.

Chari, V.D., Prasad, S.R.P., Murthy, S.R. 2015. Hollow silica: A novel material for methane storage. *Oil & Gas Science and Technology*, 70(6):1125-1132.

Chattaraj, P.K., Bandaru, S., Mondal, S. 2011. Hydrogen storage in Clathrate Hydrates. *Journal Physical. Chemistry. A*, 155:187-193.

Chatti, I., Delahaye, A., Fournaison, L., Petitet, J.P. 2005. Benefits and Drawbacks of Clathrate Hydrates: A Review of Their Areas of Interest. *Energy Conversion and Management* 46(9-10):1333-1343.

Chejara, A., Kvamme B, Vafaei M.T, Jemai K. 2013. Simulations of long-term methane hydrate dissociation by pressure reduction using an extended RetrasoCodeBright simulator, *Energy Conversation Management*, 68:313–23.

Chen, Y.A., Chu L.K, Chu C.K., Ohmura, R., Chen L.J. 2019. Synthesis of methane hydrate from Ice powder accelerated by doping ethanol into methane gas. *Scientific Reports. Nature research*, 9:12345.

Chen, Y., Gao, Y.H., Chen, L.T., Wang, X.R., Liu, K., Sun, B.J. 2019. Experimental investigation of the behaviour of methane gas hydrate hydrates during depressurisation assisted CO₂ replacement. *Journal of Natural Gas Science and Engineering*, 61:284-292

Choi, J.W., Chung, J.T., Kang, Y.T. 2014. CO₂ hydrate formation at atmospheric pressure using high efficiency absorbent and surfactants. *Energy*, 78:869-876.

Cousins, A., Huang, S., Cottrell, A., Feron, P.H.M., Chen E., Rochelle, G. T. 2015. Pilot-scale parametric evaluation of concentrated piperazine for CO₂ capture at an Australian coal-fired power station. *Greenhouse Gases: Science and Technology*; 5:7-16.

Cowdhury, F.A., Yamada, H., Higashii, T., Goto, K., Onoda, M. 2013. CO₂ capture by tertiary amine absorbents A performance comparison study. *Industrial & Engineering Chemistry Research*, 52(24):8323-8331.

Cranganu, C. 2009. In-situ thermal stimulation of gas hydrates. *Journal of Petroleum Science and Engineering*, 65:76-80.

Croeser N. 2017. Preliminary investigation into the use of gas hydrate technology for the treatment of Vinasse. MSc.Eng. thesis. Chemical Engineering Department, University of KwaZulu-Natal, Durban, South Africa.

Croeser, N., Babae, S., Naidoo, P., Ramjugernath, D. 2019. Investigation into the use of Gas Hydrate technology in the treatment of vinasse. *Fluid Phase Equilibrium*. 492, 67-77.

Dagdougui, H., Ouammi, A., 2018. Compressed Hydrogen Storage - an overview Science Direct Topics.

Dai, S., Santamarina, J.C., Waite, W.F., Kneafsey, T.J. 2021. Hydrate morphology: Physical properties of sands with patchy hydrate saturation. *Journal of Geophysical Research: Solid Earth*, 117: B11.

Daily, A. and Poirier, E. 2011. Evaluation of an industrial pilot densified MOF-177 adsorbent as an on-board hydrogen storage medium. *Energy Environmental Science* 4, 3527-3534.

Daniel, A. 2019. In Iceland, Turning CO₂ into Rock could be a big breakthrough for Carbon dioxide capture. *Pulitzer Center on Crisis Reporting.*, May 06, 2019.

Davoodabadi, A., Mahmoudi, A., Ghasemi, H. 2021. The potential of Hydrogen hydrate as a future Hydrogen Storage medium. *ISCIENCE*, 2021: 101907.

Deaton, W. M. & Frost, E.M., 1946. Gas hydrates and their relation to the operation of natural gas pipelines. *Oil Gas J*, 45, 170-178.

Demirbas, A. 2010. Methane hydrates as a potential energy resource: Part 2- Methane production processes from gas hydrates. *Energy Conversion and Management* 51: 1562-1571.

Demirbas A. 2009. Methane from gas Hydrates in the Black Sea. *Energy Sources*, Part 1: Recovery, Utilization, and Environmental Effects, 32(2):165-71.

Deng, Z., Wang, Y., Yu, C., Lang, X., Wang, S., Fan, S. 2021. Promoting methane hydrate formation with expanded graphite additives: Application to solidified natural gas storage. *Fuel*, 299:120867.

Deuser, C., Bigalke, N., Kossel, E., Haeckel, M. 2012. Methane production from gas hydrate deposits through injection of supercritical CO₂. *Energies*, 5:2112-2140.

Deschamps, J., Dalmazzone, D. 2010. Hydrogen storage in Semi clathrate hydrates of Tetrabutyl Ammonium Chloride and Tetrabutyl Phosphonium Bromide. *Journal Chemical Engineering Data*, 55:3395-3399.

Dicharry, C., Duchateau C., Asbaï, H., Broseta D., Torre J.P. 2013. Carbon dioxide gas hydrate crystallization in porous silica gel particles partially saturated with a surfactant solution. *Chemical Engineering Science*, 98:88-98.

Ding, Y.L., Wang, H.Q., Xu, C.G., Li, X.S. 2020. The effect of CO₂ partial pressure on CH₄ recovery in CH₄-CO₂ swap with simulated IGCC Syngas. *Energies*, 13:1017.

Ding, Y.L., Xu, C., Yu, Y., and Li X. 2017. Methane recovery from natural gas hydrate with simulated IGCC syngas., *Energy*, 120:192-198.

Duarte, A.R.C., Shariati, A., Peters, C.J. 2009. Phase Equilibrium measurements of Structure sH Hydrogen Clathrate hydrates with various promoters. *Journal Chemical Engineering Data*, 2009; 54:1628-1632.

DW documentary, 2021. Norway and CO₂ emissions. [Beneath the waves - Norway and CO2 emissions – DW – 11/21/2020.](#)

Dyadin, Y.A., Bondaryuk, I.V., Aladko, L.S. 1995. Stoichiometry of Clathrates. *Journal of Structural Chemistry*, 36(6):1088-1141.

Dyadin, Y.A., Larionov, E.G., Manakov, A.Y., Zhurko, F.V., Aladko, E.Y., Mikina, T.V., Komorov, V.Y. 1999. Clathrate hydrates of hydrogen and neon. *Mendeleev Commun.*, 9(5): 209-210.

Einloft, S. 2020. Encapsulated liquid sorbents for CO₂ capture. Franciele Longaray Bernard, in *Advances in Carbon Capture*.

Energy Africa, 2022. Sasol, ArcelorMittal to jointly explore green hydrogen, carbon capture projects. *Mining.com*. 18 October. <https://www.mining.com/web/sasol-arcelormittal-to-jointly-explore-green-hydrogen-carbon-capture-projects/>

Englezos, P., Ripmeester, J.A., Kumar, R., Linga, P. 2008. Hydrate processes for CO₂ capture and scale-up using a new apparatus. *Proceedings of the 6th International Conference on Gas Hydrates (ICGH 2008)*, Vancouver, British Columbia, Canada.

Englezos, P., & Hall, S., 1994. "Phase equilibrium data on carbon dioxide hydrate in the presence of electrolytes, water-soluble polymers and montmorillonite". *Journal of Chemical Engineering*, 72, 887–793.

Environmental care, 2021. Carbon capture, storage and use partnership. [society.sasol.com/carbon-storage-and-use-partnership](https://www.sasol.com/carbon-storage-and-use-partnership).

Elwell, L. C. & Grant, W.S. 2006. Technology options for capturing CO₂ –Special reports. *My Power -Business & Technology for the Global Generation Industry Since 1882*.

Eslamimanesh, A., Mohammadi, A. H., Richon, D., Naidoo, P., Ramjugernath, D. 2012. Application of gas hydrate formation in separation processes: A review of experimental studies. *Journal of Chemical Thermodynamics*, 46:62–71.

Fakir, T., Babae, S., Naidoo, P. 2021. Application of gas hydrate for the treatment of vinasse: Phase equilibrium and kinetic investigations. *Journal of Chemical & Engineering data*. 66(1), 504-14.

Fan, S., Yu, W., Wang, Y., Lang, X., Wang, S., Li, G., Huang, H. 2022. Investigation of enhanced exploitation of natural gas hydrate and CO₂ sequestration combined gradual heat stimulation with CO₂ replacement in sediments. *Journal of Natural Gas Science and Engineering*, 104:104686.

Farahani, V.M., 2021. Insights into climate-driven evolution of gas hydrate-bearing permafrost sediments. Ph.D thesis. The School of Energy, Geoscience, Infrastructure and Society. Heriot-Watt University. Edinburgh, UK.

Farrusseng, D., Daniel, C., Connor, H., McCloskey, P., Didriksen, T., Blom, R., Velte, R., Fuedener, G., Gantenbein, P., Persdorf, P., Dagueneget, F.X., Meunier, F. 2018. Pilot scale production and demonstration of low cost MOFs for chilling applications. MOF2018. Auckland New Zealand.

Flak, A. 2011. South Africa's top polluters. <https://www.reuters.com/article/safrica-carbon-emitters/table-south-africas-top-carbon-polluters-idUSL6E7IK1ZU20111006>. Carbon Disclosure Project 2010. Retrieved 15 April, 2019.

- Filarsky, F., Schmuck, C., Schultz, H.J. 2019. Development of a gas hydrate absorption for Energy storage and gas separation-Proof of concept based on natural gas. 10th International conference on Applied Energy (ICAE2018), 22-25 August 2018, Hong Kong, China. Energy Procedia, 158:5367-5373.
- Fitzgerald, G.C. 2014. Multi-scale Analysis of Methane Gas Hydrate Formation and Dissociation via Point Source Thermal Stimulation and Carbon Dioxide Exchange. Ph.D. Thesis. Columbia University.
- Florusse, L.J., Peter, C.J., Schoonman, J., Hester, K.C., Koh, C.A., Dec, S.F., Marsh, K.N., Sloan, E.D. 2004. Stable low-pressure hydrogen clusters stored in a binary Clathrate hydrate. Science, 306:469.
- Frye M, 2008. Preliminary Evaluation of in place Gas Hydrate Resources: Gulf of Mexico Outer Continental Shelf: MMS OCS Report 2008-004.
- Furukawa, H., Cordova, K., O’Keeffe, M., Yaghi, O.M., 2013. The chemistry and application of metal-organic frameworks. Science, 341, 1230444.
- Galfre.A., Brantuas P., Cameirao A., Ouabbas Y., Bouillot B., Herri J. M. Herslund P.J., Solms N.V. 2014. CO₂ capture by using hydrates: 1) The benefits and the counterpart of thermodynamic additives. The 8th International Conference on Gas Hydrates, Jul 2014 Perkin, China pp T1-73.
- Galloway, T. J. Travis J., Ruska, W., Chappellear, P. S., Patsy S., Kobayashi, R. 1970. Experimental Measurement of Hydrate Numbers for Methane and Ethane and Comparison with Theoretical Values. Industrial Engineering Chemical Fundamentals (2), 237-243.
- Gambelli, A.H. 2021. An experimental description of the double positive effect of CO₂ injection in methane hydrate deposits in terms of climate change mitigation. Chemical Engineering Science, 233:116430.
- Gambelli, A.M., Rossi, F. 2019. Natural gas hydrates: Comparison between two different applications of thermal stimulation for performing CO₂ replacement. Energy, 172:423-434.
- Ganji, H., Manteghian, M., Mofrad, H.R. 2007. Effect of mixed compounds on methane hydrate formation and dissociation rates and storage capacity. Fuel processing Technology, 88:891-895.
- Ge, B.B., Zhong, D.L., Lu, Y.Y. 2019. Influence of water saturation and particle size on methane hydrate formation and dissociation in fixed bed of silica sand. Energy Procedia, 158:5402-5407.
- Geng, C.Y., Wen, H., Zhou, H. 2009. Molecular simulation of the potential of methane reoccupation during the replacement of methane hydrate by CO₂. J. Phys. Chem, 113:5463-5469.
- Gentzis, T. 2000. Subsurface sequestration of carbon dioxide-an overview from an Alberta 9(Canada) perspective. International Journal of Coal Geology, 43(1-4):287-305.
- Ghaani, M.R., Allen, C.C.R., Young, J.M., Nandi, P.K., Dandare, S.U., Skvortsov, T., English, N.J. 2019. Microbial stabilization, and kinetic enhancement of marine methane hydrates. Geomicrobiology Journal, 37(3) 279-286.
- Gielen, D. 2003. Proceedings of the 2nd annual conference on carbon sequestration. International Energy Agency, 9 Rue de la Fédération, Paris, France Alexandria, VA; May 5–8 (2003).

Gimaltdinov, K., Stolpovskii, M.V., Khasanov, M.K. 2018. Recovery of methane from gas hydrates in a porous medium by injection of carbon dioxide. *Journal of Applied Mechanics and Technical Physics*, 59, (1):1-8.

Goel, N. 2006. In situ methane hydrate dissociation with carbon dioxide sequestration: Current knowledge and issues. *Journal of Petroleum Science and Engineering*, 51:169-184.

Grim, R. G., Barnes, B C., Lafond, P.G., Kockelmann, W.A., Keen, D.A., Soper, A.K., Hiratsuka, M., Yasuoka, K., Koh, C.A., Sum, A.K. 2014. Observation of Interstitial Molecular Hydrogen in Clathrate Hydrates. *Angewandte Communications Chem Int Ed*, 53:10710-10713.

Grim, R.G., Kerkar, P.B., Sloan, E.D., Koh, C.A., Sum, A.K. 2012. Rapid hydrogen hydrate growth from non-stoichiometric tuning mixtures during liquid nitrogen quenching. *The Journal of Chemical Physics*, 136 234504.

Guerin, G., Goldberg, D., Collett, T.S. 2005. Sonic attenuation in the JAPEX/JNOC/GSC et al. Mallik 5L-38 gas hydrate production research well; in *Scientific Results from the Mallik 2002 Gas Hydrate Production Research Well Program, Mackenzie Delta, Northwest Territories, Canada*, (ed.) S.R. Dallimore and T.S. Collett; Geological Survey of Canada, Bulletin, 585;9

Gulen, S.C, 2022. Green hydrogen powering gas turbines: realistic strategy? *Turbine Power Plants – Applications in Sustainable Power*. Cambridge University Press.

Guo, D., Wang, H., Shen, Y., An, Q. 2020. Thermal decomposition and diffusion of methane in clathrate hydrates from quantum mechanics simulations. *Royal Society of Chemistry*, 10:14753-14760.

Gupta, A., Baron, G.V., Pereault, P., Lenaerts, S., Ciocarlan, R.G., Cool, P., Mileo, P.G.M., Rogge, S., Speybroeck, V.V., Watson, G., Voort P. V. D., Houllberghs, M., Breynaert, E., Martens, Denayer, J.F.M. 2021. Hydrogen clathrates: Next generation hydrogen storage materials. *Energy Storage Materials*, 41:69-107.

Gupta, A. 2009. Modelling pure methane hydrate dissociation using a numerical simulator from a novel combination of X-ray computed tomography and macroscopic data. Lawrence Berkeley National Laboratory, 2009.

H₂ Bulletin, 2021. Kawasaki working on hydrogen storage infrastructure, 8 January 2021. h2bulletin.com/kawasaki-working-on-hydrogen-storage-infrastructure/.

Haeckel, M. 2008. GEOMAR Helmholtz Centre for Ocean Research Kiel: Submarine Gas Hydrate Reservoirs.

Haeckel M., Suess E., Wallmann K., Rickert, D. 2004. Rising methane gas-bubbles form massive hydrate layers at the seafloor. *Geochimica et Cosmochimica Acta* 68(21), 4335-4345

Hassan, H., Javidani, A.M., Mohammadi, A., Pahlavanzadeh, H., Farizhendi, S.A., Mohammadi A.H. 2021. Effects of Graphene oxide Nanosheets and Al₂O₃ nanoparticles on CO₂ uptake in semi-clathrate hydrates. *Chemical Engineering. Technology*, 44(1):48-57.

Hassanpouryouzband, A., Joonaki, E., Farahani, M.V., Takeya, S., Carolyn R., Yang, J., English, N.J., Schicks, J.M., Edlmann, K., Mehrabian, H., Aman, Z.M., Tohidi B. 2020. Gas hydrates in Sustainable Chemistry. *Royal Society of Chemistry*, 49: 5225-5309.

- Hassanpouryouzband, A., Yang, J., Okwananke, A., Burgass, R., Tohidi, B., Chuvilin, E., Istomin, V., Bukhanov, B. 2019. An Experimental investigation on the kinetics of integrated methane recovery and CO₂ sequestration by Injection of flue gas into permafrost methane hydrate reservoirs. *Science Reports*, 9(1):1-9.
- Hassanpouryouzband, A., Yang, J., Tohidi, B., Chuvilin, E., Istomin, V., Bukhanov, B., Cheremisin, A. 2018. CO₂ Capture by Injection of Flue Gas or CO₂-N₂ Mixtures into Hydrate Reservoirs: Dependence of CO₂ Capture Efficiency on Gas Hydrate Reservoir Conditions. *Environmental Science and Technology*, 52:4324-4330.
- He, Y., Sun, M, T., Chen, C., Zhang, G.D., Chao, K., Lin, Y., Wang, F. 2019. Surfactant-based promotion to gas hydrate formation for energy storage. *Journal of Materials Chemistry A*, 7:21634-21661.
- Herslund, P. J. 2013. Thermodynamic and Process Modelling of Gas Hydrate Systems in CO₂ Capture Processes. Department of Chemical and Biochemical Engineering. Lyngby, Technical University of Denmark. Ph.D.
- Herzog, H., Golomb, D. 2004. Carbon dioxide capture and storage from fossil fuel use. *Encyclopaedia of Energy*, 1:1-11.
- Heydari, A., Peyvandi, K. 2020. Study of biosurfactant effects on methane recovery from gas hydrate by CO₂ replacement and depressurization. *Fuel*, 272:117681.
- Hirohama, S. Shimoyama, Y., Wakabayashi, A., Tatsuta, S., Nishida, N. 1996. Conversion of CH₄-hydrate to CO₂-hydrate in liquid CO₂. *Journal of Chemical Engineering of Japan*, 29:1014-1020.
- Ho, L.C., Babu, P., Kumar, R., Linga, P. 2013. HBGS (hydrate-based gas separation) process for carbon dioxide employing an unstirred reactor with cyclopentane. *Energy*, 63:252-259.
- Holloway, S. 2005. Underground sequestration of carbon dioxide-a viable greenhouse mitigation option. *Energy*, 30:(11-12) 2318-2333.
- Honeywell, 2022. Sasol and ArcelorMittal join forces to develop carbon-capture technology. 18 October 2022. [Chemengonline.co/sasol-and-arcelormittal-join-forces-to-develop-carbon-capture-technology](https://www.chemengonline.co/sasol-and-arcelormittal-join-forces-to-develop-carbon-capture-technology).
- Hosseini, D., Leonel, Z.Y., Xia, L. 2015. Recent advances in gas hydrate-based CO₂ capture. Curtin University.
- Hsieh, P.Y., Sean, W.Y., Sato, T., Seo, Y.W. 2020. Mesoscale Modelling of Exploiting Methane hydrate by CO₂ replacement in homogeneous porous media. *International Journal of Heat and Mass Transfer*, 158:119741.
- Hua, T.Q., Ahluwalia, R.K., Peng, J.K., Kromer, M., Lasher, S., McKenney, K., Law, K., Sinha, J., 2011. Technical assessment of compressed hydrogen storage tank systems for automotive applications. *International Journal Hydrogen Energy* 36, 3037–3049.

Hydrogen society roadmap for South Africa, 2021. Department of Science and Innovation. Securing a clean, affordable and sustainable energy future for South Africa. https://www.dst.gov.za/images/South_African_Hydrogen_Society_RoadmapV1.

IEA, 2019. The Future of hydrogen - Analysis. IEA, Japan. <https://www.iea.org/reports/the-future-of-hydrogen>.

Jadhwar, P., Yang, J.H., Chapoy, A., Tohidi, B. 2021. Subsurface carbon dioxide sequestration and storage in methane hydrate reservoirs combined with clean methane energy recovery. *Energy Fuel*, 35(2):1567-1579.

Janicki, G., Schluter, S., Henning, T., Lyko, H., Deerberg, G. 2011. Simulation of methane recovery from gas hydrates combined with storing carbon dioxide as hydrates. *Journal of Geological Research*, 1-15.

Jayasinghe, A.G., and Grozic, J.L.H. 2013. Estimating pore space hydrate saturation using dissociation gas evolution measurements: In relevance to laboratory testing of natural or artificially synthesised hydrate-bearing soil specimens. *Journal of Geological Research*, 815841.

Jinhai, Y., Okwananke A., Tohidi, B., Chuvilin, E., Maerle, K., Istomin, V., Bukhanov B., Cheremisin, A. 2017. Flue gas injection into gas hydrate reservoirs for methane recovery and carbon dioxide sequestration. *Energy Conversion and Management*, 136:431–438.

Joseph, J., Singh, D.H., Kumar, P., Dewri, S.K., Tandi, C., Singh, J., 2015. State of the art Gas Hydrates and Relative Permeability of Hydrate Bearing Sediments. *Marine Georesources & Geotechnology*, 34(5): 450-464.

Jung, J.W., Espinoza, D.N., Santamarina, J.C. 2010. Properties, and phenomena relevant to CH₄-CO₂ replacement in hydrate-bearing sediments. *Journal of Geophysical Research*, 115: B10102.

Kamran-Pirzaman, A., Pahlavanzadeh, H., Mohammadi, A.H. 2013. Hydrate phase equilibria of furan, 1,4-dioxane, TBAC and TBAF. *The Journal of Chemical Thermodynamics*, 64:151-158.

Kang, S. P., Pee J., Seo, Y. 2013. Pre-combustion capture of CO₂ by gas hydrate formation in silica gel pore structure. *Chemical Engineering Journal* 218: 126-132.

Karame, I., Shaya, J., Srour, H. 2018. Carbon dioxide chemistry capture and oil recovery. Interchopen London.

Kashiev, D., & Firoozabadi, A. 2002. Nucleation of gas hydrates. *Journal of Crystal Growth*, 243:476-89.

Kashkouli, P.I. 2015. Thermodynamic studies on CO₂ capture through gas hydrate formation technology. PH. D thesis. School of Chemical Engineering. University of KwaZulu Natal.

Kaye, S.S., Daily, A., Yaghi, O., Long, J.R. 2007. Impact of preparation and handling on the hydrogen storage properties of Zn₄O(1,4-benzenedicarboxylate)₃ (MOF-5). *Journal of American Chemical Society*, 129; 14176-14177.

Kezirian, M. T., & Phoenix, S. L. 2017. Natural Gas Hydrate as a Storage Mechanism for Safe, Sustainable and Economical Production from Offshore Petroleum Reserves. *Energies*, 10:828.

Khalik, M. S., & Behzad, P. 2018. Recent advances on carbon dioxide capture through a hydrate-based gas separation process. *Green processes and technologies* 11: 22-26.

Khlebnikov, V.N., Antonov, S.V., Mishin, A.S., Bakulin, D.A., Khamidullina, I.V., Meng, L., Vinokurov, V.A., Gushchin, P.A. 2017. A new method for the replacement of CH₄ with CO₂ in natural gas hydrate production. *Natural Gas Industry*, 1-7.

Khot, S. & Sanjay, Y. 2017. Methane Hydrate Gas Storage Systems for Automobiles. *International Journal of Renewable Energy Research*, 7.

Kim, E.J., Siegelman, R.L., Jiang, H.Z.H., Forse, A.C., Lee, J.H. 2020. Cooperative carbon capture and steam regeneration with tetraamine-appended metal-organic frameworks. *Science*, 369(6502):392-396.

Klauda, J.B., & Sandler, S.I. 2001. Modelling gas hydrate phase equilibria in laboratory and natural porous media. *Industrial & Engineering Chemistry Research*, 40:4197-208.

Klauda, J. B., & Sandler, S.I. 2000. A fugacity model for gas hydrate phase equilibria. *Industrial Engineering Chemical Research* 39, 3377–3386.

Kleinberg, R.L., Flaum, C., Griffin, D.D., Brewer, P.G., Malby, G.E., Peltzer, E.T., Yesinowski, J.P. Deep Sea NMR: 2003. Methane hydrate growth habit in porous media and its relationship to hydraulic permeability, deposit accumulation and submarine slope stability. *Journal of Geophysical Research*, 108:2508.

Koga, T., Wong, J., Endoh, M.K., Mahajan, D., Gutt, C., Satija, S.K. 2010. Hydrate Formation at the Methane/Water Interface on the Molecular Scale. *Langmuir*, 26(7): p. 4627-4630.

Koh, C.A., Sloan, E.D., Sum, A.K., Wu, D.T. 2011. Fundamentals and Applications of Gas Hydrates, in *Annual Review of Chemical and Biomolecular Engineering*, Vol 2, J.M. Prausnitz, Editor. 2011, Annual Reviews: Palo Alto. p. 237-257.

Komatsu, H., Ota, M., Smith jr, R.L., Inomata, H. 2013. Review of CO₂-CH₄ clathrate hydrate replacement reaction laboratory studies-Properties and kinetics. *Journal of the. Taiwan Institute of Chemical Engineering*, 44:517-537.

Kossel, E., Bigalke, N.K., Deusner, C., Haeckel, M. 2021. Microscale Processes and Dynamics during CH₄-CO₂ guest-molecule exchange in gas hydrates. *Energies*, 14:1763.

Kumar, A., Maini, B., Bishnoi, P., Clarke, M., Zatsepina, O., Srinivasan, S., 2010. Experimental determination of permeability in the presence of hydrates and its effect on the dissociation characteristics of gas hydrates in porous media. *Journal of Petroleum Science and Engineering*, 70(1-2):114-22.

Kumar P., Turner D., Sloan E. D. 2004. Thermal diffusivity measurements of porous methane hydrate and hydrate-sediments mixtures. *Journal of Geophysical Research*, 109: B0.1207.

- Kvenvolden, K.A. 1999. Potential effects of gas hydrate on human welfare. National Academy of Sciences colloquium "Geology, Mineralogy, and Human Welfare,". Arnold and Mabel Beckman Center in Irvine, CA.: Proc. Natl. Acad. Sci.,
- Kvenvolden, K.A. 1988. Methane hydrates a major reservoir of carbon in the shallow geosphere *Chemical Geology*, 71:41-51.
- Lederhos, J.P., Long, J.P., Sum, A., Christiansen, R.L., Sloan, E.D. 1996. Effective kinetic inhibitors for natural gas hydrates. *Chemical Engineering of Science*, 51(8):1221-9.
- Lee, Y., Choi, W., Shin, K., Seo, Y. 2017. CH₄-CO₂ replacement occurring in sII natural gas hydrates for CH₄ recovery and CO₂ sequestration *Energy Conversion and Management*, 150:356-364.
- Lee, B.R., Koh, C.A., Sum, A.K. 2014. Quantitative measurement, and mechanisms for CH₄ production from hydrates with the injection of liquid CO₂. *Physical. Chemical Chem. Phys.*, 2014;16:14922.
- Lee, Y.J., Kawamura, T., Yamamoto, Y., Yoon, J.H. 2012. Phase equilibrium studies of tetrahydrofuran (THF) + CH₄, THF + CO₂, CH₄ + CO₂, and THF +CO₂ + CH₄ hydrates. *Journal of Chemical and Engineering Data*, 57, 3543-3548.
- Lee, J. Y., Ryu, B.J., Yun, T.S., Lee, J., Cho, G. 2011. Review on the Gas hydrate development and production as a new Energy Resource. *KSCE Journal of Civil Engineering* 15(4): 689-696.
- Lee, M.W., & Collet, T.S. 2009. Gas hydrate saturations estimated from fractured reservoirs at Site HGHP-01-10 Krishna-Godavari Basin India. *Journal of Geophysical Research*, 114.B07102.
- Lee, J.Y., Yun, T.S., Santamarina, J.C. 2007. Observations related to tetrahydrofuran and methane hydrates for laboratory studies of hydrate-bearing sediments. *Electronic Journal of the earth Science*, 8(6).001531.
- Lee, J., Lee, J., Kim, Y. 2016. Enhanced Gas Hydrate Methane Recovery Using Platinum Nanoparticles: Molecular Dynamics Simulation Study. *Journal of Physical Chemistry C*, 120(20), 10962-10969.
- Lee, H., Lee, J.W., Kim, D.Y., Park, J., Seo, Y.T., Zeng, H., Moudrakovski, I.L., Ratcliffe, C.I., Ripmeester, J.A. 2005. Tuning clathrate hydrates for hydrogen storage. *Nature*, 434:743.
- Lele, A. F., Hu, J., F. Kuznik, F., Osterland, T., Ruck W. K. L. 2015. Numerical Investigations of a Thermochemical heat storage system during the discharging. *ASME-ATI-UIT Conference on Thermal Energy Systems: Production, Storage, Utilization and the Environment* 17-20 May 2015.
- Leung, D.Y.C., Caramanna, G. and Valer, M.M.M. 2014. Overview of current status of carbon dioxide capture and storage technologies. *Renewable and Sustainable Energy Reviews*, 39:426-443.
- Li, Z.D, Tian, X, Li, Z, Xu, J, Zhang, H.X, Wang, D.J. 2020. Experimental study on growth characteristics of pore-scale methane hydrate. *Energy Reports*, 6:933-43.
- Li, L., Chung, T.-S., & Kulprathipanja, S. 2018. Mixed matrix membranes for CO₂ capture: a review. *Separation and Purification Technology*, 197, 306-327.

- Li, G., Kobayashi, H., Taylor, J.M., Ikeda, R., Kubota, Y., Kato, K., Takata, M., Yamamoto, T., Toh, S., Matsumura, S., Kitagawa, H., 2014. Hydrogen storage in Pd nanocrystals covered with a metal-organic framework. *Nature. Materials*. 13(8), 802–806.
- Li, X., Xu, C., Chen, Z., Wu, H., Cai, J. 2011. Effect of temperature fluctuation on hydrate-based CO₂ separation from fuel gas. *Journal of Natural Gas Chemistry*,20:647–653C.
- Li, X.S., Xu, C.G., Chen, Z.Y., Wu, H.J. 2011b. Hydrate-based pre-combustion carbon dioxide capture process in the system with tetra-n-butyl ammonium bromide solution in the presence of cyclopentane. *Energy*, 26:2518-2527.
- Lijith, K.P., Malagar, B.R.C., Singh, D.N. 2019. A comprehensive review on the geochemical properties of gas hydrate bearing sediments. *Marine and Petroleum Geology*, 104:270-285.
- Linga, P., Daraboina, N., Ripmeester, J.A., Englezos, P. 2012. Enhanced rate of gas hydrate formation in a fixed bed column filled with sand compared to a stirred vessel. *Chemical Engineering Science*, 68:617–623.
- Linga, P., Haligva, C., Nam, S.C., Ripmeester, J.A., Englezos P. 2009. Gas Hydrate Formation in a Variable Volume Bed of Silica Sand Particles. *Energy Fuels* 23:5496–5507.
- Linga, P., Kumar, R., Ripmeester, J.A., Enlezo, P. 2008. Hydrate processes for the CO₂ capture and scale up using a new apparatus. *Proceedings of the 6th International Conference on Gas Hydrates (ICGH 2008)*. Vancouver, British Columbia, Canada, Jul 6-10,2008.
- Lirio, C. F.S., Pessoa, F. L. P., Uller, A. M. 2013. Storage capacity of carbon dioxide hydrates in the presence of sodium dodecyl sulfate (SDS) and tetrahydrofuran (THF). *Chemical Engineering Science*, 96:118-123.
- Liu, J., Wei, Y., Meng, W., Li, P.-Z., Zhao, Y. and Zou, R. 2019. Understanding the Pathway of Gas Hydrate Formation with Porous Materials for Enhanced Gas Separation., *Journal of Cast*, 3206024.
- Liu, J., Ding, J.X., Liang, D.Q. 2018. Experimental study on hydrate-based gas separation of mixed CH₄/CO₂ using unstable ice in a silica gel bed. *Energy*, 157:54-64.
- Liu, Y., Hou, J., Zhao, H., Liu, X., Xia, Z. 2018. A method to recover natural gas hydrates with geothermal energy conveyed by CO₂. *Energy*, 144 :256-278.
- Liu, J., Zou, R., Zhao, Y. 2016. Recent development in porous materials for H₂ and CH₄. *Tetrahedron Letters*, 57(44) 4873-4881.
- Liu, W., Wang, S., Yang, M., Song Y., Wang, S., Zhao, J. 2015. Investigation of the induction time for THF hydrate formation in porous media. *Journal of Natural Gas Science and Engineering*, 24:357-364.
- Liu, X., Chen, Y., Hu, G., & Chen, G. 2015. Experimental investigation of water consumption for gas hydrate formation from water-in-oil emulsions. *Journal of Natural Gas Science and Engineering*, 24, 87-92.(b)
- Lovedy, J.S., & Nelmes, R.J. 2007. High-pressure gas hydrates. *Physical Chemistry Chemical Physics*, 10(7):913-1068.

- Løvø V, Elverhøi A, Antonsen P, Solheim A, Butenko G, Gregersen, O, Liestøl O. 1990. Submarine permafrost and gas hydrates in the northern Barents Sea, Norsk Polar institute Report Series, 56:171.
- Lu, B., Xu, T.F., Zhang, G.B. 2018. An experimental study on gas production from fracture-filled hydrate by CO₂ and CO₂/N₂ replacement. *Energy Conservation Management*, 165:738-747.
- Lubimbi, Z. 2017. The investigation of fluorinated solvents for carbon dioxide absorption. Master of Science Degree. University of Kwazulu Natal, Durban, South Africa.
- Ma, Z.W., Zhang, P., Bao, H.S., Deng, S. 2016. Review of fundamental properties of CO₂ hydrates and CO₂ capture and separation using hydration method. *Renewable and Sustainable Energy Reviews*, 53:1273-1302.
- Ma, S. and Zhou, H.C. 2010. Gas storage in porous metal-organic frameworks for clean energy applications. *Royal Society of Chemistry*, 46:44-53.
- Machens, C. 2006. Methane in the Arctic circle. Arctic Climate Issues 2011: Changes in Arctic Snow, Water, Ice, and Permafrost <http://www.amap.no/documents/doc/arctic-climate-issues-2011-changes-in-arctic-snow-water-ice-and-permafrost/129>.
- Maeck, A., DelSonto, T., McGinnis, D.F., Fischer, H., Flury, S., Schmidt, M., Fietzek, P., Lorke, A. 2013. Sediment Trapping by dam's greatest methane emissions hot spots. *Environmental Science & Technology*, 2013;47:8130-8137.
- Mai, B., C. S. Adjiman, A. Bardow, E. J. Anthony, A. Boston, S. Brown, P. S. Fennell, S. Fuss, A. Galindo, L. A. Hackett, J. P. Hallett, H. J. Herzog, G. Jackson, J. Kemper, S. Krevor, G. C. Maitland, M. Matuszewski, I. S. Metcalfe, C. Petit, G. Puxty, J. Reimer, D. M. Reiner, E. S. Rubin, S. A. Scott, N. Shah, B. Smit, J. P. M. Trusler, P. Webley, J. Wilcox and N. M. Dowell. 2018. Carbon capture and storage (CCS): the way forward. *Energy & Environmental Science* 11: 1062-1176.
- Makgalemele, A. 2015. Opportunities within Sasol Energy-Presented to the department of Energy. <https://www.energy.gov.za/files/WOESA/2015/northwest/Opportunities-within-Sasol-Energy.pdf>
- Makogon, Y. F., Holditch S.A. and Makogon. T.Y. 2007. Natural gas-hydrates-A potential energy source for the 21st century. *Journal of Petroleum Science and Engineering* 56: 14-31.
- Malagar, B. R. C., K. P. Lijith and D. N. Singh 2019. Formation & dissociation of methane in sediments: A critical review. *Journal of Natural Gas Science and Engineering* 65: 168-184.
- Mao, W.L., Mao, H.K., Goncharov, A.F., Struzhkin, V.V., Guo, Q., Hu, J., Shu, J., Russell J. H., Maddury S., Zhao, Y. 2002. Hydrogen Clusters in Clathrate Hydrate. *Science*, 297:2247.
- Maria, G.A. 2018. Natural gas recovery from hydrate compounds using CO₂ replacement strategies: experimental study on thermal stimulation. *Energy*, 148:647-654.
- Matizakurima F. 2020. Separation of noble gas mixtures of (Xe, Ar and Kr) using gas hydrate technology. Master of Science Degree. University of Kwazulu Natal, Durban, South Africa.
- Matsui, H., Jia, J., Tsuji, T., Liang, Y., Masuda, Y. 2020. Microsecond simulation study on the replacement of methane in methane hydrate by carbon dioxide, nitrogen, and carbon dioxide-nitrogen mixtures. *Fuel* 263:116640.

- Matsumoto, Y., Grim, R.G., Khan, N.M., Sugahara, T., Ohgaki, K., Sloan, E.D. 2014. Investigating the Thermodynamics stabilities of hydrogen and methane binary gas hydrates. *The Journal of Physical Chemistry*, 118:3783-8.
- McGrail, B.P., Schaefer, H.T., White, M.D., Zhu, T., Kulkarni, A.S., Hunter, R.B., Patil, S.L., Owen, A.T., Martin, P.F. 2007. Using Carbon dioxide to Enhance Recovery of Methane from Gas Hydrate Reservoirs: Final Summary Report., U. S Department of Energy. PNNL-17035.
- Mekala P, Busch M, Mech D, Patel RS, Sangwai JS. 2014. Effect of silica sand size on the formation kinetics of CO₂ hydrate in porous media in the presence of pure water and seawater relevant for CO₂ sequestration. *Journal of Petroleum Science and Engineering*, 122:1-9.
- Minagawa H, Ohmura R, Kamata Y, Ebinuma T, Narita H, Masuda Y. 2005. Water permeability measurements of gas hydrate-bearing sediments Fifth International Conference on Gas Hydrates Trondheim, Norway.
- Moghaddam, E.A., Larsolle, A., Tidaker, P., Nordberg, A. 2021. Gas hydrates as a means for biogas and biomethane distribution. *Frontiers in Energy Research*, 568879.
- Mohammadi, A., Manteghian, M., Mohammadi, A.H., Jahangiri, A. 2017. Induction time, storage capacity, rate of methane hydrate formation in the presence of SDS and silver nanoparticles. *Chemical Engineering Communications*, 24 (12):1420-1427.
- Mohammadi, A., Manteghian, A., Haghtalab A., Mohammadi, A.H., Abkenar. M.R. 2014. Kinetic study of carbon dioxide hydrate formation in presence of silver nanoparticles and SDS. *Chemical Engineering Journal* 237:387-395.
- Mohammadi, A. H., Anderson, R., & Tohidi, B. 2005. Carbon monoxide clathrate hydrates: Equilibrium data and thermodynamic modelling. *American Institute of Chemical Engineers Journal*, 51(10), 2825–2833.
- Mohan, M., Sharma, V.K., Kumar, E.A., Gayathri, V., 2019. Hydrogen storage in carbon materials - A review. *Energy Storage* 1;35.
- Mondal, M. K., H. K. Balsora and P. Varshney 2012. Progress and trends in CO₂ capture/separation technologies: A review. *Energy* 46: 431-441.
- Mondal, S. and P. K. Chattaraj 2014. Noble gas encapsulation: clathrate hydrates and their HF doped analogues. *Physical Chemistry Chemical Physics*, 16: 17943.
- Moraveji, M.K., Golkaram, M., Davarnejad, R. 2013. Effects of CuO nanoparticle on dissolution of methane in water *Journal of Molecular Liquids*, 180: 45–50.
- Moridis, George. J., Seol, Yongkoo, Kneafsey, Timothy J. 2005. Studies of Reaction Kinetics of Methane hydrate dissociation in porous media. Norway: N.p., 2005.
- Musakaev, N.G., Khasanov, M.K., Stolpovsky, M.V. 2018. Replacemet of CH₄ with CO₂ in a hydrate reservoir at the injection of liquid carbon dioxide. *AIP conference Proceedings*, 2027, 030051.

Naidoo, P., 2004. High-pressure vapour-liquid equilibrium studies. PhD Thesis, Chemical Engineering, University of KwaZulu-Natal, Durban, South Africa.

Najibi, H., Shayegan, M.M., Heidary, H., 2015. Experimental investigation of methane hydrate formation in the presence of copper oxide nanoparticles and SDS. *Journal of Natural Gas Science and Engineering*, 23:315-325.

Nandi, M., & Uyama, H. 2014. Exceptional CO₂ Adsorbing Materials under Different Conditions. *The Chemical Records*, 14(6):1134-1148.

Nasir, Q., Suleman, H., Elsheikh. 2020. A review on the role and impact of various additives as promoters/inhibitors for gas hydrate formation. *Journal of Natural Gas Science and Engineering*, 76:103211.

Nashed, O., Sabil K.M.M., Ismail L., Jaafar A. 2014. Hydrate equilibrium measurement of single CO₂ and CH₄ hydrates using Micro DSC. *Journal of Applied Sciences* 14(23): 3364-3368.

Naquash, A., Qyyum M.A., Haider, J., Bokhari, A., Lim, H., Lee, M. 2022. State-of-the-art assessment of cryogenic technologies for biogas upgrading: Energy, economic, and environmental perspectives. *Renewable and Sustainable Energy Reviews* 154: 111826.

Nazari, K., Taheri, Z. and Mehrabi, M. 2011. Natural gas hydrate production and transportation. *Proceedings of the 7th International Conference on Gas Hydrates (ICGH 2011)*, July 17-21, 2011. Edinburgh, Scotland, United Kingdom.

Ndlovu, P., Babae, S., Naidoo, P. 2022. Review on CH₄-CO₂ replacement for CO₂ sequestration and CH₄/CO₂ hydrate formation in porous media. *Fuel*, 320:123795.

Nelson, W. M., Naidoo, P., Ramjugernath, D. 2015. Phase equilibrium data for potentially hazardous binary mixtures involving dichlorosilane, trichlorosilane and silicon tetrachloride. *Journal of Chemical Thermodynamics*, 91,420-426.

Net Zero Coalition – The United Nations, Climate Action 2022. <https://www.un.org/en/cliimatechange/Net Zero Coalition | United Nations>

Ngema, P.T., Petticrew. C., Naidoo. P., Mohammadi, A.H., Ramjugernath, D. 2014. Experimental measurements and thermodynamic modelling of the dissociation conditions of clathrate hydrates for (refrigerant + NaCl + water) systems. *Journal of Chemical Engineering Data* 59, 466-475.

Ngema, P.T., Naidoo P., Mohammadi, A.H., Ramjegernath, D. 2019. Phase stability conditions for clathrate hydrate formation in (fluorinated refrigerant + water + single and mixed electrolytes + cyclopentane) systems: Experimental measurements and thermodynamic modelling. *Journal of Chemical Thermodynamics*.136, 59-76.

Ngema, P. T. 2014. The use of fluorinated refrigerants in the application of gas hydrates for desalination. Master of Science Degree. University of Kwazulu Natal, Durban, South Africa.

Nguyen, N.N., Galib, M., Nguyen, A.H. 2020. Critical Review on Gas Hydrate Formation at Solid Surfaces and in Confined Spaces – Why and How Does Interfacial Regime matter? *Energy & Fuels*, 34(6):6751-60.

- Nguyen, H.D., Chauvy, F., Herri, J.M. 2007. CO₂ capture by hydrate crystallization – A potential solution for gas emission of steelmaking industry *Energy Conversion and Management*, 48:1313–1322.
- Nguyen, N.N. 2017. Effects of additives on the formation of methane and carbon dioxide gas hydrates. PH. D thesis School of Chemical Engineering. The University of Queensland, Australia.
- Nguyen, T. T., Petuya, C., Talaga, D., Desmedt, A. 2020. Promoting the Insertion of Molecular Hydrogen in Tetrahydrofuran Hydrate with the help of Acidic additives. *Frontiers in Chemistry*, 8:550862.
- Ogata, K., Hashimoto, S., Sugahara, T., Moritoki, M., Sato, H., Ohgaki, K. 2008. Storage capacity of hydrogen in tetrahydrofuran hydrate. *Chemical Engineering Science*, 63:5714-5718.
- Ohgaki, K., Takano K, Sangawa H, Matsubara T, Nakano.S. 1996. Methane exploitation by carbon dioxide from gas hydrates phase equilibria for CO₂-CH₄ mixed hydrate system. *Journal of Chemical Engineering Japan*, 29:478-483.
- Osmolovskiy, P.I., Titov, G.K., Gopko, A.A., Guikov, A.N. 2018. Simulation of gas hydrates deposits CH₄/CO₂ replacement process using gas inhibitor. *AIP Conference Proceedings*, 2051:020220.
- Ota, M., Abe, Y., Watanabe, M., Smith, R.L., Inomata, H. 2005b. Methane recovery from methane hydrate using pressurized CO₂. *Fluid Phase Equilibrium*, 228:553–59.
- Ota, M., Morohashi, K., Abe, Y., Smith, L.R., Inomata, H. 2005a. Replacement of CH₄ in the hydrate by use of liquid CO₂. *Energy Conversion and Management*, 46:1680-91.
- Ota, M., Saito, T., Aida, T., Watanabe, M., Sato, Y., Smith Jr., R.L. Inomata, H. 2007. Macro and Microscopic CH₄-CO₂ Replacement in CH₄ Hydrate Under Pressurized CO₂. *Environmental and Energy Engineering AIChE Journal*, 53:2715-2721.
- Ouyang, O., Fan, S., Wang, Y., Lang, X., Wang, S., Zhang, Y., Yu, C. 2020. Enhanced methane production efficiency with in-situ intermittent heating assisted CO₂ replacement of hydrates. *Energy and Fuel*, 34(10):12476-85.
- Oyama, A., & Masutani, S.M., 2017. A Review of the methane hydrate Program in Japan. *Energies*, 10:1447.
- Ozaki, M., Tomura, S., Ohmura, R., Mori, Y.H., 2014. Comparative study of large-scale hydrogen storage technologies: Is hydrate-based storage at advantage over existing technologies? *International Journal of Hydrogen Energy* 39, 3327–3341.
- Pahlavanzadeh, H., Rezaei, S., Khanlarkhani, M., Manteghian, M., Mohammadi, A.H., 2016. Kinetic study of methane hydrate formation in the presence of copper nanoparticles and CTAB. *Journal of Natural Gas Science & Engineering*, 34:803-810.
- Pahlavanzadeh, H., Khanlarkhani, M., Rezaei, S. and Mohammadi, A., 2019. Experimental and modelling studies on the effects of nanofluids (SiO₂, Al₂O₃, and CuO) and surfactants (SDS and CTAB) on CH₄ and CO₂ clathrate hydrates formation. *Fuel*, 253:1392-1405.

- Palodkar AV, Jana AK. 2019. Modelling recovery of natural gas from hydrate reservoirs with carbon dioxide sequestration: Validation with Ignik Sikumi field data. *Scientific Reports. Nature research*,9:18901.
- Pan, D.P., Zhong, X.P., Li, B., Li, X.T., Chen, C. 2020. Experimental investigation into methane production from hydrate bearing clayey sediment by CO₂/N₂ replacement. *Energy Exploration and Exploitation*, 0(0):1-17.
- Pan, Z., Liua, Z., Zhangb, Z., Shang, L., Ma, S. 2018. Effect of silica sand size and saturation on methane hydrate formation in the presence of SDS. *Journal of Natural Gas Science and Engineering*, 56: 266-280.
- Pandey, J.S., Solms, N.V. 2019. Hydrate stability and methane recovery from gas hydrate through CH₄-CO₂ replacement in different mass transfer scenarios. *Energies*, 12;2309.
- Park, S.S., An, E.J., Lee, S.B., Chun, W.G., Kim, N.J. 2012. Characteristics of methane hydrate formation in carbon nanofluids. *Journal of Industrial and Engineering Chemistry*,18:443–448.
- Partoon, B., Sabil, K. M., Lau, K.K Lal, B. Nasrifar, K. 2018. Production of gas hydrate in a semi-batch spray reactor process as a means for separation of carbon dioxide from methane. *Chemical Engineering Research and Design*,138:168–175.
- Partoon, B., Sabil K.M., Keong, L. K. 2015. Capturing Carbon Dioxide through a Gas Hydrate-Based Process. *Chemical Engineering Transactions*,45.
- Petroleum Agency SA, 2022. Explore South Africa. Offshore - Ultra deep offshore and gas hydrates. <https://www.petroleumagencyrsa.com/index.php/25-frontiergeology/51-offshore>.
- Perathoner, S., Centi, G. 2009. Opportunities and prospects in the chemical recycling of carbon dioxide to fuels. *Catalysis Today*, 148 (3-4):1991-205.
- Perrin, A., Celzard, A., Maríché, J.F. Furdin, G. 2003. Methane storage within dry and wet active carbons: A comparative study. *Energy & Fuels*, 17(5):1283-1291.
- Prasad(a), P.S.R., Sungahara, T., Sum, A.K., Sloan, E.D., Koh, C.A. 2009. Hydrogen Storage in Double Clathrates with tert-Butylamine. *The Journal of Physical Chemistry A Letters*, 113:6540-6543.
- Prasad(b), P.S.R., Sowjanya, Y., Prasad, K. S. 2009. Micro-Raman investigations of mixed gas hydrates. *Vibrational Spectroscopy*, 50;319-323.
- Prashant, J., Yang, J., Tohidi, B. 2005. Preliminary experimental investigation on replacing methane in hydrate structure with carbon dioxide in porous media. Centre of Gas hydrate research, Institute of Petroleum Engineering Heriot-Watt University Edinburgh, U.K. Conference Paper Jan 2005.
- Priegnitz M. 2015. Development of geophysical methods to characterize methane hydrate reservoirs on a laboratory scale. PH. D thesis. Helmholtz-Zentrum Postdam.
- Priest JA, Rees EVL, Clayton C.R.I. 2009. Influence of gas hydrate morphology on the seismic velocities of sands. *Journal of Geophysical Research*, 114: B11.

- Pruteanu, C.G., Ackland, G.J., Poon, C.K., Loveday, J.S. 2017. When immiscible becomes miscible-methane in water at high pressures. *Science Advance*, 3, 1-5.
- Qorbani, K., Kvamme, B., Kuznetsova, T. 2017. Simulation of CO₂ storage into methane hydrate reservoirs, non-equilibrium thermodynamic Approach. *Energy Procedia*, 114:5451-5459.
- Raal, J.D., & Muhlbauer, L. M. 1998. *Phase Equilibria: Measurement and Computation*. Taylor & Francis, USA.
- Raman, A.K.Y., Koteeswaran, S., Venkataramani, D., Clark, P., Bhagwat, S., Aichele, C.P. 2016. A comparison of the rheological behavior of hydrate forming emulsions stabilized using either solid particles or a surfactant *Fuel*, 179:141-149.
- Ramesh, A., Jeyavelan, M., Hudson, M.S.L., 2018. Electrochemical properties of reduced graphene oxide derived through camphor assisted combustion of graphite oxide, *Dalton Transactions* 47; 5406-5414.
- Ravanchi, M.T., & Sahebdehfar, S. 2021. Catalytic conversions of CO₂ to help mitigate climate change: Recent process developments. *Process Safety and Environmental Protection*, 145:172-194.
- Research News, September 2005. *Materialstoday*. <https://www.nature.com/nmat/articles/type-research-news>.
- Rhodes, C.J. 2012. Progress in Science: Current Commentary. *Science Progress*, 95(4):473-483.
- Roberts, A.V., Czujko, T., Wronski, Z.S. 2009. *Nanomaterials for solid state hydrogen storage*. Fuel cells and hydrogen energy. Springer.
- Roberts, O.L., Brownscombe, E. R., Howe, L. S. 1940. Constitution diagrams and composition of methane and ethane hydrates. *Oil & Gas Journal*. 39 (30), 37-43.
- Ruffine, L. 2005. Exploring methane-hydrate formation and dissociation in geologic materials through laboratory experiments: Kinetic behaviour and morphology. *Fuel*,141:173-184.
- Rungrussamee, S., Inkong, K., Kulprathipanja, S. and Rangsunvigit, P. 2018. Comparative Study of Methane Hydrate Formation and Dissociation with Hollow Silica and Activated Carbon. *Chemical Engineering Transactions*, 70:1519-1524.
- Ruppel, C. 2011. Methane Hydrates and the Future of Natural Gas. In: S.P.O.M.H. MITEI Natural Gas Report, 2011, (Ed.).
- Sa, J.H.A. Melchuna, X. Hang, M. Rivero, P. Glenat and A.K. Sum 2019. Investigating the effectiveness of anti-agglomerates in gas hydrates and ice formation. *Fuels* 255: 115841.
- Said S, Govindaraj V, Herri J.M, Ouabbas Y, Khodja M, Belloum M, Sangwai JS, Nagarajan R. 2016. A study on the influence of nanofluids on gas hydrate formation kinetics and their potential: Application to the CO₂ capture process. *Journal of Natural Gas Science and Engineering* 32:95-108.
- Safari, F.and Dincer, I. 2020. A review and comparative evaluation of thermochemical water splitting cycles for hydrogen production. *Energy Conversion and Management*, 205:112182.

Sasol, 2021. Sasol in society report 2021. Responding to the needs of our communities. [sasol.com/sites/default/files/2022-06/SASOL%20In Society%202021_V17_29Nov_Single_0](https://sasol.com/sites/default/files/2022-06/SASOL%20In%20Society%202021_V17_29Nov_Single_0).

Sasol limited, 2021. Climate change report. Purpose innovating for better world. sasol.com/sites/default/files/2022-06/Sasol%20Climate%20change%20report_2021_22Sep21_0.

Saw, V.K., Udayabhanu, G., Mandal, A., Laik, S. 2015. Methane hydrate formation and dissociation in the presence of silica sand and bentonite clay. *Oil & Gas Science Technology*, 70 (6):1087-1099.

Sazali, N. 2020. Emerging technologies by hydrogen:a review. *International Journal of hydrogen Energy*, 45:18753-18771.

Schoderbek D. 2011. Ignik Sikumi #1, gas hydrate test well, successfully installed on the Alaska North Slope. US Department of Energy, Office of Fossil Energy, National Energy Technology Laboratory 'Fire in the Ice', 11(1):1-5.

Seo, Y., Lee, S., Lee J. 2013. Experimental verification of methane replacement in gas hydrate by carbon dioxide. *Chemical Engineering Transactions*, 32.

Seo, Y., Kang, S.P. 2010. Enhancing CO₂ separation for pre-combustion capture with hydrate formation in silica gel pore structure. *Chemical Engineering Journal*, 2010;161:308–312.

Sevilla, M., Fuertes, A.B., Mokaya, R., 2011. High density hydrogen storage in super activated carbons from hydrothermally carbonized renewable organic materials, *Energy & Environmental Science*, 4; 1400-1410.

Shaibu R, Sambo C, Guo B, Dudun A. 2021. An assessment of methane gas production from natural gas hydrates: Challenges, technology and market outlook. *Advances in Geo-Energy Research*, 5(3):318-32.

Shifeng, L., Shuanshi, F., Jinqu, W., Xuemei, L., Yanhong., W. 2010. Clathrate hydrate capture of CO₂ from simulated flue gas with cyclopentane/water emulsion. *Chinese Journal of Chemical Engineering*, 18(2):202-206.

Shihui, M., Zhen, P., Ping, L., Yuguo, W., Bingfan, L., Jinke, K. Zhien, Z. 2017. Experimental Study on Preparation of Natural Gas Hydrate by Crystallization, *China Petroleum Processing and Petrochemical Technology*, 19:106-113.

Shin, K., Kim, Y., Strobel, T.A., Prasad, P.S.R., Sugahara, T., Lee, H., Sloan, E.D., Sum, A.K., Koh, C.A. 2009. Terta-n-butylammonium Borohydride Semi clathrate: A Hybrid Material for Hydrogen Storage. *The Journal of Physical Chemistry A*, 113:6415-6418.

Siangsai, A., Rangsunvigit, P., Kitiyanan, B., Kulprathipanja, S., Linga P. 2015. Investigation on the roles of activated carbon particle sizes on methane hydrate formation and dissociation. *Chemical Engineering Science*, 126:383-89.

Siazik, J., Malcho M., Lenhard R. 2017. Proposal of an experimental device for the continuous accumulation of primary energy in natural gas hydrates. *EPJ Web of Conferences* 143: 02106.

Sloan, E.D. and C.A. Koh, 2008. Clathrate Hydrates of Natural Gases, Third Edition. Clathrate Hydrates of Natural Gases, Third Edition. Vol. 119. Boca Raton: Crc Press-Taylor & Francis Group. 1-701.

Sloan, Jr. E.D., 2003. Fundamental principles and applications of natural gas hydrates. Nature, 426(6964); 353-363.

Smith JM, Van Ness HC, Abott MM. 1996. Introduction to Chemical engineering thermodynamics. McGraw-Hill International editions. Fifth edition. Chemical Engineering series.

Solomon, S., D. Qin, M. Manning, Z. Chen, M. Marquis, K. B. Averyt, M. Tignor and H. L. Miller (2007). IPCC Climate Change 2007: The Physical Science Basis EXITEXIT EPA WEBSITE. Contribution of Working Group I to the Fourth Assessment Report of the Intergovernmental Panel on Climate Change. C. U. Press. Cambridge, United Kingdom 996 pp.

Song, Y., Wang, S., Jiang, L., Zhang, Y., Yang, M. 2016. Hydrate phase equilibrium for CH₄-CO₂-H₂O system in porous media. The Canadian Journal of Chemical Engineering. 94:1592-1598.

Songolzadeh, M., M. T. Ravanchi and M. Soleimani 2012. Carbon Dioxide Capture and Storage: A General Review on Adsorbents. World Academy of Science Engineering and Technology 70: 225-232.

Spangenberg, E., Priegnitz, Heesche, K., Schicks, J.M. 2014. Are laboratory-formed hydrate-bearing systems analogous to those in nature? Journal of Chemical Engineering data 60(2):258-268.

Stamatakis, E., Zoulias, E., Tzamalidis, G., Massina, Z., Analytis, V., Christodoulou, C., Stubos, A., 2018. Metal hydride hydrogen compressors: Current developments and early markets. Renewable Energy, 127; 850-862.

Steyn, L. 2022. Sasol, ArcelorMittal launch carbon capture, 'green steel' plans for Vanderbijlpark, Saldanha. News24. 18 October. <https://www.news24.com/fin24/Companies/Sasol-ArcelorMittal-launch-carbon-capture-'green-steel'-plans-for-Vanderbijlpark-Saldanha-Business-news24.com>.

Strobel, T.A., Koh, C.A., Dendy Sloan, E.D. 2008. Water Cavities of sH Clathrate hydrate stabilized by molecular Hydrogen. The Journal of Physical Chemistry B, 112:1885-1887.

Strobel, T.A., Koh, C.A., Sloan, E.D. 2007. Hydrogen storage properties of Clathrate hydrate materials. Fluid Phase Equilibria, 261:382-389.

Strobel, T.A.; Taylor, C.J; Hester, K.C.; Dec, S.F.; Koh, C.A.; Miller, K.T.; Sloan, E.D. 2006. Molecular Hydrogen Storage in Binary THF-H₂ Clathrate Hydrates." Journal of Physical Chemistry B, 110, 17121-17125.

Sugahara, T., Haag, J.C., Prasad, P.S.R., Warntjes, A.A., Sloan, E.D., Sum, A.K., Koh, C.A. 2009. Increasing Hydrogen Storage Capacity using Tetrahydrofuran. Journal of American Chemical Society Communications, 131(41):14616-14617.

Sum, A.K., Koh, A., Sloan, E.D. 2009. Clathrate Hydrates: From Laboratory Science to Engineering Practice, Ind Chem Res, 48:7457-7465.

- Surovtseva, D., Amin, R., Barifcani, A. 2011. Design and operation of pilot plant for CO₂ capture from IGCC flue gases by combined cryogenic and hydrate method. *Chemical Engineering Research and Design*, 89(9):1752-1757.
- Susilo R, Ripmeester JA, Englezos P. 2007. Methane conversion rate into structure H hydrate crystals from ice. *American Institute of Chemical Engineers*, 53(9):2451–60.
- Takeya, S., Kida, M., Minami, H., Sakagami, H., Hachikubo, A., Takahashi, N., Shoji, H., Solviev, V., Wallmann, K., Biebow, N., Obzhirov, A., Salomatin, A., Poort, J. 2006. Structure and thermal expansion of natural gas clathrate hydrates. *Chemical Engineering Science* 61(8):2670-2674.
- Tajima, H., A. Yamasaki and F. Kiyono 2004. Energy consumption estimation for greenhouse gas separation processes by clathrate hydrate formation. *Energy* 29: 1713-1729.
- Taylor, C.J., Miller, K.T., Koh, C.A., Sloan, E.D. 2007. Macroscopic investigation of hydrate film growth at the hydrocarbon/water interface. *Chemical Engineering Science*, 62(23): p. 6524-6533.
- Taylor, B. N. and Kuyatt, C. E. 1994. Guidelines for evaluating and expressing the uncertainty of NIST measurement results, US Department of Commerce, Technology Administration, National Institute of Standards and Technology Gaithersburg, MD.
- Tohidi, B., Anderson, R., Clennell, M.B., Burgass, R.W., Biderkab, A.B. 2001. Visual observation of gas-hydrate formation and dissociation in synthetic porous media by means of glass micromodels. *Geology*, 29 (9):867-870.
- Torre, J.P., Dicharry, C., Ricaurte, M., Delphine D.D., Broseta D. 2011. CO₂ capture by hydrate formation in quiescent conditions: in search of efficient kinetic additives. *Energy Procedia*, 4: 621-628.
- UNEP, 2018. United Nations Environment Assembly of the United Nations Environment Programme. 3/8 Preventing and reducing air pollution to improve air quality globally.
- Uchida, T., Ebinuma, T., Takeya, S., Nagao, J., Narita, H. 2002. Effects of pore sizes on dissociation temperatures and pressures of methane, carbon dioxide, and propane hydrates in porous media. *Journal of Physical Chemistry B*, 106:820-826.
- U.S Department of Energy, 2015. Quadrennial Technology Review. Advancing systems and technologies to produce cleaner fuels.
- Vafaei MT, Kvamme B, Chejara A, Jemai K. 2014. A new reservoir simulator for studying hydrate dynamics in reservoir. *International Journal Greenhouse Gas Control*, 23:12-21.
- Valderrama, J. O., 1990. A generalized Patel-Teja Equation of State for polar and nonpolar Fluids and their Mixtures. *Journal Chemical Engineering. Japan*. 23, 87–91.
- Veluswamy, H.P., Kumar, A., Seo, Y., Lee, J.D., Linga, P., 2018. A review of solidified natural gas (SNG) technology for gas storage via clathrates hydrates. *Applied Energy* 262-285.
- Veluswamy, H. P., Premasinghe, K.P., Linga, P. 2017. CO₂ Hydrates-Effects of additives and operating conditions on the Morphology and hydrate growth. The 8th International Conference on Applied Energy – ICAE2016. *Energy Procedia*, 105:5048 – 5054.

- Veluswamy, H.P., Kumar, R., Linga, P., 2014. Hydrogen storage in clathrate hydrates: Current state of art and future directions. *Applied Energy*, 01;063.
- Waite, W.F., Winters, W.J., Mason, D.H. 2004. Methane hydrate formation in partially water-saturated Ottawa sand. *American Mineralogist*, Volume,89:1202-1207.
- Wall, T.F. 2007. Combustion processes for carbon capture. *Proceedings of the combustion Institute*, 31(1):31-47
- Walsh, M. R., Rainey, J.P., Lafond, G., Park, D.H., Beckham, G.T., Jones, M.D., Lee, K.H., Koh, C.A., Sloan, E.D., Wu, D.T., Sum, A.K. 2011. The Cages, Dynamics, and Structuring of Incipient Methane Clathrate Hydrates., *Phys. Chem. Chem. Phys.*, 13:19951-19959.
- Walsh, M.R., Koh, C.A., Sloan, E.D., Sum, A.K., Wu, D.T. 2009. Microsecond Simulations of Spontaneous methane hydrate nucleation and growth. *Science*, 326(5956):1095-1098.
- Wan, L., X. Zhou, P. Chen, X. Zang, D. Liang and J. Guan 2019. Decomposition Characterizations of Methane Hydrate Confined inside Nanoscale Pores of Silica Gel below 273.15 K. *Crystals* 9.
- Wang, Y., Lang, X., Fan, S., Wang, S., Yu, C., Li, G. 2021. Review on enhanced technology of natural gas hydrates recovery by carbon dioxide replacement. *Energy Fuels*35(5):3659-3674.
- Wang, X. and C. Song 2020. Carbon capture from flue gas and the atmosphere: A perspective. *Frontiers in Energy Research* 560849.
- Wang, Y., Dong, S., Zhang, M., Wu, Q., Zhang, X., Zhang, P 2020. Experimental study of the formation rate and distribution of methane hydrate in layered sand. *America Chemical Society Omega* 5(46):29882-29888.
- Wang, M., Wang, G., Sun, Z., Zhang, Y., Xu, D. 2019. Review of renewable energy-based hydrogen production processes for suitable energy innovation. *Global Energy Interconnect*, 2:436-443.
- Wang, X.H., Sun, Y.F., Wang Y.F., Li, N., Sun, C.Y., Chen, G.J., Liu, B., Yang, L.Y. 2017. Gas production from hydrates by CH₄-CO₂/H₂ replacement. *Applied Energy*, 188:305-314.
- Wang, F., Luo, S.J., Fu, S.F., Jia, Z.Z., Dai, M., Wanga, C.S., Guo, R.B. 2015. Methane hydrate formation with surfactants fixed on the surface of polystyrene nanospheres. *Journal of Materials Chemistry A*3,8316-8323.
- Wang, Y., Lang, X., Fan, S. 2012. Accelerated nucleation of tetrahydrofuran (THF) hydrate in presence of ZIF-61. *Journal of Natural Gas Chemistry*, 21:299-301.
- Wang X, Schultz AJ, Halpern Y. 2002. Kinetics of methane hydrate formation from polycrystalline deuterated ice. *Journal of Physical Chemistry A*, 106(32):7304-09.
- Watanabe, S., Takahashi, S., Mizubayashi, H., Murata, S., Murakami, H., 2008. A demonstration project of NGH land transportation system, in: *Proceedings of the 6th international conference on gas hydrates*, British Columbia, Canada.

- Wilder, J.W., Seshadri, K., Smith, D.H. 2001. Resolving apparent contradictions in equilibrium measurements for clathrate hydrates in porous media. *The Journal of Physical Chemistry B*, 105(41) 9970-9972.
- Xia, Y., Yang, Z., Zhu, Y., 2013. Porous carbon-based materials for hydrogen storage: Advancement and challenges. *Journal of Material Chemistry A* 1;9365–9381.
- Xie, Y., Zhu, Y.J., Zheng, T., Yuan, Q., Sun, C.Y., Yang, L.Y., Chen, G.J. 2021. Replacement in CH₄-CO₂ hydrate below freezing point based on abnormal self-preservation differences of CH₄ hydrate. *Chemical Engineering Journal*, 403;126283.
- Xiong, L., Li, X., Wang, Y., Xu, C. 2012. Experimental study on Methane hydrate dissociation by depressurization in porous sediments. *Energies*, 5:518-530.
- Xu, C.G., Cai, J., Yu, Y.S., Chen, Z.Y., Li, X.S. 2018. Research on micro-mechanism and efficiency of CH₄ exploitation via CH₄-CO₂ replacement from natural gas hydrates. *Fuel*, 216:255-265.
- Xu C.G, Li X.S. 2014. Research progress of hydrate-based CO₂ separation and capture from gas mixtures. *Royal Society of Chemistry*, 4(35):18301-16.
- Xu, C. G., Z. Y. Chen, J. Cai and X. S. Li, 2014. Study on Pilot-scale CO₂ separation from flue gas by the hydrate method. *Energy&Fuels* 28: 1242-1248.
- Xuab, C. G. and X. S. Li 2014. Research progress of hydrate-based CO₂ separation and capture from gas mixtures. *Royal Society of Chemistry*, 4: 18301–18316.
- Yakushev VS, Chuvilin EM. 2000. Natural gas and gas hydrate accumulations within permafrost in Russia. *Cold Regions Science and Technology*, 31(3):189-97.
- Yang, M., Song, Y., Jiang, L., Zhao, Y., Ruan, X., Zhang, Y., Wang, S. 2014. Hydrate-based technology for CO₂ capture from fossil fuel power stations. *Applied Energy*, 116:26-40.
- Yang, M., Song, Y., Liu, W., Zhao, J., Ruan, X., Jiang, L., Li, Q. 2013. Effects of additive mixtures (THF/SDS) on carbon dioxide hydrate formation and dissociation in porous media. *Chemical Engineering Science*, 90:69-76.
- Yang, M., Zhou, H., Wang, P., Li, N., Song, Y. 2017. Hydrate-based CO₂ capture from flue gas in constant pressure process with the presence of THF. 9TH International Conference on Applied Energy, ICAE2017, 21-24 August 2017, Cardiff, UK. *Energy Procedia*, 142:3939-3943.
- Yevi, G. Y. and Rogers, R. E. 1996. Storage of Fuel in Hydrates for Natural Gas Vehicles (NGVs). *Journal of Energy Resources Technology*, 118:209-213
- Yin Z., and Linga, P. 2019. Methane hydrates: A future clean energy resource. *Chinese Journal of Chemical Engineering*, 27(9):2026-2036.
- Yoon, J.H., Kawamura, T., Yamamoto, Y., Komai, T. 2004. Transformation of methane hydrate to carbon dioxide hydrate: In Situ Raman Spectroscopic observations. *J Phys. Chem A*, 108:5057-5059.
- Yousif, M.H., Sloan, E.D. 1991. Experimental investigation of hydrate formation and dissociation in consolidated porous media. *SPE Reserv. Eng.* (11):452-458.

Yu, Y., Zhou, S., Li, X. and Wang, S., 2016. Effect of graphite nanoparticles on CO₂ hydrate phase equilibrium. *Fluid Phase Equilibria*, 414:3-28.

Yuan Q, Sun CY, Liu B, Wang X, Ma ZW, Ma QL, Yang LY, Chen GJ, Li QP, Li S, Zhang K. 2013. Methane recovery from natural gas hydrates in porous sediment using pressurized liquid CO₂. *Energy Conversion and Management*, 67:257-64.

Yuan, Q., Sun, C.-Y., Liu, B., Wang, X., Ma, Q.L., Yang, L.Y., Chen, G.L., Li, Q.P., Li, S., Zhang, K. 2012. Recovery of methane from hydrate reservoir with gaseous carbon dioxide using a three-dimensional middle-size reactor. *Energy*, 40:47-58.

Yuan, Q., Sun, C.Y., Liu, B., Wang, X., Ma, Z.W., Ma, Q.L., Yang, L.Y., Chen, G.J., Li, Q.P., Li, S., Zhang, K. 2013. Methane recovery from natural gas hydrates in porous sediment using pressurized liquid CO₂. *Energy Conversion and Management*, 67:257-264.

Zanjani, N.G., Moghaddam, A.Z., Nazari, K., Taheri, M.M. 2012. Increasing the Storage capacity and selectivity in the formation of Natural gas hydrates using porous media. *Chemical Engineering Technology*, 35(11):1973-1980.

Zanota, M.L., Camby, L.P., Chauvy, F., Brullé, Y., Herri, J.M. 2005. Improvement of methane storage in activated carbon using methane hydrate. *Fifth International Conference on Gas Hydrates (ICGH 5)*, Tromsheim: Norway.

Zhang, F., Wang, X., Lou X., Lipinski, W. 2021. The effect of Sodium dodecyl sulfate and dodecyl trimethyl ammonium chloride on the kinetics of CO₂ hydrate formation in the presence of tetra-n-butyl ammonium bromide for carbon capture applications. *Energy*, 227: 120424.

Zhang, L., Yang, L., Wang, J., Zhao, J., Dong, H., Yang, M., Liu, Y., Song, Y. 2017. Enhanced CH₄ recovery and CO₂ storage via thermal stimulation in the CH₄/CO₂ replacement of methane hydrate. *Chemical Engineering Journal*, 2017;308:40-49.

Zhang, Y., Cui, X., Li, X., Li, Y., & Li, J. 2017. Kinetic study on gas hydrate formation and dissociation processes with different water contents. *Journal of Molecular Liquids*, 241, 1096-1102.(b)

Zhang, L., S. Zhou, S. Wang, L. Wang and J. Li 2013. Surfactant surface tension effects on promoting hydrate formation: An experimental study Fluorocarbon surfactant (Intechem-01) +SDS composite surfactant. *Journal of Environmental Protection* 4: 42-48.

Zheng, J., Chong, Z.R., Qureshi, M.F., Linga, P. 2020. Carbon dioxide sequestration via Gas hydrates: A potential pathway toward decarbonisation. *Energy and Fuels*, 34:10529-10546.

Zhong, D.L., Le, Z., Lu, Y.Y., Sun, D.J. 2014. Phase equilibrium data of gas hydrates formed from a CO₂ + CH₄ gas mixture in the presence of Tetrahydrofuran. *Journal of Chemical & Engineering data*, 59(12):4110-4117.

Zhong, D. L, He, S.Y, Sun, D.J., Yang, C. 2014. Comparison of methane hydrate formation in stirred reactor and porous media in the presence of SDS. *The 6th International Conference on Applied Energy-ICAE2014*. *Energy Procedia*, 61:1573 – 1576.

Zhong, D.L., Ding, K., Yang, C., Bian, Y., Ji, J. 2012. Phase Equilibria of Clathrate Hydrates formed with $\text{CH}_4 + \text{N}_2 + \text{O}_2$ in the presence of Cyclopentane or Cyclohexane. *Journal of Chemical & Engineering Data*, 57:3751-3755.

Zhong, Y. & Rogers, R.E. 2000. Surfactant effects on gas hydrate formation. *Chemical Engineering Science*, 55:4175-4187.

Zhao, J., Xu, K., Song, Y., Liu, W., Lam, W., Liu, Y., Xue, K., Zhu, Y., Yu, X., Q.L., 2012. A Review on Research on Replacement of CH_4 in Natural Gas Hydrates by Use of CO_2 . *Energies*, 5(2):399-419.

Zhao, J., Zhang, L., Chen, X., Fu, Z., Liu, Y., Song, Y. 2015. Experimental study of conditions for methane hydrate productivity by the CO_2 swap method. *Energy Fuels*, 29(11):6887-6895.

Zhao, J., Zhang, L., Chen, X., Zhang, Y., Liu, Y., Song, Y. 2016. Combined replacement, and depressurization methane hydrate recovery method. *Energy Exploration and Exploitation*, 34(1) :129-139.

Zheng, J., P. Zhang and P. Linga 2017. Semiclathrate hydrate process for pre-combustion capture of CO_2 at near ambient temperatures. *Applied Energy*, 194: 267-278.

Zhou, X., Zang, X., Long, Z., Liang, D. 2021. Multistage analysis of the hydrate-based carbon capture from gas mixtures containing carbon dioxide. *Scientific Reports*, 11: 9197.

Zhou, S., Yan, H., Su, D., Navaneethakannan, S., Chi, Y. 2018. Investigation on the kinetics of carbon dioxide hydrate formation using flow loop testing. *Journal of Natural Gas Science and Engineering*, 49:385-392.

Zhou, C., Chen, Z., Li, Y. (2016). Enhanced Replacement of Methane by Carbon Dioxide in Gas Hydrate Reservoirs Using Copper Nanoparticles. *Journal of Natural Gas Science and Engineering*, 32: 69-77.(a)

Zhou, C., Chen, Z., Li, Y. 2016. Enhanced Replacement of Methane by Carbon Dioxide in Gas Hydrate Reservoirs Using Silica Nanoparticles. *Energy & Fuels*, 30(8): 6343-6351.(b)

Zhou, S., Yu, Y., Zhao, M., Wang, S. and Zhang, G., 2014. Effect of Graphite Nanoparticles on Promoting CO_2 Hydrate Formation. *Energy fuels*, 28:4694-4698.

Zhou, X., Liang, D.Q., Liang, S., Yi, L.Z., Lin, F.H. 2015. Recovering CH_4 from Natural gas hydrates with the Injection of $\text{CO}_2\text{-N}_2$ Gas mixtures. *Energy & Fuels*.

Zhou, X., Fan, S., Liang, D., Du, J. 2008. Replacement of methane from Quartz Sand-Bearing Hydrate with Carbon dioxide-in-water Emulsion. *Energy & Fuels*, 22:1759-1764.

Zhou L. 2005. Progress and problems in hydrogen storage methods. *Renewable and Sustainable Energy Review* 9(4): 395-408.

Zohuri, B., Zohuri, B., 2019. Cryogenics and Liquid Hydrogen Storage, in: *Hydrogen Energy*. Springer International Publishing, pp. 121–139.

Zhu, B., Henneberger, R., Weissert, H., Zeyer, J., Schroth, M. H. 2018. Occurrence and origin of methane entrapped in sediments and rocks of a calcareous alpine glacial catchment. *Journal of Geophysical Research*, 123:3633-3648.

Appendices

Appendix A

A.1: CH₄-CO₂ gas exchange models

Several models have been developed to interpret the replacement process. Ota et al., (2005a; 2005b) developed a model for the decomposition of CH₄ hydrate and the formation of CO₂ hydrate in the replacement process based on the fugacity difference between the gas and hydrate phase being the driving force. The model for CH₄ hydrate composition was given by;

$$\frac{dn_{CH_4, H}}{dt} = -k_{Dec}A(f_{CH_4, H} - f_{CH_4, G}) \quad (A.1)$$

$$\frac{1}{k_{Dec}} = \frac{1}{k_{Dec, R}} + \frac{1}{k_{Dec, D}} \quad (A.2)$$

where $n_{CH_4, H}$ is the remaining amount of CH₄ in the hydrate gas phase, t is the reaction time, f is the fugacity, and A is the surface area available for contact between the gas phase (G) and the hydrate(H). k_{Dec} is the overall rate constant of the decomposition, $k_{Dec, R}$ is the reaction rate constant of decomposition, and $k_{Dec, D}$ is the rate constant of mass transfer in the hydrate phase.

For the CO₂ hydrate formation model during the replacement, the model was given by the following equation;

$$\frac{dn_{CO_2, H}}{dt} = -k_{Form}A(f_{CO_2, H} - f_{CO_2, G}) \quad (A.3)$$

$$\frac{1}{k_{Form}} = \frac{1}{k_{Form, R}} + \frac{1}{k_{Form, D}} \quad (A.4)$$

where $n_{CO_2, H}$ is the amount of CO₂ in the hydrate phase, and k_{Form} is the overall rate constant of the formation, summation of $k_{Form, R}$ is the rate constant for hydrate formation and $k_{Form, D}$ is the rate constant of mass transfer in the hydrate phase.

Palodkar et al., (2019) proposed a theoretical model to explain the CH₄-CO₂ swapping process in natural gas and CO₂ in deep sea beds and in the permafrost region. The theory is based on the transition of gas and water to hydrate, taking into consideration a possibility of the existence of four phases, gas(G), aqueous (A), solid ice (I) and hydrate (H);



Where g is the guest gas molecule, n_w is the hydration number, w is the water species and h is the hydrate component.

Hydrate formation and dissociation kinetics prior to the replacement is modelled with the hydrate kinetics affected by the water consumption rate except for the driving force $\Delta\mu$. The reaction rate is given by:

$$r = \frac{1}{A_E} \frac{dn_{g,H}}{dt} = (kn_{H_2O,L}) \left[\frac{\mu_w^H}{RT} - \frac{\mu_w^L}{RT} \right] \quad (A.6)$$

$$\text{Where } n_{H_2O,L} = n_{H_2O,T} - n_H \sum_{i=1}^{N_c} n_{g_i,H} = n_{H_2O,T} - n_H n_{g,H} \quad (A.7)$$

k is the rate constant, $n_{H_2O,T}$ is the total moles of water initially present, $n_{H_2O,L}$ is the residual moles of water in a liquid phase, $n_{g,H}$ are the moles of guest gas in hydrate phase, N_c is the number of gas components.

Guest gas dynamics is given by;

$$\frac{dn_{g,H}}{dt} = k_0 \exp \left[\frac{-\Delta E}{RT} \right] A\beta_0 \exp(-Ct) (\Delta\mu) (n_{H_2O,T} - n_H n_{g,H}) \quad (A.8)$$

This is derived from equation 6; the integral of this formulation represents the guest gas dynamics during hydrate formation and growth in saltwater with porous media.

Hydrate dissociation kinetics are governed by;

$$-\frac{dn_{g,H}}{dt} = kA_e \Delta\mu n_{H_2O,H} \quad (A.9)$$

This is derived from equation 6 where $n_{H_2O,H}$ denotes the moles of water in the hydrate phase. The integral represents hydrate dissociation in porous media and saline environments.

The replacement process, is based on the rate of methane displacement and is given by;

$$\frac{dn_{CH_4,H}}{dt} + k_d A_{e,d} (\Delta\mu)_{CH_4} n_{H_2O,H} = \xi k_f A_{e,f} (\Delta\mu)_{RA} n_{H_2O,L} \quad (A.10)$$

Where subscript f and d refer to the formation and dissociation of hydrate, respectively, ξ is the ratio of fractional occupancy of CH_4 to that of replacement agent (subscript 'R.A.' that is pure/mixed CO_2) in both the small and large cages. Langur equation can be used to determine this factor.

Similarly, Yuan et al., (2013) studied CH₄-CO₂ replacement reaction and focussed solemnly on CH₄ replacement rate, which is shown in equation 2.11. This expression is similar to the equation utilised by Palodkar et al., (2019) to represent hydrate formation and dissociation.

$$r_{replace} = \frac{1}{n_{CH_4,H}^{end}} \frac{dn_{CH_4,reactor}^t}{dt} \quad (A.11)$$

Where $n_{CH_4,reactor}^t$ is the mole of CH₄ replaced from the hydrate at the moment t , which is calculated from the mole fraction of CH₄ in the reactor measured at an instant.

Qorbani et al., (2017) utilised a reactive transport simulator, RetrasoCodeBright, to formulate a model for the CH₄-CO₂ replacement process. The basic assumption for this work was that CH₄ hydrate was intact and did not dissociate and solid stage exchange of CH₄ with injected CO₂, that is;



This model is restricted by solid diffusivity and thus occurs relatively slowly. In this model, formed mixed CO₂/CH₄ hydrate and CO₂ hydrate are thermodynamically favoured above CH₄ hydrate.

The models' dissociation rates for CH₄ hydrate were zero to mimic an intact CH₄ hydrate, while CO₂ hydrate phase transitions were calculated according to kinetic rates introduced in the studies referenced. CO₂ was considered the only gas in the system filling the large cavities of the hydrate structure I. The growth rate of the CO₂ hydrate within CH₄ hydrate was computed by Classical nucleation theory:

$$R = R_o e^{-\beta \Delta G} \quad (A.13)$$

where R is the kinetic rate of CO₂ hydrate growth.

Gibb's free energy minimisation was utilised to calculate competing for hydrate phase transitions. The free energy difference was calculated as;

$$\Delta G = \delta [x_w^H (\mu_w^H - \mu_w^f) + x_{guest}^H (\mu_{guest}^H - \mu_{guest}^f)] \quad (A.14)$$

Equation 14 shows the chemical potential difference between the hydrate and the hydrate formers, x is the mole fraction, and μ is the chemical potential. Subscript 'H' and 'F' denotes hydrate phase and former phase, respectively. Hydrate growth and decomposition are described

by δ assuming +1 and -1, respectively. Kinetics rate calculations and other details are detailed in other literature sources (Vafaei et al., 2014; Chejara et al., 2013)

A model for analysing the physical mechanisms for the CO₂-CH₄ replacement utilises the Avrami equation (Susilo et al., 2007) and shrinking models (Wang et al., 2002). These are well known for physical models for crystallisation kinetics, with the Avrami model applicable in the initial reaction stage of the hydrate film and the shrinking core model for diffusion through the hydrate film. Generally, CH₄-CO₂ follows the same reaction pattern, with the surface reaction first, then CO₂ is diffusion-limited by interior hydrate layers (Lee et al., 2014; Zhao et al., 2016)

$$\text{Avrami model; } \alpha = 1 - \exp(-k_1 t^n) \quad (\text{A.15})$$

$$\text{Shrinking core model; } 1 - \alpha)^{1/3} = -\frac{\sqrt{2k_2(t-t^*)}}{r} + (1-\alpha^*)^{1/3} \quad (\text{A.16})$$

where α is the hydrate conversion ratio at time t , α^* is the hydrate conversion ratio when diffusion through hydrate film starts at time t^* , k is the rate constant with the subscript indicating the growth stage, n is the Avrami exponent, and r is the radius of the particle. The hydrate conversion ratio as a function of time is regressed with both equations to obtain the rate constant k_1 , k_2 and the Avrami exponent n .”

The models detailed above illustrate a recurring pattern of having the diffusivity coefficient in all the relations. This is in line with experimental observation stating that the CH₄-CO₂ hydrate layer formed on the methane surface hinders perpetual substitution.

A.2: CH₄-CO₂ Replacement summary

Table A.1: Summary of factors affecting CH₄-CO₂ Replacement Reaction.

Reference	Nature of Study	Results and Observations
Effects of secondary gas		
Zhou et al., (2015)	Injection of CO ₂ /N ₂ gas mixtures into natural gas hydrates to recovery CH ₄	Addition of N ₂ gas reduced the recovery rate of CH ₄ resulting in the reaction being pressure dependent. Also, as N ₂ was captured in the hydrate cages its restricted CO ₂ passage leading to lower CH ₄ replacement. Average values for CH ₄ production using CO ₂ and 75mol % CO ₂ /25mol % N ₂ were 19.2 % and 13.3 % respectively.
Ding et al., (2017)	Investigation of CH ₄ recovery form natural gases by utilizing simulated IGCC syngas.	H ₂ molecules were not present in the final hydrate after replacement reaction, showing that CO ₂ and H ₂ do not complete for cages in the hydrate structure.
Wang et al., (2017)	CH ₄ production from hydrates using CO ₂ /H ₂ gas mixture.	Increase in the amount of H ₂ in the replacement gas mixture resulted in enhanced CH ₄ production. Though, lowering the amount of CO ₂ stored up. The mole fraction of H ₂ gas remained constant throughout the reaction and served only to destabilize the hydrate. 49 % CH ₄ recovery was reported with 36mol % CO ₂ /64mol % H ₂ .
Xu et al., (2018)	Investigation on micro-mechanism and efficiency of CH ₄ exploitation via CH ₄ -CO ₂ replacement from natural gas hydrates with CO ₂ /N ₂ , CO ₂ /H ₂ , CO ₂ /He gas mixtures at 4.5 MPa and 274.0 K.	Adding small gas molecules enhanced the replacement reaction greatly and adding He and N ₂ leads to weakening of the van der Waals forces between CH ₄ molecules and hydrate crystals thus improving the efficiency of CH ₄ exploitation.
Effects of kinetic and thermodynamic promoters		
Lee et al., (2017)	Investigation of CH ₄ -CO ₂ replacement in the sII natural gas hydrates for CH ₄ hydrate recovery and CO ₂ sequestration.	Replacement of sII CH ₄ +C ₃ H ₈ in natural gases increased with increase in CO ₂ injection pressure. Moreover, most of CH ₄ was found to reside in sII hydrate.

Table A.1: Summary of factors affecting CH₄-CO₂ Replacement Reaction. (*continued*)

Khlebnikov et al., (2016)	Devised a method for enhancing CH ₄ recovery from natural gas hydrate using thermodynamic hydrate inhibitor technology, an electrolyte and alcohol solution.	The decomposition rate of CH ₄ hydrate reached 0.01194 0.00086 and 0.00141 mol/h with methanol, sodium chloride and magnesium chloride respectively. Hence, in the study Methanol concluded to be the best solution to accelerate the rate of CH ₄ dissociation thus enhancing CH ₄ recovery.
Pandey et al., (2019)	Study of 500 ppm of SDS a hydrate promoter and pressure effects on mixed hydrate stability and CH ₄ recovery by CO ₂ and CO ₂ /N ₂ injection.	CH ₄ recovery observed to be pressure dependent with SDS proving insignificant on the replacement reaction. CH ₄ recovery efficiency of 41 % was obtained with 10 % CO ₂ /90 % N ₂ .
Adibi et al., (2020)]	Experimental study of using combined CH ₄ /CO ₂ replacement and thermal stimulation for CH ₄ production form gas hydrates utilizing SiO ₂ and ZnO nanoparticles.	Conditions for CH ₄ recovery were 4.5 MPa and 281.15 K with 37.7 and 51.9 % CH ₄ recovery as well as 54.6 and 68.9 % were obtained with SiO ₂ and ZnO nanoparticles respectively.
Heydari et al., (2020)	Investigation of rhamnolipid a biosurfactant and SDS effects in CH ₄ -CO ₂ replacement.	Induction time and duration of replacement reaction were reduced by 99 and 84 % by rhamnolipid and SDS respectively. Rhamnolipid enhanced the kinetics of the replacement by 39 % when injected with carbon dioxide and improve gas storage by 20 %.
Effects of Pressure		
Yoon et al., (2005)	Transformation of CH ₄ hydrate to CO ₂ hydrates employing In Situ Raman Spectroscopic observations.	Shielding effects of CO ₂ hydrate in the outer layer impeded CH ₄ hydrate dissociation from the core.
Ota et al., (2007)	CH ₄ -CO ₂ replacement in CH ₄ hydrate using pressurized CO ₂ . Raman spectroscopy was utilized for compositional analysis.	Replacement rates increased with increasing pressure up to 3.6 MPa thereafter no significant change up to the upper pressure limit of the experiment which was 6.0 MPa. Compositional analysis of the hydrate 0.69 CH ₄ /0.31 CO ₂ and 0.64 CH ₄ /0.36 CO ₂ at 3.2 and 3.6 MPa respectively. Moreover, fugacity difference between the fluid and the hydrate phase was reported to be the driving force of the reaction.

Table A.1: Summary of factors affecting CH₄-CO₂ Replacement Reaction. (*continued*)

Zhao et al., (2016)	Combined replacement and depressurization for CH ₄ gas recovery from CH ₄ hydrate.	Experimental reaction reported to occur in two stages two: viz, fast surface reaction and a slow reaction due to the hydrate layer blocking CO ₂ diffusion pathways. Depressurization resulted in opening new pathways for CO ₂ to penetrate inner parts of the hydrate resulting in increased replacement reaction.
Ding et al., (2020)	The effects of CO ₂ partial pressure on CH ₄ recovery in CH ₄ -CO ₂ swap with simulated IGCC syngas.	CH ₄ concentration in the gas increased from 2 to 18.6 % and 17.8 % in the first 3 days and remained unchanged for the next 5 days at 4.4 MPa. Whereas, at higher pressure the CH ₄ concentration increased from less than 2 to 9.71 % and 7.67 % in the first 2 days. Overall CH ₄ yield for low-pressure experiment was 71 % and for high pressure experiment was 32 %.
Effects of Carbon dioxide state		
Prashanti et al., (2005)	Thermodynamics feasibility studies and experimental work on CH ₄ -CO ₂ replacement reaction in porous media.	Slow release of CH ₄ gas and CO ₂ gas encapsulation was possible under excess CO ₂ gas conditions. Rate of CH ₄ improved as reaction temperature was doubled.
McGrail et al., (2007)	Utilization of emulsion of water and CO ₂ in replacing CH ₄ with CO ₂ in gas hydrate reservoirs.	Replacement thermodynamically feasible with 20 % excess heat generated by CO ₂ hydrate formation than produced from CH ₄ dissociation.
Zhou et al., (2008)	Replacement of CH ₄ from quartz sand-bearing hydrate with CO ₂ -H ₂ O emulsion.	Emulsion resulted in improved CH ₄ gas yield when compared to liquid CO ₂ . Replacement rate of CH ₄ was initially high but decreased with time, with the fastest rate of 0.608 l/h and slowest rate of 0.063 l/h reported with 90:10 CO ₂ : H ₂ O resulting in the best yield.
Zhao et al., (2012)	Review of replacement of CH ₄ in natural gas hydrates by using CO ₂ in different states.	CO ₂ emulsion had the fastest reaction rate compared to other forms of CO ₂ . The factors influencing the replacement were the phase of CO ₂ , the initial pressure and temperature as well as additives. Simulations of replacements are not fully developed, and the micro-mechanism of the replacement are still in its infancy.

Table A.1: Summary of factors affecting CH₄-CO₂ Replacement Reaction. (*continued*)

Lee et al., (2014)	Quantitative measurement and mechanisms for CH ₄ production from hydrates with the injection of liquid CO ₂ .	The mechanism of exchange could be deduced from the depth of CO ₂ penetration and kinetic models describing the physical the physical process of diffusion. Two stages of reactions were suggested, fast surface reaction which is reaction limited for exchange and a diffusion limited process at the hydrate core.
Effects of Porous Media		
Babu et al., (2014)	CH ₄ production from natural gas hydrates through CO ₂ fixation.	Low recovery rates of CH ₄ were obtained due to mass transfer rate of CO ₂ into the core of the hydrate being the hindrance.
Song et al., (2016)	Investigation of CO ₂ -CH ₄ -H ₂ O hydrate phase equilibrium to obtain CO ₂ /CH ₄ thermodynamic data in the porous media to enhance CO ₂ /CH ₄ replacement reaction.	The equilibrium pressure of CO ₂ in porous media was lower than that of CH ₄ at the same temperature. An improved thermodynamic model was proposed from the study.
Pan et al., (2020)	Experimental study on CH ₄ production from hydrate bearing clay and sand sediments by CO ₂ /N ₂ replacement.	Clay hindered gas diffusion in the initial stage of the experiment hence reducing CH ₄ recovery rate. Clay interlayer later leads to geometric constraints, moreover, thermodynamics gas inhibition between CO ₂ /N ₂ and CH ₄ in the hydrate. 80.4 % of CO ₂ sequestration was obtained with sand only as well as a replacement efficiency of 30 % obtained with 50 % clay.
Kossel et al., (2021)	Microscale process and process dynamics and guest-molecule exchange in gas hydrate in the presence of porous media.	50 % of CO ₂ was involved in the CH ₄ exchange while 50 % of CO ₂ formed new formation of CO ₂ hydrates. Sand matrix affected the experiment in two ways, viz: sinuous pathways hindered transport of the constituents in the sample also the chemical potential of the gas hydrates proximately to the surface of sand. Moreover, at 272 K and 3-3.5 MPa D _{CH₄} (diffusion coefficient) was approximately 10 ⁻¹⁶ – 10 ⁻¹⁸ m ² /s and values for D _{CO₂} was in the order of magnitude 10 ⁻¹⁵ – 10 ⁻¹⁷ m ² /s.
Effects of Thermal Simulation		

Table A.1: Summary of factors affecting CH₄-CO₂ Replacement Reaction. *(continued)*

Zhang et al., (2017)	Study of CH ₄ /CO ₂ replacement with thermal simulation applied to enhance CH ₄ recovery and storage.	CH ₄ replacement effectively improved from 21.06 to 63.13 % and from 11.55 to 59.16 %. CO ₂ was observed to be sensitive to free water in pores of the methane sediments. CO ₂ storage efficiency improved also influence of free water on CO ₂ storage lightened.
Maria et al. (2018)	Natural gas recovery from hydrate compounds using CO ₂ for replacement with thermal stimulation	Flux of CO ₂ hydrate formation at the same time forms a hydrate layer above the CH ₄ thus hindering the replacement reaction. Furthermore, increasing the temperature after injecting CO ₂ , produces an incomplete replacement
Gambelli et al., (2019)	investigated replacement reaction using two methods. In one method after CH ₄ hydrate formation, CO ₂ was introduced into a cell with a solid phase of CH ₄ hydrate and a gaseous phase composed of both CH ₄ and CO ₂ then the temperature was increased. In the second method after CH ₄ hydrate formation temperature was increased after which CO ₂ was introduced.	The intention was to move the thermodynamic condition from a region where both CH ₄ and CO ₂ hydrates can form easily to a region where only CO ₂ hydrate formation is possible without any addition of thermal energy. Thus, the CO ₂ hydrate formed immediately, and massive heat energy was released. The amount of CH ₄ released and CO ₂ stored did not differ for the two methods, but the lower thermal energy was required for the second method.
Ouyang et al., (2020)	A novel method where in-situ intermittent heating assisted CO ₂ replacement (IIAR) method to enhance CH ₄ production from hydrates was utilised. An electrode simulating the in-situ heating was used in investigation.	Presence of N ₂ and liquid CO ₂ was conducive to CH ₄ hydrate exploitation. Increasing temperature and decreasing pressure aids IIAR to partially dissociate the hydrates and promote CH ₄ -CO ₂ /N ₂ replacement. Maximum CH ₄ recovery was 52.42 % obtained at 8.01 MPa, and 279.15 K in 48 hours. Improved recovery indicated that IIAR was better than pure CO ₂ and CO ₂ /N ₂ replacement and CO ₂ replacement combined with thermal stimulation
Xie et al., (2021)	Investigation of CH ₄ -CO ₂ hydrate replacement below freezing point of water. Construction of a porous CO ₂ hydrate layer was suggested to counter-act the reformation of a compact CO ₂ which impedes gas diffusion through in either direction.	The multi-defective ice generated from dissociated CH ₄ formed porous CO ₂ hydrate be which enhanced the replacement reaction. It was observed that replacement was more efficient at a higher temperature of 272.15 K with extent of replacement being 51.50 % than 268.15 K were extend of reaction was 25.75 %.

Table A.1: Summary of factors affecting CH₄-CO₂ Replacement Reaction. (*continued*)

Fan et al., (2022)	Investigated CH ₄ -CO ₂ replacement in natural gases by utilising gradual heat stimulation with CO ₂ replacement in the sediments	The gradual heat injection enhanced replacement method (GHIR) enhanced CH ₄ recovery percentage from 8.0% to 25.4%. The maximum amount of CO ₂ sequestered was 64%.
Effects of Saturation		
Yuan et al., (2021)	Utilized three groups of hydrate bearing sediment samples and a middle-size reactor to investigate the favourable conditions for CH ₄ recovery from hydrate reservoir with gaseous CO ₂ .	The hydrate reservoir with the underlying free gas, high saturation of free gas and low saturation of water was most appropriate for the replacement reaction.
Yuan et al., (2013)	Investigation of the dynamics of CH ₄ replacement in natural gas hydrate with liquid and gas CO ₂ at high pressure. Quartz and brine solution were used in the experiment.	The replacement percent of CH ₄ hydrate increases with the decrease of the hydrate saturation and the increase of water saturation. The method of replacing CH ₄ from the hydrate without gaseous CO ₂ , but with liquid CO ₂ is also suitable because the fugacity of liquid CO ₂ decreases very little during the replacement reaction thus the driving force for the replacement reaction remains relatively high.
Theoretical Studies		
Janicki et al., (2021)	Study of replacement reaction of CH ₄ by CO ₂ by depressurisation and/or by CO ₂ injection numerically in a STAR (Steam, Thermal and Advanced Process Reservoir Simulator) code from CMG (Computer Modelling Group) and HyRes (Hydrate Reservoir simulator) in subsea sediment which were 900 m by 20 m by 450 m at 283.15 K.	Permeability proved to be the most important factor for methane gas production while decomposition kinetics and gas-liquid mass transfer are of lower relevance. 75 % CO ₂ saturation was achievable in after six years due to unfavourable P, T conditions in the simulation for hydrate formation.

Table A.1: Summary of factors affecting CH₄-CO₂ Replacement Reaction. (*continued*)

Qorbani et al., (2017)	Numerical simulator reactive transport simulator, RetrasoCodeBright (RCB) working on nonequilibrium systems was utilised to examine the formation of CO ₂ hydrate in a CH ₄ hydrate bed. Simulator was based on a two-dimensional model with length of 1000 m and height of 300 m.	Results confirmed the formation of CO ₂ hydrate around the injected well with horizontal distribution pattern being observed within the CH ₄ hydrate reservoir as porosity of the top layer gradually decreased due to CO ₂ hydrate formation in the top layer. Later, hydrate formation plugged lower parts of the reservoir at the same time-consuming free water limiting hydrate formation in the upper layer of the reservoir.
Osmolovski et al., (2018)	Simulation of gas hydrates deposits CH ₄ / CO ₂ replacement process using gas inhibitor Experimental calculations were made based on Mendeleev-Klaiperon equation.	An analysis of results showed that the 80 % CO ₂ /20 % N ₂ gas mixture affected the amount of CH ₄ extraction in comparison to pure CO ₂ and 120 hours were required for to maximise CH ₄ recovery from the hydrate.
Liu et al., (2018)	Developed a numerical simulation model to investigate heat exchange performance when (GACR) geothermal-assisted CO ₂ replacement method. Carbon dioxide was injected from a well head of a heat exchanger to a well wellbore in geothermal reservoir.	To accelerate the rate of natural gas hydrate (NGH) dissociation the heated CO ₂ flows upwards into the hydrate bearing layer (HBL). In comparison with depressurization method and the case with no geothermal reservoir, cumulative CH ₄ production after 20 years of development can increase by 30.5 and 51.9 % respectively and CO ₂ storage volume of 2*10 ⁷ m ³ .
Gimaltdinov et al., (2018)	A mathematical model for investigating CH ₄ -CO ₂ replacement by injection of carbon dioxide in porous media rich in methane reservoir of infinite length.	Rate of replacement was found to be limited by CO ₂ feed rate which is directly proportional to pressure and reservoir permeability. The amount of CO ₂ needed for CH ₄ in hydrate is directly proportional to the initial hydrate saturation of the reservoir.
Musakaev et al., (2018)	Equations of multiphase media mechanics, a mathematical model were utilised for the replacement reaction of CH ₄ with CO ₂ in a porous reservoir for an infinite time duration	The replacement was initially dependent on the injection pressure and could occur with CO ₂ in liquid and gaseous phase.

Table A.1: Summary of factors affecting CH₄-CO₂ Replacement Reaction. (*continued*)

Guo et al., (2020)	Analysis of thermal decomposition and diffusion of CH ₄ in clathrate hydrates from quantum mechanics (QM) and quantum mechanics molecular dynamics (QMD) simulations.	Simulations showed that initial decomposition reaction in CH ₄ hydrate from hydrogen transfer among water molecules and attacks by fragments of O, and OH on CH ₄ molecules were responsible for the breakdown of CH ₄ molecule.
Hsieh et al., (2020)	Study to establish a mesoscale model for CH ₄ /CO ₂ replacement to precisely estimate the flux of CH ₄ hydrate dissociation and CO ₂ hydrate formation in hydrate cages. CH ₄ hydrate dissociation and CO ₂ hydrate formation were established at CH ₄ hydrate stable and unstable regions.	Most of the CH ₄ recovered dissociated from the surface of the hydrate. Formation rate of CO ₂ hydrate was found to be dominated by dissociation rate of CH ₄ . In stable regions CO ₂ was considered as the guest particle replacing CH ₄ in the hydrate due to free energy difference, hence replacement is dominated by the dissociation of CH ₄ . In the unstable region large amounts of CH ₄ dissociate hence replacement is dominated by CO ₂ hydrate formation rate.

Table A.2: Progression in hydrate clathrate investigation as an energy storage media.

Reference	Nature of study	Conditions and Additives	Equipment and Analysis	Observation and Results
Dyadin et al., (1995)	Two aspects of clathrate stoichiometry considered; elemental stoichiometry and variation in composition due to the different occupation of host cavities in the framework by guest molecules.	Additives – urea, thiourea, hydroquinone, bromide	Statistic models	Occupation of the host is in accordance with stabilisation of the clathrate framework. All clathrates are non-stoichiometric compounds. Clathrates of constant composition were formed when the hallow framework of the host was unstable.
Dyadin et al., (1999)	Clathrate of neon, argon, and krypton with hydrogen	Pressure – 15 MPa	X-ray	Classical hydrate sII structures are formed whereas argon and krypton are known as polyhedral clathrate formers at higher pressure. Stability decreases in the order from xenon to neon and the larger the guest molecule, the higher the pressure required for their formation.
Mao et al., (2002)	Study of hydrogen clusters in clathrate hydrate	Pressure – 0.01 to 0.03 MPa Temperature – 145 K	High-pressure Raman infrared, X-ray, and neutron	H ₂ and H ₂ O crystallise into sII clathrate structure with H ₂ /H ₂ O in 1:2 ratio. Clathrates were multiply occupied with two H ₂ molecules in a small cage and four in the large cage. At a pressure of 220 MPa and temperature of 234 K, H ₂ gas could form a structure II clathrate with a storage capacity of 3.8 %.
Florusse et al., (2004)	Stable low-pressure hydrogen clusters stored in a binary clathrate hydrate.	Additive-THF Pressure – 5 MPa Temperature – 279.6 K	Thermodynamic, X-ray diffraction, and Raman and Nuclear magnetic resonance spectroscopy	In a study of stable low-pressure hydrogen clusters stored in binary clathrate hydrate reported that addition of THF reduces hydrate formation conditions to 5 MPa, and 279.6 K and hydrate storage capacity was reduced.
Lee et al., (2005)	Investigating most economic means of hydrogen storage in the binary-clathrate hydrates of H ₂ and a guest molecule.	Additives - THF Pressure – 200 MPa Temperature - 277.3 K	Raman spectroscopy NMR spectroscopy	Synthesis pressure can be decreased by filling the larger cavity with THF to stabilise the material. However, this compromises the potential storage capacity of the material. The storage capacity was increased by 4 wt % at modest pressures by tuning their composition to allow the hydrogen guests to enter both the larger and the smaller cages while retaining low-pressure stability. This process is known as “tuning mechanism” and is convenient using water-soluble hydrate promoter

Table A.2: Progression in hydrate clathrate investigation as an energy storage media. (Continued)

Strobel et al., (2006)	Hydrogen storage capacity of binary THF-H ₂ clathrate hydrate as a function of formation pressure, THF composition and time was determined.	Additives – THF Pressure – 60 MPa Temperature – 250 K	NMR spectroscopy	Amount of H ₂ stored in the stoichiometric hydrate increases with pressure, exhibiting asymptotic (Langmuir) behaviour to approximately 1.0 % H ₂ . This procedure corresponds to one hydrogen molecule occupying each of the small 5 ¹² cavities and one THF molecule in each large 5 ¹² 6 ⁴ cavities in the hydrate framework. It was proven that THF preferentially occupies 5 ¹² 6 ⁴ cavities over hydrogen.
Chapoy et al., (2007)	Low-pressure molecular hydrogen storage in semi-clathrate hydrates of quaternary was investigated.	Additives – TBAB (tetra-n-butylammonium bromide), quaternary ammonium salts (QAS), tetra-n-butylammonium fluoride (TBAF) Pressure – 200 MPa Temperature – 293 K.	NMR Spectroscopy	Hydrogen can be stored in the structural cavities of a clathrate hydrate known as a semi-clathrate hydrate of QAS. Stability of binary H ₂ -TBAB and H ₂ -TBAF semi-clathrate hydrate, which is stable at ambient temperature to atmospheric pressure, as well as ease of formation/ H ₂ regeneration and low QAS vapour pressure, makes the semi-clathrate attractive as potential H ₂ storage media.
Strobel et al., (2007)	Hydrogen storage potential of several clathrate systems by direct gas release measurements, and by theoretical storage considerations was investigated.	Additives - TBAB at different compositions was utilised.	High-pressure Raman spectroscopy	New insights into the spectral properties of hydrogen molecules within hydrate cavities and maximum hydrogen storage capacity in the different clathrate structures were reported. Also, hydrogen storage potential of a semi-clathrate with TBAB was comparable to the THF-H ₂ hydrate based on small cavities occupied at the same hydrogen fugacity.
Duarte et al., (2009)	Experimental study on phase equilibrium on stabilisation of sH hydrogen clathrate hydrate with the aid of some selected promoters	Additives – THF, 1, 1 - dimethylcyclohexane, methyl tert-butyl ether (MTBE), and methylcyclohexane (MCH). Pressure – 100 MPa Temperature – 360 K	Stainless- steel optical high-pressure cell, Clausius-Clapeyron and Van der Waals	The hydrogen storage capacity of structure sH could be as high as 1.4 wt % of H ₂ , which is approximately. 40 % higher compared to the hydrogen storage capacity in structure sII. Also, the formation pressure of the system was higher than that of structure sII of hydrogen clathrate hydrate when THF was used as a promoter.

Table A.2: Progression in hydrate clathrate investigation as an energy storage media. (Continued)

Strobel et al., (2008)	Measurements on hydrogen in sH binary clathrate hydrate.	Additives – (MTBE), (MCH), 2,2,3-trimethylbutane (2,2,3-TMB), 1,1-dimethylcyclohexane (1,1-DMCH). Pressure – 150 MPa Temperature – 275 k	X-ray and Raman spectroscopic measurements	Molecular hydrogen containment within small water cavities of a binary sH clathrate hydrate using large guest molecules that stabilize the large cavity. Hydrogen storage capacity could be increased by 40 % compared with binary sII hydrates. Stabilisation of hydrogen in the hydrate structure by encapsulation of molecular hydrogen is demonstrated, indicating a potential for other inclusion compound material with ever more excellent hydrogen storage capabilities.
Shin et al., (2009)	TBAB applied as a hydrogen hybrid storage material in a semi-clathrate, and the storage of molecular hydrogen within the vacant cavities.	Additives - TBAB, THF	X-ray diffraction measurement verifying the formation of TBAB semi clathrate. Raman spectroscopic and direct gas release measurements confirmed	The decomposition temperature of tetra-n-butylammonium borohydride semi-clathrate was found to be higher than that of pure THF hydrate, with the BH ₄ ⁻ anion stabilising tetraalkylammonium hydrates and increasing the semi-clathrate storage capacity by 27 % than that of fully occupied THF + H ₂ hydrate.
Ogata et al., (2008)	Hydrogen storage in tetrahydrofuran hydrate through <i>P-V-T</i> measurements	Additives - THF Temperature – 277.15 K Pressure – 85 MPa	Raman spectroscopic analysis	The storage amount of hydrogen obtained from P-V-T measurements was 1.6 mole hydrogen /mole tetrahydrofuran (about 0.8 mass %) at 70 MPa while with maximum storage capacity of 2.0 mole hydrogen /mole tetrahydrofuran measurement
Prasad(a) et al., (2009)	Hydrogen storage in double clathrates with <i>tert</i> -butylamine	Additives - t-BuNH ₂ Pressure - 13.8 MPa Temperature - 250 K.	Powder X-ray diffraction and Raman microscopy were utilised for characterisation of binary clathrate	Structural transformation from sVI to sII of t-BuNH ₂ hydrate under high pressures. Hydrogen storage capacity in the system was approximately 0.7 H ₂ wt % at the molar concentration of t-BuNH ₂ close to sII stoichiometry. Hydrogen molecules were observed to occupy small cages and had small occupancy to hydrogen in the double THF + H ₂ clathrate hydrate
Prasad(b) et al., (2009)	Binary clathrate hydrates with (CH ₄ , 4.36 Å) and t-BuNH ₂ .	Additive - t-BuNH ₂ , 6.72 Å as guest molecules synthesised with different concentrations Pressure -7 MPa Temperature - 250 K.	Powder X-ray diffraction (PXRD) and Raman microscopy were utilised for characterisation.	The structural transformation from sVI to sII of t-BuNH ₂ hydrate was observed on pressuring with CH ₄ , sII signatures and the remnant sVI signatures were insignificant meaning that metastable nature of sVI binary hydrate. Raman spectroscopic data suggested that CH ₄ molecules occupy the small cages and vacant large cages. Methane storage capacity in the system was nearly doubled.

Table A.2: Progression in hydrate clathrate investigation as an energy storage media. (Continued)

Sugahara et al., (2009)	Increasing hydrogen storage capacity	Additives - THF	Raman Spectroscopy, Powder X-ray diffraction.	H ₂ clusters in the large cages of sII due to different hydrate preparation methods, increasing H ₂ storage by 3.4 % below the eutectic composition of THF + water binary system. To measure the amount of H ₂ in hydrate, a liquid N ₂ quenched depressurised hydrate cell will dissociate.
Walsh et al., (2009)	Simulation of microsecond growth of methane hydrate nucleation and growth was studied	Additives - THF	Ruska gasometer to measure the volume of gas released.	sI and sII were the resulting structures at the end of the simulation. Also, molecular order of the adsorbed methane molecules in the bowl-like arrangement immediately before hydrate formation and the minuscule nucleus size needed to initiate hydrate growth; the relative positions of the guest molecules, and not only the nucleus size, have a bearing on the control of hydrate nucleation.
Deschamps et al., (2010)	Determination of phase equilibrium properties of hydrogen+ semi-clathrate hydrates under pressure.	Additives - (TBAB), Tetrabutylammonium chloride (TBACI), tetrabutylphosphonium bromide (TBPB). Pressure - 15 MPa Temperature - 233 to 353 K	Differential scanning calorimetry	Amount of hydrogen stored in hydrogen H ₂ + TBACI and H ₂ + TBPB semi clathrate estimated in terms of the H ₂ to water mole ratio calculated from dissociation enthalpies and (P, T) equilibrium data was 0.12 and 0.14 % respectively.
Chattaraj et al. (2011)	Study of structure, stability, and reactivity of clathrate hydrates with or without hydrogen encapsulation are studied using standard density functional calculations.	Standard density functional calculations.	Conceptual density function theory-based reactivity descriptors and the associated electronic structure principles are used to explain the hydrogen storage properties of clathrate hydrates.	H ₂ clathrate hydrate complexes increase upon the subsequent addition of hydrogen molecules to clathrate hydrates. The art of trapping hydrogen molecules inside the cages of clathrate hydrate in an endohedral fashion depends upon the cavity sizes and shapes of the clathrate hydrates. Analysis reveals that 5 ¹² and 5 ¹² 6 ² structures can accommodate up to two H ₂ molecules while 5 ¹² 6 ⁸ can accommodate up to six hydrogen molecules.
Grim et al., (2012)	Hydrogen growth from non-stoichiometric tuning mixtures during liquid nitrogen quenching was studied.	Additive - THF Pressure – 60 and 72 MPa. Temperature – 258 and 90 K	Confocal Raman spectroscopy	New pathway discovered for large cage enclathration of hydrogen in tuning method

Table A.2: Progression in hydrate clathrate investigation as an energy storage media. (Continued)

Babae et al., (2012)	Hydrogen hydrate in the presence of different promoters	Additives-2,2,3-trimethylbutane, 2,2-dimethylbutane, 3,3-dimethylpentane, 2,3-dimethyl-1-butene, 3,3-dimethyl-1-butene, 3,3-dimethylbutyne, methylcyclohexane, methylcyclopentane, and cycloheptene	Thermodynamic models	Thermodynamic model was proposed to predict the phase equilibria of the sH clathrate hydrate of hydrogen in the presence of a promoter. The storage capacity is almost identical in the case of application of various promoters studied in this work, which lie in the range of about 50–57 vol.% of hydrate unit cell.
Lele et al., (2015)	Numerical investigation of thermochemical heat storage.	Additive – Magnesium chloride (MgCl ₂) Temperature - 288.15 to 363.15 K	Modelling and simulation	Reaction observed to be temperature dependant and pressure independent, thus the system is applicable in a vacuum. Model validated with salt hydrate in a lab scale.
Grim et al., (2014)	Experimental measurements and simulations, examining the <i>tert</i> -butylamine + H ₂ + H ₂ O hydrate system	Additive - tBuNH ₂ Pressure – 70 MPa Temperature – 190 K	In-situ neutron diffraction Raman spectroscopic measurements	Reported on the possibility of H ₂ incorporation within hydrate crystal structures by occupying intestinal sites (locations other than the interior of regular polyhedral water cages). H ₂ ability to occupy interstitial sites and fluctuate position in the crystal lattice demonstrates the dynamic behaviour of H ₂ in solids revealing insights on interactions within the clathrate hydrate with a potential of increasing the overall storage properties.
Nguyen et al., (2020)	Promoting the addition of molecular hydrogen in tetrahydrofuran hydrate with the inclusion of acidic additive was investigated.	Additives - THF Pressure – 5.5 MPa Temperature – 270 K.	In-situ confocal Raman micro spectroscopy and imaging.	Break through on hydrogen diffusion in acidic THF-H ₂ hydrate. Observed that hydrogen insertion in the THF hydrate is optimum at the operation conditions. Furthermore, the co-inclusion of acid promotes the molecular hydrogen insertion within the hydrate structure.
Davoodabadi et al., (2021)	Hydrogen hydrate as a potential future energy source.			Hydrogen is recognized as a fuel for the future with an energy content per unit mass of 142 MJ/kg. Favourable properties for the hydrogen hydrates are low energy consumption for charge and discharge, safety, cost-effectiveness, and favourable environmental features.

Appendix A.2: Exploitation and field tests on Natural occurring hydrates

Various onsite exploitation and tests have been carried out around to harness the energy contained in hydrates such as, thermal-simulation tests carried out by JAPEX/JNOC/GSC on Mackenzie Delta, Canada in 2002 (Guerin et al., 2005). In 1965 drilling carried out at Markhinskaya well down to 1800 m in Yakutia Russia was recorded as the first discovery of natural hydrates (Yakushev and Chuvilin, 2000). Barents Sea outside North America and Russia were explored by Lovo and co-workers in 1990 (Demirbas, 2009). In 2002, the U.S Department of Energy and BP Exploration (Alaska) in co-operation with the USGS initiated a research program on Alaska North Slope (ANS) gas hydrates (Lovo et al., 1990). In partnership with University of Texas at Austin, plans are in place for drilling and expedition to assess occurrence and nature of gas hydrates in deep waters of Gulf Mexico (Schoderbek et al., 2011). The U.S Department of Energy has made advanced progress in exploration of gas hydrates (Ignik Sikumi gas hydrate field) (Frye, 2008). In Japan extensive studies have been carried out on harnessing energy from methane hydrates in Japanese Sea and Okhotsk Sea by the research consortium for methane hydrate resources in Japan since 1993 (Allison and Boswell, 2000). The Black Sea has been investigated for its potential in methane rich gas hydrates. It has been reported that marine sediments from the Black Sea were observed to contain methane hydrate in 1974 (Oyana and Masutani, 2017). Japan oil and gas metals corporation (JOGMEC) have carried out large-scale field tests in Arctic Canada (1998, 2002, and 2008) and in the deep-water Nankai in Japan (2000, 2005, 2013). Multi-site drilling in the Arabian Sea, the Bay of Bengal, and the Andaman Islands was carried out by India's government in 2006 (U.S Dept Energy, 2015). The marine expedition has been carried out in China by Guangzhou Marine Geological Survey. Moreover, in 2017 at Shenhu Sea, offshore natural gas production was carried out by China by the depressurisation method (Shaibo et al., 2021).

Appendix B

Review of equipment utilised in hydrate phase equilibrium

B.1 High-pressure rocking cell Deaton and Frost (1937)

The high-pressure static cell shown in figure B.1 was among the first recorded hydrate phase equilibria. The following are the key features:

- View window on the equilibrium cell to visually observe hydrate formation, valve to regulate the flow of gas in and out of the cell, thermocouples, and pressure transducer (Borden tube gauge) were installed to measure temperature and pressure respectively. It is applicable above the freezing point of the hydrate former.
- Its main advantages were the use of little quantity of feed material, suitable for single and multiple components systems, the technique and experiment set-up were simple to carry out also phase behavior could be observed at high pressures with compositions and amount of fluid samples could be changed easily.

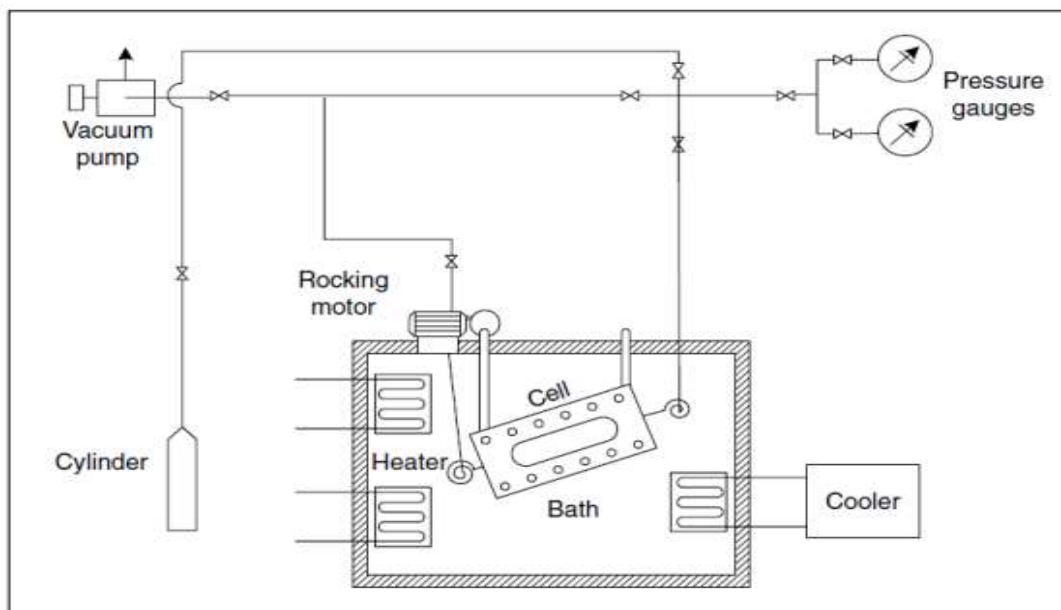


Figure B.1: Deaton and Frost's (1937) rocking apparatus for hydrate phase equilibrium (Sloan and Koh 2008).

B.2 High-Pressure Ball Mill Hydrate Apparatus

This is a high-pressure nonvisual apparatus developed by Kobayashi in the 1950s following the work began by (Katz et al., 1959). The setup consisted of a high-pressure stainless-steel cylinder stainless steel rotating about its axis as shown in figure B.2.

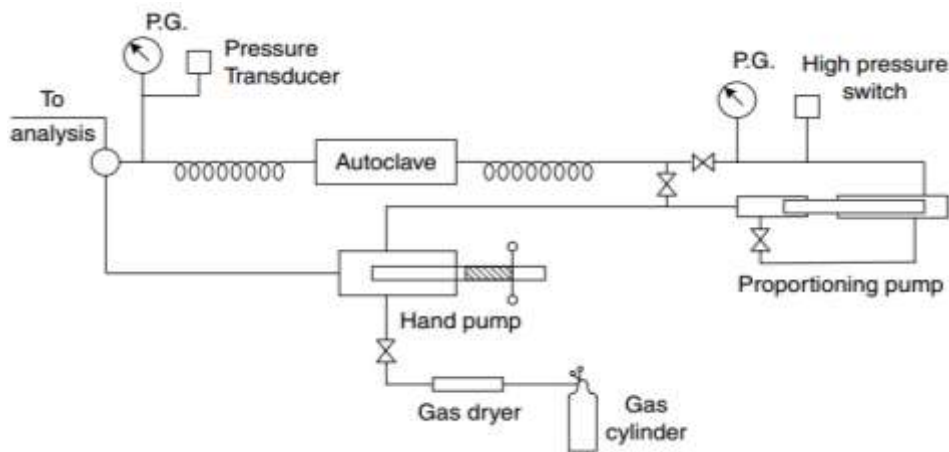


Figure B.2: Ball mill hydrate apparatus for a three-phase and two-phase hydrate equilibria (Sloan and Koh 2008).

- Galloway inserted a stainless-steel ball inside the cylinder for surface area renewal upon rotation so that water can be converted to hydrate. Equipment modifications were carried out by Aoyagi and Kobayashi (1978) so that gas could be recirculated through the cell in a semi-batch operation.
- This apparatus was utilized for two-phase analysis (H-V or H- L_HC) as well as two-phase systems such as methane + water. In this system excess gas was used to convert all the water to the hydrate phase. The ball-mill apparatus was equilibrated to convert excess water to hydrate.

B.3 Cailletet Apparatus

Cailletet is a high-pressure apparatus with a transparent wall for observation of hydrate formation as shown in figure B.3. It has a working pressure range of 0.35-15 MPa and a temperature range of 250-450 K (Peters et al., 1986., Peters et al., 1993). The following were the main feature of the apparatus:

- A 500 mm thick-walled Pyrex glass tube referred to as Cailletet tube utilized as an equilibrium cell with an inner diameter of 3 mm and an outer diameter of 10 mm. The upper end of the tube was closed, with the lower end of the tube with a conical thickening enabling the tube to be mounted in an autoclave.
- The synthetic method was utilized in the study, experimental samples of known composition are added from the top of the tube using mercury as a sealing and pressure-transmitting fluid. The open end of the tube placed in an autoclave was always immersed in mercury. Stirring of the sample in the top tube was accomplished magnetic by a soft iron rod coated with a soft iron rod.

- Cailletet tube was surrounded by a thermostat jacket, with the temperature of the sample kept constant by the circulation of the liquid through the jacket. Dead-pressure weight was used to measure equilibrium pressures, the autoclave was connected to the hydraulic oil system. Oil was pressed into the system through a screw-type hand pump.
- Its use has been discontinued due to the toxic nature of mercury and mechanical degradation of the apparatus due to regular volume adjustments:

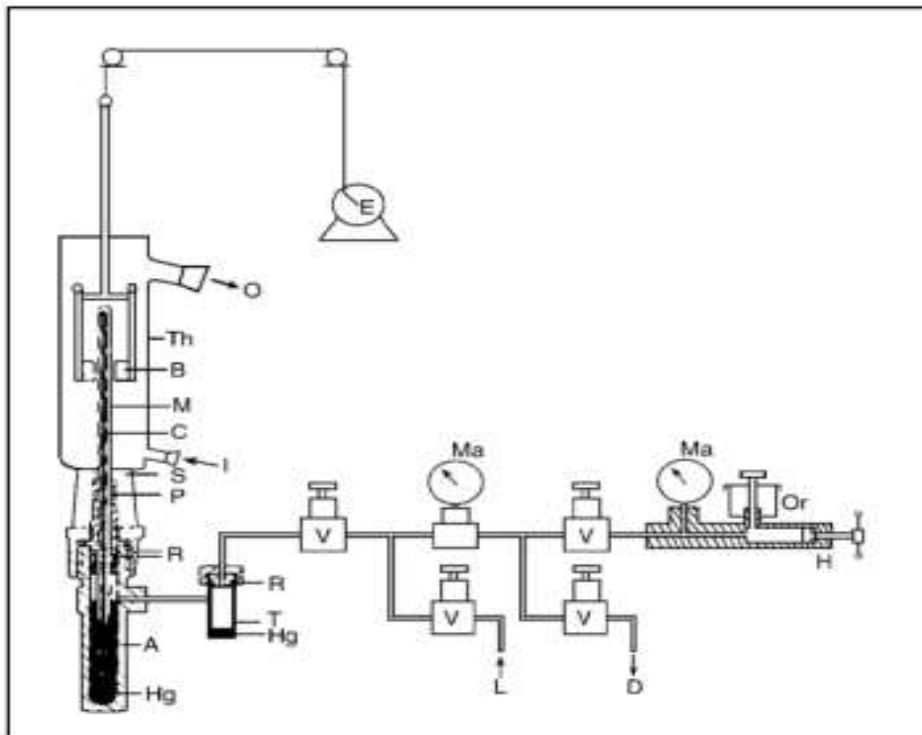


Figure B.3: Cailletet apparatus. (A) autoclave; (B) magnets; (C) Cailletet tube; (D) drain; (E) stirring motor; (H) hydraulic pump; (Hg) mercury; (I) inlet thermostat liquid; (L) connection with dead-weight pressure gauge; (M) sample of mercury; (Ma) manometers; (O) outlet thermostat liquid; (Or) oil reservoir; (P) closing plug; (R) O-rings; (S) silicone rubber stopper; (T) mercury trap; (Th) glass thermostat; (V) valve (Peters et al., 1993).

B.4 Sapphire Equilibrium Cell

This apparatus utilized an equilibrium cell made of a sapphire tube shown in Figure B.4. It was used in the measurement of gas hydrate equilibria for CO₂ + electrolytes. It had the following features:

- It consisted of a Sapphire tube with a pressure limit of 15 MPa fitted with 316 stainless steel as the top and bottom flanges with a Ruska piston pump employed to vary the volume of the equilibrium cell tapping from the mercury reservoir.

- Gas chromatography was used for vapour phase analysis, for solutions containing electrolytes pressure were estimated using data at a lower temperature (Dholabhai et al., 1993). Mercury was introduced into the reservoir once the temperature reached equilibrium to increase system pressure. Once the hydrate formed, it was decomposed by pressure decrease in the system through mercury withdrawal from the reservoir, to a value lower than the equilibrium pressure. Consequently, a new set-point of the system was set to obtain new equilibrium conditions.

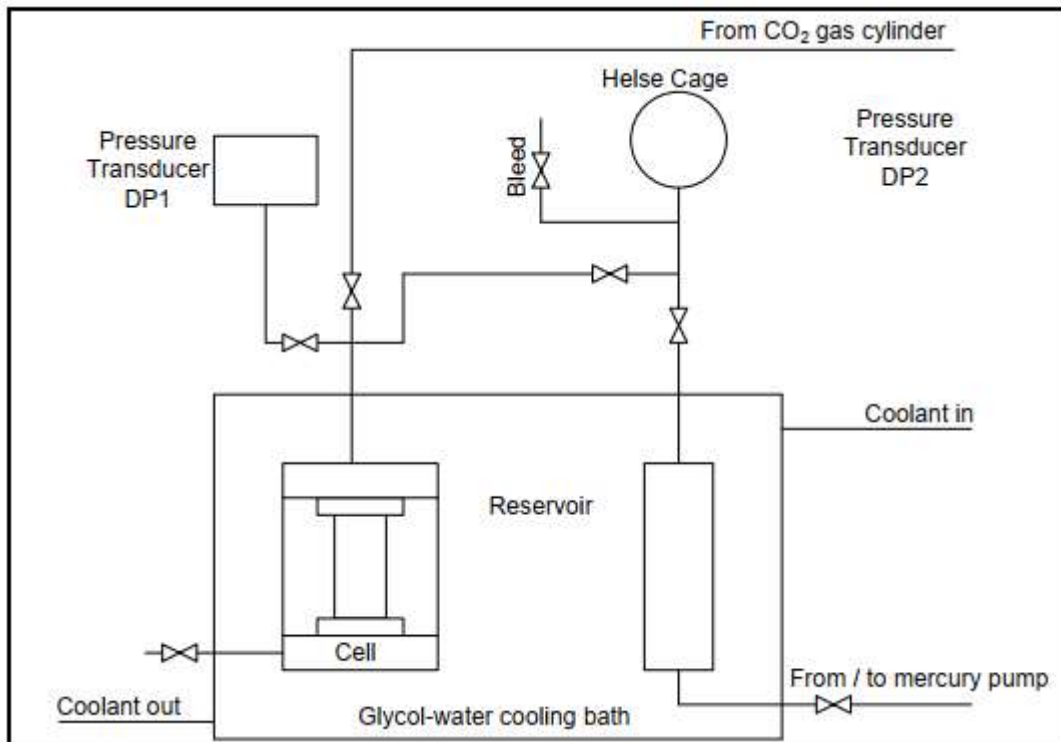


Figure B.4: Saphire equilibrium cell apparatus (Dholabhai et al., 1996).

B.5 Quartz Crystal Microbalance (QCM)

One of the modern apparatuses that have been assembled is a quartz crystal microbalance shown in figure B.5. It was first published and utilized in hydrate measurements by Mohammadi et al., (2003) with the following key features:

- A thin disk of quartz is placed between two electrodes which conduct electric current which causes the quartz disk to oscillate at a specific frequency. Hence hydrate formation and dissociation are depicted by changes in resonance frequency as the hydrate forms and detach from the quartz crystal surface.

- Temperature and pressure are measured by a thermocouple and pressure transducer respectively.
- This setup took less time compared to other apparatuses (15 min) to reach equilibrium. Furthermore, (Lee et al., 2012) improved its technique by adjusting the droplet size.

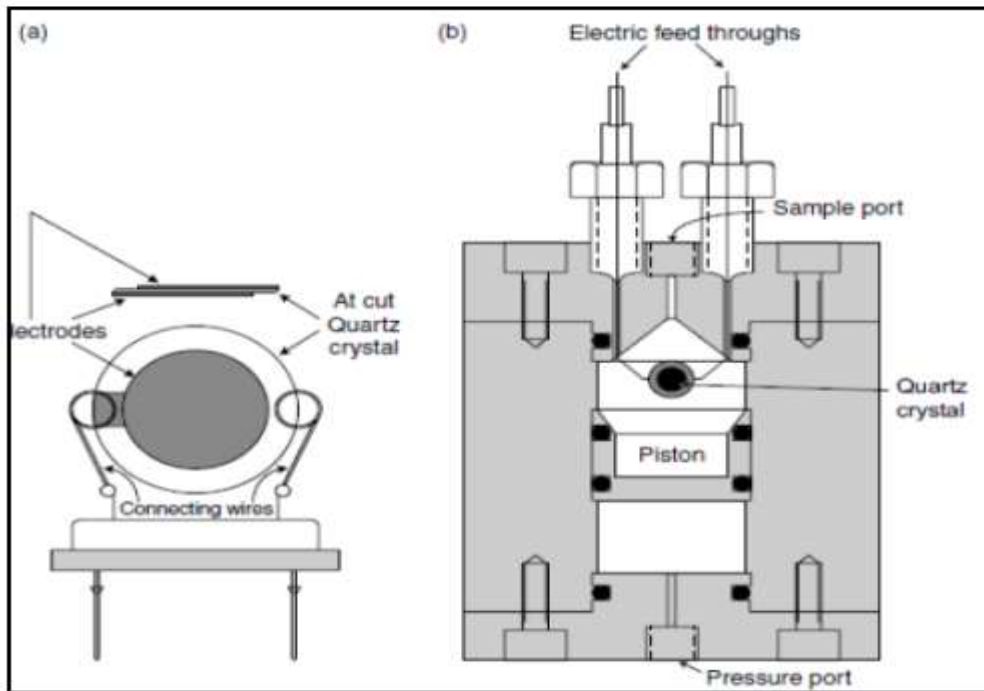


Figure B.5: Quartz Crystal microbalance (QCM) (Mohammadi et al., 2003).

B.6 Differential Thermal Analysis (DTA)

The DTA apparatus shown in figure B.6, was designed to distinguish the thermal behaviour of binary and ternary mixtures for the phase diagram of CO₂ hydrate mixtures and measurement of heat transfer as could be inferred from its name (Fournaison et al., 2004). It has the following key features:

- Composed of two symmetric transparent glass cells, one containing an experimental solution and the other with an inert solution. Hydrate formation occurs in a thermal bath, gas introduced through an injection system to set initial pressures.
- Temperature and pressure were measured with a thermocouple and two-pressure transducer respectively, in each cell. Furthermore, eight thermocouples in series connection were utilized in measuring the temperature difference between the two cells to perform DTA computations.
- The cell undergoes cyclic increasing or decreasing of temperature to permit hydrate formation and dissociation at controlled cooling and heating rates. Hence equilibrium

conditions were determined at a constant pressure by increasing the temperature while for the constant temperature they were determined by decreasing pressure.

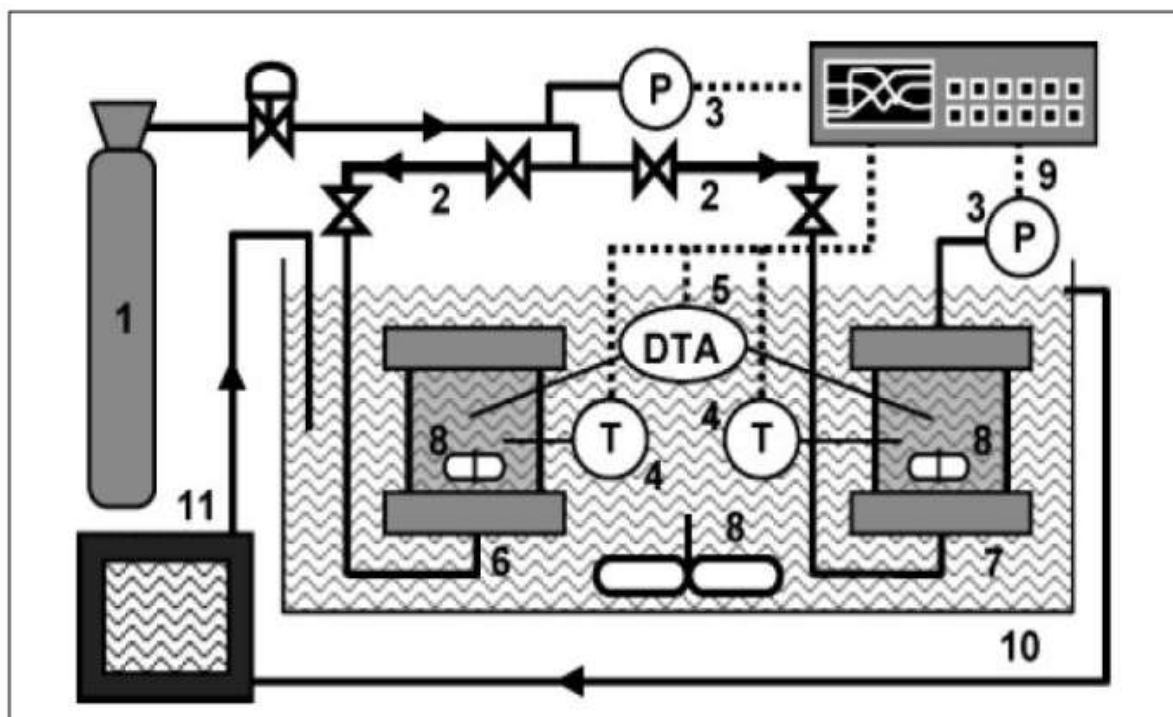


Figure B.6: Differential thermal analysis (DTA) (Fournaison et al., 2004).

B.7 Differential Scanning Calorimeter (DSC)

High-pressure DSC was a design and successfully employed for hydrate phase equilibria data as well as hydrate thermal property data (Delahaye et al., 2006). Micro-DSC analyzer in conjunction with High-pressure differential scanning Calorimetry (HP-DSC) produced excellent thermodynamics stability boundaries of methane and natural gas in the presence of inhibitors (Dalmazzone et al., 2002). DSC apparatus is shown in figure B.7: and had the following properties:

- Two pressure-controlled cells, which were, a sample cell containing the experimental solution and an empty reference cell. Once charged with the experimental system, the sample cell was placed in the furnace purged of any air by gas feed lines then gas pressure set at a constant value to obtain each experimental point. No stirring mechanism was installed in the apparatus due to the nature of the system.
- This apparatus had a simple technique, required little experimental sample, was less time consuming, and was utilized for thermodynamics and kinetic studies for the

formation of high-pressure gas hydrate for suspensions, emulsions, and complex fluids while maintaining high-level of precision as classical PVT techniques.

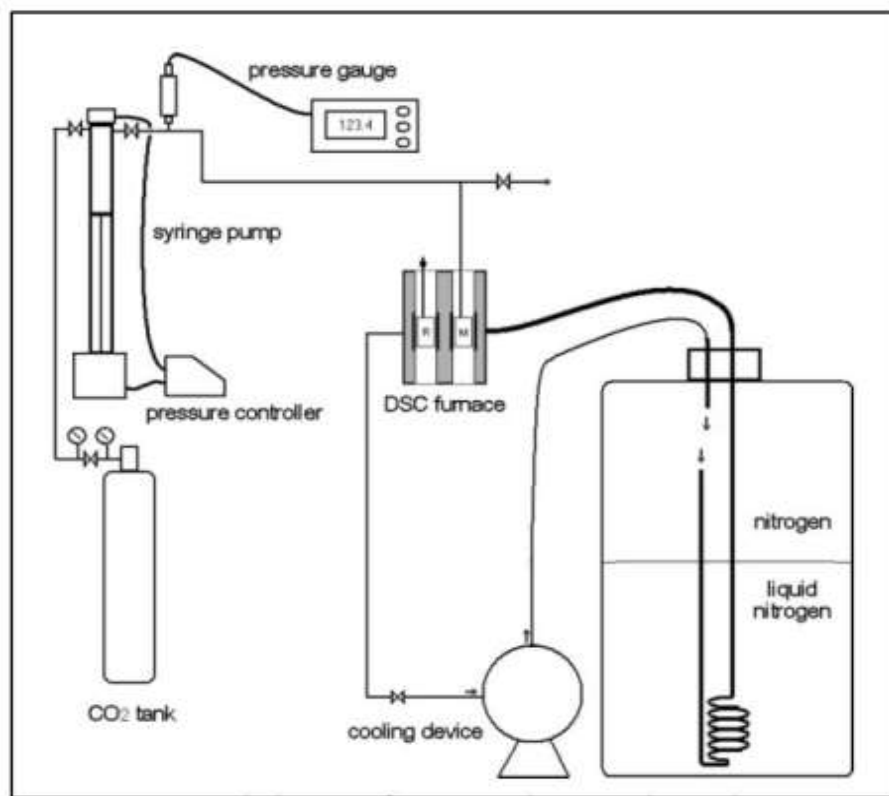


Figure B.7: Differential scanning calorimeter schematic diagram (Delahaye et al., 2006).

Appendix C: Equipment utilized in Kinetic studies

C.1: Description of equipment utilised in this study

Two set of equipment was utilised in this study, one for kinetic measurement and the second for replacement reaction without the porous media. The equipment setup utilised for the measurement of kinetics is shown in **Figure 4.1**;

The equipment in Figure 4.1, was originally designed and commissioned by Ngema (2014). The setup from the following auxiliary equipments:

- A 34972A Agilent data acquisition unit
- A pressure transmitter WIKA model P-10 range from 0 – 10 MPa
- A Class A temperature probe
- A TDGC2 model variac voltage regulator
- A Polyscience model 7312 programmable temperature circulator
- A Polyscience model KB 80 cold finger
- A mechanical jack
- One Edward's model RV3 vacuum pump
- A Proline computer
- A Shinko ACS-13A temperature controller
- A water bath with external dimension of 595 mm x 460 mm x 360 mm

C.1.1. Equilibrium Cell

The heart of the apparatus was a cylindrical equilibrium cell shown in figure C.1 and C.2 It was constructed from 316-stainless steel with volume of approximately 52 cm³ and has design pressure of 10 MPa. It has inner diameter (I.D) of 40 mm, outer diameter (O.D) of 60 mm, inner height of 45 mm, outer height of 55 mm. It has a top flange of diameter 80 m and thickness of 15 mm fixed on the cell with 6*10 mm stainless steel bolts. On top of the wall of the cell there is a 2*2mm O-ring where an O-ring was placed to ensure that the cell is airtight during

hydrate measurements. O-ring material was selected based on its compatibility with the reactant's gases and other additives. For this reason, viton, PTFE and nitrile O-ring were utilised.

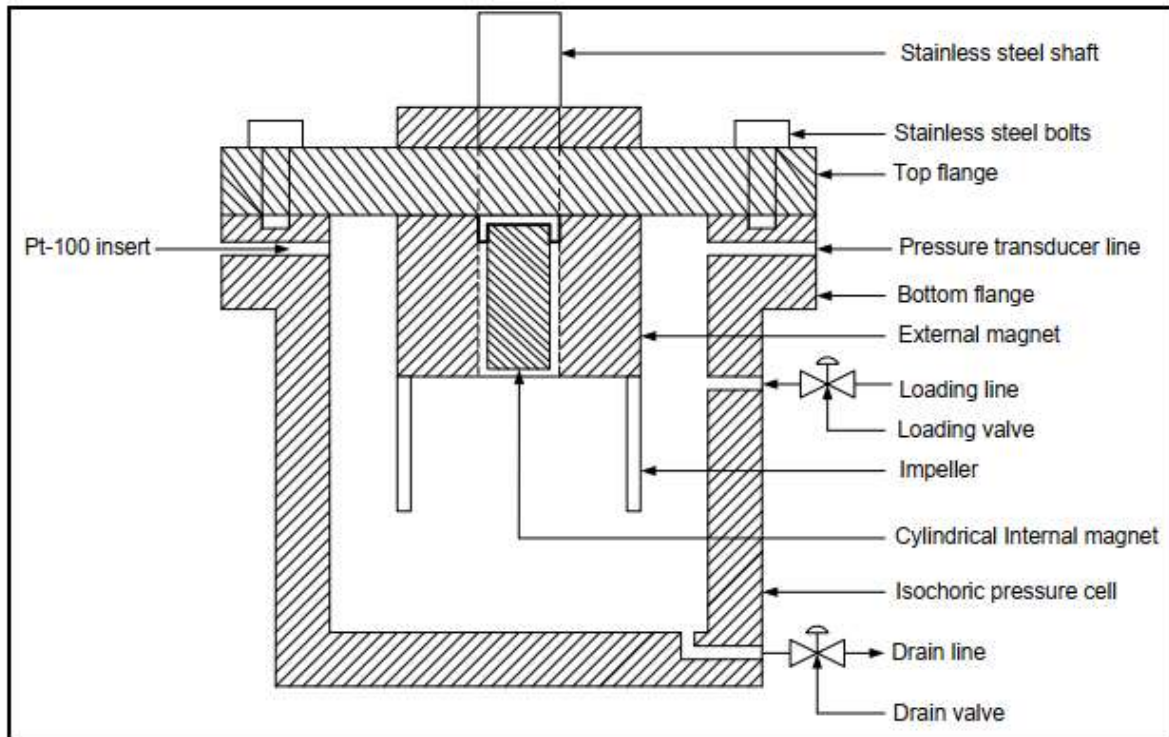


Figure C.1: Cross-sectional view of the equilibrium cell. [Ngema, 2014]

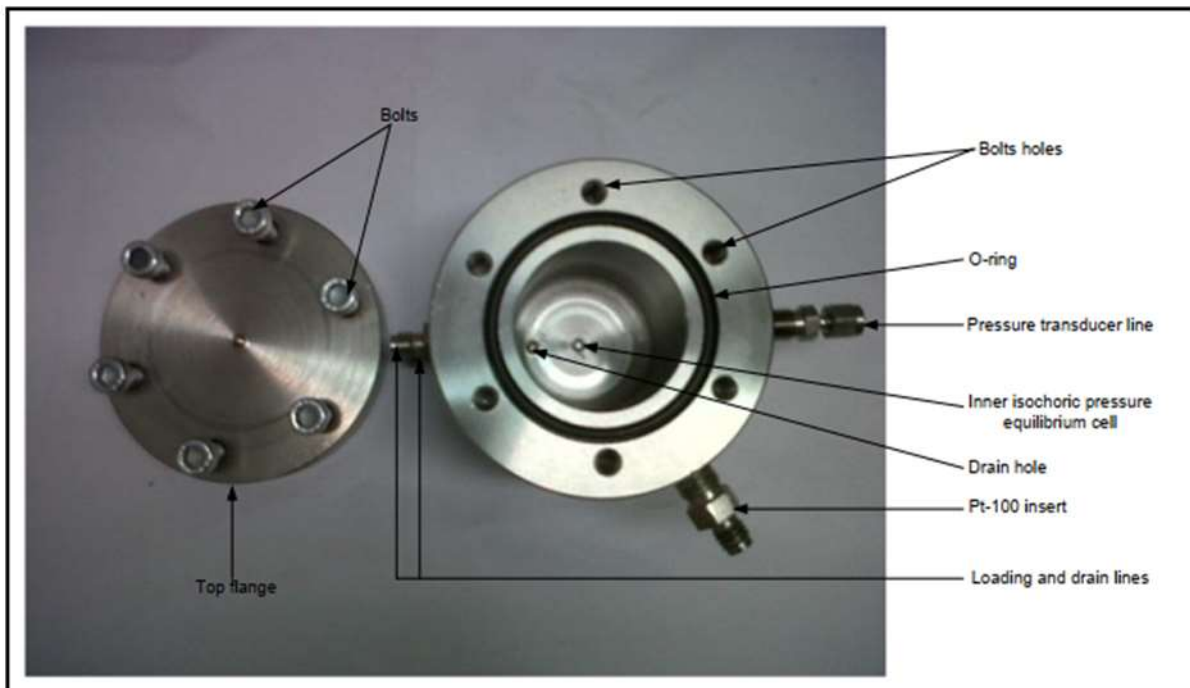


Figure C.2: Top view of the equilibrium cell and the top flange. [Ngema, 2014]

Four apertures were drilled into the sides of the cell, each fixed with a 1/8-inch fitting. One situated towards the top of the cell connected to a 1/16-inch line which connects to the pressure transducer, another one connected to the pressure transducer outlet accommodated a Pt-100 temperature probe for measuring the equilibrium cell temperature. Third hole was directly opposite the pressure transducer hole was a 1/8-inch loading situated below the top flange it had a valve close to its inlet to the cell and was utilised for evacuating the cell contents as well. The four holes was located near the base of the cell and was utilised as a cell discharge valve.

C.1.2 Agitation Device

An agitation device was utilised in order to reduce gas hydrate formation time. A Heidolp RZR 2041 overhead stirrer driven by an overhead mechanical stirrer with two speeds one in the range of 40 to 400 rpm and the other in the range 200 to 2000 rpm. It had four impeller blades with length of 5 mm and 13 mm width of 1 mm and two neodymium magnets. It is shown in figure C.3.

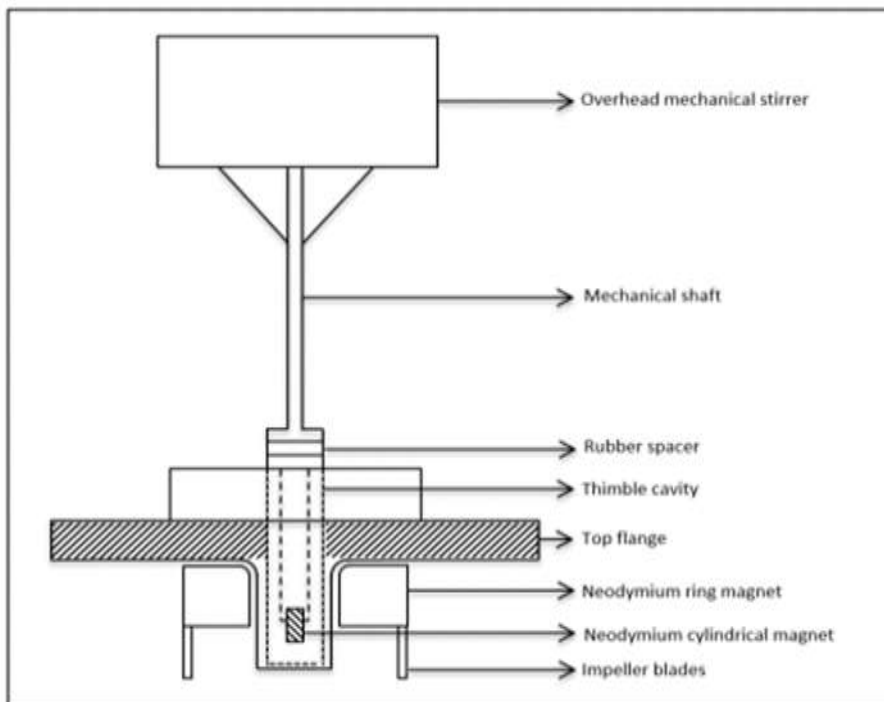


Figure C.3: Agitation Device

Four impeller blades were attached to an external magnet with an external diameter of 28 mm, internal diameter of 17 mm and a height of 10 mm shown in figure C.3. A neodymium magnet was utilised inside the stainless-steel shaft with an outside diameter of 10 mm and height of 20 mm. Vesconite was utilised for lubrication to prevent friction between the stainless-steel shaft

and neodymium magnet. The magnetic stirring device consisted of an “external” ring magnet and two removable impeller blades. Polytetrafluoroethylene (PTFE) was used to line the inner of the magnetic stirring device. In order to prevent friction between the stainless-steel shaft and the neodymium magnet. The magnetic stirring device with blades was removable from the stainless-steel shaft. The placement of the magnetic stirring device on the stainless-steel shaft allows for effective magnetic coupling between the stirring device and the cylinder magnet within the thimble-like cavity.

C.1.3 Temperature Sensor

One platinum resistance thermometer (Pt-100) supplied by WIKA was used to measure the temperature within the equilibrium cell. The Pt-100 temperature sensor had a measuring range of between 73.15 K to 1073.15 K. The probe was fitted on the side of the reactor cell by a ¼ inch fitting. The temperature reading were send to the 34972A LXI Agilent data acquisition unit which transferred them to the computer where the temperature readings were displayed and recorded with respect to time at five second intervals

C..1.4 Pressure Transducer

One WIKA pressure transducer was used to measure the cell pressure. The pressure transducer was connected by a 1/8” fitting to tape from the inside of the equilibrium cell from the side. Its working pressure range was 0 – 10 MPa. The total pressure exerted on the cell was the sum of the 0 - 10 MPa pressure transducer and the atmospheric pressure. The atmospheric pressure was taken as 101.325 kPa for all measurements. The transducer was connected to the 34972A LXI Agilent data acquisition unit where the pressure readings were recorded the same way as the temperature.

The pressure transducer was housed in a 75 x 58 x 78 mm aluminium block. Two heating cartridges, each with an outer diameter and length of 8 mm and 40 mm respectively, were inserted into the top of the aluminium block in order to supply heat energy. The heating cartridges were connected to a variac voltage regulator TDGC2 model that was controlled by a Shinko ACS-13A controller, used to supply uniform heat to the aluminium block. This ensured the pressure transducer was maintained at a constant temperature due to its sensitivity to temperature fluctuations. The transducer was maintained at 313.15 K, which was an optimum experimental temperature of the experimental apparatus.

C.1.5 Liquid bath

The equilibrium cell was kept at isothermal conditions by immersing it in a galvanized steel liquid temperature bath. The bath consisted of two metal sheets: an internal case and an external case. A polycarbonate sheet of thickness 25 mm was inserted between the two sheets as insulating material. The bath had internal dimensions of 440 mm x 350 mm x 260 mm. The dimensions resulted in an internal volume of 40 L. The bath had 2 Perspex® viewing windows with dimensions 115 mm x 80 mm on the front and back. An iron framework supported the bath. This framework also supported the equilibrium cell and its housing. A mechanical jack was used to facilitate the movement of the bath up and down to submerge the equilibrium cell in the bath fluid. The bath fluid used depends on the temperature range required for the systems to be measured. The bath fluid used in this work was a mixture of 80/20 wt % ethylene glycol and water. This allowed for operation in the temperature range of 228 K (melting point at atmospheric pressure) and 397 K (boiling point at atmospheric pressure). The top surface of the bath was covered with polystyrene foam pellets in order to prevent heat loss or gain from the surroundings.

C.1.6 Temperature Controller

The temperature of the bath was controlled using a Grant® Model TXF200 programmable controller. The temperature range of the controller for a water-glycol solution was 243.15 K to 343.15 K. It contained an immersion circulator pump with an internal temperature probe. The programmable temperature controller cooled or heated the water-glycol solution in the bath, which in turn cooled or heated the contents of the equilibrium cell. In order to ensure that adequate separation between the hydrate crystals and salt solution was achieved; the temperature of the equilibrium cell contents was controlled at a specified rate. The controller was connected to the computer set-up (PC). Software supplied by Labwise® was used to program the cooling and heating steps during hydrate formation and dissociation. The bath contents were cooled by an immersion cooler, or cold finger, supplied by Polyscience® (IP-35 model). It operated at temperatures as low as 173.15 K.

Appendix D: Uncertainty in measurements

The uncertainty of measured data is described as an interval around a data set or point such that if the measurement were to be repeated at the same conditions, the resultant value lies within the specified range. Uncertainty analysis provides validation for the given data or measured parameters. The guideline used in this work was taken from the National Institute of Standards and Technology (NIST) (Taylor et al., 1994).

The (combined standard uncertainty) CSU of measurement is obtained by combining the individual standard uncertainties by propagation of error of type A and type B uncertainties using the method of combined deviations. The combined standard uncertainty has a confidence interval of approximately 68%. The expanded uncertainty intends to improve the confidence that a reported datum is within a stated uncertainty interval. It is obtained by multiplying the CSU by the coverage factor, k , to give combined expanded uncertainty represented by $U(x)$. Hence the combined expanded uncertainty is given by:

$$U(x) = ku_c(x) \quad \text{D.1}$$

where k is the coverage factor with a typical value of 2 used to expand the interval and resulting in a level of confidence of approximately 95 %. (NIST) (Taylor et al 1994). This standard combined uncertainty in equation D.1 can be expressed as:

$$u_c(x) = \pm \sqrt{\sum_i u_i(x)^2} \quad \text{D.2}$$

where $u_i(x)$ is the standard uncertainty for a value x , such as uncertainty due to calibration correlation or standards or uncertainty due to the instrument manufacturer and uncertainty due to the repeatability of the measurement. The combined uncertainty $u_c(x)$ is calculated from the uncertainty which arises from any of the two classes of uncertainty type A or type B. The type A uncertainty is usually calculated by statistical methods in which the mean is taken to represent the true value after numerous repeated measurements at the same conditions. One

such method least squares to fit a curve to data in order to evaluate the parameters of the curve and their standard deviations. In a case of input quantity (X_i) which depends on n independent parameters of $X_{i,k}$. The uncertainty can be calculated by:

$$u(x_i) = \left(\frac{1}{n(n-1)} \sum_{k=1}^n (X_{i,k} - \bar{X}_i)^2 \right)^{1/2} \quad 4.3$$

Where;

$$\bar{X}_i = \frac{1}{n} \sum_{k=1}^n (X_{i,k}) \quad 4.4$$

D.1: Temperature and Pressure Uncertainty

In hydrate studies, temperature and pressure are the two most important parameters measured. The combined uncertainty of temperature is given by:

$$u_c(T) = \pm \sqrt{u_{calib}(T)^2 + u_{rep}(T)^2 + u_{instr}(T)^2} \quad D.5$$

where $u_{rep}(T)$ denotes the standard uncertainty because of repeatability of a measurement (Type A), $u_{instr}(T)$ is the uncertainty of the Pt-100 standard temperature probe and $u_{calib}(T)$ denotes the standard uncertainty as a result of temperature calibration and is determined by:

$$u_{calib}(T) = \pm \sqrt{u_{std}(T)^2 + u_{corr}(T)^2} \quad D.6$$

where $u_{corr}(T)$ denotes the standard uncertainty because of the temperature calibration correlation (Type B) and $u_{std}(T)$ denotes the standard uncertainty inherent in the standard temperature probe (Type B).

Likewise, the combined standard uncertainty in pressure is calculated by:

$$u_c(P) = \pm \sqrt{u_{corr}(P)^2 + u_{rep}(P)^2 + u_{std}(P)^2 + u_{instr}(P)^2 + u_{atm}(P)^2} \quad D.7$$

where $u_{corr}(P)$ is the standard uncertainty due to the pressure calibration correlation (Type B), $u_{std}(P)$ is the standard uncertainty of the pressure transducer (Type B), and $u_{rep}(P)$ is the standard uncertainty due to the repeatability of the pressure measurement (Type A). $u_{atm}(P)$ is the uncertainty due to the barometer (Type B) and $u_{instr}(P)$: Is the instrument uncertainty (Type B).

Repeatability is computed when there is temperature fluctuation in the system. The following equations are utilized in its computation:

$$u_{rep}(T) = \left(\frac{1}{n(n-1)} \sum_{k=1}^n (T_{i,k} - \bar{T}_i)^2 \right)^{0.5} \quad D.8$$

Where

$$\bar{T}_i = \frac{1}{n} \sum_{k=1}^n T_{i,k} \quad D.9$$

D.2 Uncertainty in solution concentration

In computing the uncertainty in the concentration of the solution the flowing sources uncertainty were considered from both nanoparticles and Sodium dodecyl sulfate (SDS); sample purity (SP), volumetric uncertainty and mass uncertainty. The following equation was utilized to calculate the combined uncertainty.

$$u_c(C) = \sqrt{\frac{u(SP)^2}{SP} + \frac{u(V)^2}{V} + \frac{u(m)^2}{m}} \quad D.10$$

Where sample purity is type A, volumetric uncertainty is source B and mass uncertainty is source B. In general, for given standard purity values, a rectangular probability distribution (with a divisor of 1.7321) is assumed (see GUM). The required relative standard uncertainty associated with each source is calculated. These were converted into a relative standard

uncertainty then relative standard uncertainty contributions from other sources are summed up, so that the final results (combined uncertainty and expanded uncertainty) is reported.

D.3 Phase composition

The non-negligible sources of uncertainty in the estimation of the number of moles are the accuracy in gas calibration (GC) detector calibration and the standard deviation in taking an average of the repeated samples. That is the combined standard uncertainty is comprised of the standard uncertainty as a result of sample repeatability $u_{rep}(x_i)$ (Type A), and the standard uncertainty arising from the calibration technique $u_{cali}(x_i)$:

$$u_c(x_i) = \pm \sqrt{u_{rep}(x_i)^2 + u_{calib}(x_i)^2} \quad D.11$$

In the direct injection technique for the TCD calibration, phase compositions are estimated from correlations that relate to the number of moles and the detector response area. For gaseous components, the ideal gas law is made use of in estimating the experimental uncertainty. As a result, the uncertainties in the pressure, volume, and temperature of the injected gas need to be accounted for. The standard uncertainty as a result of the TCD calibration method is evaluated as follows:

$$u_{calib}(x_i) = \sqrt{\left[\left(\frac{\partial x_i}{\partial n_i} \right)_{n_j} u(n_i) \right]^2 + \left[\left(\frac{\partial x_i}{\partial n_j} \right)_{n_i} u(n_j) \right]^2} \quad D.12$$

The standard uncertainty in the number of moles $u(n_i)$ is dependent on the standard uncertainty as a result of the correlation $u_{corr}(n_i)$ and the standard uncertainty emanating from making use of the ideal gas law $u_{ig}(n_i)$:

$$u(n_i) = \pm \sqrt{u_{corr}(n_i)^2 + u_{ig}(n_i)^2} \quad D.13$$

The standard uncertainty in the number of moles of injected gas $u_{ig}(n_i)$ is evaluated through the law of propagation of error as shown in equation E.4

$$u_{ig}(n_i) = \sqrt{\frac{u(P)^2}{P} + \frac{u(V_g)^2}{V} + \frac{u(T)^2}{T}} \quad D.14$$

Where the standard uncertainties in pressure, volume and temperature are evaluated as follows:
 $u(P)$ - treating the certainty in the Mensor CPC 3000 barometer (0.025%) as Type B

u(V) - Assuming the error in repeatedly drawing the same volume of the syringe, which is inherent in the operation of the GC syringe is 2% and including the aforementioned error in the evaluation of the Type B standard uncertainty.

u(T) – the maximum possible temperature fluctuation that could occur due to the handling of the syringe was assumed to be 2K and standard uncertainty was then evaluated as Type B.

The uncertainty due to the calibration polynomial is expressed as:

$$u_{corr}(n_i) = \frac{n_i \left(\left| \frac{n_{i,TRUE} - n_{i,CALC}}{n_{i,TRUE}} \right|_{max} \right)}{\sqrt{3}} \quad D.15$$

D.4 For a ternary mixture

$u_{bal}(x_i)$ is determined using equation D.16

$$U_{bal} = \sqrt{\left(\frac{dx_1}{dm_1} * Um_1\right)^2 + \left(\frac{dx_1}{dm_2} * Um_2\right)^2 + \left(\frac{dx_1}{dm_3} * Um_3\right)^2} \quad D.16$$

$$x_1 = \frac{\frac{m_1}{MM_1}}{\left(\frac{m_1}{MM_1} + \frac{m_2}{MM_2} + \frac{m_3}{MM_3}\right)} \quad D.17$$

$$\frac{dx_1}{dm_1} = \frac{1}{MM_1 \left(\frac{m_3}{MM_3} + \frac{m_2}{MM_2} + \frac{m_1}{MM_1}\right)} - \frac{m_1}{MM_1^2 \left(\frac{m_3}{MM_3} + \frac{m_2}{MM_2} + \frac{m_1}{MM_1}\right)^2} \quad D.18$$

$$\frac{dx_1}{dm_2} = - \frac{m_1}{MM_1 MM_2 \left(\frac{m_3}{MM_3} + \frac{m_2}{MM_2} + \frac{m_1}{MM_1}\right)^2} \quad D.19$$

$$\frac{dx_1}{dm_3} = - \frac{m_1}{MM_1 MM_3 \left(\frac{m_3}{MM_3} + \frac{m_2}{MM_2} + \frac{m_1}{MM_1}\right)^2} \quad D.20$$

D.5: Percentage Uncertainty

$$\text{Percentage Uncertainty} : \frac{\text{uncertainty}}{\text{measurement(value)}} \times 100 \quad D.21$$

D.6 Uncertainty in methane trapped in the hydrate

Equation D.22 was utilized to calculate the uncertainty in the number of moles trapped in the methane hydrate.

$$u_c(n_{hyd}) = \sqrt{\left[\frac{(\partial n_{hyd})}{\partial V_{hyd}} \times u(V_{pore})\right]^2 + \left[\frac{(\partial n_{hyd})}{\partial T} \times u(T)\right]^2 + \left[\frac{(\partial n_{hyd})}{\partial P} \times u(P)\right]^2} \quad D.22$$

Where

$$\frac{(\partial n_{hyd})}{\partial V_{hyd}} = \frac{P_i Z_f - P_f Z_i}{Z_f \left(RT - \frac{P_f}{\rho_{hyd}} \right)} \quad D.23$$

$$\frac{(\partial n_{hyd})}{\partial T} = - \frac{[V_{pore}(P_i Z_f - P_f Z_i)] Z_f R}{\left[Z_f \left(RT - \frac{P_f}{\rho_{hyd}} \right) \right]^2} \quad D.24$$

$$\frac{(\partial n_{hyd})}{\partial P} = \frac{Z_f \left(RT - \frac{P_f}{\rho_{hyd}} \right) [V_{pore}(Z_f - Z_i)] - [V_{pore}(P_i Z_f - P_f Z_i)] \left(\frac{Z_f}{\rho_{hyd}} \right)}{\left[Z_f \left(RT - \frac{P_f}{\rho_{hyd}} \right) \right]^2} \quad D.25$$

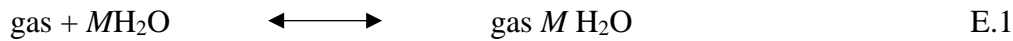
In this calculations R, Z and ρ_{hyd} were considered to be constant.

Appendix E

E.1 Kinetic Model.

The kinetic models have been utilized by Babaei et al., (2019) and Fakir et al., (2021). The parameters estimated from the kinetic measurements were the amount of CH₄ gas consumed, the water-to hydrate conversion, storage capacity (SC), rate of hydrate formation, and the apparent rate constant.

The physical reaction of hydrate former and water which leads to the formation of hydrate can be described using the following equation [E.1]



where gas represents CO₂ or CH₄, M represents the hydration number and can be calculated using the equation below

$$M = \frac{46}{6\theta_L + 2\theta_S} \quad \text{E.2}$$

where θ_L and θ_S are the fractional occupancy of large and small cavity, respectively, and can be calculated using the Langmuir adsorption theory, illustrated below;

$$\theta_i = \frac{C_i f_g}{1 + C_i f_g} \quad \text{E.3}$$

where C_i represents the Langmuir constant of carbon dioxide in type i cavity and f_g represents the fugacity of the hydrate former, CO₂/CH₄

The amount of gas consumed during the experiments was calculated using the real gas law shown as

$$\Delta n_{gas} = \frac{P_0 V_0}{Z_0 R T_0} - \frac{P_t V_t}{Z_t R T_t} \quad E.4$$

where P and T represents the pressure and temperature of the vessel, respectively, V is defined as the volume of gas inside the vessel, Z is the compressibility factor calculated from the VPT-EoS (Valderrama et al., 1990). R is the Universal gas constant, and the subscripts time =0 and t, respectively.

The molar volume of the gas hydrate is different from the molar volume of the aqueous solution. Furthermore, the formation of the gas hydrates changes the volume of gas inside the reactor. Hence the time-dependent volume of gas inside the reactor, V_t , was calculated using the following equation;

$$V_t = V_{cell} - V_{so} - V_{RWt} - V_{Ht} \quad E.5$$

where V_{cell} represents the volume of the reactor; V_{so} is the initial volume of the aqueous solution; V_{RWt} is the volume of the water reacted; and V_{Ht} is the volume of hydrate produced. The volume of water reacted V_{RWt} can be calculated using the following equation;

$$V_{RWt} = M \times \Delta n_{gas} \times v_w^L \quad E.6$$

where v_w^L is the molar volume of liquid water which was calculated using equation (E.7)

In order to calculate the molar volume of water, the following equation is used (Babaei, 2015).

$$v_w^L = 18.015 \times \{1 - 1.0001 \times 10^{-2} + 1.33391 \times 10^{-4} [1.8(T - 273.15) + 32] + 5.50654 \times 10^{-7} [1.8(T - 273.15) + 32]^2\} \times 10^{-3} \quad E.7$$

The CO₂ /CH₄ hydrate forms the structure I and equation (E.8) presented, Klauda and Sandler, (2000) was applied to calculate the molar volume of empty hydrate lattice for structure I as a function of temperature and pressure

$$v_w^{mt}[I] = (11.835 + 2.217 \times 10^{-5}T + 2.242 \times 10^{-6}T^2)^3 \frac{\times 10^{-30}N_A}{46} - 8.006 \times 10^{-9}P + 5.448 \times 10^{-12}P \quad E.8$$

where N_A represents Avogadro's number and T and P are the temperature (K) and (P) respectively.

Equation E.9 describes the molar volume of the hydrate at time t (Mohammadi et al., 2014)

$$V_{Ht} = M \times \Delta n_{gas} \times v_w^{MT} \quad E.9$$

The rate of gas consumed $r(t)$ during hydrate formation is defined using the equation shown below (Babae, 2015)

$$r(t) = \frac{n_{gas,2,i-1} - n_{gas,i-1}}{(t_{i+1} - t_{i+1})n_{wo}} \quad E.10$$

where $n_{gas,i-1}$ and $n_{gas,i+1}$ are the number of moles of carbon dioxide in the gas phase at t_{i+1} and t_{i-1} which are calculated using the real gas law and n_{wo} is the initial number of moles of water.

To estimate the apparent rate constant of the reaction during hydrate formation the following equation was used (Babae et al., 2015).

$$k_{app} = \frac{r(t)}{f_{gas}^G - f_{equilib}^G} \quad E.11$$

The storage capacity (SC) is defined as the standard volume of gas stored per volume of the hydrate. The equation below can be used to calculate SC (Babae et al., 2015).

$$SC = \frac{V_{STP}}{V_H} = \frac{n_{gas}RT_{STP}/P_{STP}}{V_H} \quad E.12$$

The subscript STP stands for standard conditions and V_H is the volume of gas hydrate (Babae et al., 2015).

The water to hydrate conversion is defined as the number of moles of water converted to hydrate per mole of feed and is given by the following equation (Babae et al., 2015).

$$\text{Water to hydrate conversion} = \frac{M \times \Delta n_{gas}}{n_{w_0}} \quad E.13$$

E.2 Methane hydrate kinetic

The extent of the difference between the initial pressure and hydrate equilibrium pressure is defined as the degree of subcooling or driving force for gas hydrate formation. As shown in Figure E.1, increasing the initial pressure of CH₄ leads to a higher degree of subcooling, resulting in an increase in the rate of hydrate formation.

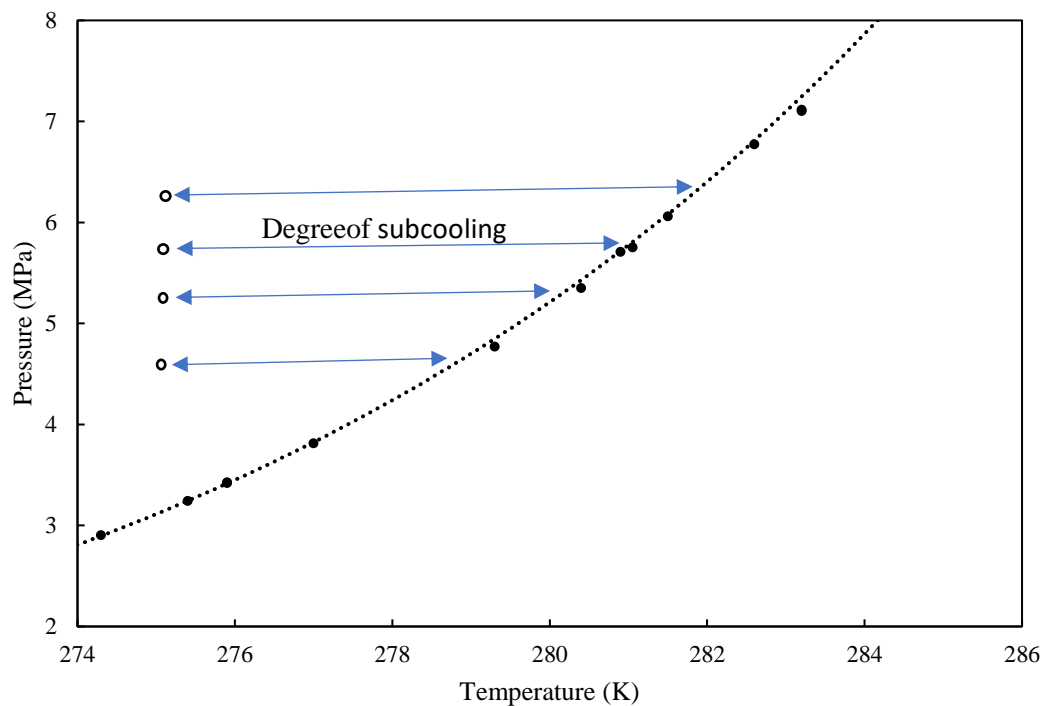


Figure E.1: The driving force between the initial kinetic experimental conditions and CH₄ hydrate equilibrium line (○) initial pressure, (●) dissociation points for CH₄.

Table E.1: Description of the properties of graphene nanoparticles

Property	Specification
Form	powder, hydrophobic
thickness	a few nm
Particle size	> 25 μ m
Composition	Carbon, >95 wt.% Oxygen, <2wt.%
Average surface Area	750 m ² /g
Bulk density	0.04/cm ³
Molecular weight	12.01
CAS Number	7782-42-5

Table E.2; Equilibrium data for Carbon dioxide gas hydrate dissociation points

Reference	Pressure (MPa)	Temperature (K)
Deaton and Frost et al (1946)	4,32	282,9
	4,13	282,6
	3,71	281,9
	3,53	281,5
	3,21	280,9
	2,76	279,8
	2,79	279,8
	2,43	278,7
	2,08	277,6
	2,1	277,6
	1,61	275,4
	1,39	274,3
	1,42	274,3
	1,32	273,7
Englezos & Hall (1994)	4,16	282,7
	3,49	281,6
	2,6	279,2
	2,13	277,7
	1,95	277,1
	1,54	275,1
Mohmmadi et al (2005)	4,02	282,5
	3,84	282,2
	2,05	277,5

Table E.3: Equilibrium data for Methane gas hydrate dissociation points

Reference	Pressure (MPa)	Temperature (K)	
Deaton and frost 1946	273,7	2,765	
	274,3	2,903	
	275,4	3,241	
	275,9	3,42	
	275,9	3,427	
	277	3,813	
	279,3	4,771	
	280,4	5,35	
	280,9	5,709	
	281,5	6,06	
	282,6	6,771	
	284,3	8,122	
	285,9	9,784	
	Roberts 1940	273,2	2,641
		280,9	5,847
286,5		10,632	
Gallowing 1970	286,7	10,804	
	283,2	7,102	
	283,2	7,115	
	288,7	13,114	
	288,7	13,107	

E.2.1 CO₂ Induction time

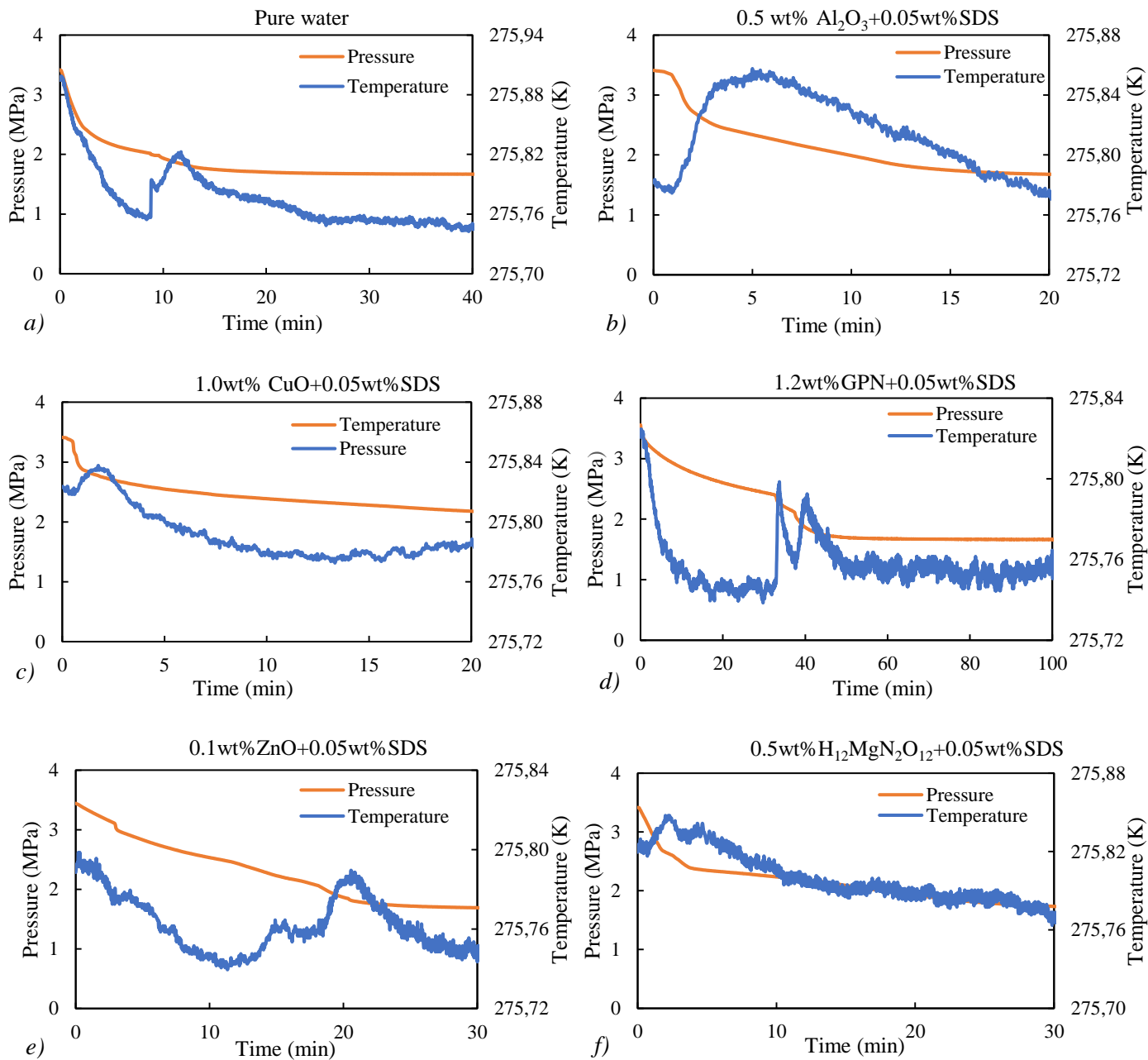


Figure E.2: Induction time for a) Pure water, b) 0.5 wt. % Al₂O₃ + 0.05 wt. %, c) 1.0 wt. % CuO + 0.05 wt. % SDS, d) 1.2 wt % GPN + 0.05 wt. % SDS, e) 0.1 wt. % ZnO + 0.05 wt. % SDS, f) 0.5 wt. % H₁₂MgN₂O₁₂ + 0.05 wt. % SDS. *Uncertainty $U(T) = \pm 0.1 K$, $U(P) = 0.01 MPa$ $U_{aditive} (wt\%) = 0.06\%$ $U(t) = 0.01s$*

E.2.2 CH₄ Induction time

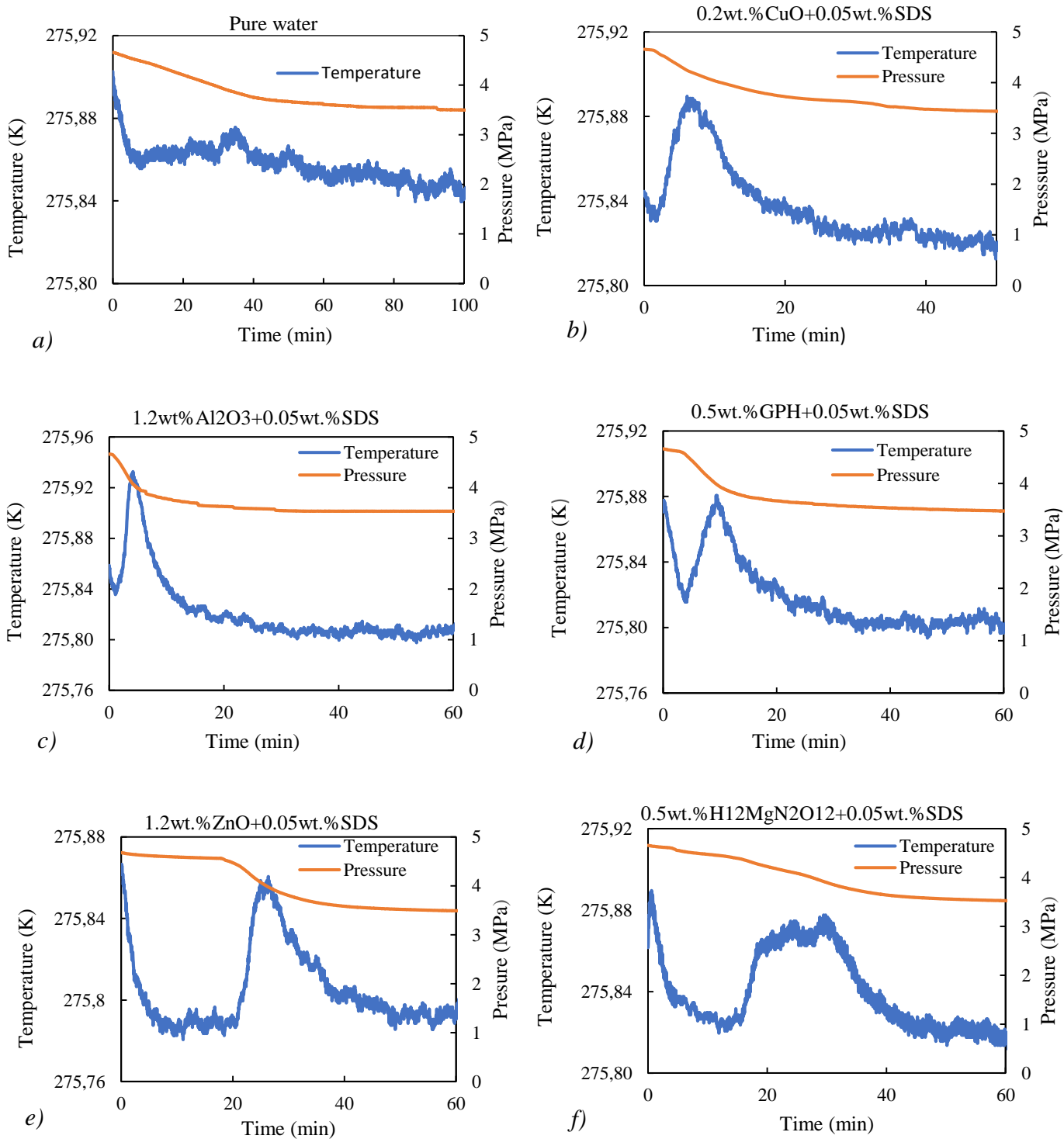


Figure E.3: Induction time of CH_4 hydrate in the presence of different additives a) Pure water b) 0.2 wt.% CuO+0.05 wt.% SDS c) 1.2 wt.% Al_2O_3 +0.05 wt.% SDS d) 0.5wt.% GPN+0.05 wt.% SDS e) 1.2 wt.% ZnO+0.05 wt.% SDS f) 0.5 wt.% H12MgN2O12+0.05 wt.% SDS. *Uncertainty* $U(T) = \pm 0.1 \text{ K}$, $U(P) = 0.01 \text{ MPa}$ $U_{\text{additive}} (\text{wt}\%) = 0.06\%$ $U(t) = 0.01 \text{ s}$.

E.2.3 Temperature and Pressure Variations

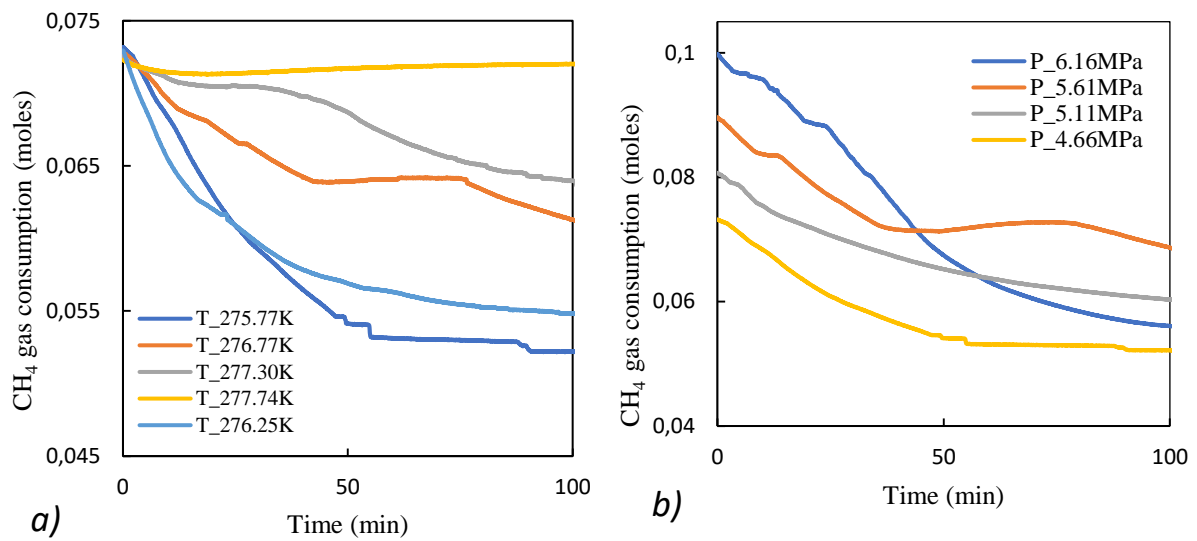


Figure E.4: Amount of CH₄ moles consumed during hydrate formation at different initial temperature and pressure conditions a) temperature variation b) pressure variation. *Uncertainty* $U(T) = \pm 0.1 \text{ K}$, $U(P) = 0.01 \text{ MPa}$ $U_{\text{concentration}} (\text{wt}\%) = 0.06\%$ $U(t) = 0.01 \text{ s}$.

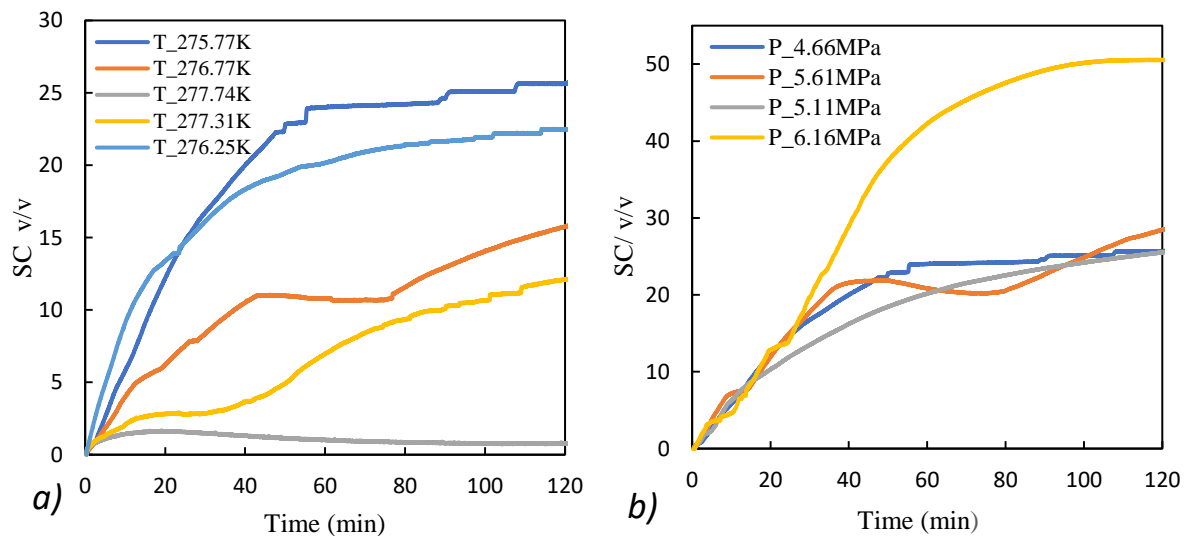


Figure E.5: Storage capacity for CH₄ hydrate formation at different initial temperature and pressure conditions a) temperature variation b) pressure variation. *Uncertainty* $U(T) = \pm 0.1 \text{ K}$, $U(P) = 0.01 \text{ MPa}$ $U_{\text{concentration}} (\text{wt}\%) = 0.06\%$ $U(t) = 0.01 \text{ s}$.

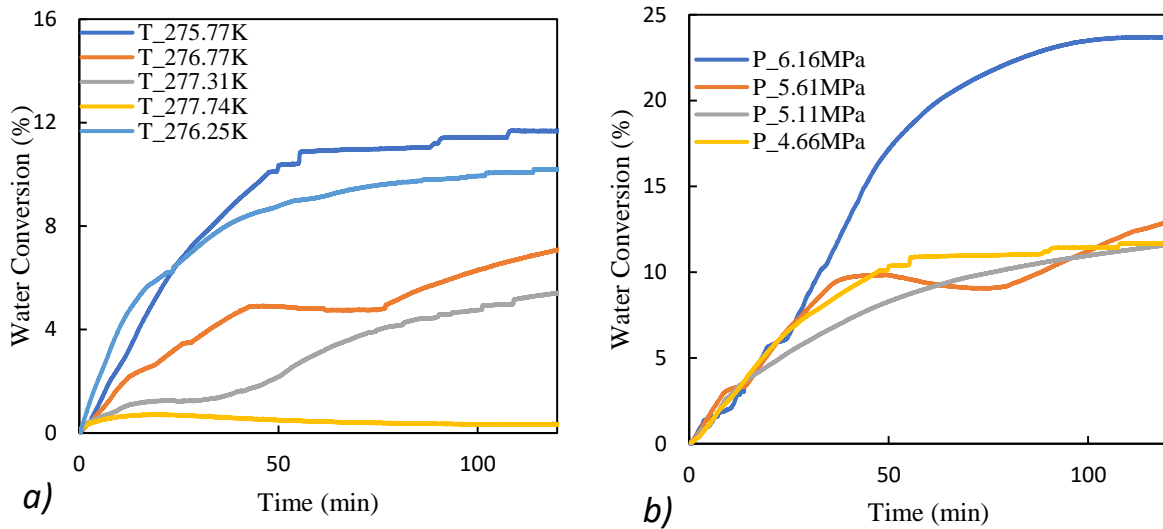


Figure E.6: Water-to-hydrate conversion during CH₄ hydrate formation a) temperature variation b) pressure variation. *Uncertainty* $U(T) = \pm 0.1$ K, $U(P) = 0.01$ MPa $U_{concentration}$ (wt%)=0.06% $U(t)=0.01$ s.

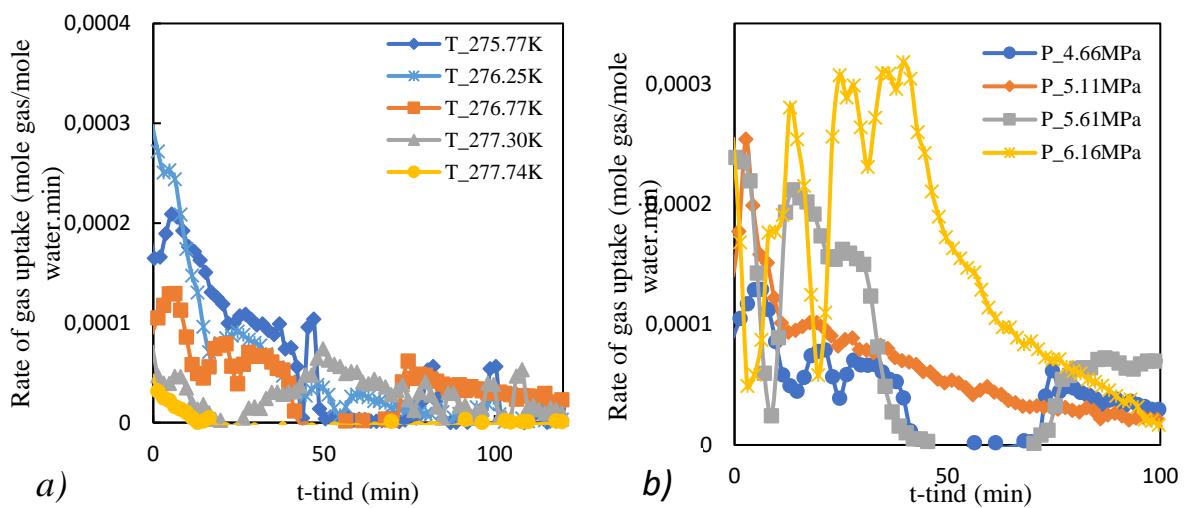


Figure E.7: Rate of CH₄ consumption during hydrate formation at different initial temperature and pressure conditions a) temperature variation b) pressure variation. *Uncertainty* $U(T) = \pm 0.1$ K, $U(P) = 0.01$ MPa $U_{concentration}$ (wt%)=0.06% $U(t)=0.01$ s.

E.2.4 Gas Consumption

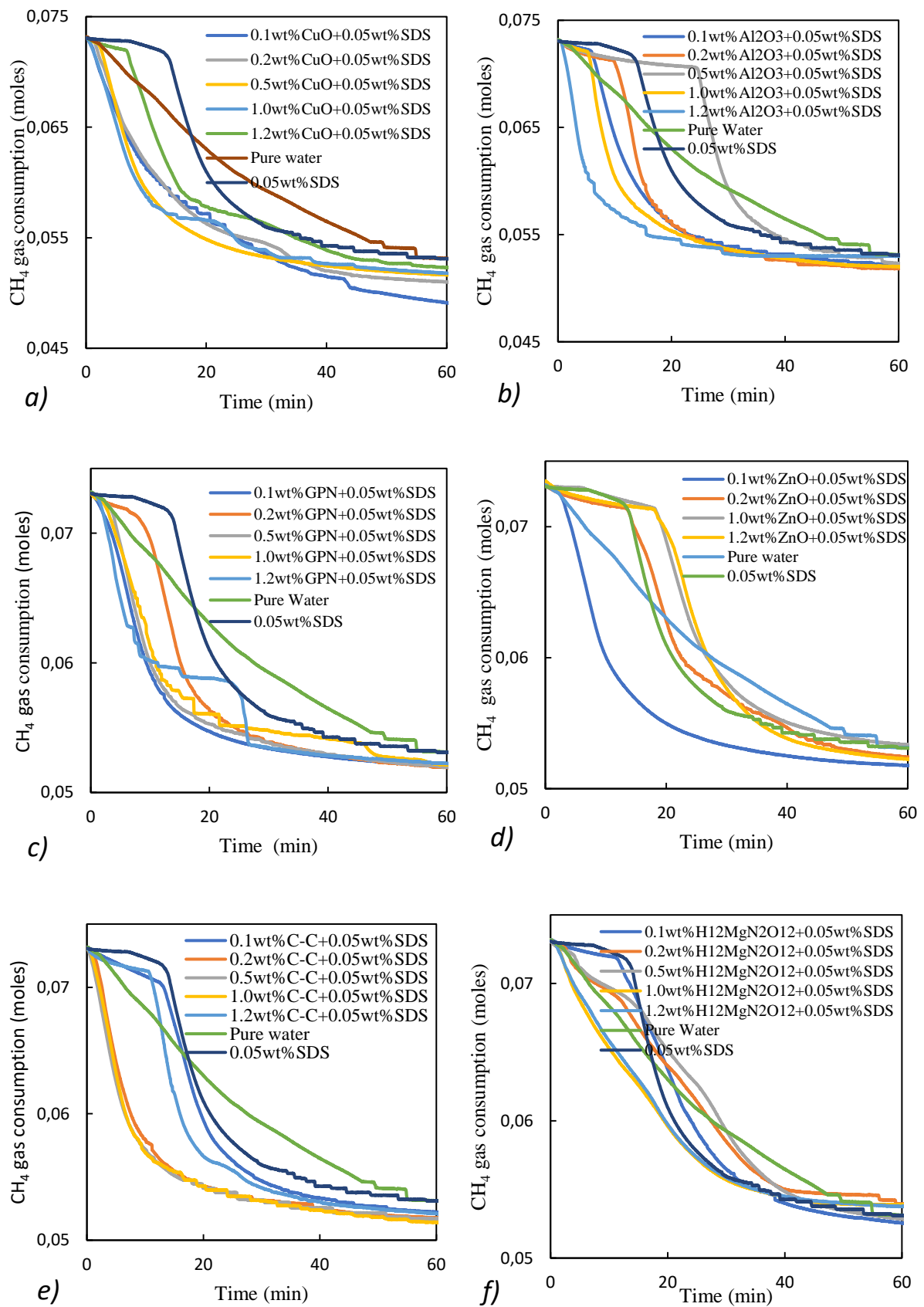


Figure E.8: Amount of CH₄ moles consumed during hydrate formation in the presence of different additives *a*) copper Oxide (CuO) nanoparticles, *b*) aluminium Oxide (Al₂O₃) nanoparticles, *c*) graphene

nanoplatelets *d*) zinc oxide (ZnO) powder *e*) graphite (C-C) powder *f*) magnesium nitrate hexahydrate ($\text{H}_{12}\text{MgN}_2\text{O}_{12}$) crystals. at 275.8K and 4.66MPa in concentrations specified in the graphs.
 Uncertainty $U(T) = \pm 0.1 \text{ K}$, $U(P) = 0.01 \text{ MPa}$ $U_{\text{concentration}} (\text{wt}\%) = 0.06\%$ $U(t) = 0.01 \text{ s}$.

E.2.5 Storage Capacity

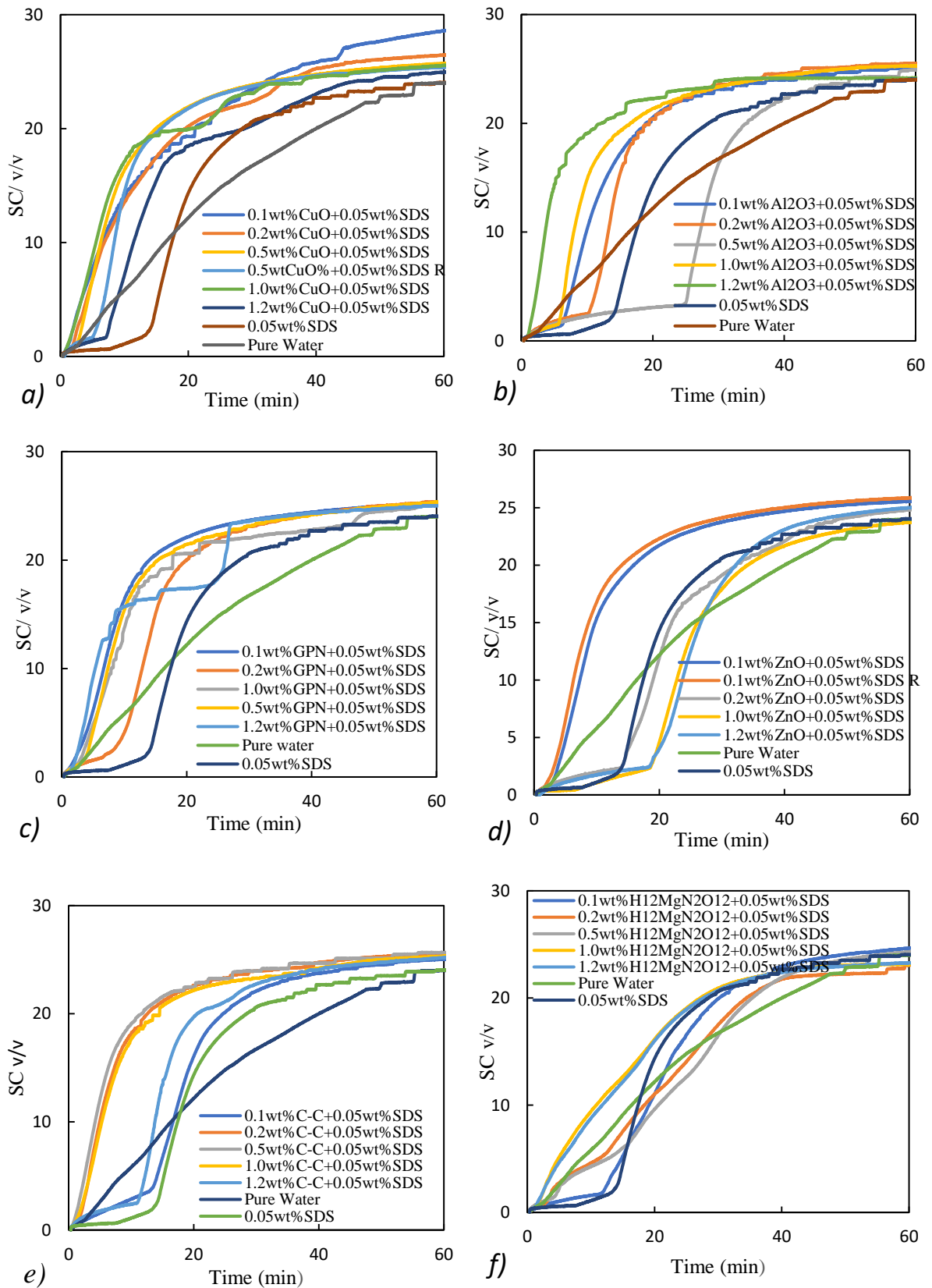
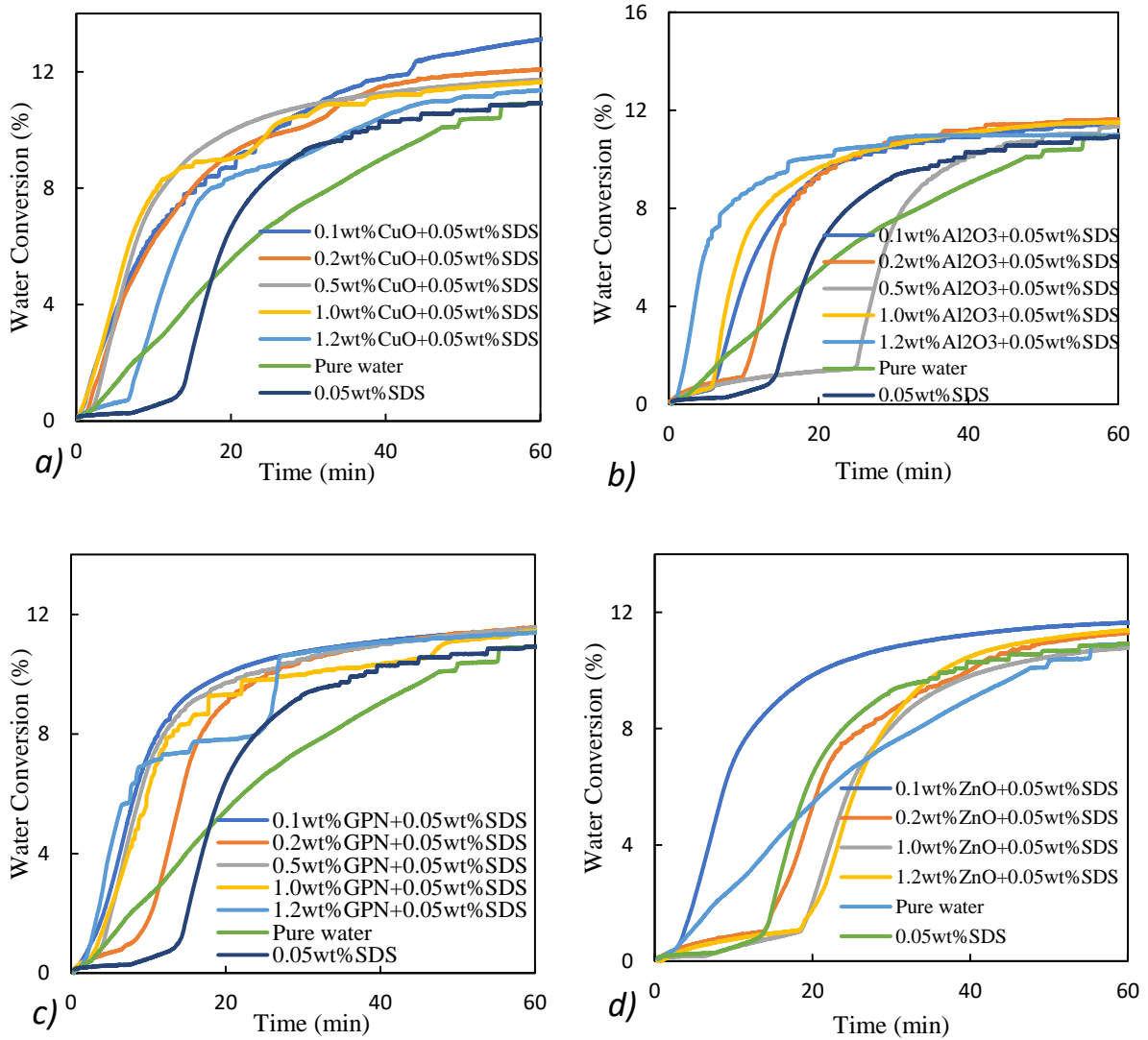


Figure E.9: Amount of CH₄ stored in hydrate formation in the presence of different additives *a*) copper Oxide (CuO) nanoparticles, *b*) aluminium Oxide (Al₂O₃) nanoparticles, *c*) graphene nanoplatelets *d*) zinc oxide (ZnO) powder *e*) graphite (C-C) powder *f*) magnesium nitrate hexahydrate (H₁₂MgN₂O₁₂) crystals.at 275.8K and 4.66MPa in concentrations specified in the graphs. *Uncertainty* $U(T) = \pm 0.1 K$, $U(P) = 0.01 MPa$ $U_{concentration} (wt\%) = 0.06\%$ $U(t) = 0.01s$.

E.2.6 Water Conversion



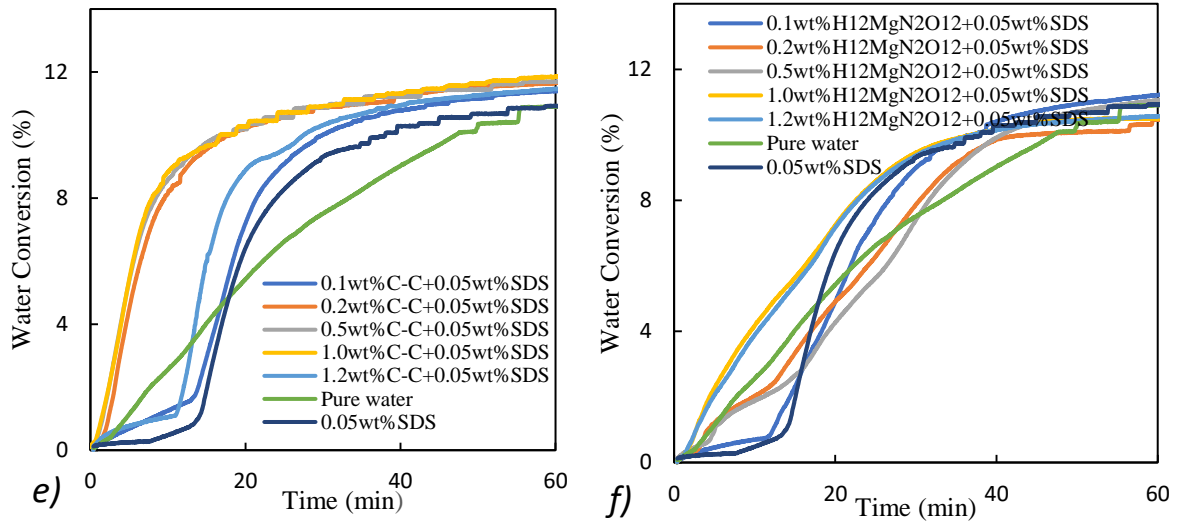
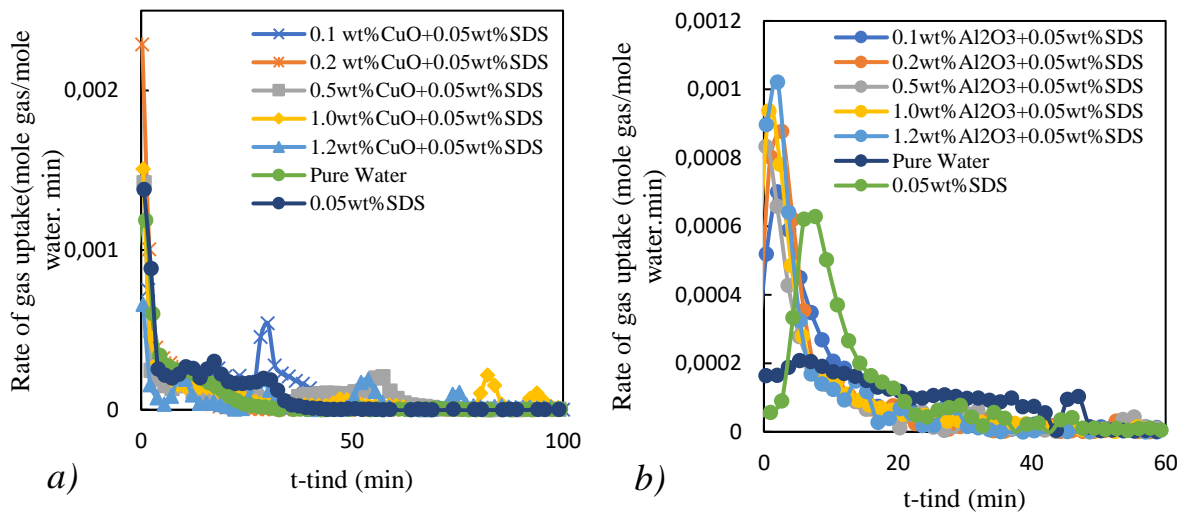


Figure E.10: Water-to-hydrate conversion during CH_4 hydrate formation in the presence of *a*) copper Oxide (CuO) nanoparticles, *b*) aluminium Oxide (Al_2O_3) nanoparticles, *c*) graphene nanoplatelets *d*) zinc oxide (ZnO) powder, *e*) graphite (C-C) powder *f*) magnesium nitrate hexahydrate ($\text{H}_{12}\text{MgN}_2\text{O}_{12}$) crystals at 275.8K and 4.66MPa in concentrations specified in the graphs. *Uncertainty* $U(T) = \pm 0.1 \text{ K}$, $U(P) = 0.01 \text{ MPa}$ $U_{\text{concentration}} (\text{wt}\%) = 0.06\%$ $U(t) = 0.01 \text{ s}$

E.2.7 Rate of gas uptake



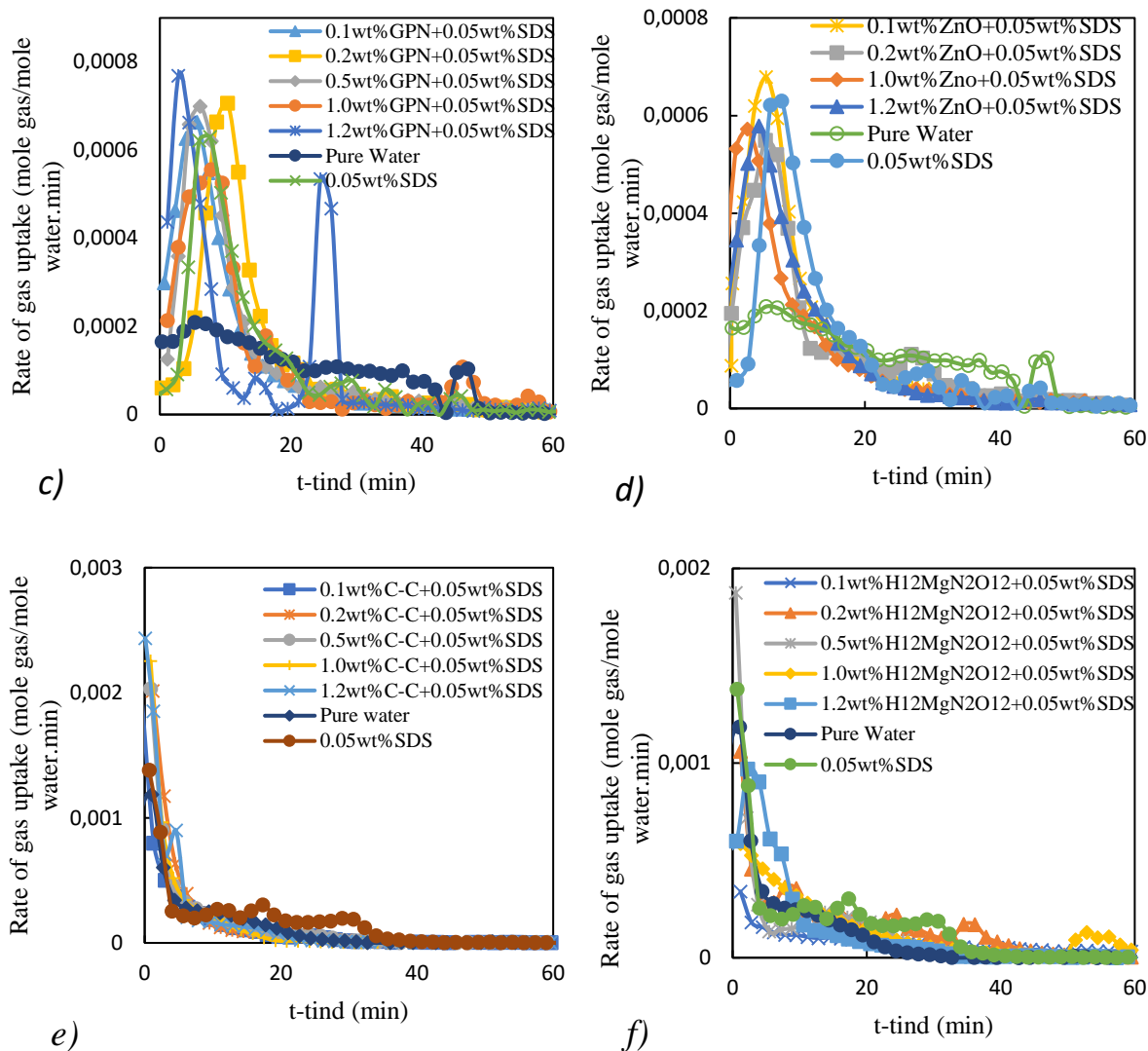


Figure E.11: Rate of CH₄ consumption during hydrate formation at an initial temperature of 275.8K and pressure of 4.66MPa for a) copper Oxide (CuO) nanoparticles, b) aluminium Oxide (Al₂O₃) nanoparticles, c) graphene nanoplatelets d) zinc oxide (ZnO) powder e) graphite (C-C) powder f) magnesium nitrate hexahydrate (H₁₂MgN₂O₁₂) crystals. *Uncertainty $U(T) = \pm 0.1$ K, $U(P) = 0.01$ MPa $U_{concentration}$ (wt%)=0.06% $U(t)$ =0.01s*

Appendix F: Equipment utilized in replacement without porous media

F.1 Equipment Description

The following are the equipment auxiliaries for the experimental setup shown in Figure 5.1 utilised for the replacement reaction:

- 52 cm³ 316SS equilibrium cell
- Agitation system for the equilibrium cell contents
- WIKA (0-16 MPa) Gauge pressure transmitter
- Two class A Pt-100 thermocouple thermometers (model REB)
- Rolsi™ sampling device
- Shimadzu 2014 gas chromatography equipped with a TCD
- Stainless steel temperature bath with dimensions 43 cm × 35 cm × 26 cm
- Cold finger (Polyscience® immersion probe cooler)
- Agilent data acquisition of model LXI Agilent 34972A
- ISCO syringe pump model 260D
- Grant 200 temperature controller
- RV12 Edwards rotary vane vacuum pump.

F.1.1 Equilibrium cell

A 316 stainless steel equilibrium cell with a design volume of 52 cm³ was employed at the heart of the equipment. This reactor vessel was utilised in the CH₄-CO₂ replacement. The cell was designed by Babae (2015) with a height of 45 mm, an internal diameter of 36 mm, and maximum working pressure of 20 MPa. The reactor vessel had one drain valve drilled toward the bottom end, and two side holes to house the temperature probes. Three additional holes were positioned on the top flange of the reactor vessel, one accommodates a 1/8-inch pressure transducer fitting, ROLSI™ connection, and the third a 1/8-inch feeding line. The agitation device was operated from the bottom of the cell. The pictorial view of the reactor is shown in figure F.1 below.

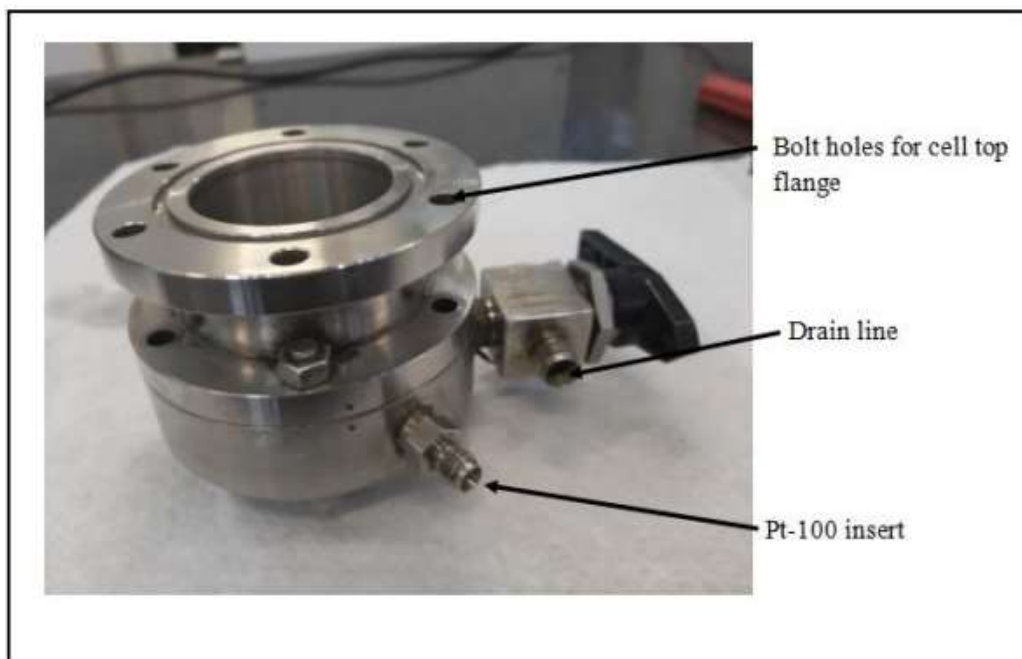


Figure F.1: Pictorial view of the equilibrium cell utilised in the $\text{CH}_4\text{-CO}_2$ replacement reaction.

The top flange was fixed on the reactor cell by 6×10 mm stainless steel bolts. To attain an air-tight seal, an O-ring was placed in a groove on the top surface of the cell. The cross-sectional view of the cell is shown in Figure E.2.

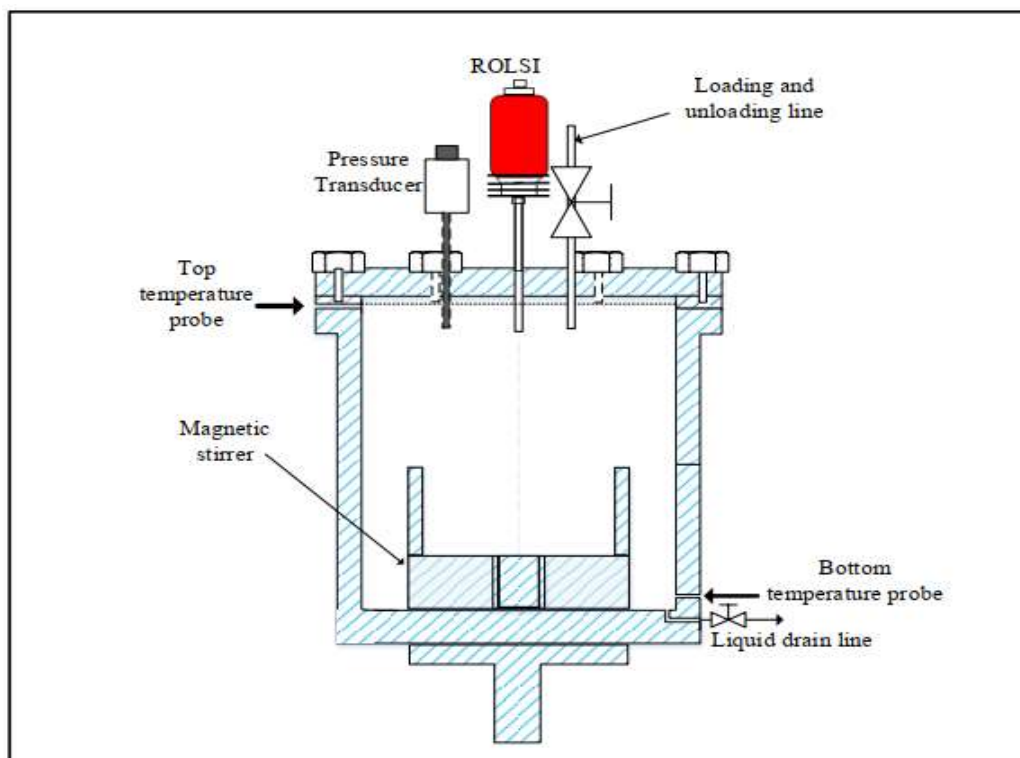


Figure F.2: Cross-sectional view of the equilibrium cell.

F.1.2 Sampling Device

An automated electromagnetic online micro sampler sampled the composition of the cell (rapid online sampling injector (ROLSI™) fixed at the top of the reactor vessel denoted by red code in Figures F.1 and figure F.2. Guilbot et al., (2000) and figure E.3 gives a full description of the device and how it was operated. The volume of the sample taken was determined by the opening time of the ROLSITM which could be varied. this was physically the time in which the seal between the piston and the capillary of the ROLSITM was broken. The amount of the sample taken from the cell was insignificantly small (1-5 μ L) compared to the volume of the reactor vessel (52 cm³) to ensure that there is no thermodynamic disturbance during sampling. Hydrogen gas was used as a carrier gas to transmit the sample from the equilibrium cell to the G.C. column for analysis. The sampler was electric-powered thus the capillary was normally closed for the highest safety.

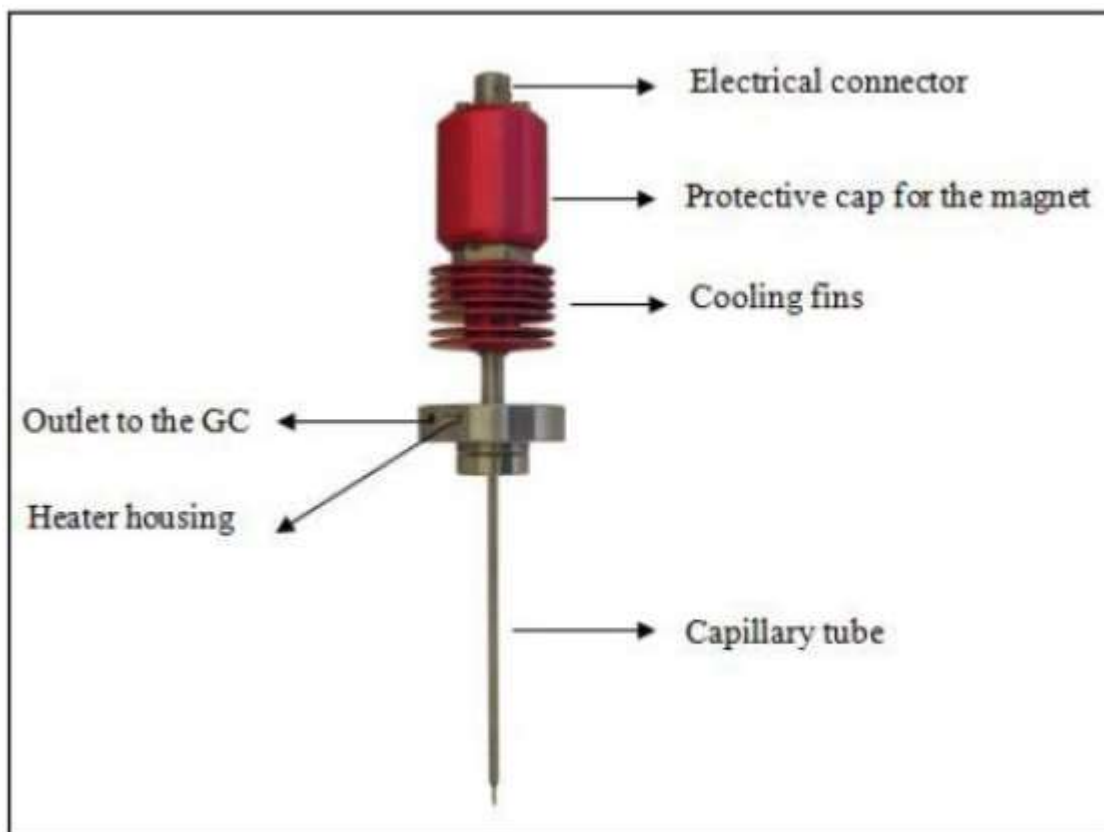


Figure F.3: Pictorial description of ROLSITM (Matizakurima, 2020).

F.1.3 Stirring Device

A Heidolph RZR 2041 motor with an operating range of 0-200 rpm was utilised in this design to effect stirring of reactor cell contents; it was stirring from the bottom of the cell. A 30 mm outer diameter neodymium magnet and inner diameter of 18 mm and height of 11mm was

situated inside the stainless-steel shaft. The rotation device had three blades with Teflon on the inner side to reduce friction during rotation and a strong external magnet. As the motor rotates, it turns the gear system with chains and sprockets which turns the external magnet. As the external magnet turns, it causes the internal magnet to turn due to magnetic force, thus causing the stirring device to turn. For this work a stirring speed of 200-250 rpm was selected. The components of the stirring device are shown in figure F.4.

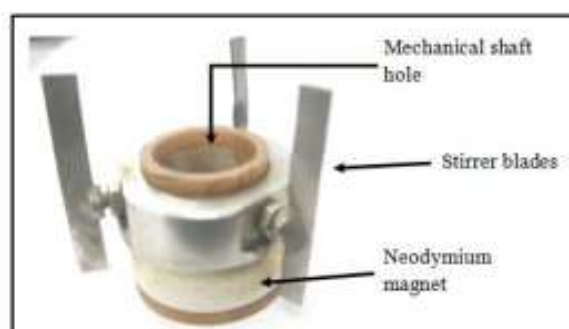


Figure F.4: Components of stirring device housed in the equilibrium cell.

F.1.4 Syringe Pump

A 260 D ISCO Syringe pump was utilised in measuring and pressurising the equilibrium cell with the reactant fluids (methane and carbon dioxide). The pump had an installed capacity of 266 mL and an upper-pressure limit of 517 bars. Furthermore, the pump had a chilling jacket that was utilised to adjust the temperature of the gas flowing through the pump. Connecting two pumps side by side can provide the capability to meter solvent modifiers into the flow stream or deliver non-stop continuous flow. The inlet and outlet have to 1/8" Valco fittings for connection in either direction. It is operated from a controller which is standard for all ISCO pump models. It has an RS-232/485 serial interface for computer control or monitoring operating parameters.

F.1.5 Vacuum Pump

A vacuum pump was utilised in cell evacuating before the beginning of every run. This was done to get rid of air and incondensable gases. The vacuum cell was switched on and allowed to run for 15 -30 minutes.

F.1.6 Temperature Control of the bath

The water bath temperature was controlled with the aid of a glycerol-water solution to prevent ice formation. It was made from 50 % water and 50 % glycerol. A chiller (cold finger) was used to cool the bath solution while TXF200 Polyscience programmable temperature controller with an operational temperature of between 243.15 to 323.15 K was employed to increase or maintain the temperature. The controller had an inbuilt temperature probe for detecting the temperature of the bath. The equilibrium cell was completely submerged in the water bath to equilibrate its temperature; this was achieved with an aid of a jack.

F.1.7 Chiller

A Thermo fisher scientific EK90 immersion cooler was employed to cool the water bath. It has a temperature range of -90 to 40 °C. It does not regulate the temperature of the water bath and does not display the temperature of the bath thus it works alongside a temperature controller. It has its own controller for temperature accuracy of approximately 1 to 2 °C with its own air-cooled circuits.

F.1.8 Temperature probe

A platinum resistance thermometer (Pt-100) supplied WIKA was utilised to measure the temperature within the equilibrium cell. The Pt-100 can measure temperature between 73.15 K and 1073.15 K with an accuracy of ± 0.03 K. The temperature probes were fixed to the side of the equilibrium cell. Then the probe was connected to the 34972A LXI Agilent data acquisition unit where the temperature readings were displayed electronically with respect to time and logged at two-second intervals.

F.1.9 Pressure

A WIKA pressure transducer was used to measure the cell pressure. The pressure transducer was connected to the top flange of the equilibrium cell. The measuring range of the pressure transducer was 0-10 MPa, with a stated accuracy of 0.05 % (full span). The transducer was connected to the 3497A LXI Agilent data acquisition unit where the pressure readings were electronically displayed with respect to time at every two-second interval. A 1/8-inch line was employed in connecting the pressure transducer to the equilibrium cell.

F.1.10 Data logger

The pressure transmitter and the temperature probe were connected to an Agilent data acquisition unit which logged the data every 5 seconds and transmitted it to the computer. The

software was set to log one data point data every 2 seconds continuously for the duration of the experiment. The data logger sends the data to the CPU of a computer and uses the monitor interface. The data is transferable to excel at any point in time for analysis.

F.1.11 Shimadzu Gas Chromatograph

A Shimadzu GC-2014 model was utilised in the study. A Gas chromatograph is a liquid-gas partition device, it is applied for analytical purposes. The gas chromatograph consists of a stationary phase and a mobile phase which is the flow of inert gas or hydrogen gas. The main components of the G.C are the detector, the column placed in an oven, and the injection system. The gas inlet is through the injector port into the G.C column where separation takes place. The column is housed in a temperature-controlled oven. The compounds in the mobile phase are adsorbed to the stationary phase; thus, the interaction of these two phases bring about a separation of the components entrained in the mobile phase due to difference in retention time.

The thermal conductivity detector in the G.C measures the heat conductivity of each separated compound that flows through the column giving a peak area signal output. The peak area obtained is proportional to the amount of each component in the gas mixture or the feed. The G.C retention time is sensitive to column temperature, carrier gas flow rate, and detector temperature thus these are supposed to be kept constant. For any gas mixture, it is necessary to find the optimal conditions to achieve separation of components. The separation of components in the feed is affected by column packing type, column temperature, carrier gas flow rate, and the physical properties of the components. Table F.1 shows conditions selected to affect the CH₄ and CO₂ gas mixture separation.

Table F.1: Gas Chromatography Specifications for CH₄ and CO₂ feed mixture.

Data Acquisition Software	G.C. Solutions
Detector	Thermal conductivity conductor (TCD)
Stationary phase	Carbon molecular sieve phase
Column type	Packed column, Porapak Q
Polarity	Polar
Maximum temperature (K)	250
Carrier gas	Hydrogen
Carrier gas flow rate (mL/min)	15
Column length (m)	2.2
Injector temperature (K)	473.15
Detector temperature (K)	473.15
Column temperature (K)	303.15

F.2 Preparation of Gas mixtures

A Mixing vessel with a volume of 699 ml and maximum working pressures of 8 MPa (shown in figure E.5) was utilised in making gas mixtures. The vessel had an internal magnetic stirring system which was used to maintain uniform gas composition of the gas mixture in the mixing vessel. The mass of the gas and the mixing vessel was determined by an OHAUS PA4202C top pan balance with an accuracy of 0.0001 g.

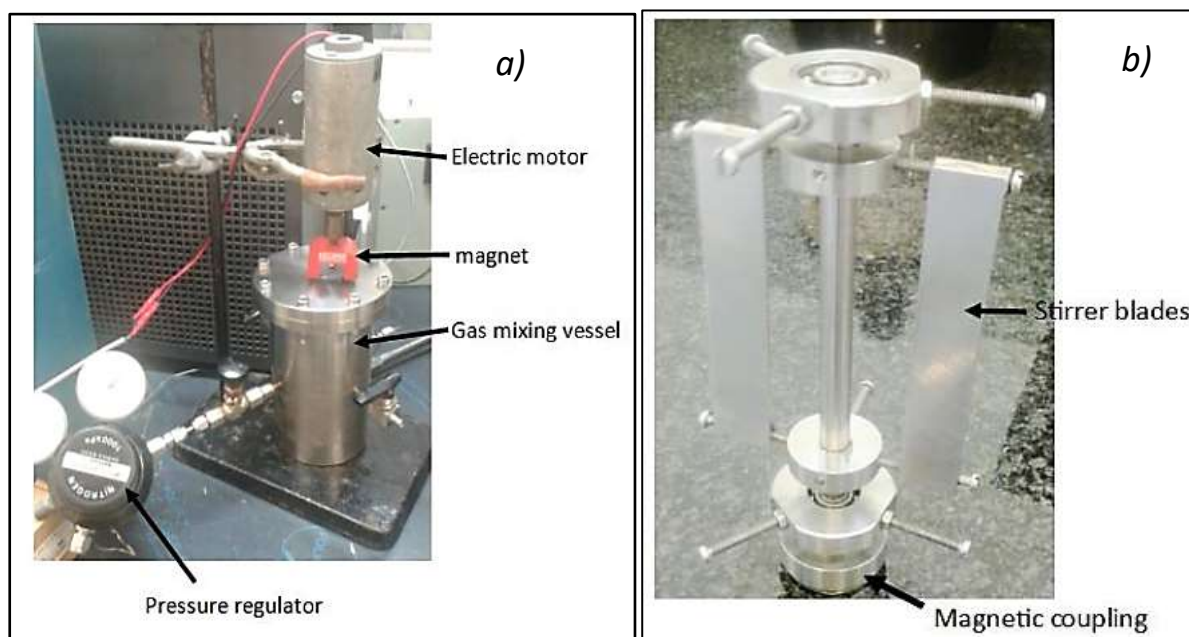


Figure F.5: a) mixing vessel with magnetic stirrer b) stirring device inside the cell.

Table F.2: Properties of Silica sand utilised in the study

Pore volume	0.75 mL/g
Specific surface BET	500m ² /g
Particle size	0.071-0.63 mm
Average particle size	0.280 mm
pH stability	2.0-8.0
Pore size	60 Å
Particle shape	Irregular
Particle type	Fully porous particle (FPP)
Storage temperature	RT

F.3: Replacement measurements carried with Argon (Ar) gas.

Argon gas was utilised as a secondary in the replacement without porous media. The experimental runs are summarized in this section.

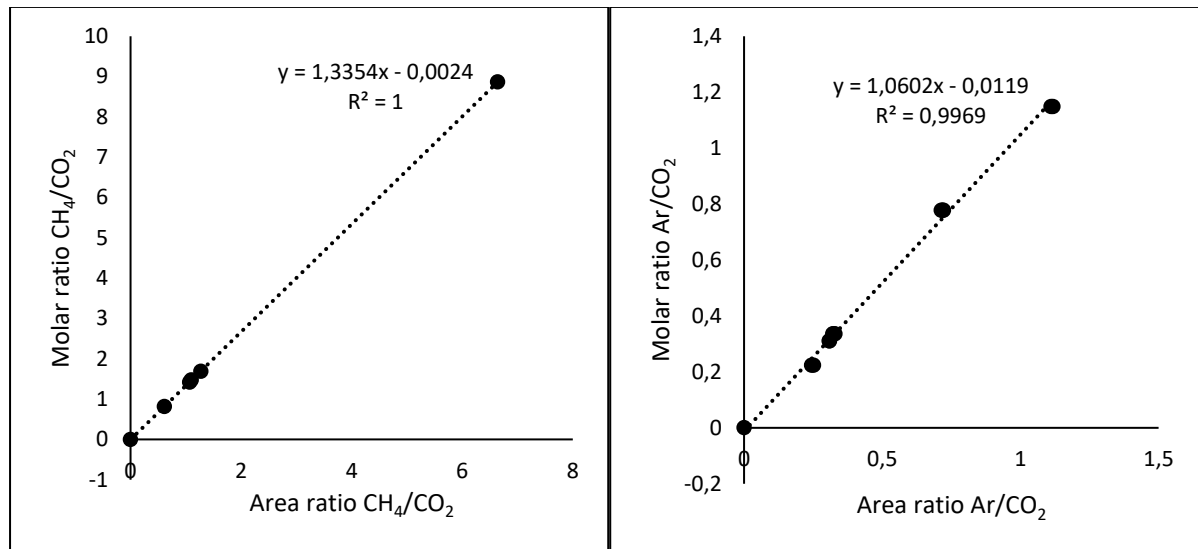


Figure F.6: GC detector calibration for methane-carbon dioxide (LHS) and argon-carbon dioxide (RHS) calibration curve for Argon-Methane-Carbon dioxide system.

Table F.3: Methane- hydrate formation and replacement analysis with CO₂/Ar gas mixture.

Experimental run	1	2	3
Feed solution	water	water	0.05 wt.% SDS+0.5 wt.-% GPN
Water fed (ml)	22	22	20
Pressure (MPa)	8.17	7.54	7.88
Pressure end of hydrate (MPa)	4.40	3.08	3.10
Duration of replacement (hour)	120.2	94.12	158.06
Stirring rate (rpm)	250	250	250
Moles CH ₄ charged	0.1004	0.0955	0.1031
Methane balance			
(a) Initial CH ₄ moles in hydrate	0.0427	0.0550	0.0598
(b) CH ₄ released from hydrate in replacement	0.0026	0.0034	0.0097
(c) CH ₄ from hydrate at the end of the replacement	0.0001	0.0001	0.0036
% CH ₄ replacement efficiency	6.06	6.19	16.28

Expanded uncertainties (k=2): $U(T) = \pm 0.09 K$, $U(P) = \pm 0.02 MPa$, $U(n_i) = 0.005$

Table F.4: Carbon dioxide encapsulation in the replacement process with CO₂/Ar gas mixture.

	1	2	3
Feed for replacement	83.7% CO ₂ / 16.3mol%Ar	98mol%CO ₂ / 2mol%Ar	90.2 mol% CO ₂ / 9.8 mol% Ar
Replacement feed pressure (MPa)	3.15	2.55	4.26
Replacement reaction pressure (MPa)	2.01	1.81	2.08
Replacement temperature (K)	274.98	274.97	274.96
Carbon dioxide balance			
Moles Charged for replacement	0.0329	0.0315	0.0403
Moles trapped in the hydrate	0.0031	0.0032	0.0064
% CO ₂ sequestration ratio	9.51	10.19	15.88
Argon balance			
Moles fed for replacement	0.0068	0.0000	0.0147
Moles in the hydrate	0.0001	0.00000	0.0003
% gas trapped in the hydrate	0.90	0.000	2.13

Expanded uncertainties (k=2): $U(T) = \pm 0.09 K$, $U(P) = \pm 0.02 MPa$, $U(n_i) = 0.03$.

Figure E.7 shows a reaction profile for CH₄ +83.7 mol% CO₂/16.3 mol% Ar gas mixture + H₂O system. As observed in the figure, the composition of CH₄ gas increases as the reaction progresses while argon remaining constant. Furthermore, CO₂ decreases replacement progression.

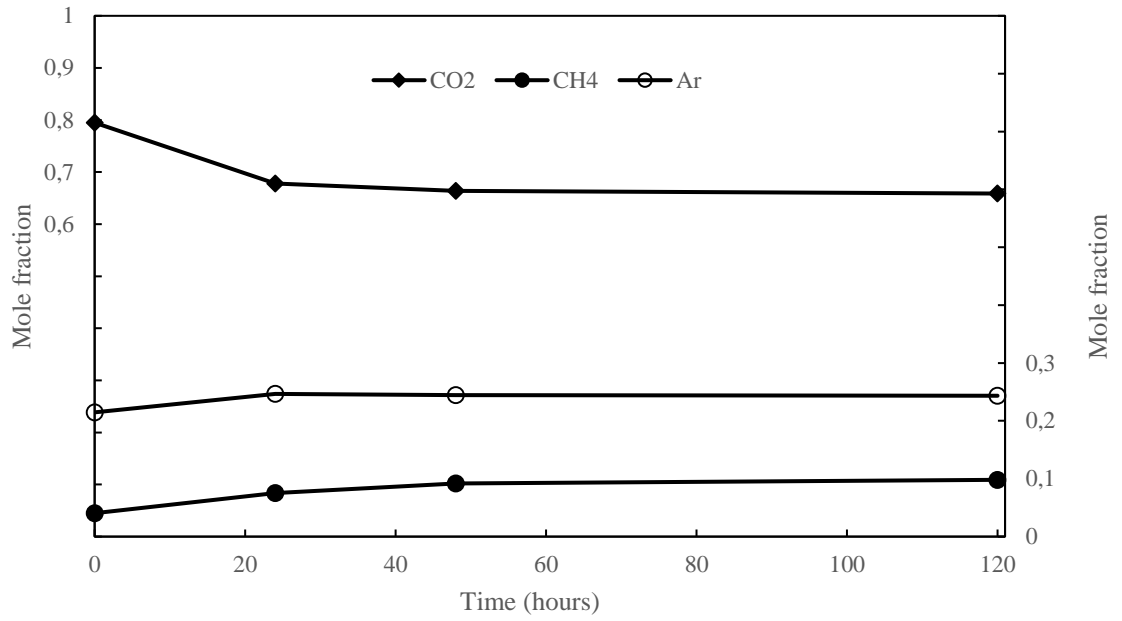


Figure F.7.:CH₄- 83.7mol% CO₂/16.3%mol% Ar -H₂O replacement reaction profile $U(n_i) = 0.03$.

With 90.2 mol% CO₂/9.8 mol% Ar gas, CH₄ replacement efficiency of 16.28% was obtained with 15.88% CO₂ sequestrated. Thus, the presence of argon improved the replacement efficiency though reducing the amount of carbon dioxide stored.

Appendix G: Design of Cell utilized in replacement with porous media

Appendix G.1: Cell Design calculations

Static pressure = $\rho * g * h$

$$= 1000 * 9.81 * 0.15$$

$$= 1471.5 \text{ Pa.}$$

Pressure in the reactor from the steam tables using maximum temperature of the fluid in the vessel = 101.33kPa

Total pressure in the reactor = 1.4715 + 101.33 = 102.802 kPa

Maximum allowable internal design pressure is chosen to be 15 % above operating pressure

$$= 1.15 * 102.213$$

$$= 118.22 \text{ kPa}$$

$$= \mathbf{0.11822 \text{ MPa}}$$

Design stress stainless steel 316 design stress (f) for temperature 100 °C is 150 N/mm².

G.2: Design Equations

Cell thickness e;

$$\begin{aligned} e &= \frac{P_i D_i}{2f - P_i} \\ &= \frac{0.11822 * 50.0}{(2 * 150) - 0.11822} \\ &= 0.01971 \text{ mm} \end{aligned}$$

Where P_i = internal pressure

f = design stress

e = minimum thickness required

D_i = internal diameter

Corrosion allowance is 3mm, hence $e = 3 + 0.01971 = 3.01971 \text{ mm}$

$\frac{D_i}{e} = \frac{50.0}{3.01971} = 16.558 > 10$, hence cell is a thin-walled pressure vessel under internal pressure

Design of flat ends:

$$\begin{aligned} e &= C_p D_e \sqrt{\frac{P_i}{f}} \\ &= 0.55 * 70 \sqrt{\frac{0.11822}{150}} \\ &= 1.081 \text{ mm} \end{aligned}$$

Where C_p = a design constant, dependent on the edge constraint

D_e = nominal plate diameter

f = design stress

P_i = internal pressure

e = minimum thickness

Using design parameter of Bolted end cover with a narrow-face gasket, $C_p = 0.55$ and D_e equal to the mean diameter of the gasket

Adding corrosion allowance of 3 mm, e becomes $3 + 1.081 = 4.081$ mm round off to **5 m**.

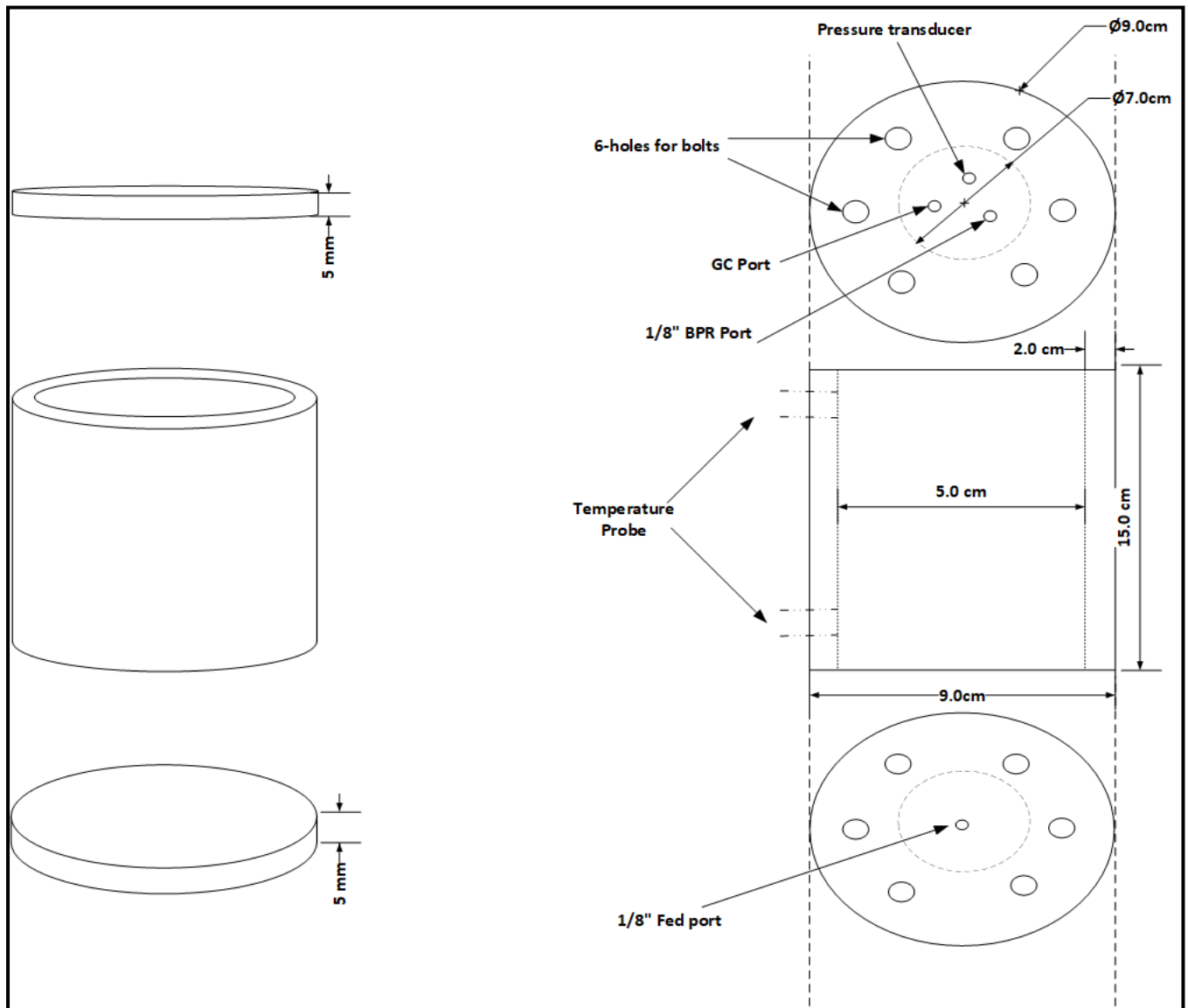


Figure G.1: Cell design dimensions and specifications

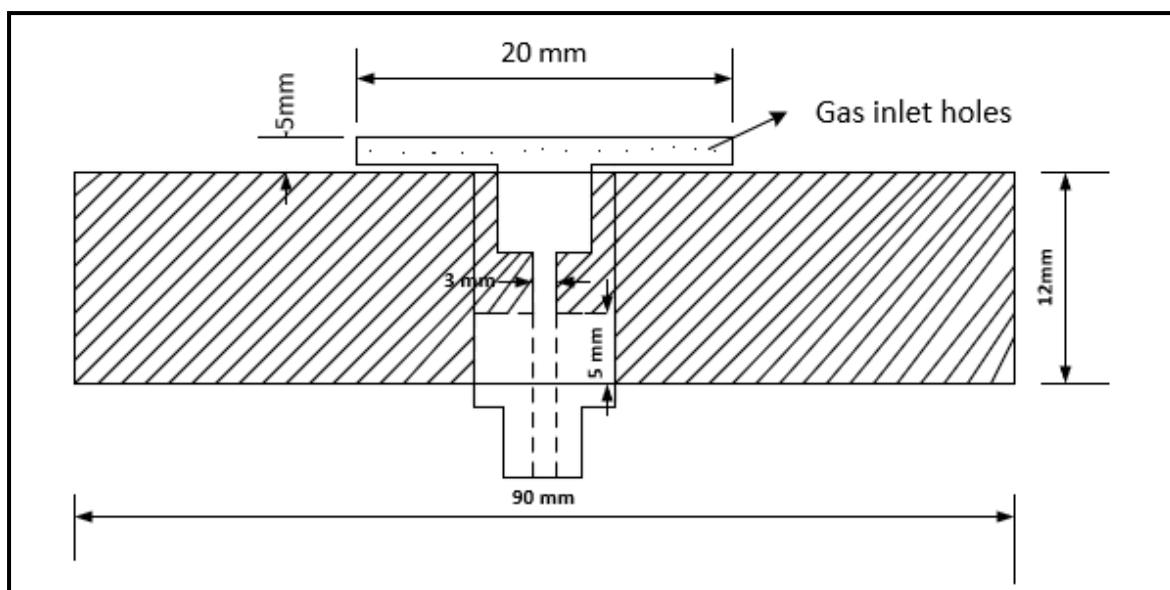


Figure G.2 : Cross section view of the bottom flange.

G.3 Mass balance

A DE150K2DL Kern floor standing scale (non-automatic balance) was acquired to meter the mass of canister utilized to make gas mixtures. The scale had a maximum weight limit of 150 kg, a minimum weight limit of 4 g, readability, and reproducibility of 5 g. Its uncertainty as specified by the supplier was ± 2 g with a stabilisation time of 2.5 s. The measuring platform dimensions in the format (B×D×M) mm were: (522×406×100) mm. The canister was placed manually at the centre of the weighing plate. When a stable weighing value was observed on the balance the canister weighing value could be read. Its operating temperature was between 5 and 35 °C, it could tolerate the air humidity of up to 80%.

Table G1: Tabulated data for the dissociation points utilised in Figure 6.8.

	Temp (K)	Press (Mpa)	In P	1/T	Calibr	del LnP
75-90 μm silica – CH₄-H₂O in 52 ml cell	278,23	4,60	1,53	0,00359	1,73	0,20
	277,70	4,56	1,52	0,00360	1,65	0,14
	283,30	6,67	1,90	0,00353	2,42	0,52
	283,06	6,49	1,87	0,00353	2,38	0,51
	280,97	5,69	1,74	0,00356	2,10	0,37
	276,66	4,19	1,43	0,00361	1,51	0,08
280 μm silica -CH₄-H₂O in a 300 ml cell	286,04	8,10	2,09	0,00350	2,78	0,69
	285,79	7,98	2,08	0,00350	2,75	0,67
	286,55	8,23	2,11	0,00349	2,85	0,74
	282,87	6,34	1,85	0,00354	2,36	0,51

	281,62	5,63	1,73	0,00355	2,19	0,46
	286,07	8,07	2,09	0,00350	2,78	0,69
	286,00	8,06	2,09	0,00350	2,77	0,69
100 nm porous glass (Uchida et al., 2002)	274,20	2,95	1,08	0,00365	1,16	0,08
	274,20	3,01	1,10	0,00365	1,16	0,06
	275,60	3,41	1,23	0,00363	1,36	0,13
	277,60	4,12	1,42	0,00360	1,64	0,22
	279,50	5,02	1,61	0,00358	1,90	0,29
	281,00	5,72	1,74	0,00356	2,11	0,36
50nm porous glass (Uchida et al., 2002).	278,70	4,80	1,57	0,00359	1,79	0,22
	281,30	6,42	1,86	0,00355	2,15	0,29
	281,50	6,61	1,89	0,00355	2,17	0,29
	281,60	6,68	1,90	0,00355	2,19	0,29
CH₄ -water system in 52 ml cell	278,89	4,50	1,50	0,00359	1,82	0,31
	279,88	4,97	1,60	0,00357	1,95	0,35
	277,11	3,78	1,33	0,00361	1,57	0,24
	283,21	7,12	1,96	0,00353	2,40	0,44
	279,87	4,97	1,60	0,00357	1,95	0,35
	280,66	5,48	1,70	0,00356	2,06	0,36
	285,72	9,40	2,24	0,00350	2,74	0,50
	284,61	8,22	2,11	0,00351	2,59	0,48
	281,06	5,75	1,75	0,00356	2,11	0,36
280 µm silica – CH₄-H₂O in 52 ml cell	284,94	7,32	1,99	0,00351	2,63	0,64
	283,97	7,27	1,98	0,00352	2,50	0,52
	281,65	5,56	1,72	0,00355	2,20	0,48
	282,51	6,09	1,81	0,00354	2,31	0,50
	282,28	5,86	1,77	0,00354	2,28	0,51

Table G.2: Summary of the replacement reaction carried out in the study.

		silica				0.5wt.% graphene nanoparticles			
		Trial Run	Run 1	Run 2	Run 3	Run 4	Run 5	Run 6	Run 7
H ₂ O charged	mol	5,555556	3,888889	3,888889	3,888889	3,888889	3,888889	3,888889	3,888889
CH ₄ Initial Pressure	bar	85,6739	89,6503	87,7617	88,3769	88,0108	82,5122	89,4092	83,6115
CH ₄ charged	mol	0,512295	0,653373	0,518036	0,664158	0,816744	0,70835	0,937064	0,914718
CH ₄ Unused	mol	0,49844	0,388364	0,362391	0,494965	0,66228	0,517099	0,664263	0,671405
CH ₄ trapped in hydrate	mol	0,113237	0,265009	0,155645	0,169193	0,154464	0,191251	0,272801	0,243314
H ₂ O remaining free	mol	3,656187	2,298837	2,95502	2,87373	2,962108	2,741382	2,252082	2,429007
%CH ₄ converted to hydrate	%	22,10382	40,5601	30,04516	25,47484	18,91211	26,99952	29,11234	26,59984
Soaking CH₄-hydrate in gas CO₂									
CO ₂ charged	mol	0.497	0,328449	0,525169	0,675489	0,868483	0,746279	0,777548	0,714149
Initial state									
Pressure	bar	50,51573	40,15963	70,10861	76,47852	80,03159	84,93106	80,62736	73,9626
Temperature	deg	3,796551	-0,50661	3,279564	0,277998	1,435644	2,288368	2,07133	1,734463
CH ₄ fraction in gas phase	mol	0,021917	0,03331	0,018436	0,005708	0,001066	0,00356	0,031769	0,086521
Final state									
Pressure	bar	40,95187	37,7379	40,27666	45,27384	41,398	50,63777	60,6206	55,31801
Temperature	deg	1,446794	1,253178	3,287674	0,940176	1,265342	4,321648	4,221613	2,911828
CH ₄ fraction in gas phase	mol	0,007798	0,158571	0,222314	0,139283	0,139283	0,125219	0,0584	0,025814
Discharge at the end of the reaction									
CH ₄ in the gas phase		0,001147	0,036338	0,058348	0,058584	0,049675	0,04527	0,03009	0,013136
CO ₂ from gas phase		0,146005	0,192823	0,238614	0,362025	0,306974	0,316258	0,005664	0,011632
CH ₄ from hydrate		0,22251	0,08951	0,2797	0,39132	0,3022	0,22536	0,05708	0,04289
CO ₂ from hydrate		0,046733	0,129632	0,218637	0,130269	0,100602	0,11604	0,001324	0,004352
N ₂ in the gas phase								0,747181	0,640728
N ₂ from the hydrate								0,018942	0,027539
Material balance (%)									
% CH ₄ replacement efficiency		1,013353	13,71212	37,48782	34,62527	32,15981	23,67058	11,03017	5,398894
%CO ₂ sequestration		51,73803	39,27005	54,56423	38,08813	64,61621	51,72827	76,63403	62,58446